INTERACTION STUDIES OF NANOMATERIALS WITH PLASMA PROTEINS USING EXPERIMENTAL AND COMPUTATIONAL METHODS

Myalowenkosi I. SABELA

(Reg. No: 2051394)

.

Submitted in fulfilment of the requirements of the Doctor of Philosophy in Chemistry in the Faculty of Applied Sciences at the Durban University of Technology

Year 2018

DECLARATION

I **Myalowenkosi I SABELA** hereby declare on my honour that the thesis submitted for the degree of Philosophy Degree (PhD) in Chemistry at the Durban University of Technology has not been submitted to any other university. Any portion of this work that has been published or under consideration for publication elsewhere is stated or cited accordingly.

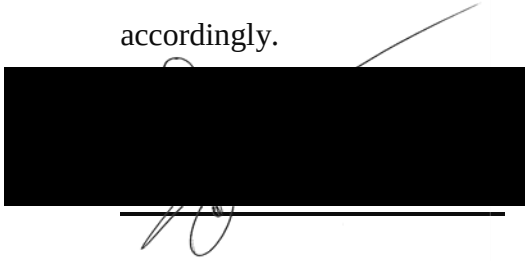

01 / 02 / 2018

Signature of Mr M. SABELA (Student) Date

02 / 02 / 2018

Signature of Prof K. BISETTY (Promoter) Date

02 / 02 / 2018

Signature of Prof S. SAGRADO (Co-Promoter 1) Date

02 / 02 / 2018

Signature of Prof B. MWAKIKUNGA (Co-Promoter 2) Date

ACKNOWLEDGEMENT

It is with the greatest delight that I salute my family for their audacious and daring support in many ways including academic adventures.

My grateful acknowledgment goes to Prof K. Bisetty for his companionate support since the day I started this journey.

I offer my sincerest gratitude to my co-supervisors, Prof Salvador Sagrado (University of Valencia, Spain) and Dr. B Mwakikunga (CSIR, Pretoria, South Africa) for their tirelessly support thrilled with great determination.

My deepest thanks also goes to Dr S. Kanchi and Dr D. Sharma for their openness in sharing knowledge and ideas. Through you, I have grown academically from strength to strength.

To all my friends, I thank you for your support, and motivation towards finishing this study.

I would also like to extend my gratitude to Durban University of Technology, and National Research Foundation (NRF) from South Africa for financial support. It is also my great pleasure to acknowledge Erasmus Mundus-EUROSA scholarship for the 10 months exchange program at the University of Montpellier, France wherein I received esteem host supervision from Dr M. Bechelany and Prof S. Balme for during my visit in the University of Montpellier, France.

My grateful acknowledgement goes to the Centre for High Performance (CHPC), Cape Town, South Africa for the access to the Accelrys Materials Studio 8.0 license.

Myalowenkosi I. SABELA

ABSTRACT

Nanomaterials have received considerable attention due to their unique physicochemical properties and various applications. The present study attempts to fill in the knowledge gaps by investigating the synthesis, stability, antimicrobial, and antioxidant properties, along with their sensing capabilities. For this purpose, chemical and green methods were used to synthesise silver nanoparticles, titanium dioxide nanomaterials and zinc oxide nanoparticles. For the chemical synthesis, bio-discrimination of macromolecules were investigated by calorimetric methods. Whereas for green synthesis, silver nanoparticles and zinc oxide nanoparticles were synthesized using plant extracts and tested for cytotoxicity and antioxidant properties followed by the electrochemical sensing of silymarin. The synthesized nanomaterials were analyzed by high-resolution transmission electron microscopy, X-ray diffraction, photoluminescence, fourier transform infrared spectroscopy, thermogravimetric analyzer, dynamic light scattering and zeta potential analyzer to better understand the morphology and capping. In addition, computational modelling techniques were implemented to assess the adsorption and interaction of nanomaterial with biomolecules through docking. The results arising from this work are presented in a case-study fashion ranging from colorimetry, protein-nanomaterial interactions through to biosynthesis.

For the colorimetric discrimination an extensive literature survey revealed that silver nanoparticles and gold nanoparticles based colorimetric assays, are widely used for screening in biosciences and metal analysis. A detailed review of colorimetric-based assays and identification of the fundamental parameters that influences such strategies are presented in this work. Accordingly, colorimetric discrimination of bovine serum albumin, lysozyme, single-stranded deoxyribonucleic acid, double-stranded deoxyribonucleic acid, and polynucleotides using silver nanoparticles was performed. This work demonstrates the importance of the starting material for colorimetric measurements preferably, with particles that are active in a wider absorbance region. Furthermore, an in-depth statistical analysis of the colorimetric data using principal

component analysis provided a framework for sensing of the selected proteins, deoxyribonucleic acid, and polynucleotides by simultaneously varying the concentration of a salt and biomacromolecules from 10 to 100 mM and from 0.1 to 10 μg mL^{-1} respectively.

In the case of the protein-nanomaterial interaction, the bioconjugate formation was studied between human serum albumin and TiO_2 nanostructures. The TiO_2 nanostructures were prepared by microwave assisted calcination at 200, 400, 700, and 900 °C. The results revealed that calcination above 400 °C had a significant impact on the surface of the nanomaterial, resulting in a lower surface adsorption of the protein confirmed by characterization techniques mentioned above. To further elucidate interactions between human serum albumin and titanium dioxide nanostructures, computational molecular docking studies were performed, resulting in the characteristic shapes of TiO_2 nanostructures correlating well with the experimental observations. The nanowires and nanotubes showed the much greater binding energy of –2.33 Kcal mol^{-1} and -2.85 Kcal mol^{-1}, respectively. In contrast to the nanotubes, the docked conformation of the nanowires showed a greater number of interactions.

In regard to the biosynthesis of silver nanoparticles prepared from aqueous plant extracts of *Iboza riparia leaf* and *Ilex Mitis* root bark, the formation of nanoparticles were due to the reduction of silver ions caused by electron transfer from the electron rich atoms of the extracts such as saponins and diterpenes. Therefore, relevant cytotoxicity studies were conducted with the MTT assay on HEK293T followed by an antioxidant activity with ABTS. Antimicrobial activity analysis depicted susceptibility of microorganisms in the order of nanoparticles by diterpenes (156 nm) followed by nanoparticles by saponins (50 nm).

Another biosynthesis of zinc oxide nanoparticles was performed using the extracts from *jacaranda mimosifolia* flowers and the c*arica papaya* seeds. The composition of both extracts was analyzed by gas chromatography–mass spectrometry. Oleic acid was found to be the major component in the extract of *jacaranda mimosifolia* flowers. The microwave assisted biosynthesis of nanoparticles was successfully completed within 5

Abstract

---

min resulting in 2–4 nm particle size. Further characterization was performed using the aforementioned instruments. The zinc oxide nanoparticles from *jacaranda mimosifolia* flowers were used to test the viability of gram-negative *Escherichia coli* and gram-positive *Enterococcus faecium* bacteria, which was found to be 48% and 43% respectively. In order to better understand the influence of oleic acid on the size and shape of nanoparticles, its adsorption on the different facets was explored computationally. The preferential passivation of the (101) facet was evident from the concentration profiles with an average distance of 1.4 Å for oleic acid. On the other hand, facets (100) and (002) were located at varying distances of 4 and 9 Å respectively. Overall the results indicated that the presence of oleic acid could drive the preferential growth of zinc oxide nanomaterials to nanorod array and other structures.

Furthermore, the composition of the zinc oxide nanoparticles from the *carica papaya* seed extracts was also identified using the aforementioned techniques. The results highlighted the role of oleic acid as a capping agent for these nanoparticles. In relation to their electrochemical applications, they were also tested for sensing activities of silymarin by incorporating them with multiwalled carbon nanotubes immobilized on the surface of a glassy carbon electrode. The electrochemical signals obtained from the modified electrode was 2-fold higher than *that of a* bare glassy carbon electrode. The electrode based on zinc oxide nanoparticle was able to detect silymarin in the commercial Milk Thistle tablet.

LIST OF CONTENTS

List of Content

----------o0o----------

LIST OF TABLES

LIST OF FIGURES

List of Figures

----------*o0o*----------

List of Figures

----------*o0o*----------

List of Figures

----------*o0o*----------

----------*o0o*----------

LIST OF SCHEMES

ACRONYMS AND SYMBOLS

ABTS	2,2'-azino-bis(3-ethylbenzothiazoline-6-sulphonic acid)
AgNPs	Silver nanoparticles
AgNP10	Silver nanoparticles with 10 nm size
AgNP50	Silver nanoparticles with 50 nm size
Arg_6	Six arginine residues
ATR-FTIR	Attenuated total reflectance fourier transform infrared
ATP	Adenosine triphosphate
AuNPs	Gold nanoparticles
BSA	Bovine serum albumin
CFU	Colony forming unit
DFT	Density functional theory
DLS	Dynamic light scattering
DS	Discovery studio
DSC	Differential scanning calorimetry
DTPs	Diterpenes
E. Coli	*Escherichia coli*
EDX	Energy dispersive X-ray
E. faecium	*Enterococcus faecium*
FTIR	Fourier transform infrared
FTMA	Fourier transform mass analyzers
FWHM	Full width half maximum
GCE	Glassy carbon electrode
GC-MS	Gas chromatography –Mass spectroscopy
HRTEM	High-resolution transmission electron microscopy
HPLC	High performance liquid chromatography
ICR-MS	Ion cyclotron resonance-Mass spectrometers
IR	Infrared

IT	Ion trap
JMFs	*Jacaranda mimosifolia* flowers
LDR	Linear dynamic range
LOD	Limits of detection
LP	Lattice parameters
Lys	Lysozyme
μHS	Microwave-assisted hydrothermal synthesis
MOs	Molecular orbitals
MS	Material studio
MALDI	Matrix-assisted laser desorption ionization
NIST	National institute of standards and technology
NM	Nanomaterial
NPs	Nanoparticles
NR	Nanorod
NS	Nanosheet
NT	Nanotube
NW	Nanowire
NNLS	Non-negative least squares
NR	Not reported
OTC	Ochratoxin
PBS	Phosphate-buffered saline
PGA	Penicillin G acylase
PL	Photoluminescence
PVT	Physical vapor transport
PCA	Principal component analysis
PKA	Protein kinase A
polyA	Polyadenylic acid
polyC	Polycytidylic acid
polyU	Polyuridylic acid

PVA	Poly(vinyl alcohol)
PLD	Pulse layer deposition
RMSD	Root mean square deviation
ROS	Reactive oxygen species
TOF	Time of flight
SPNs	Saponins
SEM	Scanning electron microscope
SIMS	Secondary ion mass spectrometry
AgNPs	Silver nanoparticles
SPR	Surface plasmon resonance
SQW	Square wave
TRF	Time resolved fluorescence
TCSPC	Time-correlated single photon counting
XRD	X-Ray diffraction
UCV	Unit cell volume

----------*o0o*----------

LIST OF PUBLICATIONS

Published

Deepali Sharma, **Myalowenkosi I. Sabela,** Suvardhan Kanchi, Phumlane S. Mdluli, Gulshan Singh, Thor A. Stenström, Krishna Bisetty, Biosynthesis of ZnO nanoparticles using *Jacaranda mimosifolia* flowers extract: Synergistic antibacterial activity and molecular simulated facet specific adsorption studies, *Journal of Photochemistry & Photobiology*, B: Biology 162 (2016) 199–207

Myalowenkosi Sabela, Sebastien Balme, Mikhael Bechelany, Jean-Marc Janot, and Krishna Bisetty, A Review of Gold and Silver Nanoparticle-Based Colorimetric Sensing Assays, *Advanced Engineering Materials*, 19, (2017) 1700270 (1 to 24)

Myalowenkosi I. Sabela, Talent Makhanya, Suvardhan Kanchi, Mohd. Shahbaaz, Danish Idress, Krishna Bisetty, One-pot biosynthesis of silver nanoparticles using Iboza Riparia and Ilex Mitis for cytotoxicity on human embryonic kidney cells, *Journal of Photochemistry & Photobiology, B: Biology*, 178 (2018) 560–567

Under review

Myalowenkosi I. Sabela, Mikhael Bechelany, Jean-Marc Janot, Krishna Bisetty and Sebastien Balme, Silver nanoparticles based colorimetric-spectroscopic discrimination of proteins, polynucleotides and DNAs, *Analytical Biochemistry*, 30 November 2017

Myalowenkosi I. Sabela, Bonex Mwakikunga and Krishna Bisetty, Crucial role of microwave-hydrothermal synthesis of TiO_2 nanostructures for bioconjugate formation with human serum albumin, *Journal of Colloids and Interfaces*, Sent 30 January 2018

CHAPTER 1

1 INTRODUCTION

This chapter provides a brief overview of chemical synthesis and green synthesis of nanoparticles along with interaction studies between biomacromolecules and nanomaterials. The need for reliable synthesis and an understanding of biomacromolecular interactions with nanoparticles is also reported in this work. Furthermore, the synergies between computational chemistry tools in relation to interactions between biomolecules and nanoparticles are presented in this section. This chapter is followed by the aims and objectives and a brief outline of the thesis.

1.1 Synthesis and biomacromolecular interactions with nanomaterials

The interest of researchers in nanotechnology has increased dramatically with the advancement in the synthesis of nanomaterial which enhances their fascinating and remarkable properties for diverse applications. The synthesis of nanomaterials at the dimensional scale is not new, but silver nanoparticles (AgNPs) and gold nanoparticles (AuNPs) have been used to color the ceramic glazes and stained glass for the applications in that involve materials such as proteins, enzymes, DNAs etc. Recent literature reviews reveal that the majority of the methods used in the synthesis of AgNPs are the physical and chemical methods. Biosynthesis of AgNPs is a bottom-up approach that mostly involves reduction/oxidation reactions. In such synthesis, the whole plant or its leaves, roots, flowers or fruits have selectively been used in the green synthesis of AgNPs. Due to differences in the synthesis process, it is often observed that the green synthesized nanoparticles have different properties and activities compare with synthetic AgNPs. Hence it is noteworthy to study the interactions of green synthesized nanoparticles and protein.

Currently, green fabrication of chemicals/materials plays a key role in the well-being of mankind including a sustainable environment. ‘Green Chemistry’, in contrast to

chemical methods promotes a greener, safer, and alternative methods of fabrication of materials. Therefore, the principles of green chemistry are currently utilized to design nanoscale products, the production of nanomaterials, method development, and the potential application of nanomaterials. The biological route of synthesizing nanoparticles has additional advantages, such as the stable production of nanoparticles with controlled sizes and shapes, the lack of subsequent complex chemical synthesis, the lack of toxic contaminants, and the ability for rapid synthesis using numerous medicinal plants and microorganisms. The use of biogenic synthesis is not limited to reduced environmental impact compared with some of the physicochemical production methods, but also because it can be used to produce large quantities of nanoparticles that are free of contamination with a well-defined size and morphology. The source of the plant extracts is known to influence the characteristics of the nanoparticles. This is because different extracts contain different concentrations and combinations of the organic reducing agent. In general, functionalization processes are applied to the synthesis of nanoparticles in order to improve the morphology, surface area, minimize aggregation, eliminate interaction amongst nanomaterials, and improve their microbial activities.

A good platform therefore exists for nanomaterials and its applications in daily use especially in healthcare products, but the level of toxicity remains a concern for using NPs at very low concentrations. Greater challenges exist nowadays for the application of nanoparticles in drug delivery systems. Nanoparticles are a type of colloidal drug delivery systems which can without problems cross blood-brain barrier enabling the interaction with cellular parts like protein, DNA, and enzymes which may indeed alter the conformation or functions of cellular biomacromolecules, resulting in unanticipated reactions. For this purpose, the broader goals of this work were to gain a better understanding of the interaction of nanoparticles with biomacromolecules. Notably, studies on the synthesis and interactions of AgNPs or zinc oxide nanoparticles (ZnONPs) or with biomolecules and cytotoxicity, using chemical and green methods are equally important. However, the toxicology of noble metals is unknown, but its applications and importance are well realized, despite an increase in the quantity of nanoparticles produced

on a daily basis. Accordingly, in this work the synthesized nanomaterials have been characterized by high-resolution transmission electron microscope (HRTEM), scanning electron microscope (SEM), X-ray diffraction (XRD), dynamic light scattering (DLS), Ultraviolet-visible (UV–Vis) spectroscopy, Fourier transform infrared (FTIR) and fluorescence. The resulting insights are expected to provide useful information for the use of green AgNPs and ZnONPs in medical application.

1.2 Aims and Objectives

This study is aimed at investigating the behavior of nanoparticles in the presence of biomacromolecules using experimental and computational techniques.

Objectives:

- To use natural plants for the biosynthesis of AgNPs and ZnONPs
- To synthesize TiO_2 nanostructures of various shapes for protein interactions
- To use the green synthesized ZnONPs to develop an electrochemical sensor for silymarin
- To elucidate the contribution of biomolecules in the formation of ZnONPs, its adsorption on different facets of ZnO using computational methods
- To develop and optimize a bivariate colorimetric method for the discrimination of proteins, DNAs and polynucleotides with unmodified AgNPs
- To use principal component analysis for clustering population from bare-eye colorimetric assay
- To study computationally, the adsorption of biomolecules on the surface of TiO_2 nanoparticles
- To study the antibacterial activity of the synthesized nanoparticles against gram-positive, *Enterococcus faecium*, and gram-negative, *Escherichia*.
- To evaluate the antioxidant activity of ABTS and its inhibitory effect on the human embryonic kidney cells in a concentration dependent manner.

1.3 Thesis Outline

Following the introduction, further chapters in this thesis are expanded as follows:

Chapter 2: This chapter provides general reviews on the nanoparticle-based colorimetric applications using gold and silver nanoparticles. Furthermore, the medicinal plants of interest for the green synthesis of silver nanoparticles and zinc oxide nanoparticles are explored. A brief review of the computational chemistry tools in relation to the adsorption of biomolecules onto nanoparticle surfaces is also introduced in this section.

Chapter 3: This chapter focuses on the theoretical principles underpinning the instruments that were used for experimental and computational studies carried out in this study. Furthermore, the equations in relation to the operation of the techniques are presented. Special attention is given to the DFT and molecular docking as implemented within the computational methods.

Chapter 4: This chapter details the chemical and reagents that were used in this study. The experimental and computational methodologies for all the case studies are also described. Other aspects of the methodology are embedded within the case studies to maintain clarity.

Chapter 5: This chapter reports on a bivariate colorimetric approach for the discrimination of proteins, DNAs and polynucleotides bio-conjugated with unmodified silver nanoparticles. The bare-eye colorimetric assay was supported by spectroscopy through to the evaluation of surface plasmon resonance properties. This approach is supported by a principal component analysis for clustering population.

Chapter 6: This chapter deals with the response factors of human serum albumin to various shapes of TiO_2 nanostructures supported by characterization studies.

Chapter 7: The characterization of AgNPs by green synthesis is described here, followed by the evaluation of its antioxidant activity on ABTS and the inhibitory effect on human embryonic kidney cells in a concentration dependent manner.

Chapter 8: This chapter reports on the biologically inspired route for the synthesis of ZnONPs with the composition of the extract identified and characterized by a host of analytical instruments.

Chapter 9: As an application of the work carried out in this study, this chapter reports on the electrochemical sensing of silymarin with a glassy carbon electrode, modified with multiwalled carbon nanotubes, and by green synthesized zinc oxide ZnONPs from *carica papaya* seed extract.

Chapter 10: A summary of the main findings is presented as an overview of the concluding remarks

Chapter 11: A list of references used within this thesis are enclosed.

1.4 Structure of the project

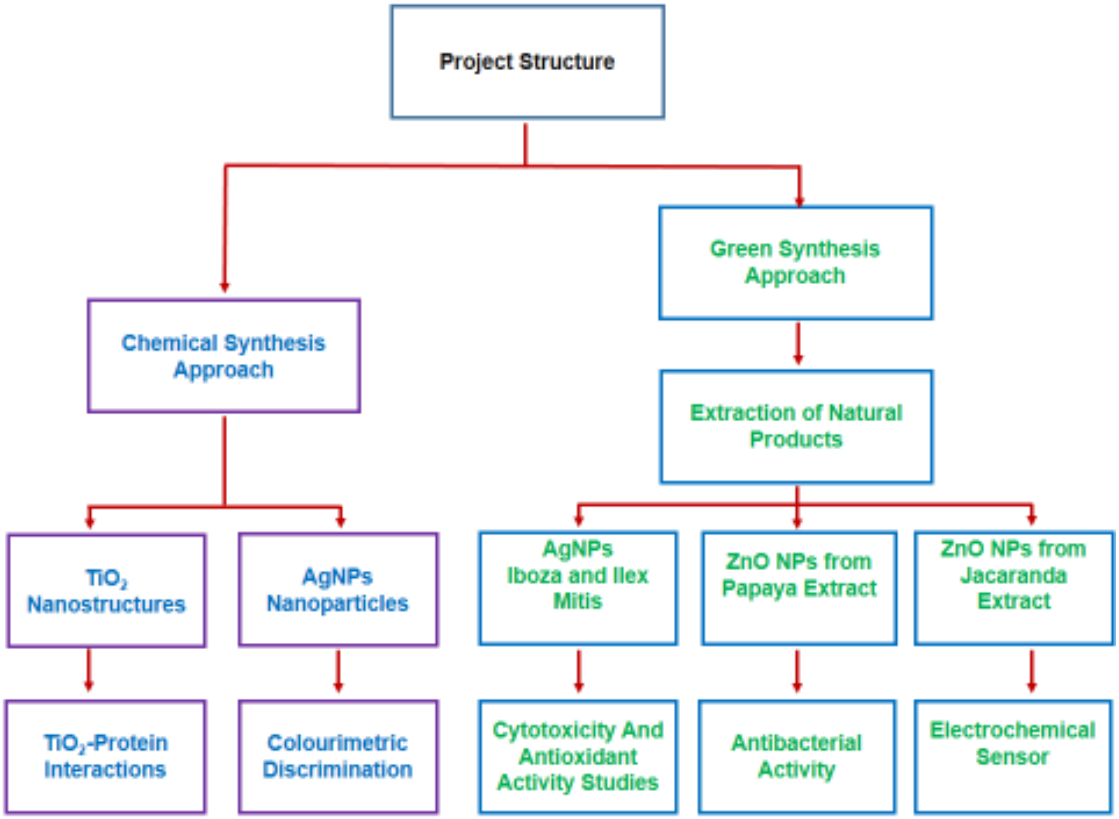

CHAPTER 2

2 LITERATURE REVIEW

This chapter provides brief details on the advantages of green synthesis of nanoparticle using natural plant extracts. It also provides a detailed literature review on the colorimetric applications for gold and silver nanoparticle. Furthermore, the synergies between computational chemistry tools in relation to adsorption of biomolecules onto nanoparticle surfaces is presented. This is followed by the theoretical principles of the experimental and computational protocols that were used.

2.1 Medicinal Plants for Nanoparticle-based biomedical applications

Medicinal plants have been used for centuries as traditional treatments for numerous human diseases throughout the world. This has attracted a vast interest from researchers to improve phyto-medicines and biologically active compounds that are isolated from medicinal plants. When the nanoparticles are stabilized with the bioactive natural extract, they form a corona. The bioactive compositions of the corona will influence the reaction between the biological fates and nanoparticles (Gunawan *et al.* 2014). Currently, several physical and chemical processes are widely used to synthesize metal nanoparticles, which allows one to obtain particles with the desired characteristics (Okitsu *et al.* 2007). However, these methods are usually expensive, labor-intensive, and are potentially hazardous to the environment and living organisms (Sharma *et al.* 2009; Gan *et al.* 2012). Thus, there is an obvious need for an alternative, cost-effective and at the same time a safe and environmentally sound method of nanoparticle production (Raveendran, Fu and Wallen 2003; Sharma *et al.* 2009; Narayanan and Sakthivel 2010; Shamaila *et al.* 2016; Shamaila *et al.* 2017). Despite the fact that "green" synthesis of nanoparticles using plant material is of considerable interest, it is worth studying those nanoparticles produced through physical and chemical methods. As a consequence of this,

there was a dramatic emergence of green synthesis of nanoparticles extracted from plants due to the natural products' ability to reduce the cytotoxicity of nanoparticles and with a less intricate process involved in their synthesis (Ravichandran *et al.* 2016). Hence, plant extracts remained the most affordable and accessible source for the green synthesis of bioactive nanoparticles. Several South African plants play a pivotal role as sources for new drugs and treatment of many kinds of diseases. Therefore, these medicinal plants have a long historical usage by traditional healers and knowledgeable elders (Ndamane *et al.* 2013). The *Ilex* Mitis plant shown in Figure 2-1(A) consists of saponins which are secondary metabolites with high molecular weight. They can be synthesized naturally by various plant species. They are glycosides with foaming characteristics and they normally consist of a polycyclic aglycones that are attached to one or more sugar side chains (Horo *et al.* 2015; Guo *et al.* 2016; Mikołajczyk-Bator *et al.* 2016). They also consist of either sterols or triterpenoids and water soluble sugar residues. Due to their amphiphilic nature, they are highly surface active and their biological activities are related to their chemical structures (Kerem, German-Shashoua and Yarden 2005; Lencina *et al.* 2011; Huang *et al.* 2016; Lu *et al.* 2016). Total saponins isolated from *Radix et Rhizoma Leonticis* have been reported to suppress the growth of tumour cells (Zhan *et al.* 2016).

Figure 2-1: Pictures of (A) *Ilex Mitis* and (B) Iboza *Riparia*

On the other hand, the *Iboza* Riparia plant shown in Figure 2-1(B) also known as *Tetradenia riparia* or Ginger Bush, is traditionally used as a medicinal plant by mainly Zulu and Tswane people in South Africa (SA) to treat chest complaints, stomach ache, relieve headaches and malaria (Gairola *et al.* 2009). More importantly, these plants have an acceptable therapeutic index for the development of novel drugs. The compounds previously isolated from such species include diterpenes and triterpenes, namely: ibozol (Zelnik *et al.* 1978), umuravumbolide, deacetylumuravumbolide, deacetylboronolide (Van Puyvelde *et al.* 1979), 8(14),15-sandaracopimaradiene-7α,18-diol (Van Puyvelde *et al.* 1986). Shakeel and co-workers have reported a one-step method for the green synthesis of AgNPs using *Withania* somnifera, *Crotolaria* retusa extracts with exceptional antimicrobial and catalytic activities (Ahmed *et al.* 2016a; Ahmed *et al.* 2016b). Extensive literature studies exist on the green synthesis of AgNPs however, this is the first report using *Iboza* Riparia leaf and *Ilex* Mitis root bark extracts for the biosynthesis of AgNPs. Some of the other green materials reported for the synthesis of AgNPs are shown in Appendix 1, Table A1. However, in contrast to the vast analysis available on nanoparticle bacterial activity, there are limited reports on the biocompatibility studies such as MTT assays.

Among different semiconductors and metal oxides, ZnO is one of the most promising materials because of its unique characteristics which are responsible for novel biological functionalities. The nanostructure form has become the focus of attention for the research community due to its unique antifungal (Sharma *et al.* 2010), antibacterial (Lakshmi Prasanna and Vijayaraghavan 2015), antiviral (Antoine *et al.* 2012), wound healing (Barui *et al.* 2012), UV filtering properties, , excellent stability, biocompatibility, high catalytic and photochemical activity (Sun *et al.* 2014; Tamuly *et al.* 2015). Therefore, it is crucial to devise tunable synthesis of ZnONPs with desired morphology and size to further explore their unveiled potentials thereby enabling researchers to manipulate the present material for the fabrication of devices. Literature studies provide an insight into different approaches for the fabrication of ZnO nanostructures like gas phase methods which include chemical vapor deposition (CVD), physical vapor transport (PVT) and

pulsed layer deposition (PLD) (Andrey *et al.* 2014). Chemical methods are cost effective in contrast to gas phase methods. Mechanochemical (Liming *et al.* 2006; Lu, Ng and Yang 2008), solvothermal (Ghoshal *et al.* 2009; Bai *et al.* 2015), sol-gel (Zhang *et al.* 2009; Lima *et al.* 2014), precipitation (Zhan *et al.* 2016), hydrothermal (Søndergaard *et al.* 2011; Ramimoghadam, Bin Hussein and Taufiq-Yap 2013) and microwave methods (Bilecka, Elser and Niederberger 2009; Sharma *et al.* 2011) have been classified under chemical methods. Among these, the hydrothermal method is widely used due to green, low cost, and low temperature synthesis. This method is modified with the use of capping or templating agents, which aid in modifying the shape of a NPs by adsorbing on the specific facet of a metal oxide crystal (Ramakrishnan *et al.* 2015).

In the recent years, different types of plant extracts have been reported to be used as reducing or capping agents in the synthesis of NPs. Some of the examples include the eco-friendly synthesis of ZnONPs using leaf extracts of *Pongamia pinnata* (Sundrarajan, Ambika and Bharathi 2015), *Nerium oleander* (Lakshmeesha *et al.* 2014), aloe leaf broth (Gunalan, Sivaraj and Rajendran 2012), *Solanum nigrum* (Ramesh, Anbuvannan and Viruthagiri 2015), apple pectin (Wang *et al.* 2012) and aqueous extract of *Vitex negundo L.* (Ambika and Sundrarajan 2015). The biomolecules present in the plant extracts act as efficient capping agents thereby playing a pivotal and versatile role in the NP synthesis. The capping agents appear to stabilise NPs by different mechanisms that include electrostatic stabilization, steric stabilization, stabilization by hydration forces, depletion stabilization and stabilization using van der Waals forces. The stabilization of NPs is important for their functions and different applications (Ajitha *et al.* 2016).

Flowers are of great aesthetic value and maintain ecological balance in the environment. They are mainly utilized for their beauty as they radiate different colors to the surroundings. They serve the purpose when they bloom but once they wilt, they fall off as trash. *Jacaranda mimosifolia* belongs to the bignoniaceae family and is widely grown in warm parts of the world. It has showy blue or violet flowers and has been found to have antiseptic and antibiotic qualities. Traditionally, the flowers, leaves and barks are used to ease neuralgia, varicose veins and to treat leukemia (Joselin *et al.* 2013). In the

present work, the fallen flowers of *Jacaranda mimosifolia* plant normally regarded as waste were used for the biosynthesis of ZnONPs for the first time to the best of our knowledge. ZnO nanostructures have been reported to be effective against the growth of bacteria (Akhil *et al.* 2016). Thus, the synthesized ZnONPs were evaluated for the antibacterial activity against gram positive (*Enterococcus Faecium*) and gram negative (*Escherichia coli*) bacteria. Generation of reactive oxygen species (ROS) mainly hydroxyl and superoxide radicals resulting in the oxidative stress is found to be the underlying mechanism for the bacterial cell death or static growth. The release of metal ions on interaction with the cellular components contributes to the bioactivity of the NPs (He *et al.* 2014). To elucidate the contribution of oleic acid in the formation of ZnONPs, its adsorption on different facets of ZnONPs was carried out computationally as the shape and size are dependent on the exposure of different facets of a crystal.

2.2 Colorimetric Reviews

2.2.1 Detection of small molecules using AuNPs and AgNPs

This section focuses on small molecules particularly cysteine and dopamine, because they have been extensively studied using colorimetric methods. A summary of possible colorimetric detection approaches for metals, ligands, and macromolecules is provided in Appendix 2: Figure A1.

Cysteine has been employed as a common strategy for the detection of metals, but it also can be quantified by colorimetric assays. Metal ions are used as cross-linking agents for cysteine-AuNP or –AgNP pairs to induce NP aggregation confirmed by a red to blue color change of the NP solution. The degree of aggregation depends on the cysteine concentration and the average AuNPs diameter in the presence of different cysteine concentrations. In such colorimetric assays, the organic molecules bind to the Au/AgNPs surface via their amine ($-NH_2$) (blue) or thiol ($-SH$) (yellow) terminal groups (Figure 2-2).

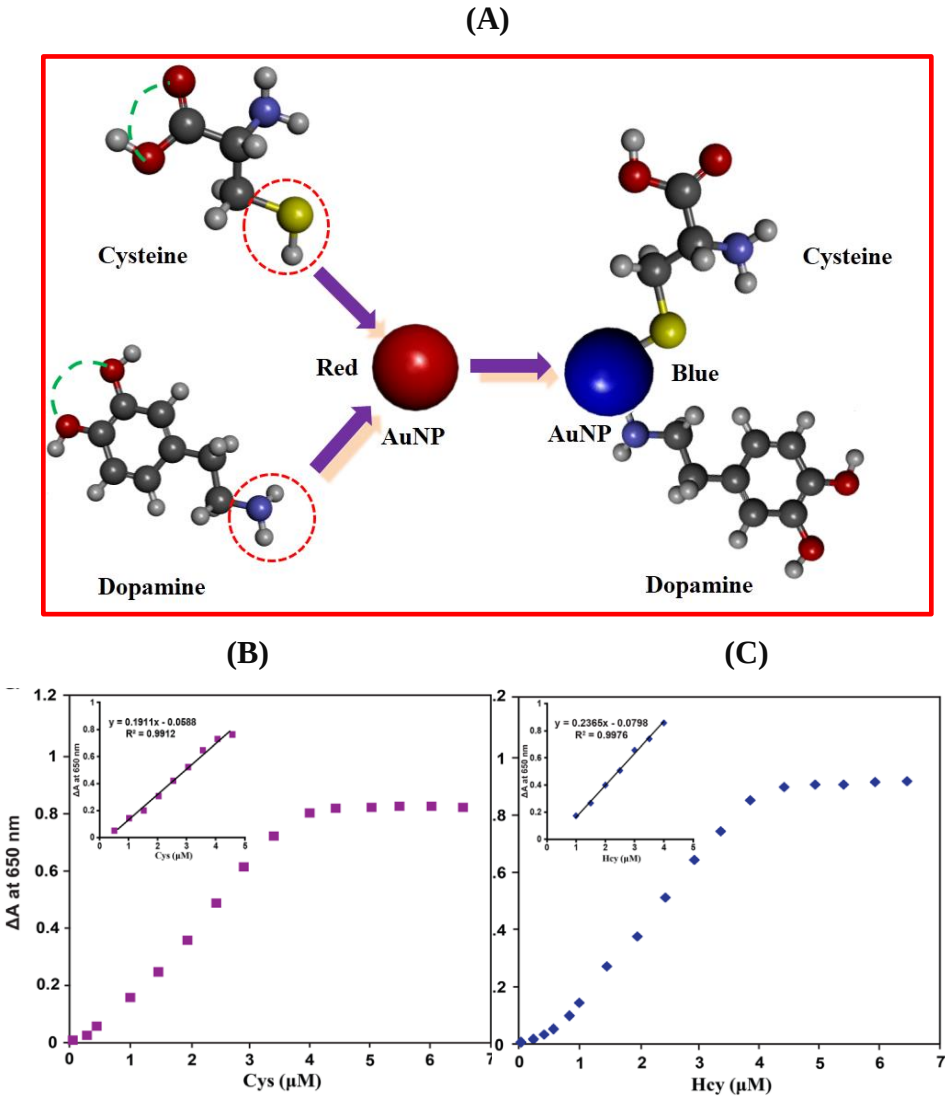

Figure 2-2: (A) Chemisorption model for cysteine and dopamine on the AuNP surface. (B) and (C) shows the linear relationship of nonionic fluorosurfactant-capped gold nanoparticles versus Cys and Hcy 650 nm.

Ligands with the $C_6H_8O_6$ formula, such as ascorbic acid which have no $-NH_2$ or $-SH$ functional groups, preferably bind to the AuNPs surface, and are highly unlikely to induce

AuNPs aggregation (Kuhnle *et al.* 2002; Aryal *et al.* 2006; Zhang, Li and Xu 2010; Jongjinakool *et al.* 2014).

The thiol groups of cysteine interact with the surface of colloidal AuNPs or AgNPs via chemisorption-type interactions; however, cysteine can complex with metal ions, such as Pb^{2+}, Zn^{2+}, Cu^{2+} (Li and Li 2009; Zhang, Li and Xu 2010), Ca^{2+} (Hajizadeh *et al.* 2012; Han *et al.* 2014), Cr^{3+} (Ravindran *et al.* 2011), with a ratio of two cysteine molecules per metal ion (Li and Li 2009; Lee *et al.* 2013). In the presence of metal ions, cysteine can induce AgNP and AuNP aggregation with a color change from yellow to purple and blue to red, respectively (Li and Li 2009; Ravindran *et al.* 2011; Hajizadeh *et al.* 2012; Jongjinakool *et al.* 2014). These assays are based on the NP distance-dependent optical properties after coordination, as confirmed by the change in the zeta potential from -30.7 mV for pure AgNPs to -19.63 mV after interaction with cysteine and Cr^{3+} (Ravindran *et al.* 2011). Specifically, Hajizadeh *et al.* reported that cysteine can rapidly induce AgNP aggregation (yellow-to-red color change) in the presence of Ca^{2+} and 10 mM NaCl, leading to a decrease in electrostatic repulsion and faster aggregation (Hajizadeh *et al.* 2012). Cysteine concentration can be determined also by using AuNPs and a UV-Vis spectrometer with a LOD of 10 nM (Li and Li 2009). The ratio between absorption at 524 nm and absorption at 396 nm (A_{524}/A_{396}) is linear with a cysteine concentration range from 0.25 to 10 mM ($R^2 = 0.993$) with a LOD of 83 nM (Hajizadeh *et al.* 2012). Jongjinakool and co-workers detected cysteine in a concentration range from 0.1 to 0.6 ppm with a LOD of 0.01 ppm (Jongjinakool *et al.* 2014). Figure 2-2B and C demonstrate that cysteine and homocysteine were identified based on the different SPR wavelengths induced by aggregation of non-ionic fluoro-surfactant-functionalized AuNPs upon addition of a mixture of the amino acids. The absorbance changes due to AuNPs aggregation induced by cysteine and homocysteine increases the individual absorbance values (LDR from 0.5 to 4.5 μM for cysteine and LOD (S/N=3) of 0.4 μM for homocysteine) (Gao *et al.* 2013).

When dopamine and Cu^{2+} solutions are mixed, the amine group directly coordinates with Cu^{2+} without nitrogen atoms bonded to the gold surface (Zhang, Li and

Xu 2010). In contrast to cysteine-based methods, the LOD of 30 nM for dopamine with a linear calibration curve for two concentration ranges (33 to 100 nM and 0.3 to 4.5 µM) and with correlation coefficients of 0.9981 and 0.9979, respectively (Zhang, Li and Xu 2010). Likewise, the addition of 5.0 mM Cu^{2+} improves the colorimetric probe to a LOD value of 200 nM (Su *et al.* 2012). AuNPs also can be used for the quantitative colorimetric detection of neurotransmitters that mediate the generation and growth of AuNPs, with a LOD of 20 µM for adrenaline, 2.5 µM for dopamine, L-dopamine and noradrenaline (Baron, Zayats and Willner 2005).

The metal ion-Au/AgNPs interaction is mainly due to coulombic interactions with their strengths directly related to the molecular structure and charged groups. Therefore, selectivity can be improved by working on these two parameters (Chen *et al.* 2014). For instance, researchers highlighted the excellent selectivity of AuNP-based colorimetric assays for cysteine compared with other biomolecules, such as thioglycolic acid and mercaptoethyl alcohol (Li and Li 2009), glutathione (Li and Li 2009; Ghasemi, Hormozi-Nezhad and Mahmoudi 2015b) glutathione disulfide (Ghasemi, Hormozi-Nezhad and Mahmoudi 2015b), aspartic acid and glutamic acid (Qian *et al.* 2012). Moreover, the selectivity also changes when using cysteine derivatives, namely glycine, dipeptide Cys-Gly, cysteamine, mercaptopropionic acid, S-protected (S-methyl-L-cysteine), N-protected (N-acetylcysteine) and O-protected cysteine (L-cysteine methylester hydrochloride), as indicated by the color change ranging from yellow to pink and peak broadening (Athilakshmi, Mohan and Chand 2013). Therefore, it is imperative to investigate the detection of sulfur-containing amino acids compared with other standard amino acids (Athilakshmi, Mohan and Chand 2013). Chen *et al.* used 19 naturally occurring amino acids, but they could not improve the colorimetric response of cysteine (Chen *et al.* 2009).

Another strategy shown in Figure 2-3. for cysteine detection is based on the observation that when cysteine is added to AuNPs/ssDNA, the ssDNA molecules that stabilise AuNPs against salt-induced aggregation are displayed spontaneously by cysteine encapsulation on the AuNPs surfaces, via an Au–S bond (Chen *et al.* 2009). The salt-

induced aggregations result in a characteristic AuNPs color change from red to blue (Chen *et al.* 2009; Athilakshmi, Mohan and Chand 2013). According to Chen *et al.* (Chen *et al.* 2009) this approach is not feasible with other amino acids.

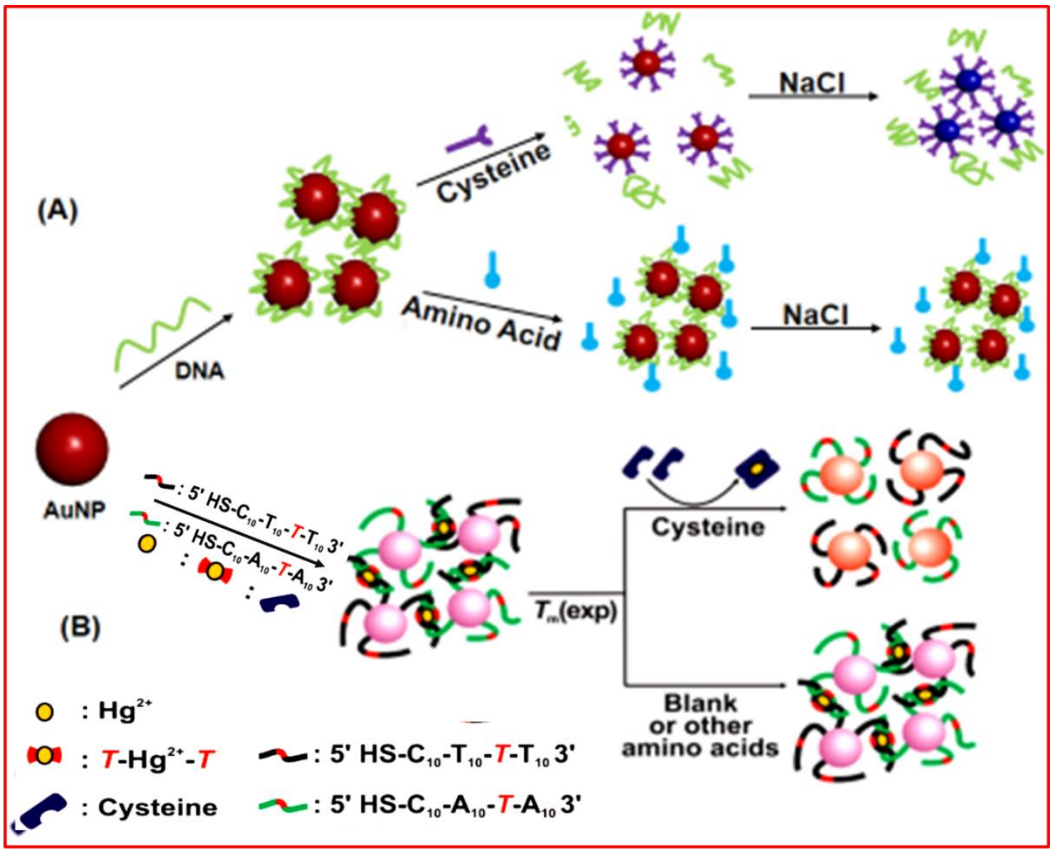

Figure 2-3: (A) In the presence of cysteine, the ssDNAs is displayed by cysteine on AuNPs surface resulting in AuNP aggregation and in a color change from red to blue upon addition of NaCl. Other amino acids do not lead to a color change due to the absence of thiol groups (Chen *et al.* 2009). (B) Cysteine colorimetric detection using AuNPs probes that contain T-T mismatches complexed with Hg^{2+}: competitive approach in which cysteine can displace Hg^{2+}(Lee *et al.* 2008)

In this system shown in Figure 2-3, the A_{640}/A_{525} ratio is linearly dependent on the cysteine concentration ranging from 0.1 to 5.0 µM with LOD of 100 nM (Chen *et al.* 2009). In

contrast to methods that require AuNPs modification, this approach is simple and fast, but it requires specific links between the biomolecules and AuNPs to allow ssDNA displacement from the NPs surface. On the other hand, Mirkin's group developed a cysteine detection assay shown in Figure 2-3B where two sets of AuNPs probes are functionalised with different oligonucleotide sequences (probe A: 5' HS-C10-A10-T-A10 3'; probe B: 5' HS-C10-T10-T-T10 3') to rapidly form aggregates upon combination through the thymidine-thymidine (T-T) mismatches complexed with Hg^{2+} with LODs as low as a 100 nM (Lee *et al.* 2008). Comparison of the two methods (ssDNA-AuNPs and mismatch assay) suggests that they rely on the distance-dependent optical properties of AuNPs, the sharp melting transition of oligonucleotide-AuNPs aggregates and the very selective coordination of Hg^{2+} with cysteine during which the purple-to-red color change occurs (Lee *et al.* 2008; Chen *et al.* 2009). However proteins with one free cysteine residue, such as human serum albumin, can spontaneously attach to AuNPs surfaces through Au-S bond formation (Schofield *et al.* 2006). These studies demonstrate that the presence of negatively-charged carboxyl groups in the cross-linkers are essential to induce AuNPs aggregation through ion pair interactions between amino groups present in cysteines and carboxyl groups in the cross-linkers (Qian *et al.* 2012; Athilakshmi, Mohan and Chand 2013). In comparison to dopamine- and cysteine-based methods it was evident that functionalised groups present on the surface also plays a key role in metal detection.

2.2.2 Recognition of chiral molecules

Stereochemistry plays a central role in molecular recognition and interactions. Indeed, the molecule's chemical and biological properties depend not only on the nature of their constituent atoms, but also on their position in space (Kuhnle *et al.* 2002). Currently, chiral molecules are mostly separated with techniques like capillary electrophoresis, high-performance liquid, and gas chromatography. Nanoparticles allow for the easy detection of chiral molecules by the naked eye. For instance, the color of the AuNPs solution changes from red to blue in the presence of D-tryptophan (LOD of 0.1

µM and LDR of 0.2–10 µM), but not of L-tryptophan (Zhang *et al.* 2014). Interestingly, AuNPs can selectively adsorb D-tryptophan, and therefore, L-tryptophan molecules can easily be separated by simple centrifugation of the tryptophan/AuNP solution (Zhang *et al.* 2014). The infrared spectra confirmed the D-tryptophan absorption to AuNPs by the disappearance of the NH (NH^{3+}) stretching absorption peaks (3078 and 3038 cm^{-1}), leaving the carboxylic group (-COOH) and the nitrogen atom of the indole ring free for further coordination. This distinctive feature allows for binding of one Cu^{2+} ion to two tryptophan molecules by coordination with the COOH and nitrogen atom of the indole ring, hence allowing for chiral recognition (Zhang *et al.* 2014). Another reported visual differentiation is between the D- and L-mandelic acid, this was based on their chirality towards 13 nm l-tartaric acid-capped AuNPs. The L- mandelic acid solution was able to change the red color of l-TA-capped AuNPs to a bare-eye observable blue, while d-MA did not trigger any color change (Song, Xu and Li 2015). The AgNPs capped with a novel chiral R-mandelic acid-derived calix[4]arene (R-MAC4), for it good optical and structural properties. These self-assembled NPs were used to recognize the N-Fmoc-D/L-aspartic acid (D/L-FAA)(Sun *et al.* 2015).

2.2.3 Detection of macromolecules

Nanoparticles can be easily modified by replacing surface-adsorbed weak ligands (e.g., negatively charged citrate ions) with thiolated macromolecules that are difficult to displace due to their strong binding to the surface. The literature survey is tabulated in appendix 2; Table A2.1.

Xue and co-workers described citrate-AuNP-based assays for trypsin and arginine residues screening as can be seen in Figure 2-4. The aggregation of negatively charged citrate-capped AuNPs in the presence of a peptide composed of six arginine residues (Arg_6) occurred mainly through electrostatic interactions, and led to a red-shift of the usual SPR profile (Xue, Zhang and Zhang 2011). However, when the Arg_6 peptide was hydrolyzed into fragments upon trypsin addition in the solution, the electrostatic

interactions between AuNPs and Arg_6 residues were weakened and, therefore, neither AuNPs aggregation nor SPR shift was observed.

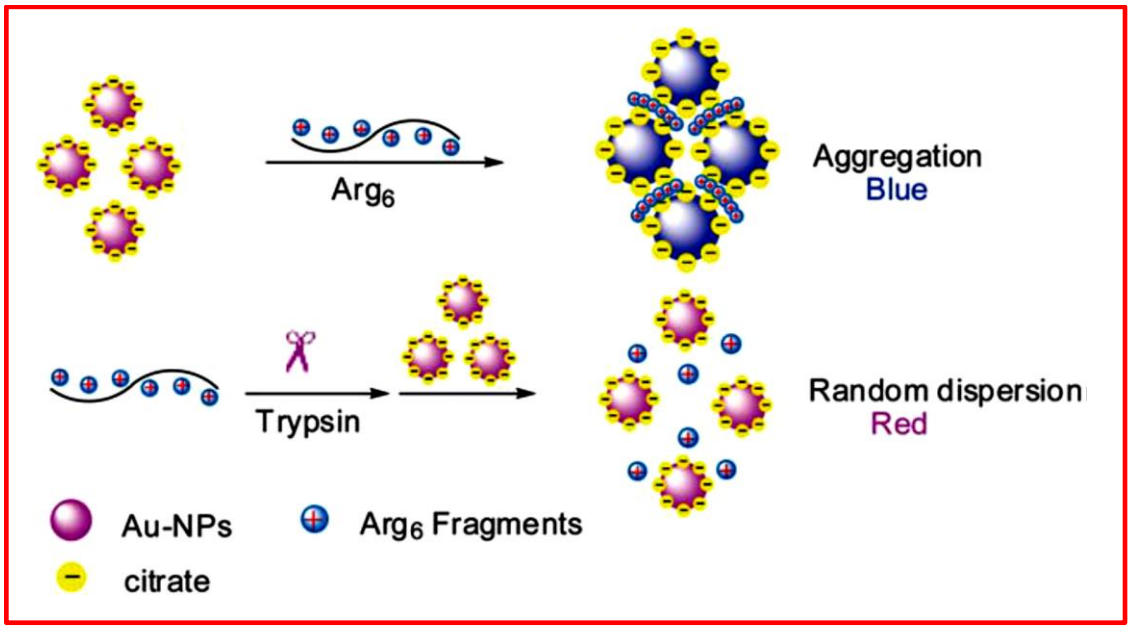

Figure 2-4: Colorimetric assay for trypsin by using AuNP aggregation based on trypsin-catalyzed hydrolysis of Arg_6 for random dispersion of citrate capped AuNPs. Reproduced with permission from (Xue, Zhang and Zhang 2011).

Moreover, Arg_6 hydrolysis catalyzed by trypsin is retarded if trypsin inhibitors are present in the solution. This feature was used to develop a label-free assay for trypsin (LOD: 1.6 ng mL^{-1}) and Arg_6 residues screening with AuNPs (Xue, Zhang and Zhang 2011). Similarly, the interaction of citrate-AuNPs with fibrinogen to form fibrinogen–AuNPs through electrostatic and hydrophobic interactions were used for the detection of thrombin (LOD: 0.04 pM and LDR: 0.1–10 pM; R^2 = 0.96) (Chen, Huang and Chang 2010). Although the mechanism of detection was the same, the molecular interactions were different. Indeed, fibrinogen was adsorbed on NPs before the addition of thrombin (Chen, Huang and Chang 2010). Conversely, trypsin interacts with Arg_6 before the NPs addition

into the system (Xue, Zhang and Zhang 2011). Detection of thrombin has been improved by the use of catalytic enlargement as shown in Figure 2-5 (Pavlov *et al.* 2004).

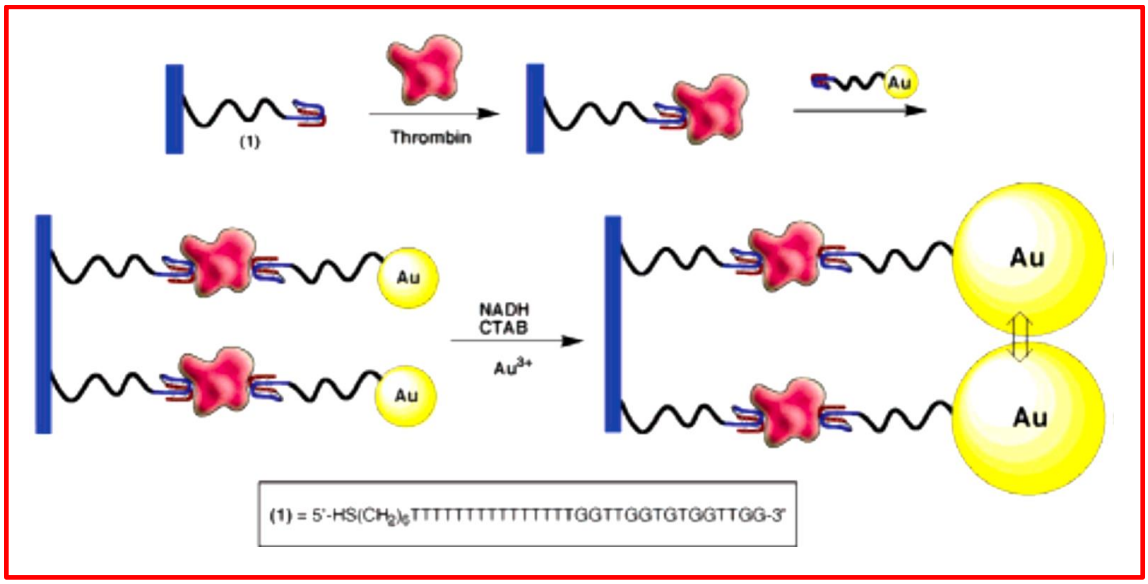

Figure 2-5: Amplified thrombin detection on surfaces by catalytic enlargement of thrombin-aptamer-functionalised AuNPs (Pavlov *et al.* 2004). As the concentration of thrombin increases, the surface loading of bound thrombin is higher, resulting in a number of AuNP seeds for enlargement.

Specifically, upon aptamer-AuNPs reaction with thrombin, AuNPs aggregate. But in the presence of other proteins such as 200 nM bovin serum albumin (BSA) or human IgG antibodies), the aptamer-AuNPs do not precipitate implying that the precipitation originates from the specific interaction between aptamer and thrombin (LOD: 20 nM) (Pavlov *et al.* 2004). Chen's group adopted a similar strategy, where they evaluated the possibility of using mannopyranoside-encapsulated AuNPs/concanavalin (Man-AuNPs/Con A) complexes for a competitive colorimetric assay for ten proteins. However, only thyroglobulin, *bandeiraea simplicifolia* lectin I (BS-I), soybean agglutinin (SBA) and *maackia amurensis* (MAL) significantly modified the absorption spectrum of Man-AuNPs/Con A complexes (Tsai, Yu and Chen 2005). In contrast to the method proposed

by Xue *et al.* whereupon the introduction of thrombin in the fibrin–AuNP solutions, catalyses the polymerization of the free and conjugated fibrinogen species to form insoluble fibrillar fibrin–AuNP agglutinates (Chen, Huang and Chang 2010; Xue, Zhang and Zhang 2011). Lastly, Guarise *et al.* exploited the fact that, compared with the native peptide substrates, protease-cleaved peptides do not induce NPs aggregation (and thus the color of the solution does not change) to detect two proteases (thrombin and lethal factor) (Guarise *et al.* 2006).

Quercetin-AuNPs have been used as a colorimetric probe for the detection of amino acids, such as arginine (Arg), histidine (His) and lysine (Lys). Indeed, quercetin-AuNPs aggregation caused by amino acids leads to a color change from red to blue (Rawat and Kailasa 2014). In optimal conditions, a linear relationship exists between the absorption ratios at different wavelengths (A_{702}/A_{525} for Arg, A_{693}/A_{525} for His, and A_{745}/A_{525} nm for Lys). Corresponding concentration ranges from 1.25 to 2.50 µM for Arg; from 1 to 1,00 µM for His and Lys, with LOD values of 0.04, 0.03, and 0.02 µM, respectively, at pH 5.0 (Rawat and Kailasa 2014). Siddhartha and Debabrata (2010) reported that protein estimation is within a LOD of 10-80 µg mL^{-1} using unmodified AgNPs (Siddhartha and Debabrata 2010).

It has almost been a decade since the sequence-length-dependent adsorption of ssDNA on AuNPs has been investigated for colorimetric nuclease assays and measurement of oxidative DNA damage (Shen *et al.* 2009). Based on ssDNA adsorption rate on citrate-AuNPs, it can be hypothesised that incubation with AuNPs for a specific period of time can lead to differential adsorption of short and long ssDNA. Consequently, the stability of the ssDNA-AuNPs complex in the presence of salt could be influenced by the ssDNA length (Shen *et al.* 2009). The confirmation of this hypothesis led to the development of colorimetric assays taking advantage of ssDNA length to improve adsorption. For example, when ssDNA is cleaved by the S1 nuclease or –OH radicals in small fragments, this shorter ssDNA can be rapidly adsorbed on AuNPs and significantly

enhance the negative charge density on each AuNP surface for the same time of incubation (Figure 2-6).

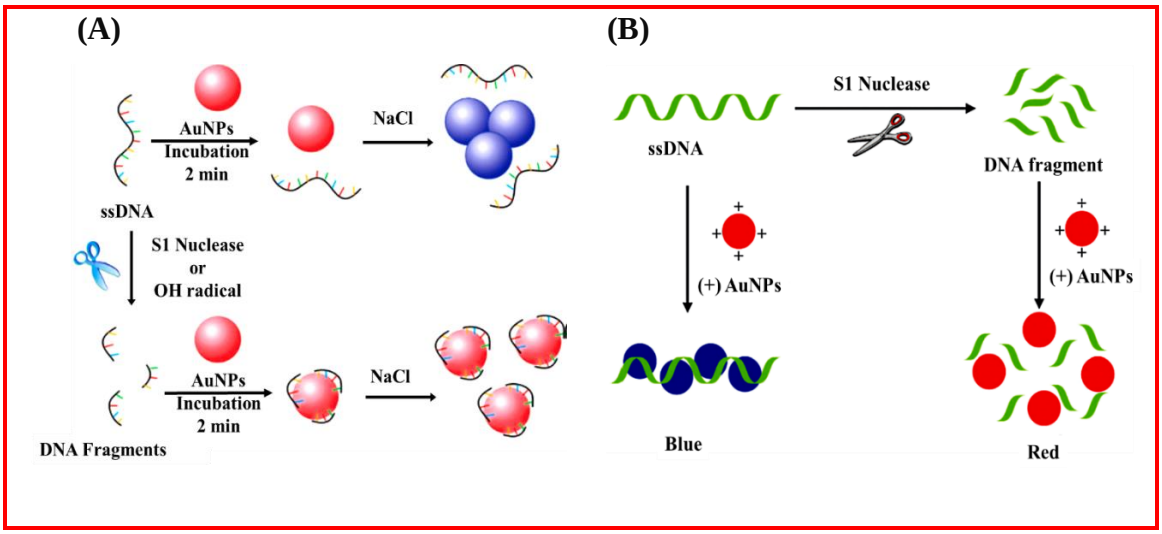

Figure 2-6: schematic representation of AuNP-based colorimetric strategies for ssDNA cleavage assays. (A) Salt-induced NP aggregation before and after ssDNA cleavage by the S1 nuclease or OH radicals. Reproduced with permission from (Shen *et al.* 2009). (B) Nuclease activity assay using positively charged AuNPs and polyanionic ssDNA ((+)AuNPs). Reproduced with permission from (Cao *et al.* 2011).

Basically, charging the NPs surface increases the electrostatic repulsion between the ssDNA-AuNPs complexes enough to inhibit NP aggregation at the same salt concentration, and the solution color does not change. Thus, DNA cleavage can be directly visualized by the naked eye (Shen *et al.* 2009). Charge interaction between positively charged AuNPs and polyanionic ssDNA leads to AuNPs aggregation that can be monitored by the color change from red to blue (Figure 2-6) (Cao *et al.* 2011). However, in the presence of the S1 nuclease, the ssDNA substrate is cleaved into small fragments, and the AuNPs solution remains red. Thus, the nuclease activity can be easily monitored by the naked eye or with a simple colorimetric reader (Cao *et al.* 2011). In this case, the exocyclic amino group of nucleotides is the main cause of nucleotide-dependent

aggregation because cysteine-capped AuNPs are positively-charged at pH 3.6 (with a *pKa* of 10.75), leading to efficient electrostatic interactions with the negatively charged DNA. These results complement each other because during S1 enzymatic activity, ssDNA is degraded into smaller fragments that cannot induce aggregation (Shen *et al.* 2009; Cao *et al.* 2011). Additionally, the non-crosslinking AuNPs aggregation induced by the loss of surface charges has also been exploited for enzymatic activity testing and screening for potential inhibitors (Zhao *et al.* 2007b). This approach has been extended to the serotype I-specific detection of dengue virus DNA. In the absence of the DNA target solution, peptide nucleic acids (PNA) induce AuNPs aggregation with a red-to-purple color change and the appearance of a second absorbance peak at 650 nm due to the AuNPs surface coating by PNA (Abdul Rahman *et al.* 2014). Likewise, the AuNP (d = 20.17 ± 1.8 nm) that are reduced and stabilised by sialic acid can be used for the colorimetric detection of influenza viruses (Lee *et al.* 2013). The discrimination of such molecules can also be standardized using chemometric techniques including hierarchical cluster analysis and principal component analysis. This approach was used to accurately classify and measure the array response of cysteine, gluthatione, glutathione disulfide and interferences without any misclassification (Ghasemi, Hormozi-Nezhad and Mahmoudi 2015a).

2.2.4 DNA-functionalised nanoparticles (aptasensors)

This is a fascinating area of NP-based colorimetric assays. Much attention has been focused on aptamers (i.e., ssDNAs and oligopeptides with high binding affinity and selectivity for target molecules) as they are powerful biological macromolecules (Appendix 2, Table A2.2). The advantages of the aptamer compared with antibodies includes; lower immunogenic response, the possibility of chemical synthesis and modification which also enhance their potential(Song *et al.* 2011). They are generally selected *in vitro* by using the systematic evolution of ligands by exponential enrichment (SELEX) technique and random-sequence nucleic acid libraries (Mehta *et al.* 2011; Song *et al.* 2011; Song *et al.* 2012; Liu *et al.* 2013; Kwon, Ahmad Raston and Gu 2014; Liu *et*

al. 2014). This allows for selection of the highest binding aptamers. Thereafter, aptamers can be capped with thiol groups that bind to two AuNPs (Mirkin *et al.* 1996; Storhoff *et al.* 1998; Rosi and Mirkin 2005). The principle of colorimetric sensing based on aptamers to detect specific DNA sequences was introduced more than a decade ago and is now a key tool in biodiagnostics (Mirkin *et al.* 1996; Rosi and Mirkin 2005). Since then, other aptamer-based sensors have been developed for the detection of metal ions, small molecules (Lee *et al.* 2008; Chen *et al.* 2009) and proteins (Huang *et al.* 2005; Wang *et al.* 2006b; Wei *et al.* 2007).

The development of DNA-aptamer-based colorimetric assays by Mirkin's group was inspired by the fact that the steps necessary for NPs modification with ligands can be tedious or time-consuming and relatively expensive (Mirkin *et al.* 1996; Storhoff *et al.* 1998; Taton, Mirkin and Letsinger 2000). The NPs that are stabilised with ssDNA aptamers do not aggregate with the addition of salt only (Liu and Lu 2006; Wang *et al.* 2006a). Conversely, in the presence of the target/analyte, the aptamer is folded because it binds to the target while desorbing from the NPs surface, which leads to NPs aggregation and colorimetric changes. Ideally, folded aptamers or dsDNAs should hardly adsorb onto the NPs. This is related to the higher structure rigidity and high proton density inside dsDNA (Li and Rothberg 2004; Wang *et al.* 2006a; Kim *et al.* 2010; Liu *et al.* 2014). Indeed, ssDNAs cannot hybridise with each other to form dsDNAs. Thus, their strategy is based on the observation that unmodified AuNPs and AgNPs can differentiate between ssDNA and dsDNA, mainly due to the higher structural rigidity of the latter (Li and Rothberg 2004; Wang *et al.* 2006a; Chen *et al.* 2013). However, not only the strands but also their lengths contribute to NP stabilization. For instance, Chen and co-workers tested ssDNAs of different length (18nt: 5′ TAG AAT ACT CCC CCAGGT 3′); 24nt: 5′ GGT TGG TCA GAT TCA GTG GGT TAG 3′, and 30nt: 5′ AAA CCC CCC TGC TAAAAC CCC AAA CCC 3′) for AuNP stabilization and consequently for detection and sensitivity. They found that the longer ssDNAs have a better stabilization effect because at the same molar concentration, longer ssDNAs have more monomeric deoxynucleotide units.

Moreover, it is difficult for cysteine to replace highly stable DNA-protected AuNPs (Chen *et al.* 2009). DNA bases possess higher affinity towards gold than silver via coordination between Au and nitrogen atoms (thus favoring DNA adsorption). However, the negatively charged surfaces of AuNPs electrostatically repel DNA phosphate backbones, thus reducing DNA adsorption (Liu and Lu 2006; Wang *et al.* 2006a).

The development of the nanotechnology for NPs functionalization with DNA and the biotechnology for the *in vitro* selection of target-specific nucleic acids offer a unique opportunity for designing colorimetric biosensors (Liu and Lu 2004; Lee *et al.* 2007). The four types of DNA aptamer-based colorimetric approaches are highlighted below:

2.2.4.1 TYPE I: Aptamers adsorbed on nanoparticles

Type I aptasensors includes two common steps: i) adsorption of the DNA unit onto the NPs surface and ii) recognition of the target molecule by the DNA strands while serving as an optical sensing element. DNA adsorption on NPs surface is favored by the high charge density and stability provided by the aptamer (Xu *et al.* 2009) (Figure 2-7). This is a crucial step because the selectivity of the targeting molecule must be retained during adsorption onto NPs, especially when the aptamer is designed for qualitative assays (Xu *et al.* 2009). The aptamer conjugation constant is stronger than that of antibodies and that of non-specific adsorption between the aptamer and NPs (Mei *et al.* 2013). With these conditions in mind, Xu and co-workers used unmodified DNA and AgNPs to detect ligands binding to homoadenine, by monitoring the color change from yellow to brown due to AgNP aggregation after salt addition. When coralyne binds to the homoadenine sequence in the aptamer, the aptamer is removed from the AgNP surface and AgNP can aggregate (Xu *et al.* 2009). The A_{550}/A_{397} ratio showed a good linear correlation with coralyne concentrations between 0.0 and 10 mM with a LOD of 0.3 mM (Xu *et al.* 2009). Using a similar strategy, DNA-AuNPs/AgNPs were used to detect several targets, such as bisphenol A (LOD: 0.1 ng mL^{-1} (Mei *et al.* 2013) and LOD: 0.01 pg mL^{-1} (Ragavan, Selvakumar and Thakur 2013)), digoxin (LOD: 571 pM) (Sarreshtehdar Emrani *et al.*

2015), oxytetracycline (OTC) (LOD: 25 nM) (Kim *et al.* 2010), thrombin, (LOD: 0.83 nM) (Wei *et al.* 2007), kanamycin (LOD: 25 nM) (Song *et al.* 2011), OTC (LOD: 0.1 nM), ampicillin (LOD: 5 ng mL^{-1}) (Song *et al.* 2012), staphylococcal enterotoxin B (LOD: 10 ng mL^{-1}) (Liu *et al.* 2013), and pyruvic acid (LOD: 3.0 μM) (Li *et al.* 2014).

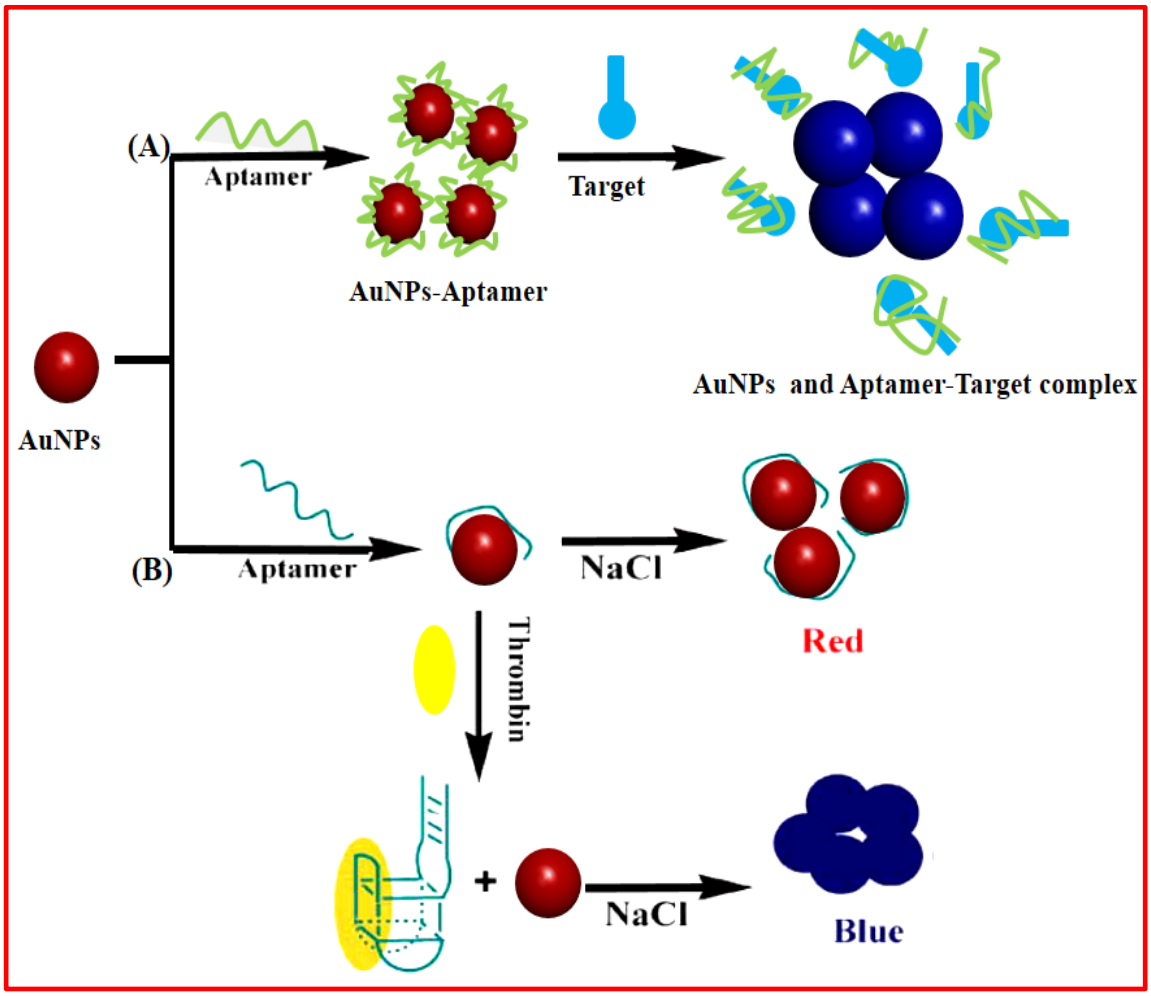

Figure 2-7: Schematic representation of Type I colorimetric aptasensors for detection (A) small (Mei *et al.* 2013; Sarreshtehdar Emrani *et al.* 2015) and (b) large molecular targets (Wei *et al.* 2007).

It is acknowledged that for many type I aptamers, addition of the target/ligand induces the aptamer release from the NP surface and consequently the color change as the salt tolerance decreased by NPs (Sato, Hosokawa and Maeda 2003; Xu *et al.* 2009; Mei *et al.* 2013; Sarreshtehdar Emrani *et al.* 2015). Two groups reported an intriguing observation using a similar approach (Famulok and Mayer 2006; Liu and Lu 2006). When aptamers are added to NPs, their interaction via hybridization leads to NP aggregation and consequently to the color change from red to blue. Addition of the target molecule (e.g., adenosine) to the aptamer-NP solution induces a dramatic conformational change of the aptamer structure that leads to the dissociation of the NP network and to a new color change (blue to red) (Famulok and Mayer 2006; Liu and Lu 2006).

The AuNPs have also been used by Dong's group (Wei *et al.* 2007) to understand the conformational changes of thrombin-binding aptamers (TBA) when they are removed from the AuNP colloidal solution in the presence or not of thrombin. Addition of 100 mL of 0.5 M NaCl causes a quick color change from red to purple in the solution with thrombin, but not in that with only TBA. Due to the color change, the TBA conformation modification from unfolded to G-quadruplex/duplex formation could be directly monitored by the naked eye, thus allowing the easy detection of thrombin (Wei *et al.* 2007). Likewise, the addition of enough salt could be used to inhibit the repulsion between unmodified negatively charged AuNPs and result in their aggregation and in the corresponding red-to-blue color change. As previously reported, there is stronger coordination interaction between the nitrogen atoms of unfolded ssDNA and AuNPs than electrostatic repulsion between the negatively charged phosphate backbone and the negatively charged AuNPs (Wei *et al.* 2007). Conversely, the relatively rigid structure of dsDNA or folded ssDNA (e.g., G-quadruplexes) prevents the exposure of the DNA bases to AuNPs and the high density of negative charges increases the repulsion between DNA and AuNPs. However, aggregation of DNA-functionalised AuNPs can be induced also by hybridization of target DNA that does not cross-link the NPs. A conceivable disadvantage

of this non-crosslinking system, compared with the crosslinking system, is the consumption of target DNA (Sato, Hosokawa and Maeda 2003).

Recently, a viable approach to overcome the limitations of type I aptamers due to the DNA length was reported. Briefly, the design of shortened aptamers is mainly based on selecting nucleotide bases characterized by high homogeneity in accordance with their conserved regions (Song *et al.* 2012; Kwon, Ahmad Raston and Gu 2014). Shortened aptamers that contain common regions have approximately the same binding affinity as the original. For instance, based on the conserved sequences with a high homogeneity of the original five 76-mer aptamers, A1 and A2 (8-mer sequences) were successfully obtained and still exhibited high affinity and specificity for tetracycline (TC) (Kwon, Ahmad Raston and Gu 2014) (Figure 2-8).

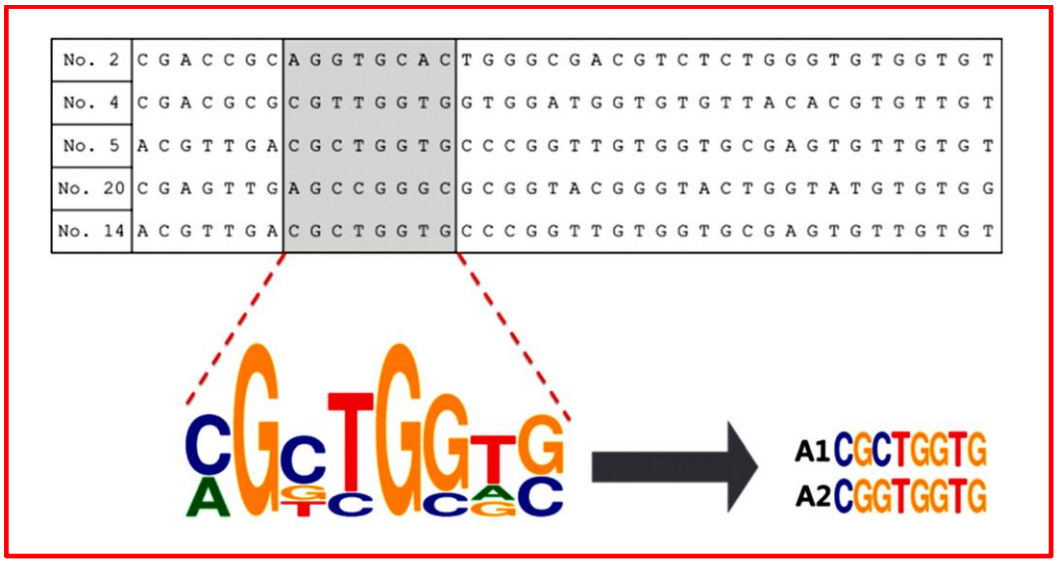

Figure 2-8: Truncation process after analysis of the sequences of the original five 76-mer aptamers that bind to oxytetracycline, 20 to 8 mer (Kwon, Ahmad Raston and Gu 2014).

Although only the original stacking pocket and six additional specific bases are present in A1 and A2, they display higher binding affinity (K_d 1.067 nM for TC). The LOD of A2 for oxytetracycline (OTC) was 0.1 nM, which is about 500-fold better than that of the

original 76-mer aptamer, and the color change can be detected in the presence of 10 nM OTC (Kwon, Ahmad Raston and Gu 2014). Similarly, based on their common sequence and predicted structure, Changill Ban's group (Song *et al.* 2012) shortened three 90-mer ssDNA aptamers that specifically bind to ampicillin to obtain AMP4 (21-mer 5′-CACGGCATGGTGGGCGTCGTG-3′), AMP17 (19-mer 5′-GCGGGCGGTTGTATAGCGG-3′), and AMP18 (21-mer 5′ TTAGTTGGGGTTCAGTTGG-3′) (Song *et al.* 2012). Comparison of AMP17, AMP4 and AMP18 (at concentrations of 100 mM, 150 mM, and 200 mM, respectively) showed that ampicillin can be detected at concentrations as low as 5 ng mL^{-1} using the AuNP-based dual fluorescence–colorimetric method and in a milk sample at 10 ng mL^{-1} (Song *et al.* 2012). Thus, the results by Song *et al.* (Kwon, Ahmad Raston and Gu 2014) and Kwon *et al.* (Song *et al.* 2012) illustrate and confirm that using aptamers harboring only the binding site/active site sequence can further improve their selective features. Importantly, the target must not react or crosslink with NPs. Moreover, the ratio between NPs and aptamer could affect the final sensitivity. Too many aptamers in the sensing system reduce the sensitivity, while too few decrease the stability of the sensing systems (Mei *et al.* 2013). One of the primary challenges of Type I approaches relies on the different binding affinities of ssDNA and dsDNA towards unmodified NPs. However, the important feature is that negatively charged ssDNA sequences can effectively stabilise NPs against salt-induced aggregation, providing a convenient route for colorimetric assays without NP surface biomodification.

2.2.4.2 TYPE II: Aptamer-target adsorbed on nanoparticles

Type II aptamers also include two common steps: (i) aptamer linkage to the target molecule to forming a complex, and (ii) aptamer-target complex adsorption onto the surface of the NP. With this approach, it is always wise to check the interaction of the pure aptamer with NPs (Type I) because the system may follow a similar mechanism (Liu, Zhang and Han 2005; Liu and Lu 2006). Ideally, aptamer adsorption onto the NP surface

should not lead to NP aggregation (and thus color change) after addition of high salt concentration. In the presence of the target, the aptamers should bind in competition with AuNPs, resulting in a color change in the presence of salts. A typical Type II system has been used by Chen *et al.* for sulfadimethoxine (SDM) detection using unmodified AuNPs. In optimal conditions (pH 8, 0.2 mM of aptamer and 2.0 M of salt), the LDR was 50.0 ng mL^{-1} to 1.0 mg mL^{-1} and the LOD was 50 ng mL^{-1} (Chen *et al.* 2013).

Upon addition of SDM, the conformation of the SDM-binding aptamer changes from a random coil structure to a more folded rigid structure that promotes the detachment of the adsorbed aptamers from AuNPs and results in the subsequent AuNP aggregation after salt addition. This leads to a color change from red to purple-blue that can be easily observed by the naked eye (Chen *et al.* 2013). Recently, Liu *et al.* assessed whether aptamer truncation could improve the sensitivity also in Type II aptamers (Liu *et al.* 2014) (Figure 2-9).

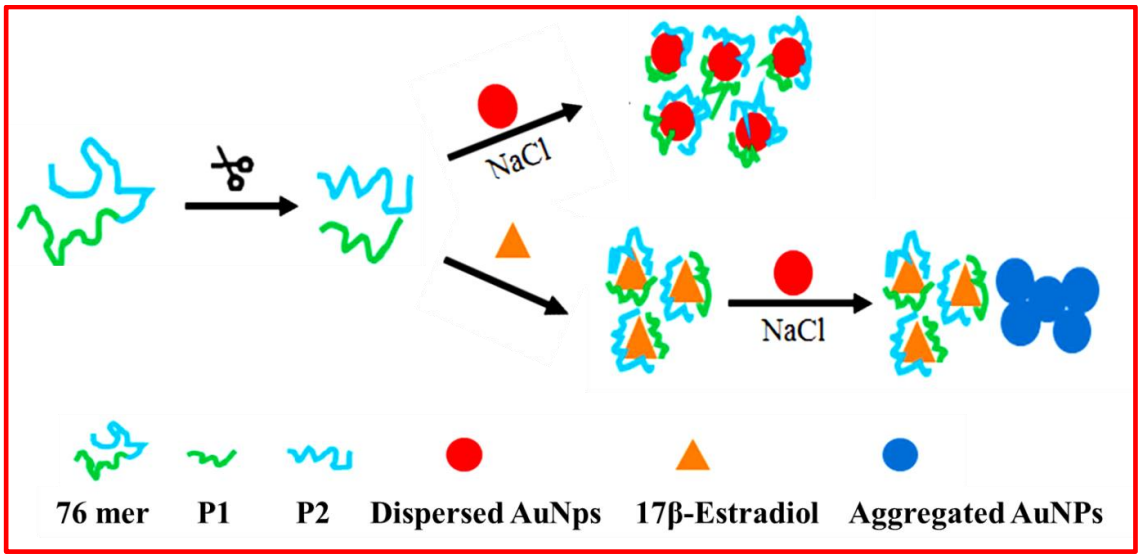

Figure 2-9: Schematic illustration of an AuNP-based colorimetric aptasensor to detect17□-estradiol using split aptamers. Reproduced from (Liu *et al.* 2014). Split aptamers binds irreversibly to the target analyte

Briefly, the long (76-mer) aptamer specific for 17β-estradiol was split into two shorter sequences (P1 and P2) that still retain the original aptamer affinity and specificity, but with 10-fold higher LODs. Indeed, 17 β-estradiol could be detected with a LDR from 0.1 ng mL^{-1} to 105 ng mL^{-1} (Liu *et al.* 2014). The authors hypothesized that this increased sensitivity is caused by the lower aptamer adsorption concentration and lower affinity for AuNPs of the shorter ssDNA sequences (Kwon, Ahmad Raston and Gu 2014; Liu *et al.* 2014). Likewise, Xie *et al.* developed an assay in which incubation of a RNA-DNA duplex with the HIV-1 reverse transcriptase (RT) leads to the production of ssDNAs and ssRNAs that can form a charged protecting layer on the AuNPs surface and consequently, to NP stabilization at a precisely defined salt concentration (Figure 2-10). In the absence of RT, the selected RNA–DNA duplex remains intact, and the unprotected AuNPs aggregate in the presence of salt with an associated change in color (Xie *et al.* 2011).

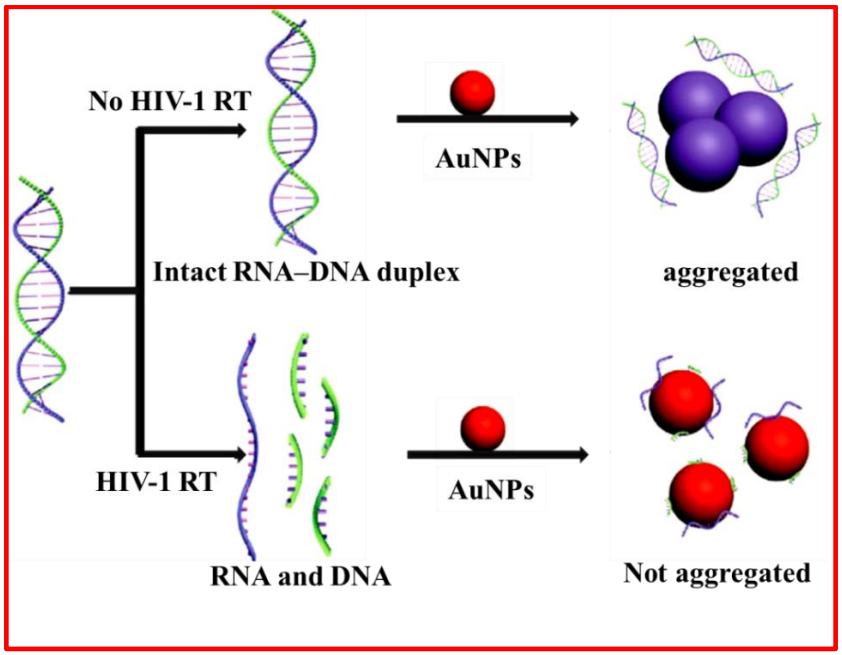

Figure 2-10: Schematic of the approach by Xie et al. A synthetic RNA–DNA duplex substrate is first incubated or not with HIV-1 RT. HIV-1 RT should cleave the RNA into fragments, resulting in the dissociation of ssDNA and ssRNA probes at room temperature (≈ 28 °C). Reproduced with permission from (Xie *et al.* 2011).

Wang *et. al* (Wang *et al.* 2006a) used K^+ as a target because it stabilises ssDNA, thus facilitating the formation of G-tetrads within 4 min. The AuNPs incubated with G-tetrads changes color from red-to-purple like unmodified AuNPs, suggesting that the G-tetrad structure is not significantly adsorbed onto AuNPs (Wang *et al.* 2006a). The presented assay, which uses C-rich (5'-CCTCCCTCCTTTTCC ACCCACC-3') oligonucleotide aptamers, cationic polymers and AuNPs, provides a platform for the detection of other ions and molecules (Wang *et al.* 2013). For instance, in the presence of Ag+, the two oligonucleotides form a tightly bound complex with a C-Ag^+-C notation and change conformation, from a random coil to a hairpin structure with a stronger π-π* transition of the bases with deoxyribose (See Figure 2-11). The resulting C-Ag^+-C complex poorly interacts with a cationic polymer known as Poly (diallyldimethylammonium chloride) (PDDA) and subsequently the polymer aggregates AuNPs through electrostatic interactions, with a color change from wine red to blue (Wang *et al.* 2013). In the absence of Ag^+, the positively charged polymer can electrostatically interact with ssDNA and destroy the charge balance, leading to induction of AuNP aggregation (LOD of 48.6 nM and LDR from 100 to 1000 nM for Ag^+). Together, the results by Wang *et al.* (Wang *et al.* 2006a; Wang *et al.* 2013) are in agreement with the hypothesis that unstructured DNA oligonucleotides strongly adsorb onto the NP surface and prevent salt-induced NP aggregation.

Recently, Zhang *et al*. (Sun *et al.* 2015) demonstrated that AuNPs possess peroxidase-like activity that can catalyze 3, 3, 5, 5-tetramethylbenzidine (TMB) in the presence of H_2O_2. AuNP peroxidase-like activity can be improved by surface activation with target-specific aptamers. However, by increasing the concentration of abrin (i.e., the target), AuNP peroxidase-like activity decreases, and the aptamer is desorbed from the AuNP surface, resulting in a decrease of AuNP catalytic activity. The LDR for the current analytical system ranges from 0.2 nM to 17.5 nM with LOD of 0.05 nM (Sun *et al.* 2015).

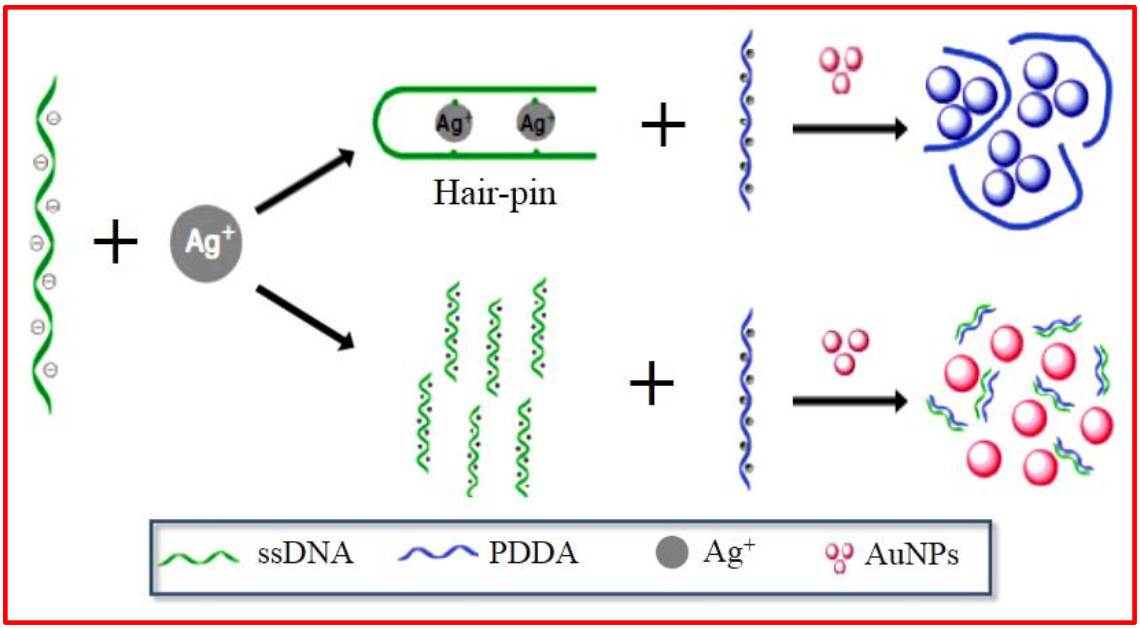

Figure 2-11: Schematic description of the colorimetric lead biosensor for Ag+ detection based on AuNP aggregation induced by PDDA and Ag^{+} aptamers (Wang *et al.* 2013).

Comparison of Type I and Type II systems shows that aptamer-NP complexes are preferentially formed in Type I and aptamer-target complexes in type II systems. It is reasonable to expect less sensitivity from Type I systems because the colorimetric changes are related to the aptamer detachment from the NP surface. The amount of aptamer removed will depend on the amount of target. On the other hand, Type II systems are limited by the fact that the aptamer is expected to retain its adsorption properties after complexation with the target. This suggests that if it is folded during target binding, it should be flexible enough to facilitate colorimetric changes. Overall it all depends on the aptamer capability because we would prefer induced aggregation in the absence of the aptamer.

2.2.4.3 TYPE III: Competition in "One-pot detection systems"

Type III approaches can be regarded as an intermediate system, between Type I and Type II, because the aptamer and the target (or targets) interacts in the presence of NPs, and therefore, this approach is often referred to as *"one-pot detection systems"*. Sometimes, more than one class of aptamers are used to stabilise NPs (Liu *et al.* 2014). Yang and co-workers (Yang *et al.* 2011) described a *"one-pot detection system"* for ochratoxin A (OTA) where phosphate buffered saline (PBS), Mg^{2+}, OTA and the aptamer are mixed with AuNPs that can undergo salt-induced aggregation within 5 min (Yang *et al.* 2011) (Figure 2-12).

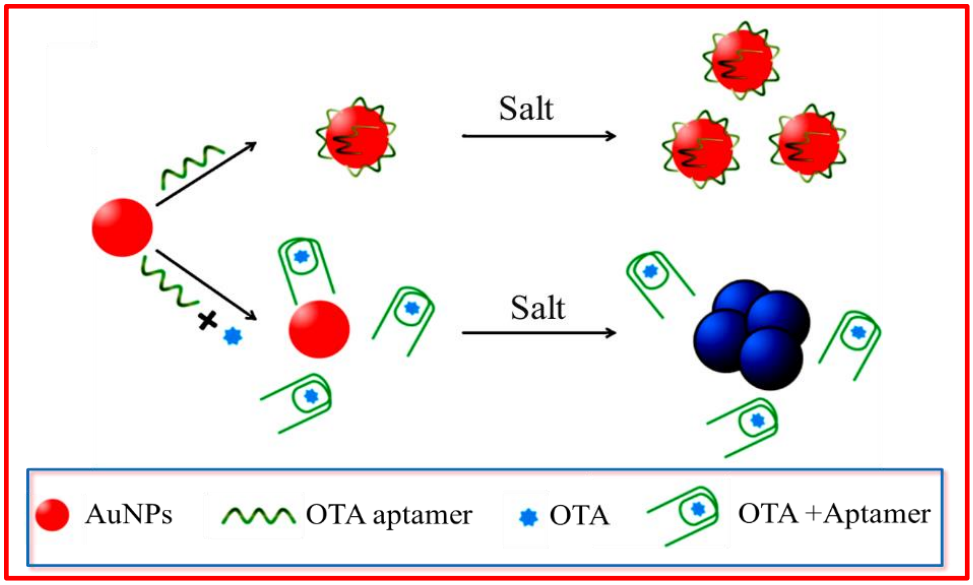

Figure 2-12: *One-pot detection system* of ochratoxin A (OTA). The target is bound to the aptamer and upon salt addition, AuNP aggregation can be detected by the solution color change.

Although the method is different, the authors hypothesised that "the duly formed G-quadruplex structure could not protect AuNPs against salt-induced aggregation, and thus the color change from red to blue could be observed by the naked eye". The observations

were in agreement with the previously proposed by Wei *et al.* and Wang *et al.* for Type I and Type II detection systems. Interestingly the LOD is 20 nM, while the LDR from 20 to 625 nM (Wang *et al.* 2006a; Wei *et al.* 2007; Yang *et al.* 2011). The major limitation of the Type III approach is that there is more than one source of electrostatic interactions that could change the solution color. For instance, if the metal is in excess, it will also contribute to the electrostatic interactions, and this can only be prevented by having ssDNA in excess. Therefore, selectivity is a major limiting factor for this approach.

2.2.4.4 TYPE IV: Multiplex Aptasensors

In this section, the systems that use more than one aptamer based on the previously described structure-switching strategies are described. In homogeneous multiplex aptasensors, more than one class of aptamer is used to stabilise NPs for detection of single or several targets (Liu *et al.* 2014). Several approaches are based on the likelihood that the target DNA molecules with one nucleotide mismatch have different melting temperatures, and therefore they can be distinguished by NPs disassociation based on temperature (Elghanian *et al.* 1997; Storhoff *et al.* 1998; Cao *et al.* 2005; Liu, Zhang and Han 2005; Lee *et al.* 2007; Xu, Han and Mirkin 2007). A typical example of such a DNA sensor was reported by Mirkin and co-workers, in which the target DNA molecules triggered AuNPs aggregation by hybridizing two complementary DNA strands on the AuNPs (Mirkin *et al.* 1996).

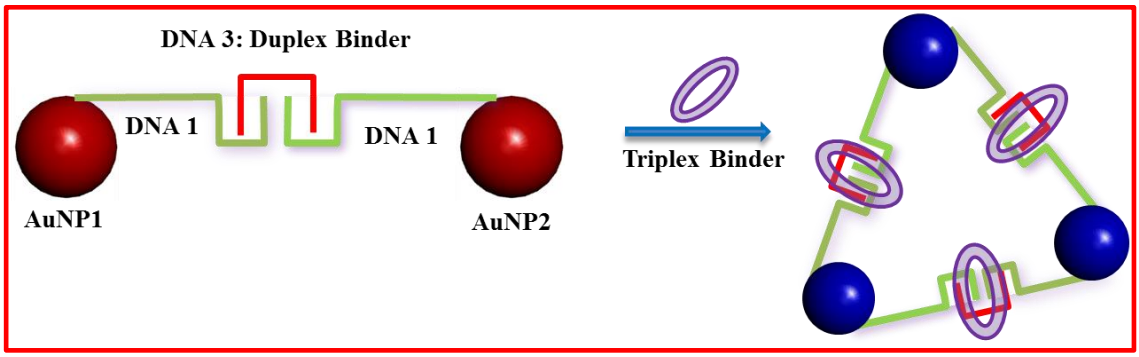

Figure 2-13: Representation of the structure and color change of nano-assemblies in the presence of a triplex binding agent at room temperature (Han, Lytton-Jean and Mirkin 2006).

Another assay includes AuNPs of different sizes (AuNP1 and AuNP2) that are functionalised with non-complementary DNAs (3' or 5' pyrimidine-rich thiol-modified oligonucleotides) (Figure 2-13). Functionalised AuNP1 and AuNP2 are then cross-linked with another complementary DNA to form non-aggregating duplexes (Han, Lytton-Jean and Mirkin 2006). Introduction of a triplex binding agent induces triplex formation through base hydrogen bonds and consequently, reversible NP aggregation that results in a red-to-blue color change (Han, Lytton-Jean and Mirkin 2006). Analysis of the aggregate melting properties suggests a lower DNA surface coverage on AgNPs functionalised with 12 mer-thiolated homo-oligonucleotides containing only adenine (AgNPs/ST) than that on AuNPs functionalised with 12 mer-thiolated homo-oligonucleotides containing only thymine (AuNPs/ST). They were also found to exhibit changes that are significantly different from those of AuNPs upon hybridization (Tokareva and Hutter 2004).

Interestingly, Sato *et, al.* (Sato, Hosokawa and Maeda 2003) demonstrated that ssDNA-AuNPs have different stability against salt-induced aggregation in the presence of complementary DNA, although there is no triplex binder (Sato, Hosokawa and Maeda 2003). Using a similar assay format, Zhao *et al.* configured oligonucleotide-modified AuNPs duplexes with a short complementary oligonucleotide. Upon addition of adenosine as the target, the aptamer switches its structure from a DNA duplex to an aptamer/target

complex, because the aptamer preferentially binds to the target molecule (Liu, Wen and Zhao 2007). Importantly, the aptamer on NP surfaces must retain its switching capability (Mirkin *et al.* 1996; Sato, Hosokawa and Maeda 2003; Han, Lytton-Jean and Mirkin 2006; Liu, Wen and Zhao 2007). Erickson's group (Mancuso *et al.* 2013) developed a multiplexed one-pot detection system for Kaposi's sarcoma-associated herpesvirus (KSHV) and Bartonella using both AuNPs and AgNPs. Specifically, when the Bartonella-targeted DNA (BA-DNA) is introduced in the solution, AgNPs aggregate and the solution turns pink, more dependent on the SRP characteristics of non-aggregated AuNPs. When KSHV-DNA was introduced, AuNP aggregate and the solution changes to a murky yellow-orange color, more dependent on AgNP aggregation (Mancuso *et al.* 2013). The multi-color change tuning of AuNPs and AgNPs gave LODs down to 1.0 nM and 2.0 nM, respectively (Mancuso *et al.* 2013).

Niu et *al.* (Liu *et al.* 2014) used more than one class of aptamers to stabilise AuNPs (Type I). Specifically, a kanamycin-specific aptamer (750 nM), a sulfadimethoxine-specific aptamer (250 nM) and an adenosine-specific aptamer (500 nM) are mixed (1:1:1 volume ratio) and adsorbed directly onto the surface of unmodified AuNPs by electrostatic interaction. Upon addition of any of the three targets, the conformation of the corresponding aptamer changes from a random coil structure to a rigid folded structure that cannot adsorb and stabilise AuNPs (Liu *et al.* 2014). Although this looks more like a type III system. However more than one aptamer is present and the reaction does not proceed sequentially.

Ultimately, multiplex systems are not straight forward because multiplex detection largely depends on the concentration of each aptamer and the buffer used for the aptamer reaction with its target (Liu *et al.* 2014). Moreover, all the aptamers in solution can be adsorbed onto the NP surface; however, the level of adsorption also depends on the neighboring aptamers. For this reason, the use of aptamers with short sequences gives better adsorption yields. It has been shown that changing the length of the ssDNA sequences yields different particle dispersion profiles on unmodified AuNPs, and that

short DNA sequences might improve the colloidal stability against salt-induced aggregation (Li and Rothberg 2004; Song *et al.* 2012; Kwon, Ahmad Raston and Gu 2014). Most importantly, the aptamer on the NP surface must retain its switching capability and for this reason the switching capability of the structures with aptamers is a key factor that determines the LOD of the assay (Liu, Wen and Zhao 2007).

The multiplex type of aptamers has proven to be useful for enzyme activity and inhibitor assays.

2.2.5 Nanoparticle-based enzyme assays

NPs can be used also to improve colorimetric assays of enzymes (Xie, Xu and Liu 2012). In such systems, the substrate for the target enzyme should also be a suitable NP stabiliser. For instance, it should be stable at a high salt concentration (approximately 100 mM). Moreover, a charged molecule that can provide electrostatic and steric stabilization is likely to yield better selectivity. The strong interaction between amino groups and AuNPs surfaces has been well confirmed and the bond energy is comparable to that of a thiol–Au bond. The rapid aggregation induced by the non-crosslinking process is a useful approach for enzyme inhibition-based colorimetric screening, as shown by several studies using assays that rely on polymeric aggregates of DNA-functionalised AuNPs (DNA-AuNPs) with DNA-duplex interconnections (Xu, Han and Mirkin 2007; Lou *et al.* 2009; Song *et al.* 2009). Mirkin's group functionalised two separate batches of 13-nm AuNPs with two different thiol-modified oligonucleotide strands (DNA-1: 5'-CTCCCTAATAACAATTTATAACTATTCCTA-A10-SH-3', and DNA-2: 5'-TAGGAATAGTTATAAATTGTTATTAGGGAG-A10- SH-3') blue and red ribbons, respectively, in Figure 2-14 (Xu, Han and Mirkin 2007).

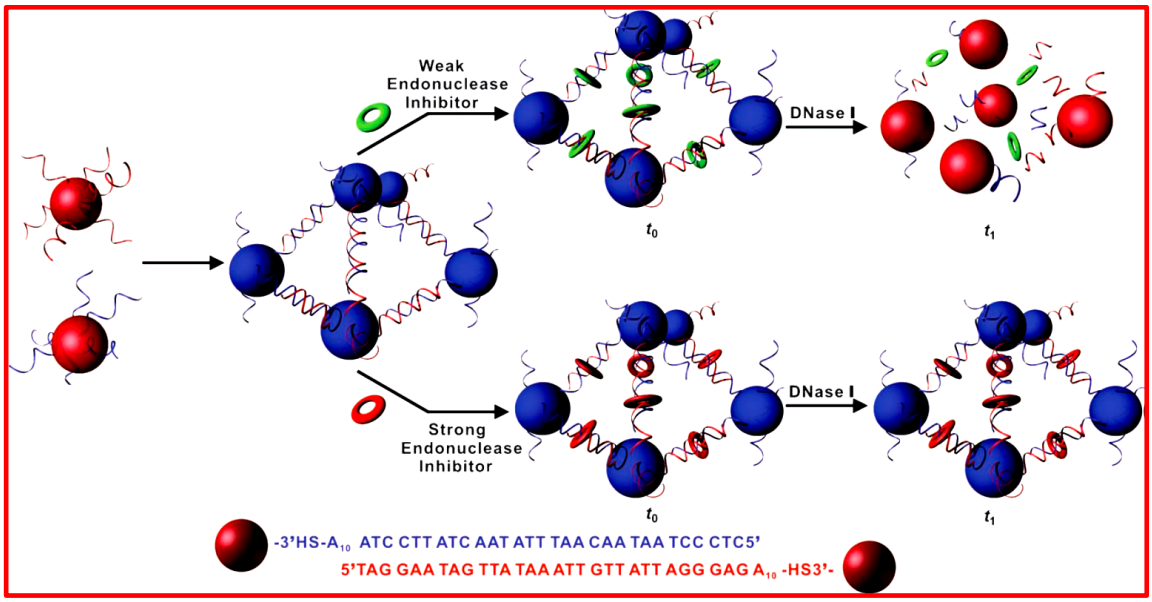

Figure 2-14: Aggregation and dissociation of the DNA-AuNPs probe used in the colorimetric screening of endonuclease inhibitors. The probe consists of spherical AuNPs functionalised with two complementary oligonucleotides (blue and red ribbons). Individual NPs (red) aggregate into a cross-linked network of NPs (blue) through hybridization of their oligonucleotide chains. Upon addition of DNase I, the aggregates remain intact longer in the presence of a strong endonuclease inhibitor (Xu, Han and Mirkin 2007).

The endonuclease (DNase I) degrades the DNA-duplex interconnections and NPs are released, thus generating a red color (Xu, Han and Mirkin 2007) (Figure 2-14). In the presence of inhibitors, the DNase 1 activity is decreased and the aggregates are strongly hydrolyzed (T_H). Consequently, the time required for the color change is much longer. Most importantly, strong inhibitors (in contrast to weak inhibitors) hinder DNase I activity to such an extent that the color change is no longer possible (Xu, Han and Mirkin 2007). In their method, endonucleases cleaves dsDNA in the absence of inhibitors and cross-linked AuNPs can separate into single AuNP molecules, as indicated by the instant color change, from blue to red. With this approach, the inhibitor performance can be directly evaluated. Similar observations were made using a system that includes a single type of

DNA-AuNPs probe and an appropriate oligonucleotide linker that can hybridize with the DNA probe. The linker was designed to contain a self-complementary region that can form a duplex structure with a base-pair overlap that contains the recognition sites and overhanging 3'-ends (Song *et al.* 2009) (Figure 2-15). Significant color change is observed when the endonuclease (DNA methyltransferase, DNA MTase) degrades the DNA duplex (Song *et al.* 2009).

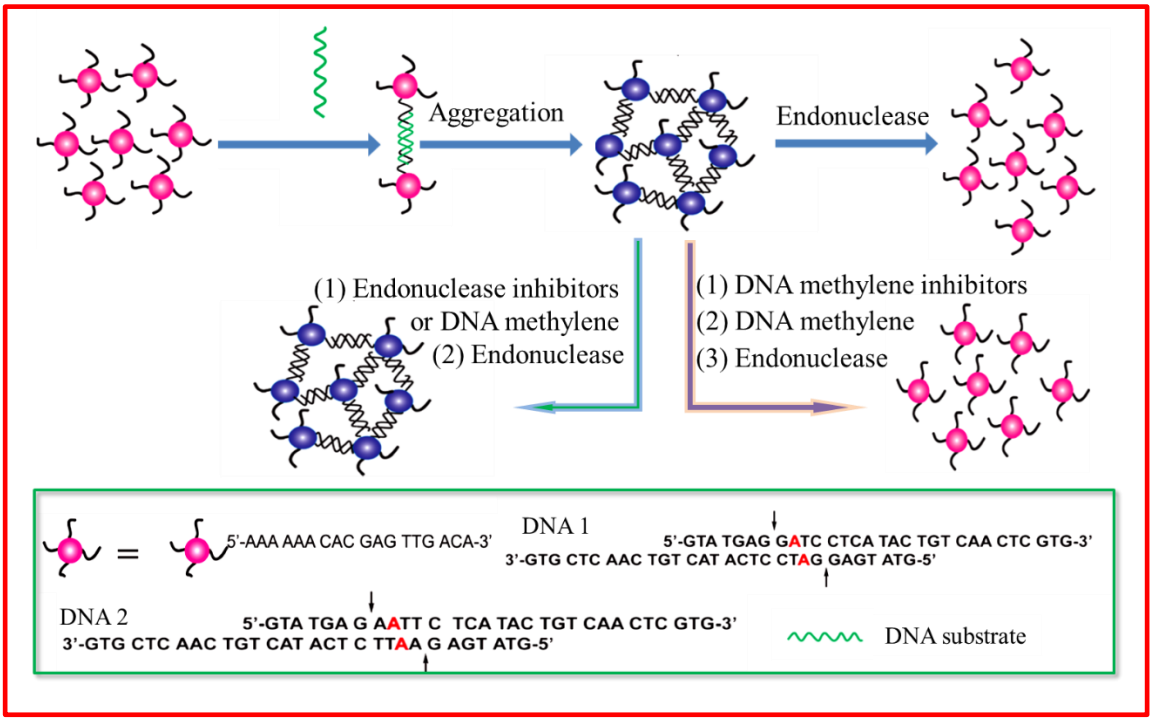

Figure 2-15: Schematic representation of the assay to assess endonuclease and methyltransferase activity and inhibition. (B) Sequences of the DNA probe, DNA-1 (recognition site for the DpnII/Dam MTase) and DNA-2 (recognition site for the EcoRI/EcoRI MTase). The arrows show the cleavage sites, and the red letters indicate the methylation sites (Song *et al.* 2009).

Although highly selective and more sensitive than conventional methods, this visual inspection assay is limited for the preparation of probes by functionalizing two separate AuNP batches with two different thiol-modified oligonucleotide strands. On the other

hand, this approach can be used for most endonucleases by simply changing the recognition sequence in the linker DNA (Song *et al.* 2009). For instance, similar assays were used for assessing adenosine triphosphate (ATP) dephosphorylation by calf intestine alkaline phosphatase (CIAP) and peptide phosphorylation by protein kinase A (PKA). ATP can protect AgNPs from salt-induced aggregation only in the absence of enzymes. Phosphorylation and dephosphorylation can be readily detected by the color change of AgNPs (CIAP LOD: 1 unit mL^{-1}, and PKA LOD: 0.022 unit mL^{-1}) (Wei *et al.* 2008). Zhao and co-workers took advantage of the non-crosslinking AuNPs aggregation phenomenon to develop a simple colorimetric assay for monitoring an enzymatic dephosphorylation reaction, where ATP is converted into adenosine by CIAP (Zhao *et al.* 2007b). AuNPs capped by adenosine 5'-monophosphate (AMP), adenosine 5'-diphosphate (ADP), or adenosine 5'-triphosphate (ATP) are progressively more stable than bare AuNPs, but their stability gradually decreases (and thus the color of the solution) with the dephosphorylation process (Zhao *et al.* 2007b). Likewise, Choi *et al.* described an alkaline phosphatase assay based on AuNPs aggregation (Choi, Ho and Tung 2007). To develop an adenosine deaminase assay, Zhang and co-workers hypothesized that the interaction between adenosine amino group and AuNPs surface will displace the weakly bound citrate ions from the AuNPs surface and thus diminish the stability of citrate-capped AuNPs, resulting in the aggregation of AuNPs in the presence of NaCl. This results in a red to blue color change. Adenosine, guanosine and cytidine (molecules that contain amino groups) strongly interact with AuNPs, causing aggregation. Conversely, inosine, thymidine and uridine have negligible effects on AuNPs stability, therefore the solution remains red because of the stronger electrostatic repulsion between the negatively charged AuNPs (Zeng, Mizukami and Kikuchi 2012). Xinhui *et al.* described a suitable method for nucleases, such as the S1 nuclease (Lou *et al.* 2009). In the presence of nucleases and their substrates, unmodified AuNPs are stabilised by dNMPs at high salt concentration and the solution remains red. Conversely, in the absence of nucleases or substrates, the unmodified

AuNP solution turns blue at high salt concentration due to the aggregate formation (Lou *et al.* 2009).

Xu and co-workers developed a colorimetric assay to screen for inhibitors of several kinases with the same type of NPs (Wang *et al.* 2006b) (Figure 2-16). The method takes advantage of peptide-capped NPs, in which 10% of peptide ligands carry an extension that is the substrate for a specific kinase (PKA or calmodulin-dependent kinase II, CaM KII). Using ɣ-biotin-ATP as a co-substrate, the kinase reaction results in substrate-AuNP biotinylation.

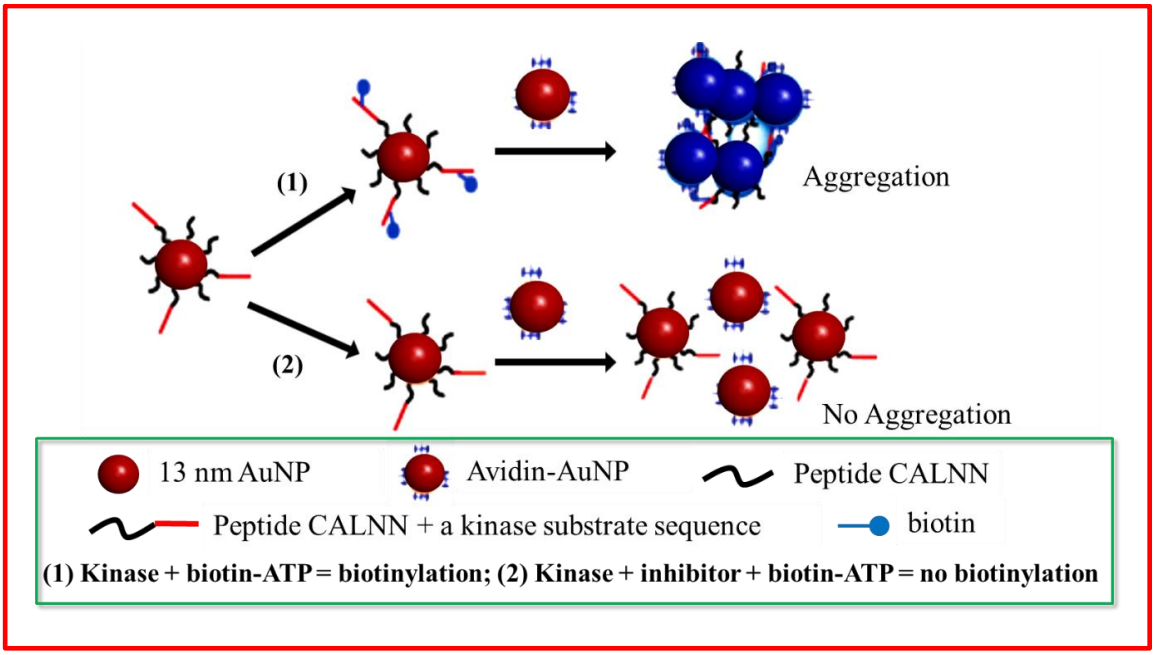

Figure 2-16: Schematic representation of phosphorylation/biotinylation of substrate-NPs followed by addition of avidin-modified NPs, in the presence and absence of a kinase inhibitor (Wang *et al.* 2006b).

When biotinylated substrate-AuNPs are mixed with AuNPs-avidin, they immediately aggregate due to the specific binding between avidin and biotin (Wang *et al.* 2006b). Similarly, Wei *et al.* reported that in the absence of the kinase, or in the presence of an efficient inhibitor, no observable color change occurs after addition of avidin-modified

NPs, and the solutions are indefinitely stable without showing signs of aggregation(Wang *et al.* 2006b; Wei *et al.* 2008). Furthermore, a hydrolysis-based colorimetric assay for acetylcholinesterase (AChE) was developed based on the finding that AChE can catalyze acetylthiocholine hydrolysis into thiocholine (Wang *et al.* 2009). AChE and acetylthiocoline are added in the AuNP solution, the generated thiocholine can take the place of citrate on the AuNP surface, promoting NP aggregation and a change of color from red to gray. The addition of the AChE inhibitor tacrine (1,2,3,4-tetrahydroacridin-9-amine) leads to less AuNP aggregation and a slower color change (Wang *et al.* 2009). Uehara *et al.* reported that gold nanocomposites conjugated with a thermo-responsive copolymer can be used in a colorimetric assay to quantify the activity of aminopeptidase N (APN). By heating the solution, the assembled gold nanocomposites disassemble and the solution color change from blue, purple to red. This process is inhibited by cysteine, therefore the enzymatic decomposition of cysteinylglycine into cysteine and glycine by APN can be monitored (Uehara, Fujita and Shimizu 2009).

Tiwari *et al.* hypothesized that particles could be used for the detection of the hydrolytic activity of penicillin G acylase (PGA) on penicillin G. This hydrolysis reaction leads to a shift in the surface plasmon band of AuNPs from 527 to 545 nm accompanied by a solution color change from red to blue. The presence of 0.007 mg mL^{-1} PGA can be detected (Tiwari 2010). The enzyme is known to hinder the salt-induced NP aggregation. Xie and co-workers found that DNA-RNA duplexes cannot stabilise unmodified NPs at a certain salt concentration, a typical type II approach. However, the addition of the active HIV-1 RNase H enzyme leads to the specific cleavage of RNA strands into RNA fragments and ssDNAs that can stabilise NPs against salt-induced aggregation (Xie *et al.* 2011). In an assay for glycosidases based on self-immolative elimination to release amines, functionalised trigger-AuNPs aggregate by electrostatic attraction upon cleavage of the trigger. The assay gives LODs for β-galactosidase (Gal) and β-glucosidase (Glc) of 9.2 and 22.3 nM, respectively, at 20 min, and they improve slightly over time (Zeng, Mizukami and Kikuchi 2012). The functionalised AuNPs (2.0 nM), which were capped

with the enzyme substrate ligand Gal-Lip (or Glc-Lip) and lipoic acid at a ratio of 1:1, showed good stability in PBS with SPR peak at 521 nm with a red shift of 2 nm compared with citrate-AuNPs. The respective addition of Gal or Glc caused a time-dependent decrease of the peak absorbance induced by NP aggregation that could be observed by naked eye.

Two different systems (the DNA endonuclease DNase I and the Pb^{2+}-dependent RNA-cleaving DNA enzyme 8-17) were chosen to demonstrate the utility of an assay for the detection of metal ions and enzyme activities based on rapid NP aggregation driven by van der Waals attraction (Zhao *et al.* 2008) (Figure 2-17).

The authors reasoned that the removal from the NP surface of DNA strands, which serve as electrostatic and steric stabilisers at relatively high salt concentrations (e.g., 40 mM $MgCl_2$), should result in AuNPs destabilization and aggregation, a process driven by van der Waals attraction (Zhao *et al.* 2008). Indeed, the addition of 100 mM Pb^{2+} generated a rapid red-to-purple color change at room temperature (Zhao *et al.* 2008).

AuNPs generation induced by neurotransmitters can be used to analyze the activity of tyrosinase, an enzyme that catalyses the O_2-induced hydroxylation of tyrosine to L-dopamine (Baron, Zayats and Willner 2005). As tyrosinase concentration increases, the SPR bands of NPs are intensified and slightly blue-shifted, suggesting that larger particles are formed, and small Au nanoclusters enlarged (Baron, Zayats and Willner 2005). This system can be used for the sensitive detection of dopamine, L-dopamine and noradrenaline (LOD of 2.5 µM) and adrenaline (0.2 µM) which normally act as an active reducing agents for Au-NP generation of Au-NPs (Baron, Zayats and Willner 2005).

Colorimetric aptasensors for the quantitative analysis of abrin using catalytic AuNPs were reported for the first time by Zhang *et al*. and Wu *et al*. The AuNP peroxidase-like activity can catalyze 3, 3, 5, 5-tetramethylbenzidine (TMB) formation in the presence of H_2O_2, leading to a color change (Wu *et al.* 2007; Sun *et al.* 2015). Particularly, Song *et al.* (Song *et al.* 2009) quote the work by Mirkin's group (Xu, Han and Mirkin 2007) and say that the rest of the methods eliminate the binder use of different

DNAs to obtain functionalised-NP1 and functionalised-NP2. However, such methods require cumbersome preparation of modified NPs and the formation of crosslinked NPs. Thus, it is not suitable for high-throughput screening.

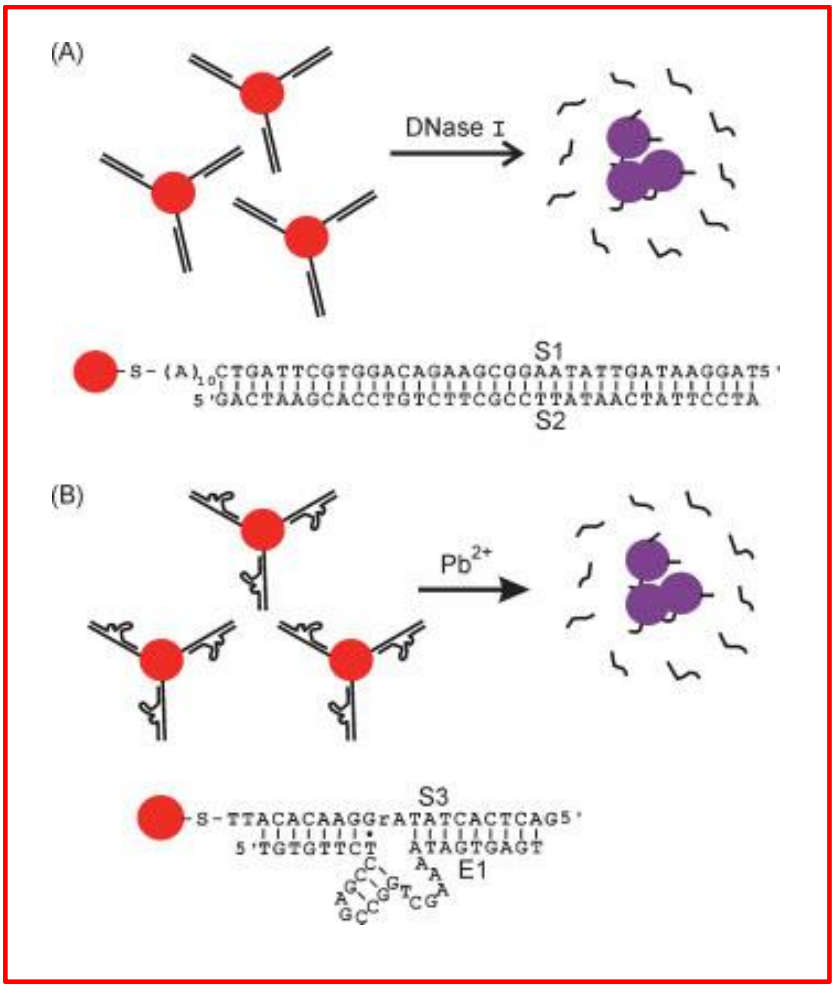

Figure 2-17: Schematic illustration of AuNP aggregation and color change triggered by the enzymatic cleavage of DNA on AuNPs. Before enzymatic cleavage, DNA-modified AuNPs are stable at a relatively high salt concentration, due to their electrostatic and steric stabilization. DNA removal from the AuNP surface by enzymatic cleavage destabilises AuNPs and results in their rapid aggregation. A) Cleavage of a DNA duplex by DNase I. B) Pb^{2+}-mediated cleavage of an RNA-containing DNA substrate by the 8-17 DNA enzyme (Zhao *et al.* 2008).

Crosslinking also offers a unique selectivity in reversibility of NP aggregation, where analytes dissociate the cross-linker and re-disperse the NP aggregates to their original color. For instance, Lu and co-workers described detection assays for Pb^{2+}, adenosine and cocaine where DNA molecules with a single RNA linkage serve as cross-linkers that bring complementary DNA-AuNPs into aggregates. The DNA enzyme catalyzes the specific hydrolytic cleavage of the substrate strand that disrupts the NP assembly, changing the color from purple to red and thus indicating the presence of Pb^{2+} (Liu and Lu 2003, 2004).

Zhao and co-workers speculated that if the substrate and product of an enzymatic reaction affect differently AuNP stability by changing their electrophoretic properties, such a reaction can be monitored colorimetrically and the enzymatic activity can therefore be determined (Zhao *et al.* 2007b).

2.3 Toxicity of nanoparticles

Since the dawn of nanotechnology research in the early 70s, nano-toxicology was relatively unknown in those years. However, metal oxides in their nano-scale dimensions such as TiO_2 (Newman, Stotland and Ellis 2009) and ZnO (Montazer and Pakdel 2011) were regarded as safe and bio-compatible. A few decades later, information started accumulating which gave awareness to the nanotechnologists and the public that most of the materials become toxic and detrimental to human and animal health with dimensions less than 100 nm (Weir *et al.* 2012; Husen and Siddiqi 2014; Catauro *et al.* 2015; Logan *et al.* 2015). However, an in-depth literature review revealed the genotoxicity of nano-sized particles (Lindberg *et al.* 2013; Meng *et al.* 2013; Nymark *et al.* 2013; Winkler *et al.* 2013). In a recent review by Song and co-workers, the neurotoxicity of nano TiO_2 is comprehensively discussed with revelations that nano TiO_2 leads to brain damage having a number of pathways from accidental inhalation and ingestion to skin exposure through cosmetics (Song *et al.* 2015).

Mechanisms of how ZnO nanoparticle exposure leads to apoptosis of neurocytes such as c-Jun N-terminal Kinase (JNK), extracellular signal-related kinase (ESRK) and p38 mitogen-activated protein kinase (p38MAPK) have been investigated (Wang *et al.* 2014). These neurocytes suffered phosphorylation effects but, among their respective inhibitors: SP600125, U0126 and SB203580, only the SP600125 inhibitor for JNK reduced the ZnO-NP-induced cleavage of cells giving clues to the pathway for the ZnO-NP-induced apoptosis of cells. Guan et al have reported dose-response studies of ZnO nanoparticles on human embryonic kidney (HEK293) cells and human hepatocytes (LO2) and have shown that the plot of ZnO dose (in mg L^{-1}) against oxidative stress markers such as Malondialdehyde (MDA), glutathione (GSH) and superoxide dismutase (SOD) revealed that MDA rises whereas both GSH and SOD decrease with increasing ZnO concentration (Guan *et al.* 2012). Although these authors were not able to discuss the important aspect of ZnO dosimetry, we have seen from their results that the increase in MDA shows a characteristic S-curve with the critical ZnO dose of about 50 mg L^{-1} beyond which both the HEK293 and LO2 cells begin to cleave and die.

TiO_2 core-shells has been used to deliver the drugs such as gambogic acid to leukemia cells. In a recent kind of chemotherapy, they proved to have high efficacy (Yue *et al.* 2014; Xu *et al.* 2015). It has been shown by Li and co-workers that nanoanatase accumulates in liver DNA either by inserting itself in rat DNA base pairs or binding to DNA nucleotide This could possibly be accomplished by the interaction of Ti-O(N) bond (of bond length 1.87 Å) with the P atoms in the DNA turning into Ti-P bonds (of bond length 2.38 Å) and hence leading to altering the conformation of DNA. The study by Li and co-workers showed that higher doses of TiO_2 led to cleavage of mice liver DNA (Li *et al.* 2010).

From a wellness perspective, the present study seeks to broaden the understanding of TiO_2 materials in relation to nano-toxicology for two reasons. Firstly, the TiO_2 based nanomaterials have unique physiochemical properties, which attracted widespread applications such as decomposing organic matters in wastewater, anticorrosion and

nanoscale-enhanced photocatalysis (Kathiravan and Renganathan 2008; Banerjee and Das 2013). Secondly, several studies have highlighted their potential adverse health effects, at least under non-overloaded conditions as biologically inactive and physiologically inert in both humans and animals (Kathiravan and Renganathan 2008). However, great caution has to prevail because much current knowledge of the potential threat of TiO_2 based materials displayed some toxicological problems (Liu, Wen and Zhao 2007; Ahmed *et al.* 2011; Zhao *et al.* 2011; Banerjee and Das 2013). For example, the study on lung toxicity of rutile and P25 degussa NPs demonstrated greater toxic effects of the mixture in contrast to rutile alone (Banerjee and Das 2013). Consequently, understanding the link between the structure and interaction dynamics is key for systematically altering and controlling the physicochemical properties of titanium-based nanomaterials, used in medical implants and prostheses (Ahmed *et al.* 2011; Zhao *et al.* 2011).

Accordingly, this study was aimed at interaction studies of titanium-based nanomaterials with HSA, a model protein that is most abundant and common in the human plasma (Liu, Wen and Zhao 2007). The availability of multiple binding sites in HSA attributes to its ability to interact with organic and inorganic molecules (Silva-Bermudez, Rodil and Muhl 2011; Bouhekka and Bürgi 2012). In this work, the microwave hydrothermally synthesized TiO_2 materials with varying shapes and sizes were investigated for their interaction protocols with HSA. The synthesis procedures and morphology, structural, optical and gas sensing properties of TiO_2 materials used here are already reported (Sikhwivhilu *et al.* 2012). The changes in the size of the nanomaterials, conformational changes of the protein and the pharmacokinetics are investigated.

CHAPTER 3

3 THEORETICAL PRINCIPLES

This chapter focuses on the basic theoretical principles underpinning the techniques that were used for experimental studies carried out. Furthermore, the equations in relation to operation of the techniques are presented. This is followed by the chemical and green synthesis using extracts from natural products. Complete characterization of the nanomaterials is also described.

3.1 Instrumental

3.1.1 Gas Chromatography –Mass Spectroscopy (GC-MS)

The need to unequivocally identify the components of complex mixtures was the motivation for the development of different instrumental coupling techniques (tandem), including the widely and successfully used gas chromatography coupled with mass spectrometry (MS). GC-MS is an extremely favorable, synergistic union, as the compounds susceptible to be analyzed by GC (low-molecular weight, medium or low polarity, in ppb-ppm concentration) are also compatible with the MS requirements (Stashenko and Martínez 2014). GC-MS is an extremely favorable, synergistic union, as the compounds with low-molecular weight, medium or low polarity, in µg L^{-1} to mg L^{-1} concentration are susceptible to be analyzed by GC, they are also compatible with the MS requirements (Stashenko and Martínez 2014).

3.1.1.1 Ionization modes

The essence of a mass spectrometric method revolves around the process of ionization of the molecule, with or without subsequent cleavage or fragmentation. In most cases the ionization of the molecule is dissociative(Stashenko and Martínez 2014).
Its mechanisms can be various, e.g., subtraction or addition of an electron, protonation or deprotonation, nucleophilic, electrophilic addition or subtraction and cluster formation,

among some other processes leading to ion formation. The ionization of a molecule is an energy consuming process, which can be supplied by accelerated or thermal electrons (electron impact or electron capture), by photons (photoionization, corona discharge, laser beam), by atoms or ions accelerated by a high electrostatic field gradient or thermal impact, among other mechanisms. A rather large number of methods have been developed to transfer energy for the ionization process, to thermolabile, high- or low-molecular weight, polar or non-polar molecules, in the gas phase (electron impact, EI, chemical ionization (CI), photoionization (PI), field ionization (FI), or in the condensed phase (field desorption (FD), laser desorption (LD) fast atom bombardment (FAB), plasma desorption, (PD), secondary ion mass spectrometry (SIMS), matrix-assisted laser desorption ionization (MALDI)(Stashenko and Martínez 2014).

3.1.1.2 Mass analyzers

The mass selective detectors are divided into two groups. The first group corresponds to scanning analyzers. These include sector analyzers, e.g., magnetic deflection of single or double focus. The magnetic sector analyzer was historically the first mass analyzer employed. However, its use in GC- MS is not common. Quadrupole analyzers are the most frequently used in tandem GC-MS systems. The second group consists of simultaneous ion transmission analyzers. These include the time-of-flight (TOF), different types of ion trap (lT) and Fourier transform mass analyzers, specifically, ion cyclotron resonance mass spectrometers (ICR-MS), which have gained recent popularity in the field of coupled techniques with both gas and liquid chromatography, because of its high resolution and sensitivity (Stashenko and Martínez 2014).

3.1.1.3 Tandem mass spectrometry

Frequently, excessive chemical noise is observed in the ion current of extracts obtained from biological samples, food, soil, etc. This leads to a failure to achieve the required specificity and to detect and identify reliably analytes of interest, when analyzing

a complex mixture with many interferences or impurities. Usually, the signal/noise (S/N) increases with the number of steps in an analytical procedure.

3.1.1.4 Data analysis and interpretation

Since the main goal is to identify compounds and compare their concentrations across and within samples. Therefore, data processing is to fulfil two criteria: Firstly, correct determination of the mass spectrum of the individual compounds for identification. Secondly, accurate calculation of the abundance of chromatographic peaks corresponding to those compounds in each sample.

3.1.1.5 Mass spectra interpretation

Analysis of GC–MS data is generally tricky because of the high complexity of data due to peaks that are overlapping, shift in retention time and low S/N ratio peaks. There are different approaches that can be used for processing raw GC–MS data such as PARAFAC2 based deconvolution and identification system (PARADISe), PARADISe is a computer platform that is independent and freely available. This software offers solution to complex chromatographic data allowing for extraction chemical information directly from the raw data(Johnsen *et al.* 2017). A good data evaluation approach will be robust towards minor variations in the input parameters. The model instruments are equipped with softwares that automatically performs peak identification based on deconvoluted mass spectra using integrated national institute of standards and technology (NIST) search engine and generates an identification report.

3.1.2 UV Visible spectroscopy

Ultraviolet and visible spectrometers have been in use for a number of decades and they continue to be one of the most important analytical instrument in the modern day analysis. The biggest advantage of UV-Visible spectrometry is its simplicity, versatility, speed, accuracy, and cost-effectiveness. It has become common practice to use a variant

of the tungsten-halogen lamp. The quartz envelope transmits radiation well into the UV region and it most common source is the deuterium lamp but the UV-Vis spectrometer have both lamp types to cover the entire wavelength range. Colors of the spectrum are as follows: violet (400 - 420 nm), indigo (420 - 440 nm), blue (440 - 490 nm), green (490 - 570 nm), yellow (570 - 585 nm), orange (585 - 620 nm), and red (620 - 780 nm).

In order to gain an understanding of the origins of practical absorption spectrometry, quantum theory is necessary. If we think of radiation as a stream of particles known as photons. Atoms and molecules exist in a number of defined energy states or levels and a change of level requires the absorption or emission of an integral number of a unit of energy called a quantum, or a photon. The propagation velocity c of electromagnetic wave (velocity of photon) with frequency ν and wavelength λ is given by the relation equation 3.1a:

$$c = \lambda\nu \tag{3.1a}$$

The energy of a photon absorbed or emitted during a transition from one molecular energy level to another is given by Equation 3.1b:

$$e = h\nu \tag{3.1b}$$

where h is known as Planck's constant (6.6260 x 10^{-34} J.s) and ν is the frequency of the photon. Since c = νλ , therefore,

$$E = \frac{hc}{\lambda} \tag{3.1c}$$

The electronic energy levels of simple molecules are widely separated and usually only the absorption of a high energy photon, that is one of very short wavelength, can excite a molecule from one level to another. In complex molecules the energy levels are more closely spaced and photons of near ultraviolet and visible light can affect the transition. These substances, therefore, will absorb light in some areas of the near ultraviolet and

visible regions. The vibrational energy states of the various parts of a molecule are much closer together than the electronic energy levels and thus protons of lower energy (longer wavelength) are sufficient to bring about vibrational changes. Light absorption due to only to vibrational changes occurs in the infrared region. The rotational energy states of molecules are so closely spaced that light in the far infrared and microwave regions of the electromagnetic spectrum have enough energy to cause these small changes.

3.1.3 Fourier transform infrared and Raman spectroscopy

Fourier transform infrared (FTIR) spectroscopy has been one of the most commonly used technique for materials analysis in the laboratory for about eight decades. The infrared spectrum provides a representative a fingerprint of a sample. This is recorded in a form of absorption peaks which corresponds to the frequencies of vibrations between the bonds of the atoms making up the material. Since the materials are generally unique in combination of the atoms, it is unlikely for two materials to produce the exact same infrared spectrum. It is for this reason that infrared spectroscopy can result in a positive qualitative analysis for different kind of material. In addition, the intensity size of the peaks in the spectrum can be correlated to the quantity of material present. FTIR spectroscopy is preferred over dispersive methods of infrared spectral analysis because of the following reasons, namely: (i) it has greater optical throughput (ii) it is mechanically simple with only one moving part. (iii) it is a non-destructive technique, (iv) requires no external calibration, (v) It operational speed can be increased, (vi) scans are collected rapidly and (vi) sensitivity can be improved by eliminating the noise.

Raman spectroscopy is a form of vibrational spectroscopy, much like infrared (IR) spectroscopy. However, whereas IR bands arise from a change in the dipole moment of a molecule due to an interaction of light with the molecule, Raman bands arise from a change in the polarizability of the molecule due to the same interaction. This means that these observed bands (corresponding to specific energy transitions) arise from specific

molecular vibrations. When the energies of these transitions are plotted as a spectrum, they can be used to identify the molecule as they provide a "molecular fingerprint" of the molecule being observed. Certain vibrations that are allowed in Raman are forbidden in IR, whereas other vibrations may be observed by both techniques although at significantly different intensities thus these techniques can be thought of as complementary.

When light is scattered from a molecule most photons are elastically scattered. The scattered photons have the same energy (frequency) and, therefore, wavelength, as the incident photons. However, a small fraction of light (approximately 1 in 10^7 photons) is scattered at optical frequencies different from, and usually lower than, the frequency of the incident photons. The process leading to this inelastic scatter is the termed the Raman effect. Raman scattering can occur with a change in vibrational, rotational, or electronic energy of a molecule. The difference in energy between the incident photon and the Raman scattered photon is equal to the energy of a vibration of the scattering molecule. A plot of intensity of scattered light versus energy difference is a Raman spectrum. Numerically, the energy difference between the initial and final vibrational levels, $\bar{\nu}$, or Raman shift in wave numbers (cm^{-1}), is calculated using equation 3.2 in which l incident and l scattered are the wavelengths (in cm) of the incident and Raman scattered photons, respectively.

$$\bar{\nu} = \frac{1}{\lambda_{incident}} - \frac{1}{\lambda_{scattered}} \tag{3.2}$$

The vibrational energy is ultimately dissipated as heat. Because of the low intensity of Raman scattering, the heat dissipation does not cause a measurable temperature rise in a material. At room temperature the thermal population of vibrational excited states is low, but not zero. Therefore, the initial state is the ground state, and the scattered photon will have lower energy or longer wavelength than the exciting photon.

3.1.4 Fluorescence and Time resolved fluorescence

Fluorescence is the emission of light by a substance that has absorbed light or other electromagnetic radiation. It is a form of luminescence. In most cases, the emitted light has a longer wavelength, and therefore lower energy, than the absorbed radiation. In general, emitted fluorescent light has a longer wavelength and lower energy than the absorbed light. This phenomenon, known as Stokes shift, is due to energy loss between the time a photon is absorbed and when it is emitted. The causes and magnitude of Stokes shift can be complex and are dependent on the fluorophore and its environment. However, there are some common causes. It is frequently due to non-radiative decay to the lowest vibrational energy level of the excited state. Another factor is that the emission of fluorescence frequently leaves a fluorophore in a higher vibrational level of the ground state.

Time-resolved fluorescence (TRF) also known as fluorescence lifetime spectroscopy is an extension of steady state fluorescence. Fluorescence lifetimes, occurring as emissive decays from the singlet-state, is approximated as the decays occurs in picoseconds to nanoseconds. Therefore, time-resolved fluorescence or fluorescence lifetimes, is basically a study where the fluorescence of a sample is monitored as a function of time after excitation by a pulse of light. The time-resolution can be obtained in a number of ways, depending on the required sensitivity and time regions. The technique called time-correlated single photon counting (TCSPC) can be used for Time-Resolved Fluorescence, which is used for the acquisition of single photons and allows for time resolutions in the range of picoseconds (ps) to nanoseconds (ns). The fluorescence lifetime is characteristic for each fluorescent or phosphorescent molecule and can thus be used to characterize a sample. The fluorescence lifetime gives an independent of concentration and allows a dynamic picture of the fluorescence to be obtained, factors that explain the appeal of this form of measurement. The fluorescence decay of the excited state of a molecule to the ground state can be expressed as

$$\frac{dn^*(t)}{dt} = -kn^*(t) + f(t) \tag{3.3}$$

Where n* is the number of excited elements at time t, k is the rate constant and f(t) is the arbitrary function of the time describing the time course of the excitation. The fluorescence anisotropy measures the depolarization of the fluorescence emission. The main reasons for depolarization include the energy transfer to another molecule with a different orientation or molecular rotation caused by Brownian motion. Molecular motion depends on local environmental factors, such as viscosity and molecular confinement, and the size of the molecule. In the simplest case the change of anisotropy with time is given by,

$$r(t) = r_0 \exp(-t/\tau_r) \tag{3.4}$$

where r_0 is the initial anisotropy and ranges from 0.4 (parallel transition dipoles) to -0.2 (perpendicular dipoles). Tau is the rotational correlation time, which can be considered a measure of the order-disorder process. It should also be noted in standard lifetime measurements, that when exciting a sample with a fast polarised laser pulse, polarisation effects can be present that can make the decay appear more complex. This relates to depolarisation effects. It is advisable to use a vertically orientated polarizer on the excitation and the emission polarizer at the magic angle (54.7° to the vertical) to remove these depolarisation effects.

3.1.5 Scanning electron microscope and high-resolution transmission electron microscopy

The quality and resolution of Scanning electron microscope (SEM) images are function of three major parameters: (i) instrument performance, (ii) selection of imaging parameters (e.g. operator control), and (iii) nature of the specimen. All three aspects operate concurrently and neither of them should or can be ignored or overemphasized. One of the most interesting aspects of SEM is the apparent ease with which the

morphology of three-dimensional objects can be interpreted with basic knowledge of the technique.

Since the SEM is operated under high vacuum the specimens that can be studied must be compatible with high vacuum (~ 10-5 mbar). This means that liquids and materials containing water and other volatile components cannot be studied directly. Also fine powder samples need to be fixed firmly to a specimen holder substrate so that they will not contaminate the SEM specimen chamber. Non-conductive materials need to be attached to a conductive specimen holder and coated with a thin conductive film by sputtering or evaporation. Typical coating materials are Au, Pt, Pd, their alloys, as well as carbon.

High-resolution transmission electron microscopy (HRTEM) is an imaging mode of the transmission electron microscope (TEM) that allows for direct imaging of the atomic structure of the sample (Laberrigue 1983). HRTEM is a powerful tool to study properties of materials on the atomic scale, such as semiconductors, metals, nanoparticles and sp^2-bonded carbon (e.g., graphene, C nanotubes). At present, the highest point resolution realised in phase contrast TEM is around 0.5 ångströms (0.050 nm). At such small scale, individual atoms of a crystal and its defects can be resolved. One of the difficulties with HRTEM is that image formation relies on phase contrast. In phase-contrast imaging, contrast is not necessarily intuitively interpretable, as the image is influenced by aberrations of the imaging lenses in the microscope. The largest contributions to uncorrected instruments typically come from defocus and astigmatism.

3.1.6 Dynamic light scattering

Light Scattering occurs when polarizable particles in a sample are bathed in the oscillating electric field of a beam of light. The varying field induces oscillating dipoles in the particles and these radiate light in all directions. This important and universal phenomena, is the basis for explaining why the sky is blue, why fog and emulsions are

opaque and other observations. It has been utilized in many areas of science to determine particle size, molecular weight, shape, diffusion coefficients. Dynamic light scattering (DLS), also known as Photon correlation spectroscopy (PCS) is one of the most popular light scattering techniques because it allows particle sizing down to 1 nm diameter. Typical applications are emulsions, micelles, polymers, proteins, nanoparticles, or colloids. The principle involves illumination of the sample by a laser beam and the fluctuations of the scattered light are detected at a known scattering angle θ by a fast photon detector. From a microscopic point of view, the particles scatter the light and thereby imprint information about their motion. Analysis of the fluctuation of the scattered light thus yields information about the particles. The intensity correlation function g2(t), whose analysis provides the diffusion coefficient of the particles, also known as diffusion constant. As per Stokes-Einstein equation 3.5, the diffusion coefficient, *D*, is related to the radius, *R*, of the particles:

$$D = \frac{k_B T}{6\pi\eta R} \tag{3.5}$$

where k_B is the Boltzmann-constant, T is the temperature (in K) and η the viscosity.

3.1.7 X-Ray Diffraction

X-ray diffraction (XRD) technique is a unique method for determination of crystallinity of a compound. It can be used to qualitatively identify crystalline material, identification of different polymorphic forms (“fingerprints”), to distinguish between amorphous and crystalline material and also quantify the percent crystallinity of a sample (Waseda, Matsubara and Shinoda 2011). In an amorphous sample such as glass, the atoms are arranged in a random way similar to the disorder in a liquid sample. In a crystalline sample, the atoms are arranged in a regular pattern, and there is as smallest volume element that by repetition in three dimensions describes the crystal. This smallest volume element is called a unit cell. The dimensions of the unit cell is described by three axes: a, b, c and

the angles between them alpha, beta, gamma. About 95% of all solids can be described as crystalline and they can be studied with Bragg's Law given by the simple equation 3.6:

$$n\lambda = 2d \sin\theta \tag{3.6}$$

explain why the cleavage faces of crystals appear to reflect X-ray beams at certain angles of incidence (theta, θ) (see Figure 3-1). The variable *d* is the distance between atomic layers in a crystal, and the variable lambda (λ) is the wavelength of the incident X-ray beam, where n is an integer.

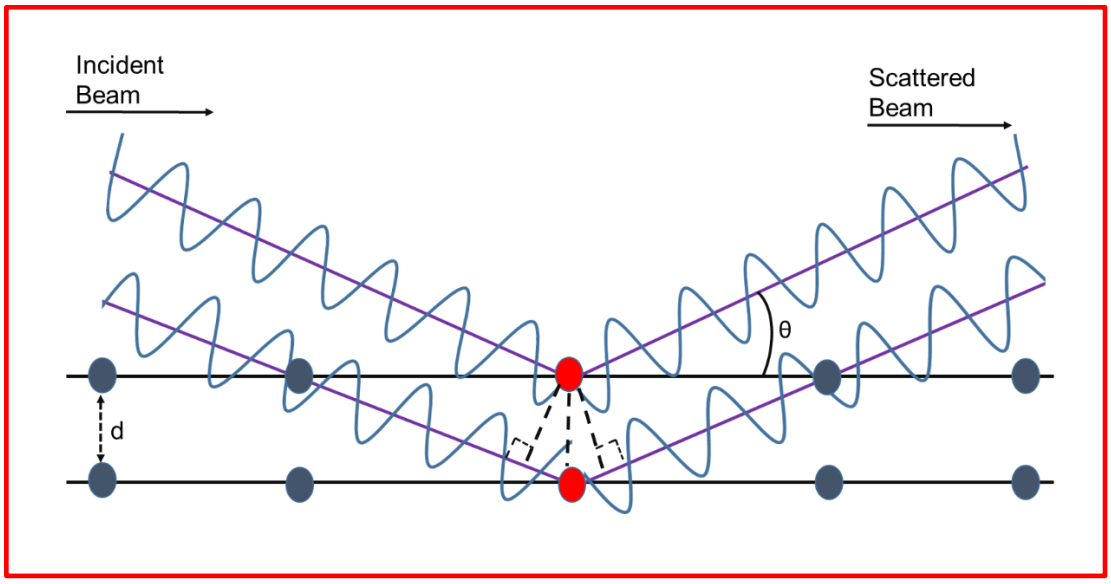

Figure 3-1: Deriving Bragg's Law using the reflection geometry.

Although Bragg's law was initially used to explain the interference pattern of X-rays scattered by crystals, diffraction has been developed to study the structure of all states of matter with any beam, e.g., ions, electrons, neutrons, and protons, with a wavelength similar to the distance between the atomic or molecular structures of interest.

3.2 Computational

Computational chemistry has been reported as an efficient tool to clarify kinetic and thermodynamic processes involved in synthesis and properties characterization.

3.2.1 Geometry optimization theory

It is a standard activity in molecular simulation to perform optimization or minimization with respect to potential energy of the system being examined. Hence there are various geometry optimization algorithms available. In generally, the structure will be optimized after sketching, since sketching often creates the molecule in a high energy configuration and starting a simulation from such an un-optimized structure can lead to inaccurate results. The optimization of a structure is a process with two steps: Firstly, the e*nergy evaluation,* where the energy expression is defined and evaluated for a given conformation. Energy expressions which include external restraining terms, to bias the optimization, may be defined in addition to the energy terms. Secondly, *conformation adjustment* which is performed to reduce the value of the energy expression. A minimum may be found after one adjustment or may require many thousands of iterations, depending on the nature of the algorithm, the form of the energy expression, and the size of the structure. The overall efficiency of the optimization is therefore dependent on the time needed to evaluate the energy expression and the number of structural adjustments (iterations) needed to converge to the minimum.

3.2.1.1 Geometry optimization algorithms

The optimization of a molecular structure can be regarded in mathematical terms as an optimization in a multidimensional space which refers to the exact number of dimensions depending on the number of atoms and the periodicity of the system. There are several standard algorithms that can be applied in geometry optimization, but we only look at steepest descents and Newton-Raphson methods

(i) Steepest descents

In the steepest descents method, the line search direction is defined along the direction of the local downhill gradient - ∇E (x_i, y_i) for the simple quadratic function. Each line search produces a new direction that is perpendicular to the previous gradient; however, the directions oscillate along the way to the minimum. This inefficient behavior is characteristic of steepest descents, especially on energy surfaces having narrow valleys.

(ii) Newton-Raphson methods

The principle behind the common variable metric optimization algorithms known as Newton-Raphson, can be described as follows. As a rule, N^2 independent data points are required to solve a harmonic function with N variables numerically. Since a gradient is a vector N long, the best possible gradient-based minimizer is converge in N steps. However, with the exploitation of the second-derivative information, an optimization could converge in one step, because each second derivative is an $N \times N$ matrix. Alternatively, in addition to using the gradient to identify a search direction, the curvature of the function (the second derivative) is also used to predict where the function passes through a minimum along that direction. Since the complete second-derivative matrix defines the curvature in each gradient direction, the inverse of the second-derivative matrix can be multiplied by the gradient to obtain a vector that translates directly to the nearest minimum. This is expressed mathematically as:

$$r_{\min} = r_o - A^{-1}(r_o) \bullet \nabla E(r_o) \tag{3.7a}$$

where r_{min} is the predicted minimum, r_0 is an arbitrary starting point, $A(r_0)$ is the matrix of second partial derivatives of the energy with respect to the coordinates at r_0 (also known as the Hessian matrix), and $\nabla E(r_0)$ is the gradient of the potential energy at r_0. The energy surface is generally not harmonic, so that the minimum-energy structure cannot be determined with one Newton-Raphson step. Instead, the algorithm must be applied iteratively as shown in equation 3.7b:

$$r_i = r_{i-1} - A^{-1}(r_{i-1}) \bullet \nabla E(r_{i-1}) \qquad (3.7b)$$

Thus, the i^{th} point is determined by taking a Newton-Raphson step from the previous point (i - 1). Similar to conjugate gradients, the efficiency of Newton-Raphson optimization increases as convergence is approached(Ermer 1976).

(iii) Drawbacks of pure Newton-Raphson method

As elegant as this algorithm appears, its application to molecular modeling has several drawbacks. First, the terms in the Hessian matrix are difficult to derive and are computationally costly for molecular forcefields. Furthermore, when a structure is far from the minimum, the optimization can become unstable. Calculating, inverting, and storing a $N \times N$ matrix for a large system can become unwieldy. Even taking into account that the Hessian is symmetric and that each of the tensor components is also symmetric, the storage requirements scale as approximately $3N^2$ for N atoms. Thus, for a 200 atom system, 180,000 elements are required. The Hessian alone for a 1,000 atom system already approaches the limits of a Cray-XMP super computer, and a 10,000 atom system is currently intractable. The iterative Newton-Raphson method can be unstable if the conformation is so far away from a local minimum that the potential energy surface is not nearly quadratic. Therefore, the steepest descents method should be the preferred choice for the first 10-100 steps of the optimization.

3.2.2 Density functional theory

The density functional theory (DFT) is presently the most successful approach to compute the electronic structure of matter. Its applicability ranges from atoms, molecules, and solids to nuclei and quantum and classical fluids. In its original formulation, the density functional theory provides the ground state properties of a system, and the electron density plays a key role (Hohenberg and Kohn 1964; Kohn and Sham 1965). DFT predicts

a great variety of molecular properties: molecular structures, vibrational frequencies, atomization energies, ionization energies, electric and magnetic properties, reaction paths. The DFT is a remarkably successful approach to finding solutions to the fundamental equation for the quantum behavior of atoms and molecules, the Schrodinger equation, in settings of practical value. The DFT begins with a theorem by Hohenberg and Kohn, later generalized by Levy which states that all ground-state properties are functionals of the charge density ρ (Hohenberg and Kohn 1964; Levy 1979). Specifically, the total energy, E_t, may be written as:

$$E_t[\rho] = T[\rho] + E_{xc}[\rho] + U[\rho] \tag{3.8}$$

where $T[\rho]$ is the kinetic energy of a system of non-interacting particles of density ρ, U $[\rho]$ is the classical electrostatic energy due to coulombic interactions, E_{xc} $[\rho]$ includes all many-body contributions to the total energy, in particular, the exchange and correlation energies. The Equation 3.8 is written to emphasize the explicit dependence of these quantities on ρ (in subsequent equations, this dependence is not always indicated). The charge density is constructed from a wave function Ψ. As in other molecular orbital methods(Roothaan 1951; Slater 1972; Dewar 1983), the wave function is taken to be an antisymmetrized product of one-particle functions, in this case molecular orbitals (MOs):

$$\psi = \frac{1}{\sqrt{n!}}(n)\left|\phi_1(1)\phi_2(2)\ldots\phi_n(n)\right| \tag{3.9}$$

When the molecular orbitals are orthonormal,

$$\left\langle \phi_i \middle| \phi_j \right\rangle = \delta_{ij} \tag{3.10}$$

the charge density is given by the simple sum:

$$\rho(r) = \sum_i \left|\phi_i(r)\right|^2 \tag{3.11}$$

where the sum is over all occupied MOs, ϕ_i. The density obtained from this expression is also known as the *charge density*. The MOs may be occupied by spin-up (*alpha*) or spin-down (*beta*) electrons. Using the same ϕ_i for both *alpha* and *beta* electrons is known as a *spin-restricted* calculation; using different ϕ_i for alpha and beta electrons results in a *spin-unrestricted* or *spin-polarized* calculation. In the unrestricted case, it is possible to form two different charge densities: one for alpha MOs and one for beta MOs. Their sum gives the total charge density and their difference gives the *spin density*, the amount of excess *alpha* over *beta* spin. This is analogous to restricted and unrestricted Hartree-Fock calculations(Pople and Nesbet 1954).

3.2.2.1 Total energy components

From the wave functions and the charge density (Equation 3.11), the energy components can be written (in atomic units) as:

$$T = \left\langle \sum_i^n \phi_i \left| \frac{-\nabla^2}{2} \right| \phi_i \right\rangle \tag{3.12}$$

$$U = \int V_N(r)\rho(r)dr + \frac{1}{2}\int \frac{\rho(r_1)\rho(r_2)}{|r_1 - r_2|} dr_1 dr_2 + V_{NN} \tag{3.13}$$

The first term represents the electron-nucleus attraction.
The second term represents the electron repulsion.
The final term, V_{NN}, represents the nucleus repulsion.

3.2.2.2 Common spin-density functionals

The simplest form of the exchange correlation potential is the form derived by Slater, which simply uses $\varepsilon_{xc}[\rho] = \rho^{1/3}$(Slater 1951). In this approximation, the correlation is not included. More sophisticated approximations use the forms derived by Vosko and team as denoted by Barth, Janak and Perdew with their co-workers. (Barth and Hedin

1972; Janak, Moruzzi and Williams 1975; Vosko, Wilk and Nusair 1980; Perdew and Wang 1992).

3.2.2.3 Density gradient expansion

The next step in improving the local density (LDA) model is to take into account the inhomogeneity of the electron gas which naturally occurs in any molecular system. This can be accomplished by a density gradient expansion, sometimes referred to as the non-local spin-density approximation (NLSD). Over the past few years, it has been well documented that the gradient-corrected exchange-correlation energy $E_{xc}[\rho, d(\rho)/dr]$ is necessary to study the thermochemistry of molecular processes as explained in the reviews (Ziegler 1991; Wiener and Politzer 1998). The commonly used NLSD functionals include the Pardew generalized gradient approximation for the correlation functional, the Becke gradient corrected exchange functional, and the gradient-corrected correlation functional of Lee and team. (Becke 1988; Lee, Yang and Parr 1988; Perdew and Wang 1992).

3.2.2.4 The total energy expression

The total energy can now be written as:

$$E_t[\rho] = \sum_i \left\langle \phi_i \left| \frac{-\nabla^2}{2} \right| \phi_i \right\rangle + \left\langle \phi_i \left| \frac{-\nabla^2}{2} \right| \phi_i \right\rangle + \left\langle \rho(r_i)[\varepsilon_{xc}[\rho(r_1)] + \frac{V_e(r_1)}{2} - V_N] \right\rangle \quad (3.14)$$

To determine the actual energy, variations in E_t must be optimized with respect to variations in ρ, subject to the orthonormality constraints in Equation 3.9 (Kohn and Sham 1965).

3.2.2.5 Kohn-Sham equations

This process leads to a set of coupled equations first proposed by (Kohn and Sham 1965)

$$\{\frac{-\nabla^2}{2} - V_n + V_e + \mu_{xc}[\rho]\}\phi_i = \varepsilon_i\phi_i \qquad (3.15)$$

The term μ_{xc} is the exchange-correlation potential, which results from differentiating E_{xc}. For the local spin-density approximation, the potential μ_{xc} is:

$$\mu_{xc} = \frac{\delta}{\delta\rho}(\rho\varepsilon_{xci}) \qquad (3.16)$$

Use of the eigenvalues of equation 3.15 leads to a reformulation of the energy expression:

$$E_t = \sum_i \varepsilon_i + \left\langle \rho(r_1)[\varepsilon_{xc}[\rho] - \mu_{xc}[\rho] + \frac{V_e(r_1)}{2}] \right\rangle + V_{NN} \qquad (3.17)$$

3.2.2.6 Periodic boundary conditions

The discussion so far has been completely general with regard to the type of systems that can be studied with DFT. Molecules, clusters, or periodic solids are treated equally in this formalism. This section addresses some issues that specifically apply to infinite periodic systems. In the sections that follow, it is assumed that the system is periodic in three dimensions.

3.2.2.7 Periodic basis functions

If we consider a crystal with lattice vectors a_i, i = 1, 2, 3. For example, in a simple cubic cell, the vectors could be a_1 = (1, 0, 0); a_2 = (0, 1, 0); and a_3 = (0, 0, 1). The basis

functions must have the translational symmetry of the crystal, so $\chi_\mu(r) = \chi_\mu(r + R)$, where r is any point in the crystal and $R = n_1a_1 + n_2a_2 + n_3a_3$, with the n all being integers.

To meet this requirement, a set of plane waves with the periodicity of the lattice is generally introduced and the periodic basis is taken as $\psi(k,r) = e^{ik.R}\chi(r)$. In principle there are infinite number of vectors k and R needed to describe the space exactly. In practice, the number of plane waves is determined by the cutoff kinetic energy which is chosen to represent physically relevant spatial harmonics of wavefunctions. The vectors k are called *k-points*, and are needed to describe the band structure correctly. In practice, only a few k-points (of the order of $1\text{-}10^2$) are needed.

3.2.2.8 Predicting chemical structure

The ability to evaluate the derivative of the total energy with respect to geometric changes is critical for the study of chemical systems. Without the first derivatives, a laborious point-by-point procedure is required, which is taxing to both computer and human resources. The availability of analytic energy derivatives for Hartree-Fock theories (to name just a few) has made these remarkably successful methods for predicting chemical structures (Pulay 1969; Pople *et al.* 1979; Brooks *et al.* 1980). DFT offers an even more straightforward formalism for evaluating energy gradients, and thus it became the method of choice for structural studies of molecules and solids alike.

3.2.3 Forcefields

A crucial part of any simulation is the choice of forcefield. The forcefield describes approximately the potential energy hypersurface on which the atomic nuclei move. Forcefields are usually tuned for particular groups of systems, so the choice of forcefield will depend on the type of structure that is being investigated. Herein we look at the two forcefields:

3.2.3.1 Chemistry at Harvard macromolecular mechanics (CHARMM)

CHARMM is the name of a widely used set of force fields for molecular dynamics, and the name for the molecular dynamics simulation and analysis computer software package associated with them (Brooks *et al.* 1983). The CHARMM force fields for proteins include: united-atom (sometimes termed extended atom) CHARMM19, all-atom CHARMM22 and its dihedral potential corrected variant CHARMM22/CMAP. In the CHARMM22 protein force field, the atomic partial charges were derived from quantum chemical calculations of the interactions between model compounds and water(MacKerell *et al.* 1998; Mackerell, Feig and Brooks 2004).

3.2.3.2 COMPASS

Condensed-phase Optimized Molecular Potentials for Atomistic Simulation Studies (COMPASS) represents a technology break-through in forcefield methods. It is the first *ab initio* forcefield that enables accurate and simultaneous prediction of gas-phase properties and condensed-phase properties for a broad range of molecules and polymers. These properties includes structural, conformational, vibrational changes, equation of state, cohesive energies etc. It is also the first high quality forcefield to consolidate parameters of organic and inorganic materials.

3.3 Docking

The binding bites of a receptor are identified, edited, and displayed. In general, the receptors should have hydrogens and complete valence shells so that they can be atom typed. They also cannot have alternate conformations. The functionality depends on the receptor being defined, including receptor-ligand hydrogen bonds. The binding site can be identified from either receptor cavities, PDB site records (for Biomacromolecules) or by manual/current selection. A shape-based binding site can be used by protocols such

as Dock Ligands (LigandFit). The volume is calculated as one of the attributes of a binding site. When using the current selection option, sphere is created around the centroid of selected objects (e.g., atoms or binding site points) with the radius adjusted to include them. If a receptor is not defined, the selected molecule is used. Receptor surfaces provide unique insight into the inner workings of a receptor. A surface is created on a receptor close to the current ligand, and missing atoms such as hydrogens are added. The ligand is defined so that as to determine the starting position of the navigation tools.

- **Analysing receptor-ligand interactions**

When analyzing the receptor-ligand interactions, non-bond interactions such as van der Waals forces can also be analysed to better understand the interactions responsible for binding. The ligand is monitored to further analyze interactions between the defined ligand and receptor. The Ligand poses are analyses using a protocol that calculates favorable and unfavorable interactions between a receptor and ligand poses. The ligands can be filtered based on receptor interactions. Finally ligand binding sites within receptor can be characterized and compared by visualizing the interactions between receptor residues and bound ligands. The interactions in a receptor-ligand complex determined by experiment or by the interactions of a set of docked ligands with a known protein structure can also be used for validation of the method.

CHAPTER 4

4 MATERIALS AND METHODS

This chapter details the chemicals and reagents used in this study. The experimental methodologies for all studies are also described including; extraction of natural products, synthesis, and characterization of nanoparticles, followed by preparation and fabrication of the nanoparticle based electrodes for electrochemical biosensor. Other parts of the methodology are embedded within the case studies to maintain clarity.

4.1 Experimental

4.1.1 Chemicals and Reagents

All reagents were of analytical grade. The biomacromolecules used for interaction and colorimetric assays namely: HSA Fraction V (lyophilized powder, ≥96%; agarose gel electrophoresis with CAS Number: 70024-90-7), Bovine Serum Albumin (BSA) (A2153), Lysozyme (Lys) from chicken egg white (62971), dsDNA from salmon testes (D1626), from herring testes (D6898), from calf thymus (D1501), low molecular weight ssDNA from salmon sperm (31149), polyadenylic acid (polyA) (P9403), polycytidylic acid (polyC) (P4903) and polyuridylic acid (polyU) (P9528), were purchased from Sigma-Aldrich and used as received. Dihydrogen phosphate dihydrate, 2, 2'-Azino-bis (3-ethylbenzothiazoline-6-sulfonic acid) diammonium salt (ABTS), Tris(hydroxymethyl)-aminomethane, sodium chloride, sodium hydroxide, methanol (CH_3OH, HPLC grade, ≥99.9%), P25 Degussa titania powder, Dimethyl sulfoxide (DMSO, 99.9 % HPLC grade), methanol (CH_3OH, HPLC grade, ≥99.9%), diethyl ether and potassium chloride (KOH) were also purchased from Sigma Aldrich. Zinc gluconate hydrate ($C_{12}H_{22}O_{14}Zn.xH_2O$, purity 97%), and sodium hydroxide (NaOH, purity ≥98%), were purchased from Alfa Aesar and Fluka respectively.

The human embryonic kidney cells (HEK293T), fresh Dulbecco's modified Eagle's medium and 20 µl MTT (from 5 mg mL^{-1} stock) were purchased from Himedia. The root bark of *Ilex Mitis* and leaves of *Iboza* plants were obtained from Durban city central market in KwaZulu Natal, South Africa (SA). *Jacaranda mimosifolia* flowers were collected in Botanic gardens, Durban, KwaZulu Natal, SA. Monosodium phosphate (NaH_2PO_4), disodium phosphate (Na_2HPO_4) used for the preparation of buffer. In order to approximate the physiological ionic strength, a phosphate-buffered saline (PBS) was used in the incubation stage consisting in a 67 mM phosphate buffer at pH 7.4 and 9 g/L of sodium chloride. The distilled water used for the preparation of the buffer and other lab necessities was produced by a MilliQ system (Millipore, France), PURITE (18 MΩ) and LABTECH, Automatic Water Still system (South Africa).

4.1.2 Methodology: Isolation and extraction of natural products

4.1.2.1 Isolation of Saponins from Ilex Mitis

The root bark sample of *Ilex Mitis*, was grounded to a fine powder and 20 g transferred into a conical flask before 100 mL of 20 % aqueous ethanol was added. The mixture was then heated over a water bath for 4 h with continuous stirring at 55 ^oC and then filtered after cooling to 25 ^oC. The extracts were concentrated to 40 mL by rotary vapor and purified with 20 mL of diethyl ether during which the aqueous layer was recovered. Subsequently, the saponins were extracted from aqueous layer using n-butanol three times and washed twice with 10 mL of 5 % aqueous sodium chloride. Finally, the organic layer was retained and concentrated by rotary vapor to dryness producing solids saponins (Edeoga, Okwu and Mbaebie 2005).

4.1.2.2 Extraction of diterpenes from Iboza Riparia (Tetradenia Riparia)

Approximately 5.0 g of *Tetradenia Riparia* fresh leaves were collected and shredded into a 250 mL beaker. Then, boiled with 200 mL deionized water at 60 ^oC for 20

min. After cooling to room temperature, the mixture was filtered with a Whatman filter paper *No.1* and the extract was stored in a refrigerator at 4 ^{o}C.

4.1.2.3 Extraction from carica papaya fruit

The seeds obtained from the ripe *Carica papaya* fruit were washed, dried and powdered. To prepare the extract used in the synthesis of ZnONPs, approximately 1.0 g of powdered seeds was dissolved in 100 mL deionized water and heated at a constant temperature of 90 °C for 1 h on a magnetic stirrer with a hot plate. The extract collected as a filtrate was further used in the NPs synthesis.

4.1.2.4 Extraction from jacaranda mimosifolia flowers

The extract used in the synthesis of ZnO nanoparticles was prepared by dissolving 1.0 g of dried and powdered *jacaranda mimosifolia* flowers (collected in Durban, South Africa) in 100 mL deionized water and heating at a constant temperature of 90 ^{o}C for 1 h on a magnetic stirrer with a hot plate. The extract was filtered and used further in the synthesis (Sharma *et al.* 2016).

4.1.3 Methodology: Synthesis and characterization of nanomaterials

4.1.3.1 Chemical synthesis of AgNPs (refer to Case Study 1)

The prism-like nanoparticles of silver colloidal solutions were prepared as per method reported in the reference (Aherne *et al.* 2008). Briefly, a seed solution was prepared by mixing aqueous trisodium citrate (5 mL, 2.5 mM), aqueous poly (sodium styrenesulphonate) (PSSS; 0.25 mL, 500 mg L^{-1}; Aldrich 1,000 kDa) and freshly prepared aqueous $NaBH_4$ (0.3 mL, 10 mM,). Thereafter, aqueous 5 mL of 0.5 mM $AgNO_3$ was added at a rate of 2 mL min^{-1} while stirring continuously. Subsequently, nanoprism like silver particles were produced by mixing (i) 5 mL distilled water, (ii) 75 mL of 10 mM

aqueous ascorbic acid (freshly prepared), (iii) 100 µL of seed solution and lastly, aqueous 3 mL of 0.5 mM $AgNO_3$ at a rate of 1 mL min^{-1}. Immediately after synthesis, the particles were protected by stabilizing with an aqueous trisodium citrate (0.5 mL, 25 mM). The formation of prism-like AgNPs denoted by a color change of the seed solution from yellow to intense blue. Upon changing the volume of the starting solution or reducing agent, it was possible to control the uniformity of the product. The final size of the AgNPs verified by TEM using the drop and dry method for preparation at 10 nm and 50 nm, is designated by AgNP10 and AgNP50 respectively (Figure 5-1). It must be highlighted that due to the short life-time of the seed solution, the timing was key to obtaining a product of high purity.

4.1.3.2 Hydrothermal synthesis of TiO_2 NPs (refer to Case Study 2)

The four types of nanomaterials here referred to as T200, T400, T700 and T900 were sintered as per Microwave-Assisted Hydrothermal Synthesis (µHS) method described elsewhere (Sikhwivhilu *et al.* 2012). The four types of sample product were divided into four equal portions and then sintered for 3 h at 200, 400, 700, and 900 °C. The resulting products were stored at dry conditions until use for interaction studies.

4.1.3.3 Green synthesis of AgNPs (refer to Case Study 3)

The bioconjugated *AgNPs* of silver colloidal solution was prepared as per method reported (Aherne *et al.* 2008) with notable modifications. Briefly, a seed solution was prepared by mixing aqueous trisodium citrate (5 mL, 2.5 mM), aqueous poly(vinyl alcohol) (PVA; 0.25 mL, 500 mg L^{-1}; Sigma Aldrich) and aqueous $NaBH_4$ (0.3 mL, 10 mM, freshly prepared). Thereafter, aqueous 5 mL of 0.5 mM $AgNO_3$ was added at a rate of 2 mL min^{-1} while stirring continuously. Subsequently, spherical like silver particles were produced by mixing (i) 5 mL distilled water, (ii) 75 mL of 10 mM aqueous ascorbic acid (freshly prepared), (iii) 100 µL of seed solution and lastly, aqueous 3 mL of 0.5 mM $AgNO_3$ at a rate of 1 mL min^{-1}. Immediately, post the synthesis, the particles were

protected by stabilizing with 0.5 mL of 25 mM aqueous trisodium citrate. The formation of AgNPs is denoted by the color change of seed solution (yellow) as added to the clear violet. When using either *Ilex Mitis* or *iboza* extracts instead of PVA, the final color of the nanoparticle solution was grey in color and the products were stable.

4.1.3.4 Green synthesis of ZnONPs using extract of jacaranda flowers and carica papaya fruit (refer to case study 4 and case study 5 respectively)

In a typical experiment, to 100 mL of zinc gluconate hydrate (0.1 M), 100 mL of extract (*Jacaranda mimosifolia* flower or *carica papaya* fruit) extract and 100 mL of NaOH (0.4 M) was added while stirring the mixture for 15 min. The mixture was then exposed to microwave irradiation for 5 min in a microwave oven (SAMSUNG ME9114W operating at 100% power of 1000 watt and frequency of 2.45 GHz). The formation of ZnONPs was indicated by the milky white precipitate powder which was filtered and subsequently washed with ethanol and deionized water. The final products were dried in an oven at a constant temperature of 60 ^{o}C for about 3 h. The final product was dried in an oven at a constant temperature of 60 °C for 3 hours. In order to know the effect of capping agent present in the extract, ZnONPs were synthesized using 0.1 M zinc gluconate hydrate and 0.4 M NaOH without the use of extract keeping the reaction conditions same(Sharma *et al.* 2016; Sharma *et al.* 2018).

4.1.3.5 Characterization of AgNPs, TiO_2 NPs and ZnONPs

The bare-eye colorimetric observations of AgNPs, were confirmed by recording absorbance spectra for 1 mL solutions at 1 nm s^{-1} on JASCO V-570 UV–vis spectrometer from 320 nm to 750 nm. Thereafter, the particle size was estimated with dynamic light scattering (DLS) on a SYMPATEC nanophox instrument that is operated with WINDOX 5.4.2.2 software. Mean size distribution was obtained using the incorporated non-negative least squares (NNLS) model because it does not assume the shape and size of the particles

in solution. Finally, the exploratory data analysis was performed with Principal Component Analysis (PCA) embedded in Unscrambler 10.3.

The morphological images were taken using an HRTEM model JEOL JSM 2100 TEM with a LaB_6-cathode operated at a voltage of 200 kV, while the SEM model JSM-7500F coupled with EDS and fitted with a LABe™ enabling for high resolution for the morphology and mapping analysis. The well-established sample preparation for TEM sample was adopted, where the copper grid was dipped into a sample solution and thereafter the solvent evaporated under the IR lamp. The sample was coated with a conductive carbon tape prior to SEM imaging.

The hydrodynamic distribution of the particle before and after conjugation was evaluated for DLS with a HORIBA LB-550 with a Light source: 650 nm Laser diode, 5 mW. All the samples were ultra-sonicated prior to measurements.

The absorbance was measured with a Perkin- Elmer LAMDA 750S UV/VIS Spectrometer at room temperature from 200−600 nm and the quenching analysis was performed at an excitation wavelength of 280 nm with a Perkin-Elmer LS-55 Fluorescence Spectrometer equipped with a diode array detector. The widths of the excitation slit and the emission slit were set to 15 nm and 2.5 nm, respectively. Appropriate blanks corresponding to the buffer were subtracted to correct the fluorescence background. Spectra were obtained by scanning simultaneously at 500.0 nm/min the excitation and emission monochromators at slits width of 5.0 nm. The wavelength for excitation and emission was located at 380 nm. The reaction medium, 67 mM phosphate buffer silane and reaction constituents were degassed in an ultrasonic bath operated at a frequency of 35 kHz (Bandelin SONOREX™ SUPER, Sigma) prior to spectroscopic measurements. A quartz cell with dimensions 4 cm × 1 cm × 1 cm was employed throughout the UV/Vis and Fluorescence Spectrometer measurements. Both the excitation and emission slit widths were set 5 nm for a constant scan rate of 500 nm/min. A Seven Component, Mettler Toledo pH/ion meter was employed to adjust the pH of buffer solutions. The phosphate buffer solution was used as the background correction prior to measurements of analytes.

The bioconjugate samples for Raman spectroscopy measurements were obtained by incubation of the mixtures for 30 min followed by centrifugation at 2000 rpm for 15 min to remove the supernatant. Measurements were performed with a Jobin Yvon LabRAM HR 800 UV-VIS-NIR. The Olympus Microscope using a 785 nm laser excitation wavelength for data acquisition at 0.33 cm^{-1} resolution.

The attenuated total reflectance - fourier transform infrared (ATR-FTIR) spectra of the milled compounds were recorded using a Varian 800 FT-IR Scimitar Series supplied by SMM Instruments (Durban, South Africa (SA)). The instrument was configured with an ATR sample cell including a diamond crystal with a scanning depth up to 2 µm. Powders samples were directly spread on the surface of the crystal then locked in place with a "clutch-type" lever before measuring transmittance.

X-ray diffraction study was carried out using a Bruker AXS D8 diffractometer with CuKα radiation (λ = 1.5418 Å) at 40 kV over a 2θ range from 10^o to 70^o at a scanning rate of 0.05 min^{-1}. The samples were dispersed in distilled water and ultrasonicated for 30 min before analysis. The absorption studies were carried out on a UV 2450 Spectrophotometer (Shimadzu, Japan). The colloidal solution of the sample was prepared by dissolving 1.0 mg of ZnO nanopowder in 50 mL ultra-pure deionized water and was run in the wavelength range 200-800 nm. FTIR spectra of ZnONPs samples and extract of *jacaranda mimosifolia* flowers and *carica papaya* were recorded in the range of 4000-500 cm^{-1} on Varian 800 FT-IR Scimitar Series supplied by SMM Instruments (Durban, SA).

The conductivity measurements on green synthesized AgNPs were performed with Metrohm, 644 conductometer at 26.5 °C.

4.1.3.6 Characterization of natural products and its nanoparticles

To predict the composition of *jacaranda mimosifolia* flowers extract and a predominant capping agent, GC-MS analysis of the methanolic extract was carried out. 1.0 mg of the dried and powdered *jaca jacaranda mimosifolia* flowers and *carica papaya* fruits were dissolved in methanol and stirred for 30 min followed by filtering through 0.45

µm nylon filter. Finnigan MAT GCQ system with splitless injector mode was employed for the sample analysis. The injector temperature was set at 250 ^{o}C and ZB-5MS fused silica capillary column with dimensions 30 m x 0.25 mm x 1 µm was used. The carrier gas was helium with a flow rate of 1 mL min^{-1} and the amount of sample injected was 1 µL. The MS conditions are as follows, scan mode: full scan in EI mode (50 to 650 amu), transfer line temperature: 270 ^{o}C and ion source temperature: 200 ^{o}C. The identification of the compounds present in the *jacaranda mimosifolia* flowers and *carica papaya* fruits extracts was compared with the NIST library.

4.1.4 Methodology: Preparation and fabrication of the *GCE/MWCNTs/ZnONPs*

The protocol used for the preparation and fabrication of GCE was adopted from Balgobind *et al*. and slightly modified (Balgobind *et al.* 2016). The GCE was manually polished with alumina slurry before being electrochemically cleaned at -0.2 to 0.8 V with 0.5 % HCl/water solution to remove any adsorbed materials from the electrode surface. The MWCNTs were modified with ZnONPs by dispersing 1:6 quantities in 5 mL dimethylformamide (DMF) and thereafter sonicated for 45 min at 60 °C resulting into a hybrid nanocomposite. Lastly, the composite was deposited onto the GCE surface and oven dried at 50 °C for 5 min.

4.2 Computational

4.2.1 Computational Protocols

The structure of HSA obtained from the PDB database (PDB ID – 1AO6) showed discontinuity in the structural coordinates. For this purpose the HSA structure was re-modelled using the modeler module of the Discovery Studio 2016, followed by minimization. On the other hand, the TiO_2 nanomaterial-based structures such as nanorods, nanowires, nanosheets, and nanotubes were constructed using the drawing utilities present in the Material Studio (MS). The DFT calculations were performed at the B3LYP level of theory using $DMol^3$ module of MS.

The optimized structures of HSA described above, along with the four generated nanomaterials were docked utilizing the AutoDock 4 software package (Morris *et al.* 2009). AutoDock 4 performs the prediction of the bound conformation based on the free energy force field coupled with the Lamarckian Genetic Algorithm (Morris *et al.* 2009). The grid box of dimensions 120 x 120 x 120 Å along the XYZ directions with a grid spacing of 0.375 Å was established using the AutoGrid module. In order to increase the efficiency, the parameters associated with Lamarckian genetic algorithm were set to 250, the maximum efficiency value of its conformational population, while the maximum number of energy evaluations were set to "longer". Resulting in 100 docked conformations grouped according to their root mean square deviation (RMSD) tolerance set at 2.0 Å. The generated conformations were rescored on the basis of the scoring function present in DrugScoreX (Neudert and Klebe 2011). The docking scores were validated using the CDOCKER module, a CHARMM (Vanommeslaeghe *et al.* 2010) based docking algorithm implemented in DS.

4.2.2. Adsorption studies using molecular modeling

To better understand the role of capping agents present in the *jacaranda mimosifolia* flowers extract, adsorption studies were carried out using adsorption locator and forcite modules in MS (Kirkpatrick, Gelatt and Vecchi 1983; Bunte and Sun 2000). The capping agent i.e. oleic acid was sketched in Accelrys Materials Studio software package and geometrically optimized with COMPASS forcefield using the forcite module to get the energy minimized structure. Three dimensional (3D) ZnO surfaces (101, 100, and 002) were built by importing the crystal structure of ZnO from the structure library of MS. The oleic acid molecules were allowed to adsorb on each of the designed ZnO surfaces by setting up the task to *simulated annealing* with *fine* quality where *adsorbate* was oleic acid with different *loading* values. The COMPASS forcefield was assigned to charges of atoms with *Ewald & group based* summation method. The concentration profile of oleic acid molecules on the ZnO surface was obtained by running the forcite calculation on the whole system (oleic acid molecules adsorbed on the surface of ZnO).

CHAPTER 5

5 Case-Study 1: Colorimetric discrimination of biomacromolecules supported by statistical methods

---

This chapter reports on a bivariate colorimetric assay for the discrimination of proteins, DNAs and polynucleotides. Silver nanoparticles were used as the source of color and therefore monitored using spectroscopy. The color changes observed were dependent on the concentration of the salt and nanoparticles. This approach is supported by principal component analysis for clustering population based on their colorimetric response.

5.1 Methodology

5.1.2 Preparation of AgNPs-Bio macromolecule mixtures

The experimental design involved a feasibility study of the influence on AgNPs color changes by the two independent variables, namely: salt (NaCl) and biomacromolecule concentrations. The salt concentration was varied from 10 to 100 mM, while that of the biomacromolecules was varied from 0.1 to 10 µg mL^{-1}. The biomacromolecules stock solution was prepared in a 10 mM Tris buffer solution, composed of 150 mM NaCl and 1 mM KCl at pH 8. Any further dilutions were carried out with deionized water to prevent additional salt contribution from the buffer. Finally, the desired salt and biomacromolecules concentrations, shown in Table 5-1 were achieved by varying the volume of the salt accordingly. The composition of the mixtures depicted in Table 5-1 were prepared to a total of 1 mL at room temperature and analyzed: (i) AgNP10 or AgNP50, (ii) deionized water, (iii) biomacromolecules, (iv) 5 min waiting period, (v) salt, (vi) 60 min waiting period, (vii) absorbance spectroscopic measurements and (viii) particle size measurements (by DLS).

Table 5-1: Experimental setup for the colorimetric and spectroscopic assay of both AgNP10 and AgNP50 upon interaction with the different biomacromolecules.

ΨAgNPs (Size nm, µM)	**Biomacromolecule (µg mL^{-1})**	**NaCl (mM)**
*AgNP10 (10 nm, 0.350 µg mL^{-1})	0.0	0.0
	0.1	10
	1.0	10
	10.0	10
	0.1	50
	1.0	50
	10.0	50
	0.1	100
	1.0	100
	10.0	100

*Similar setup was used for AgNP50 (50 nm, 0.489 µg mL^{-1})

The addition of biomacromolecules into the NPs was crucial prior to the salt, to avoid preliminary aggregation and colorimetric changes that may arise due to electrostatic interactions in the absence of the biomacromolecules. In order to find the lowest concentration of NaCl yielding a color change of the solutions, a similar approach was adopted without the addition of water was followed: (i) AgNP10 or AgNP50, (ii) biomacromolecules, (iii) 5 min waiting period, (iv) salt in the increments of 10 µL. Finally, the concentration of NaCl per solution was calculated taking into account the final volume.

5.2 Results and discussion

5.2.1 Characterisation of synthesised AgNPs

Since the main aim of this study was to discriminate biomacromolecules based on nanoparticles aggregation, therefore an in-depth understanding of the morphological characterisation was deemed necessary. The characterization of AgNPs by TEM, UV-Vis and DLS is presented in Figure 5-1. It is evident in Figure 5-1 that the two dominant shapes, spherical and prism types of nanoparticles are dispersed with average diameters

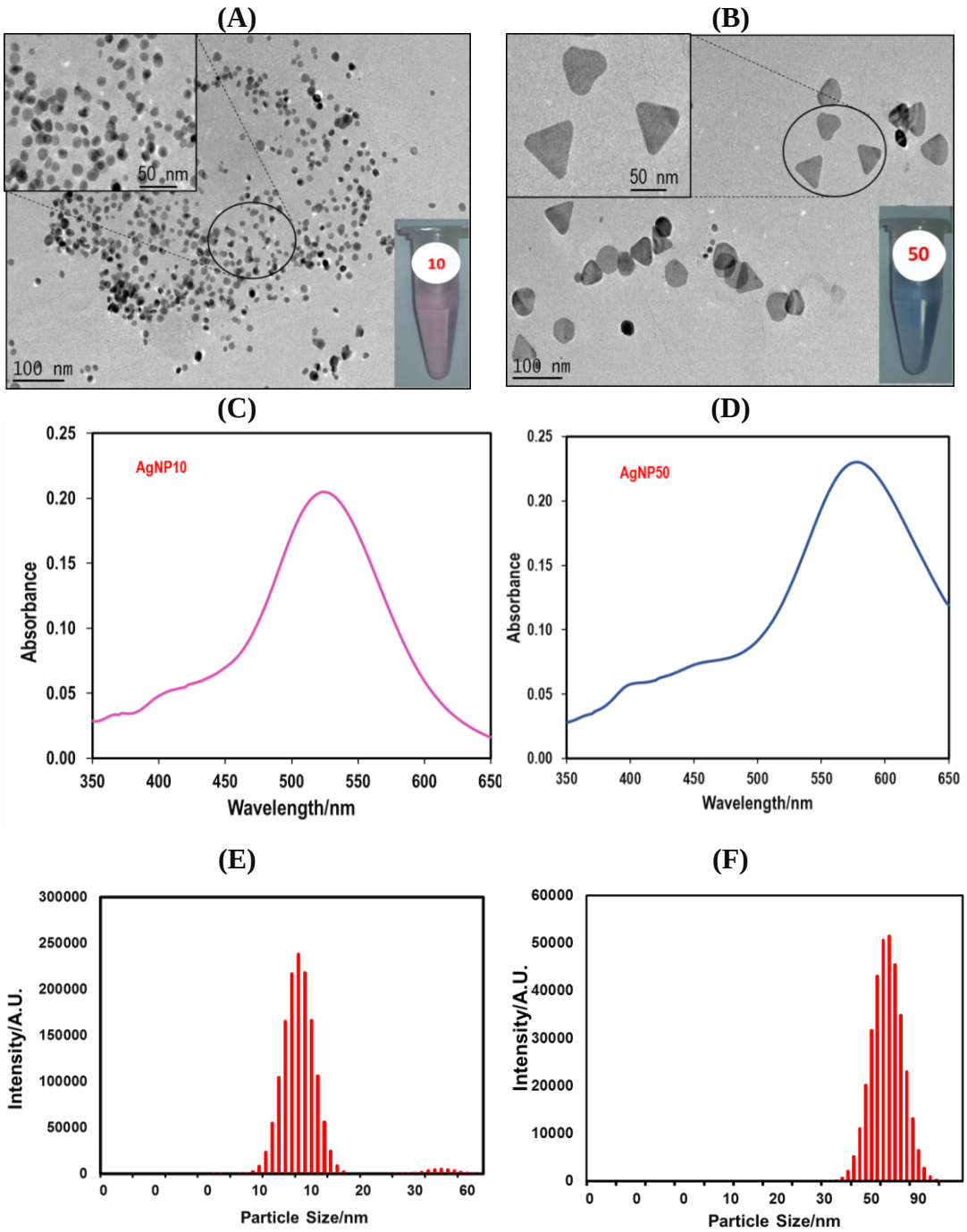

Figure 5-1 (A) and (B) are the TEM images (inset is the corresponding color of the particles dispersed in water), (C) and (D) are the absorption spectrum showing maxima at 530 and 582 nm respectively, (E) and (F) shows the average particle distribution by DLS. *10 and 50 refers to the size of the nanoparticles.

of 10 nm and 50 nm, referred to as AgNP10 and AgNP50 respectively. In addition, the UV-Vis absorbance measurements confirmed that the two nanoparticles, AgNP10 and AgNP50, differ on the surface properties with an absorbance maxima of 530 nm and 582 nm respectively (Germain *et al.* 2005). Similar trends can be seen in the color changes of the insert in Figure 5-1 (A) and (B) and they are in accordance with the differences in absorbance maxima (530.0 – 582.0 = 52.0 nm).

5.2.2 Surface plasmon resonance (SPR)

The optical adsorption spectrum of the AgNPs was dominated by the SPR and typical values of absorbance bands depending on the particle size, shape, aggregation and the surrounding dielectric medium as the salt concentrations were varied. In addition, our results revealed a shift in SPR with increasing biomacromolecules concentrations. Figure 5-2(A) and (B) depicts the plasmon peaks with minor blue shifts from 530 - 436 nm for AgNP10 and with a broader wavelength shift from 582 - 436 nm for AgNP50.

No absorbance peaks were observed for the clear solutions Figure 5-2(i) due to complete aggregation, in accordance with the results observed by S. Kundu *et al.* for typical AgNP10 in the presence of DNA mixtures (Kundu 2013). In order to better understand these observations, the biomacromolecules and the salt concentrations were independently investigated.

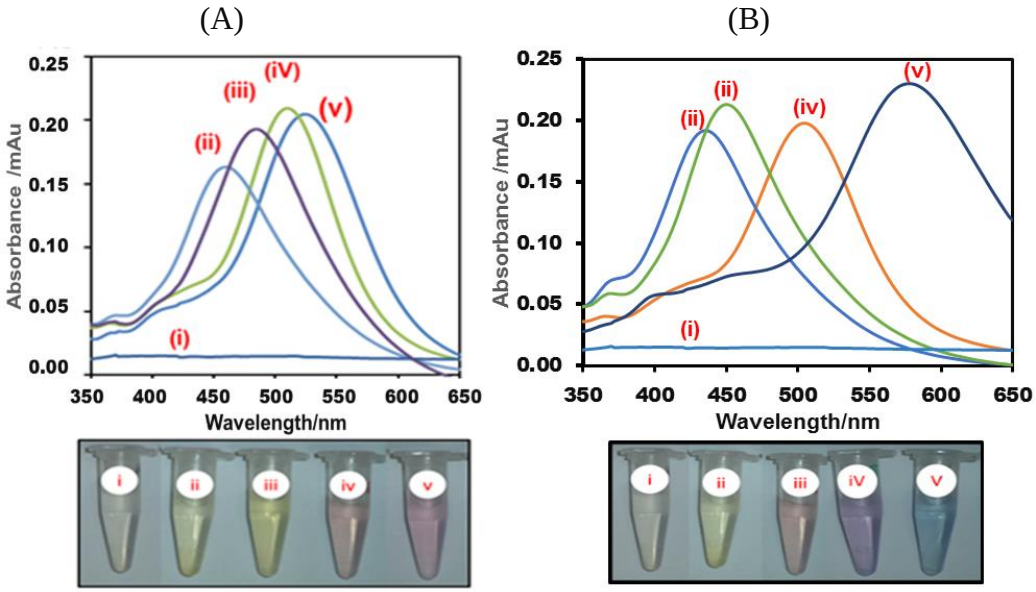

Figure 5-2: Effect of concentration in the presence of (A) AgNP10 and (B) AgNP50 solutions conjugated with BSA at various salt concentrations added (v) control: pure AgNP10/50, (iv) 100 mM, (iii) 50 mM, (ii) 10 mM and (i), NPs with 50 mM NaCl and no biomacromolecule.

5.2.3 Effect of biomacromolecules concentration

Biomacromolecules concentration is a key to surface modification of nanoparticles as they can occur through non-specific adsorption processes. The addition of the Lys to AgNPs (Figure 5-3A) without the salt addition, demonstrated a rare but rather unusual behavior where samples with the highest concentration changed from a dark blue to clear, suggesting a large degree of aggregation. In contrast, the BSA (Figure 5-3B) addition did not induce any color changes in the presence of a salt, aiding in the protection of the nanoparticle's surface.

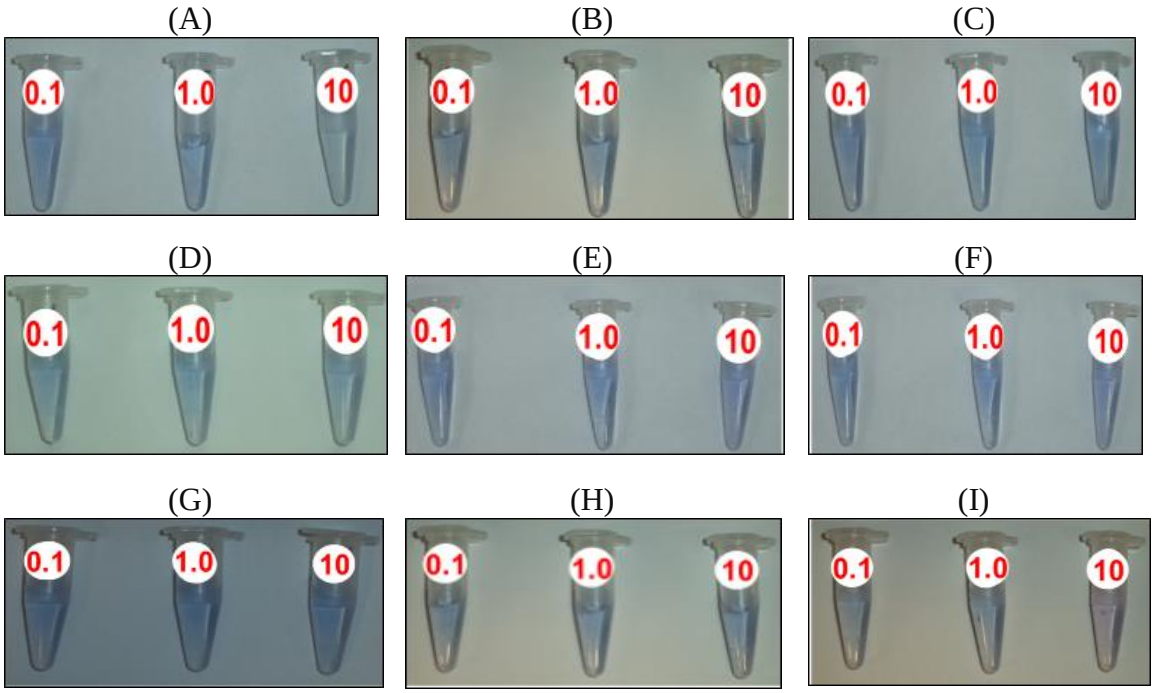

Figure 5-3: Solutions contain 0.489 µg mL^{-1} of AgNP50 and 0.0 mM NaCl with varying concentration of biomacromolecules; 0.1, 1.0 and 10 µg mL^{-1} respectively where: (A) Lys, (B) BSA, (C) ssDNA, (D) dsDNA "calf", (E) dsDNA "herring", (F) dsDNA "salmon", (G) polyA, (H) polyC, and (I) polyU.

DLS also showed that as the concentration of Lys increased, precise measurements of the particle size became difficult or impossible due to greater aggregation. However, the absorbance spectra revealed broader peaks and blue shift of maxima with an increase in Lys concentration (Table A3.1), in agreement with the color change for AgNP10 and AgNP50 from red to a clear solution. Interestingly, for AgNP10 the BSA samples with concentrations of 10 µg mL^{-1} demonstrated no sedimentation after the addition of 50 mM NaCl, despite an increase in size from 10 nm to ~50 nm (Table A3:4). This suggested that AgNP50 was more susceptible to colorimetric changes in contrast to AgNP10. All samples containing either ssDNA or dsDNA in the absence of the salt, retained the color of the nanoparticle in solution, even at their highest concentration as depicted in Figure 5-3(C)-(F). This suggests that no aggregation occurred on the nanoparticles. Similar observations

for the polynucleotides in the absence of the salt were observed, except for the polyU at 10 µg mL^{-1} with AgNP50 which resulted in a purple color thus reaffirming the influence of polyU on the aggregation. Furthermore, the effect of biomacromolecules concentration was also studied at fixed concentrations of the salt (50 mM NaCl). Figure 5-4 depicts the color changes and absorbance spectra of polyC for both AgNP10 and AgNP50 samples under a fixed salt concentration.

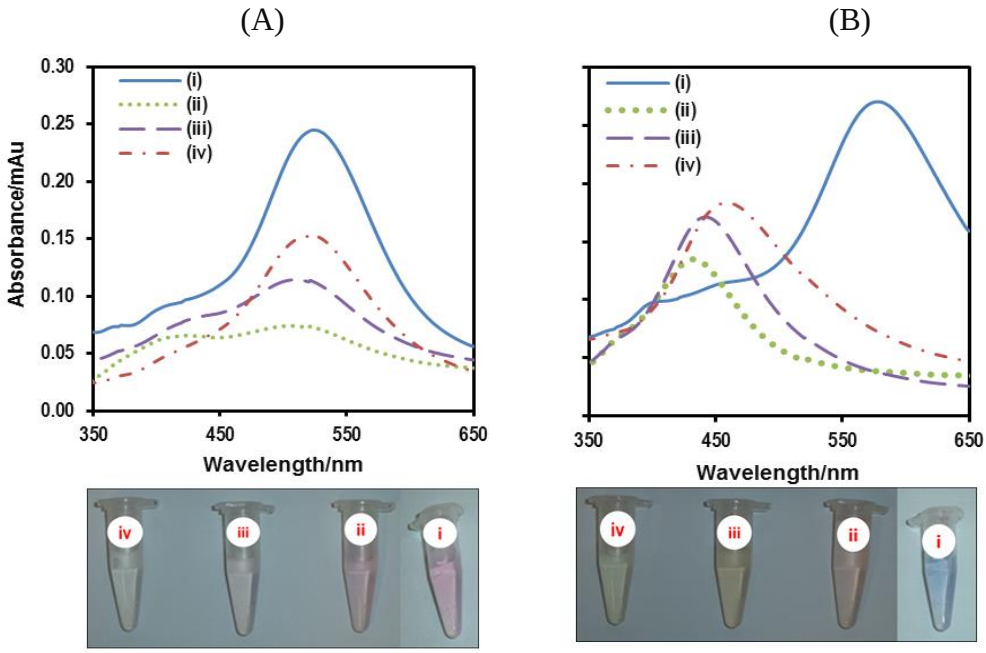

Figure 5-4: Effect of polyC concentration in the presence of 50 mM NaCl and (A) AgNP10 and (B) AgNP50 solutions: (i) control sample of pure AgNP10/50 solution in water; (ii) solution of NPs and 0.1 µg mL^{-1} polyC, (iii) solution of NPs and 1.0 µg mL^{-1} polyC and (iv) solution of NPs and 10 µg mL^{-1} polyC.

For AgNP10, the increase in polyC concentration induced a minor blue shift in absorbance spectra from 528 to 518 nm, whereas for AgNP50, a significant blue shift was observed at 425 nm. Overall observations on the effect of biomacromolecule concentrations were not significant on the color of the nanoparticle solution and the shift

in their absorbance maxima in the absence of salt, except for Lys and polyU as shown in Figure 5-3. However, when a salt was added, an increase in the biomacromolecule concentration shift in SPR band and colorimetric responses were observed as a consequence of the nanoparticle aggregation.

In contrast to all the biomolecules in the system, AgNP10-dsDNA from "calf" and AgNP50-polyU did not display any significant blue shifts, even at fixed salt concentrations (Appendix 3: Tables A3.2, A3.3 and A3.4), thus confirming the absence of aggregation. The two possibilities based on low and high concentrations of the biomacromolecules on AgNP50 are illustrated in Scheme 5-1 below. Similar results were obtained for AgNP10 but not shown here.

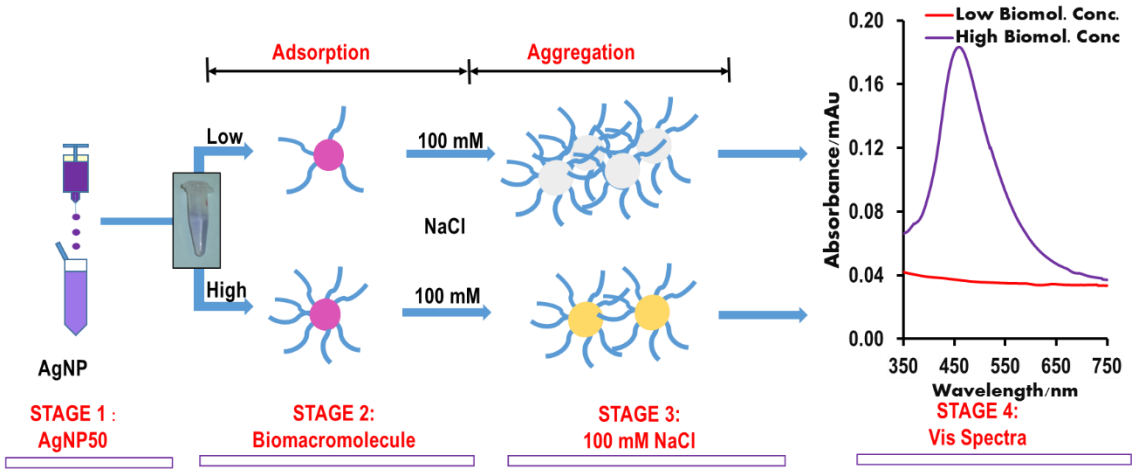

Scheme 5-1: Possible mechanism of nanoparticles (AgNP50) aggregation at low concentration (0.1 µg mL^{-1}) and high concentration (10 µg mL^{-1}) of biomacromolecules in the presence of 100 mM NaCl

Overall similar behavior was observed for both AgNP10 and AgNP50, except with Lys and polynucleotides, in the presence of a fixed salt and high biomacromolecules concentrations. This is a significant result suggesting high colorimetric responses corresponds to a lower aggregation, in contrast to lower biomolecular concentrations.

5.2.4 Effects of salt concentration

It has been previously reported that nanoparticles aggregation depends on the salt concentration; therefore we explicitly evaluated its impact on the colorimetric responses (Chen *et al.* 2008; Siddhartha and Debabrata 2010; Lepoitevin *et al.* 2015). Figure 5-5 depicts the dependency of the color changes on salt concentrations on AgNP50 and dsDNA from "calf". Overall, the color changes observed with dsDNA samples showed minor colorimetric differences based on clustering according to AgNP10 and AgNP50. No significant aggregation of the nanoparticles was observed in all dsDNA samples (calf, salmon, and herring) prior to the addition of the salt (Figure 5-2). However, a drastic color change observed with both AgNP10 and AgNP50 upon the addition of the salt (Table A2.2). Our observed results are in strong agreement with those reported by Zhang *et al.*, where the DNAs showed the ineffectiveness of salt-ageing at neutral pH (Zhang, Servos and Liu 2012a). Specifically, the dsDNA from "salmon" and "herring" were less efficient

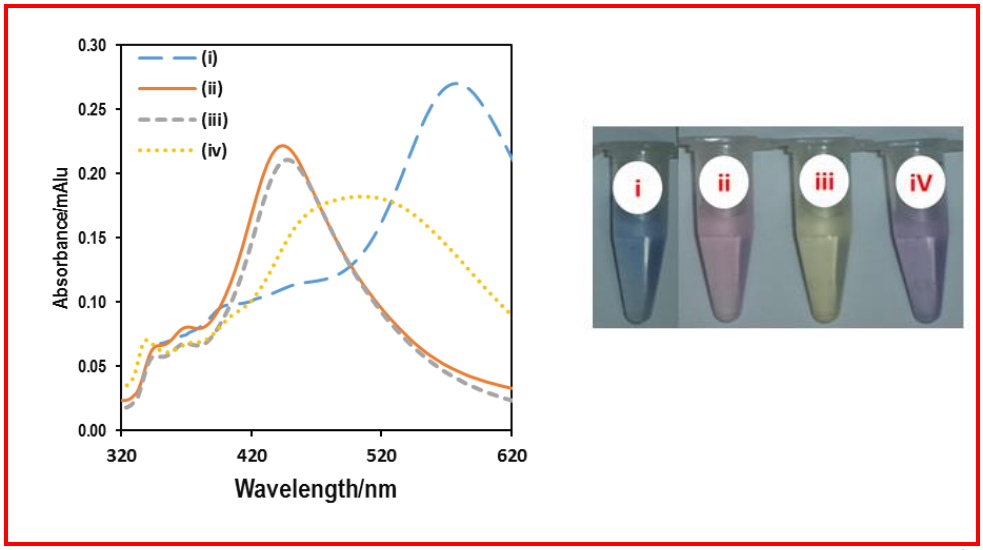

Figure 5-5: Colorimetric images and absorbance spectra of AgNP50 in 10 µg mL^{-1} dsDNA "calf recorded (i) before addition of salt (control sample) and after addition of (ii) 10 mM NaCl, (iii) 50 mM NaCl and (iv) 100 mM NaCl.

on NPs aggregation since a significant color change was observed under 50 mM NaCl (Table A3.2). This aggregation is more distinct for AgNP50. Indeed, samples containing the dsDNA from "herring" and salt gradually changed from a blue to pink color.

Interestingly, the Lys samples were clear even at the lowest concentration of the salt, while the BSA samples differed, depending on both the salt and biomacromolecules concentrations. The AgNP10 samples at 1.0 µg mL^{-1} BSA, and varying salt concentrations from 10 to 100 mM, also changed from red to colorless. Solutions with salt concentrations lower than 100 mM also demonstrated a significant color change, particularly at lower concentrations of BSA. However, a closer inspection of the AgNPs with polynucleotides solutions demonstrated no visible color changes before the addition of the salt as shown in Figure 5-4. The addition of the 10 mM and 50 mM NaCl resulted in well-defined intense absorbance peaks observed at 444 nm and 450 nm respectively. Nevertheless, no significant absorbance peaks were observed between 350 to 650 nm particularly for 0.1 and 1.0 µg mL^{-1} of polyC and polyU respective samples with 100 mM NaCl (Table A3.3), in contrast to polynucleotides that seemed to prevent aggregation (Ravindran *et al.* 2010). Accordingly, further investigation on the polynucleotides were carried out and the two corresponding absorbance spectra are depicted in Figure 5-6. Figure 5-6A shows no observable shifts in wavelength maxima with AgNP10, but with a monotonic decrease in the absorbance corresponding to an increasing salt concentration. However, in the corresponding UV-Vis adsorption spectra (Figure 5-6) a significant drop in absorbance for AgNP50 was observed as the salt concentration increased from 0 to 100 mM for wavelength ranging from 434 to 582 nm. The polyA samples for both AgNP10 and AgNP50 started showing aggregation and colorimetric changes towards clear at 50 mM NaCl (Table A3:3 and A3:4).

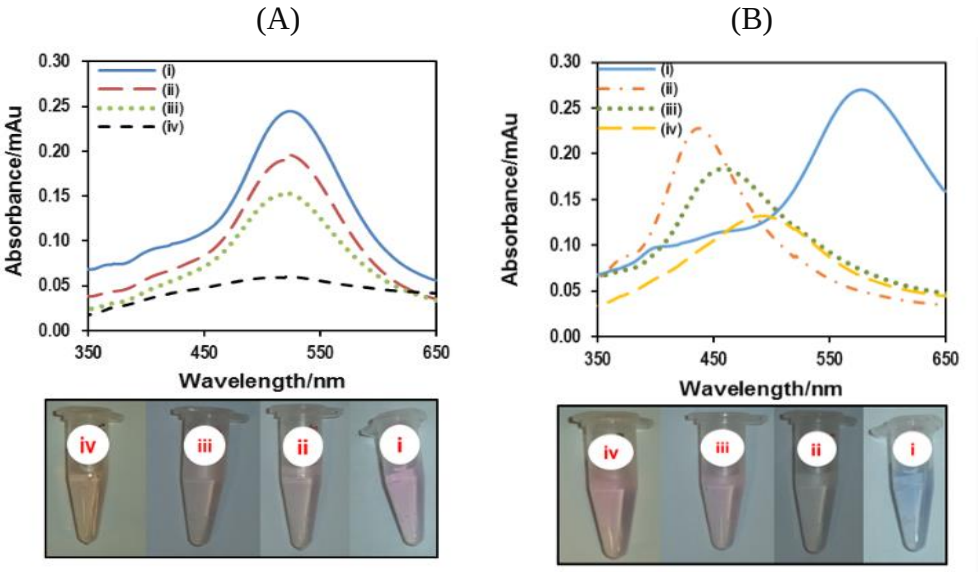

Figure 5-6: Effect of the concentration of the salt in (a) AgNP10 and (b) AgNP50 solutions: (i) control sample of pure AgNP10 or AgNP50 solution in water; (ii) solution of NPs, 10 µg mL^{-1} polyC and 10 mM NaCl, (iii) solution of NPs, 10 µg mL^{-1} polyC and 50 mM NaCl and (iv) solution of NPs, 10 µg mL^{-1} polyC and 100 mM NaCl.

Overall, the variation of salt and biomacromolecules concentrations demonstrated a significant impact on the colorimetric changes. Therefore, the information gathered from the two parameters were collectively used to discriminate the selected biomacromolecules. In summary, the lowest concentration of the salt required to trigger observable color changes are as follows: 21.05 mM (BSA), 0.0 mM (Lys), 23.08 mM (dsDNA "salmon"), 6.25 mM (dsDNA "calf"), 18.92 mM (dsDNA "herring"), 28.57 mM (ssDNA "salmon"), 6.25 mM (polyA, polyC and polyU) for AgNP10. When using AgNP50, it was 23.08 mM (BSA), 0.0 mM (Lys), 21.05 mM (dsDNA "salmon"), 3.85 mM (dsDNA "herring"), 16.67 mM (dsDNA "calf"), 28.57 mM (ssDNA "salmon"), 9.09 mM (polyA), 6.25 mM (polyC and polyU).

5.2.5 Colorimetric discrimination of biomolecules

In order to discriminate between the chosen biomacromolecules, colorimetric sensing responses involving two manual approaches were implemented in addition to PCA. The first approach involved grouping solutions on the bases of color changes at fixed concentrations of the salt (Figure 5-7). It is worth mentioning that the colorimetric classification presented in Figure 5-7 refers to 10 mM NaCl and 0.1 to 10 µg mL^{-1} biomacromolecules, resulting in three groups for both AgNP10 and AgNP50. In the case of Lys as a model, a distinct color change from a dark to a clear solution was observed, even at 0.1 µg mL^{-1}, thus enabling the ease of discrimination from other biomacromolecules. In contrast, BSA demonstrated minor changes from blue to yellow after the addition of the proteins on the AgNP50. Similarly, all the polynucleotides and dsDNA were in the same class with BSA, whereas ssDNA and Lys could be easily distinguished with AgNP50 in contrast to AgNP10.

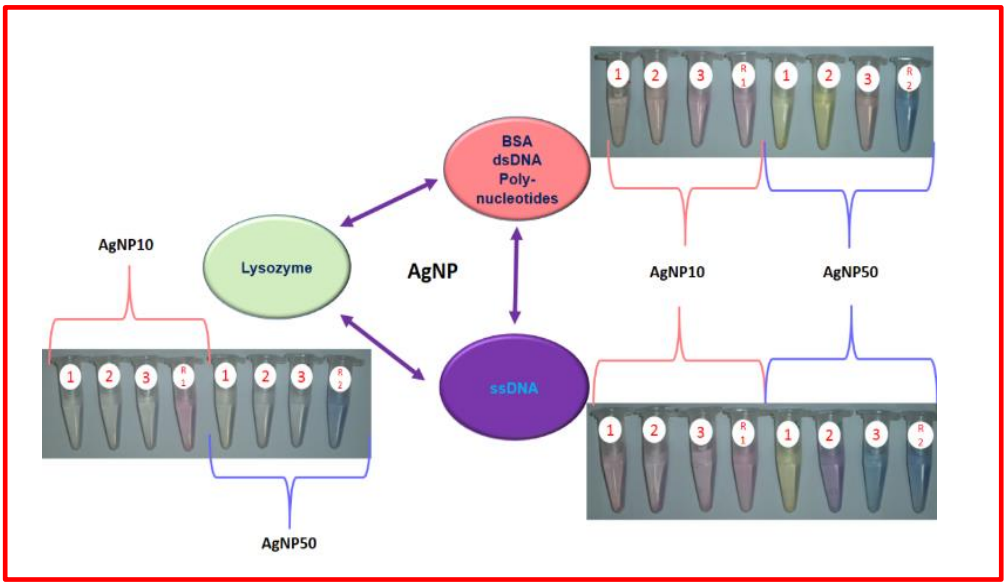

Figure 5-7: Colorimetric discrimination of AgNPs-biomacromolecules with solutions containing 10 mM NaCl and varying concentration of biomacromolecules; (1) 0.1, (2) 1.0 and (3) 10 µg mL^{-1}. R1 and R2 are reference samples of pure AgNP10 and AgNP50 respectively.

Further classification was therefore necessary for the discriminate of all the biomacromolecules of interest, because some of them kept falling in the same class. Accordingly, the second approach involved all the univariate experimental combinations to achieve satisfactory discrimination as demonstrated by the color-coding used in Table 5-2. For instance, in stage 2 of Scheme 5-1, both polyU and ssDNA belonged to the same group, but after adding salt they differed significantly depending on the concentration of the salt.

Table 5-2: Color coding assigned to possible bare-eye colorimetric observations for both AgNP10 and AgNP50

Color	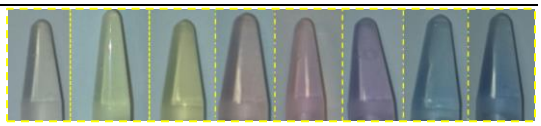							
	AgNP50							
	AgNP10							
Code	1	2	3	4	5	6	7	8

The color coding for all the colorimetric observations in relation to wavelengths is summarized in Appendix 3, Table A3.4. Data in the color-coded table were in agreement with the classification of Lys in Figure 5-7, isolated from the other biomacromolecules. This is a significant result as the table enables us to identify conditions in which particular biomolecules will behave differently. The studies on the effect of concentration demonstrated that dsDNA "calf" was more resistant to color changes as summarized in Table A3.4. It can be discriminated from either dsDNA "salmon" or dsDNA "herring" using both AgNP10 and AgNP50 based on color codes 5,5,5 and 5,3,3 respectively.

Further discrimination of polyA and polyC, showed similar color changes at concentrations of 0.1 and 1.0 µg mL^{-1} respectively. The color codes were significantly different at the highest concentration (10 µg mL^{-1}) for polyA and for polyC, suggesting that these two molecules cannot be discriminated under these conditions. This is in

contrast to AgNP50, where the discrimination of biomacromolecules concentration at 1.0 µg mL^{-1}, due to variation in the color codes for polyA and polyC. On comparing the overall results, AgNP50 showed a more distinct color change than AgNP10, complementing a wider spectral range (Figure 5-1). For this purpose, AgNP50 appeared to be more favorable in the-screening process.

5.2.6 Statistical analysis

Standard chemometric techniques involving PCA were employed to discriminate the biomolecules based on two variables, salt and biomolecules concentrations. However, all the data were mean centered and weighed per standard deviation as it contains variable scale to minimize bias. Thereafter, a full cross-validation was performed and the group analysis is pictorially represented AgNP10 and AgNP50 in Figure 5-8. In the scores plot, the horizontal analysis of AgNP10 data group shown in Figure 5-8A, revealed 49% and 26% of the data points in the PCA score for (PC1) and (PC2) respectively. The mean score obtained at a 95% confidence level, confirming the possibility to discriminate between polyA, ssDNA "calf", BSA, ssDNA, and PolyA. However, PolyC, PolyU and dsDNA "herring" could not be discriminated, due to the closeness of the data points. The corresponding correlation loading shows that solutions with 50 mM NaCl have a greater influence in comparison with 10 mM NaCl solutions. This was also confirmed by the loading correlation in Figure 5-8B, which also shows that 10 mM of salt contributes the least to the PC2 variation. Therefore, 50 mM was selected as the cut-off for a significant discrimination of AgNP10. On the other hand, 90% of the data points observed for AgNP50 are illustrated by PC1 and PC2 in Figure 5-8C. The correlation loading profile of AgNP50 (Figure 5-8D), suggests that all the concentrations of the salt had an influence greater than 50% as they fall outside the boundary, but with an even distribution of salt concentrations for PC2. The influence of the salt varies with the changes in biomolecules concentration, demonstrating a wider window for discrimination.

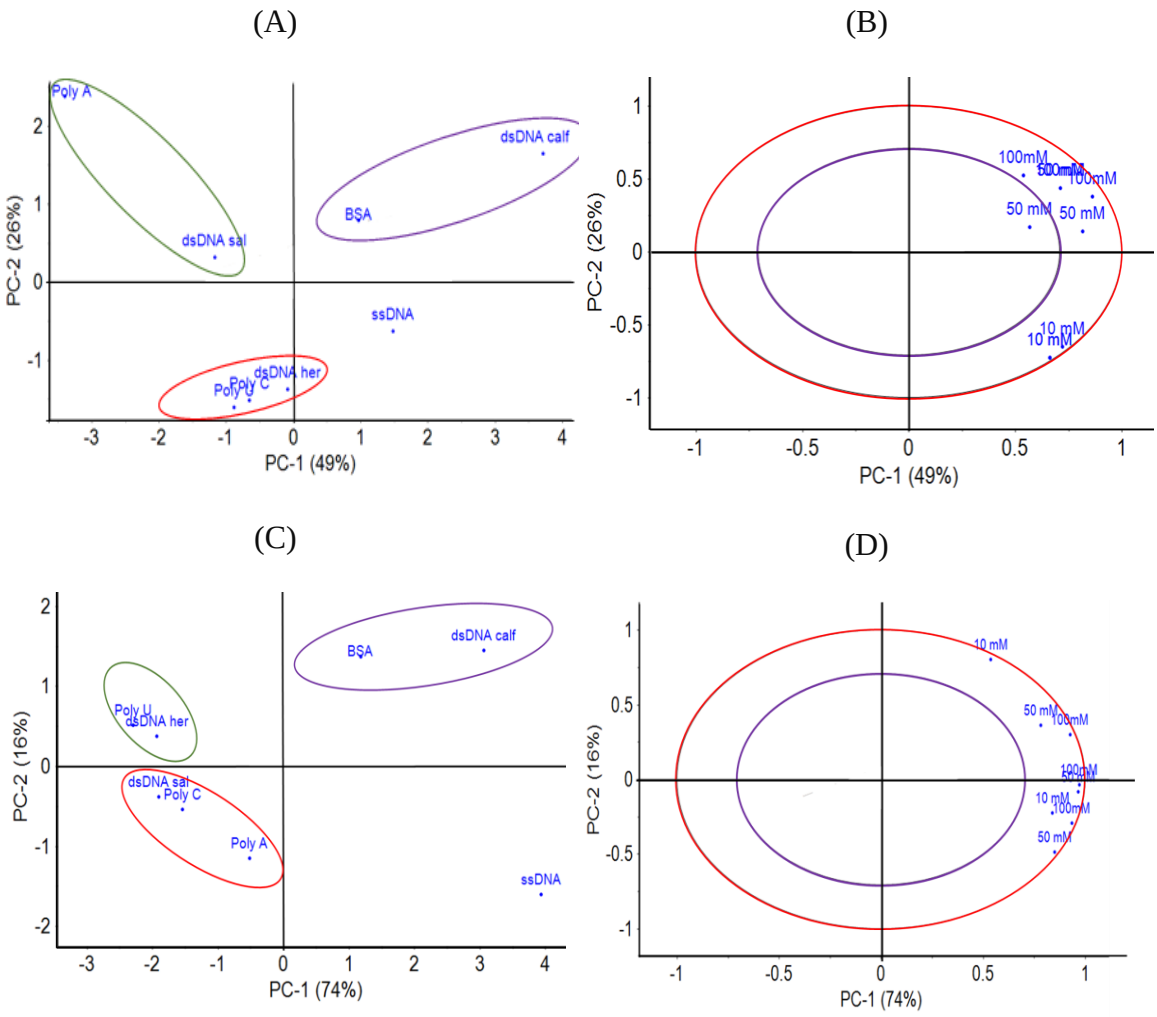

Figure 5-8 (A)and (C) showns 2D plot of scores based on the effect of salt and biomacromolecule concentrations respectively. (A)and (C) showns 2D plot of scores based on the effect of salt and biomacromolecule concentrations respectively . (B) and (C) showns correlation loading between PC1 versus PC2 based on the effect of salt and biomacromolecule concentrations respectively.

(A) and (C) are the 2D scores plot, (B) and (D) correlation loading showing PC1 versus PC2 considering the effect of salt and biomacromolecule concentrations.

On comparing AgNP10 and AgNP50 model based on the scores alone, it is clear that BSA and dsDNA "calf" falls on the same quadrant but can easily be discriminated with AgNP10

PCA, due to differences in PCA scores of 2.1 and 1.0 for PC1 and PC2 respectively. This is a significant result as the spacing between biomolecules demonstrates recognition capability of the sensor (Ghasemi, Hormozi-Nezhad and Mahmoudi). However, it is worth mentioning, that the two groups of data for AgNP10 and AgNP50 can be combined, but will complicate the system and mostly increase the influential components. Overall we obtained acceptable discrimination of analytes on two-dimensional PCA plots with our bivariate model.

5.3 Conclusions

In this chapter, we evaluated the inclusion of AgNPs for the discrimination of biomacromolecules as a colorimetric sensor. This study was based on the biomacromolecules ability to prevent NPs aggregation induced by an increase in salt concentrations. The color changes also served as a good indicator of the levels of aggregation, as confirmed by DLS. Clearly, the grouping of biomolecules based on color changes alone, was insufficient to discriminate the selected biomacromolecules. Therefore, for the first time color codes were implemented, thus offering a variety of options for the discrimination strategy. Interestingly, it is feasible to discriminate within a family of biomacromolecules such as dsDNA and polynucleotides. This was further supported by PCA analysis which confirmed that the colorimetric responses were more favourable to changes in salt concentrations. Indeed, the model was helpful in simplifying the influence of the bivariate and identification of the suitable parameters for the discrimination process. Data for both nanoparticles, favoured the one direction PC1 with all the variables outside the first region contributing to > 50 % of the variable.

In view of the availability of the precursors necessary for the synthesis of AgNP10 and AgNP50, this method is considered accommodating and user friendly, leading to the reproducibility of the model biological system. Overall, this work has the potential to

provide rational guidelines based on experimental design applicable to nanoparticles-based colorimetric sensing methods, with widespread applications.

CHAPTER 6

6 Case Study 2: Interaction study between HSA and TiO_2

In this study we report the response factors for the interaction of human serum albumin to various shapes of TiO_2 nanostructures. Charaterization studies involving transmission electron microscopy, scanning electron microscopy, fluorescence/photoluminescence spectroscopy as well as FTIR/Raman spectroscopic methods confirmed that HSA encapsulates TiO_2 nanostructures with the degree of encapsulation depending on the size and shape of the TiO_2 nanostrutures. Dosimetry studies by dynamic light scattering (DLS) revealed sigmoidal S-shaped curves in the encapsulation of size versus TiO_2 dose plots with parameters of critical dosage, log D_0, encapsulation size, ΔS, and EC_{50} being lowest for nanotubes, while the Hill coefficient being highest for the nanotubes.

6.1 Methodology:

6.1.1 Bioconjugation of TiO_2 materials

The four types of materials sintered for 3 h at 200, 400, 700, and 900 °C The nanomaterials were prepared by sonication in the phosphate buffer. Initially, both HSA protein (*P*) and TiO_2 nanomaterial (NM) models were prepared, however the NM constant yielded no conclusive results hence it is not reported. The model used had a concentration of HSA fixed at 500 nM and that of NM, varied from 0, 50, 100, 500, 1000 and 500 nM. The mixtures were prepared in duplicates with a total volume of 2 mL and then allowed to react in a static medium water bath set at 37 ^{o}C (average human body temperature) for 30 min. This process was performed in order to mimic how the human body would respond to different levels of TiO_2 nanomaterials of varying shapes and sizes. The respective solutions of 500 and 500 nM for pure HSA protein and pure NP (of varying shapes and sizes) respectively, were included as part of the model and subject to the same conditions. Thereafter samples were taken for respective characterization and measurements.

6.2 Results and discussion

6.2.1 Characterization

The sample remained tubular in shape with reasonably uniform size distribution (8−12 nm in diameter). Sintering at 400 °C led to the formation of bigger bundles (70−100 nm in diameter) and breaking of some tubes to form non one-dimensional materials. Individual tubes showed an average diameter of 14 nm suggesting particle growth. Elevating the temperature to 700 °C resulted in the formation of short rods with average diameter of 27 nm, length of 196 nm and spheres with average diameter of 61 nm in almost equal proportions. Further increase in treatment temperature to 900 °C resulted in the formation of large polygonal rods with diameter range of 78−150 nm and average length of 550 nm.

Figure 6-1 shows the scanning electron microscopy results of the pure TiO_2 materials next to the corresponding mixtures with HSA. The pure TiO_2 sample labelled T200 showed one-dimensional structures of TiO_2 interspaced by undulating lumps of nanostructures which have agglomerated to each other. This agglomeration is enhanced when these structures are mixed with HSA as seen in the image labelled T200+HSA. In the latter image one observed a smoother morphology which is an indication of the nanostructures being covered by HSA. The HSA envelope is so thick that it is not possible to resolve the TiO_2 nanostructures in T200+HSA image.

Similar enhancement of agglomeration phenomena by HSA are observed in T400 and the corresponding T400+HSA images. In this pair of figures, the enveloping HSA is so thin that one is able to see some of the TiO_2 nanostructures wrapped underneath it. In the proceeding images (T700, T700+HSA, T900 and T900+HSA) the HSA film continues to be thinner and thinner, while enveloped nanostructures are almost all visible. The observed agglomeration is probably driven by the van der Waal's forces between nanostructure and protein.

In order to better understand how this agglomeration happens, it is interesting to evaluate the TEM morphology of the same samples before and after mixing with HSA. Figure 6-2 show TEM images of pure TiO_2 nanostructures on the left and TiO_2 mixed with HSA on the right. For instance, if we look at T200 and T200+HSA paired images, (TiO_2

nanostructured annealed at 200 °C), one can clearly observe that the pure TiO_2 nanostructures have a nanotube profile. The nanotubes are well dispersed with very limited agglomerations amongst them. However, when TiO_2 nanotubes are composited in HSA, one sees larger agglomerates and lumps scattered throughout the TEM grid as shown in the T200+HSA image. As observed in SEM images above, the TEM also reveals that HSA tends to envelop the nanotubes. The dark regions in the lump confirms that the HSA film is so thick that the nanotube cannot be seen in this dark area even with the revealing transmission electron imaging.

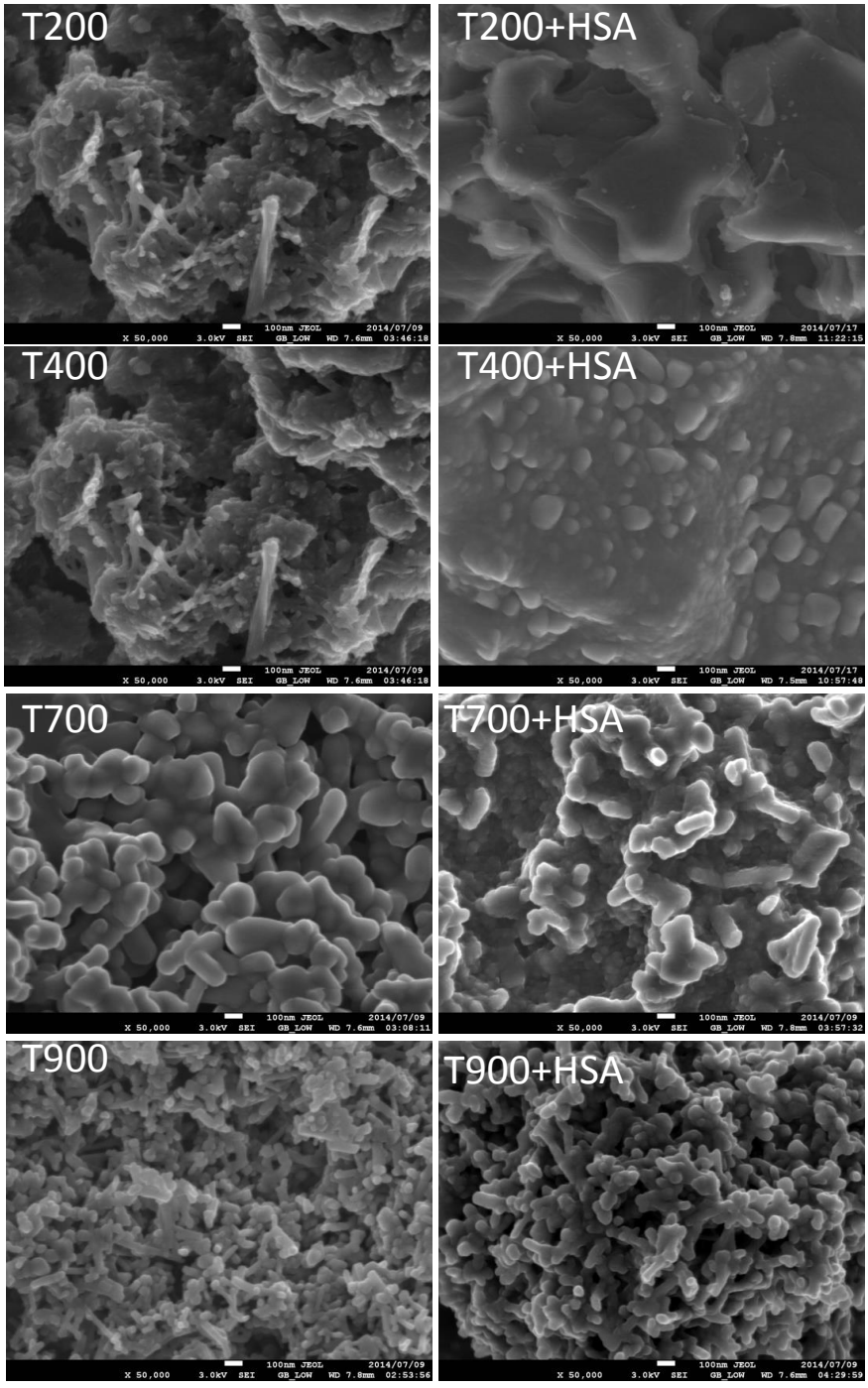

Figure 6-1: Scanning electron microscope images of pure TiO_2 nanomaterials (left) and their corresponding mixtures with human serum albumin (right). All scale bars are 100 nm.

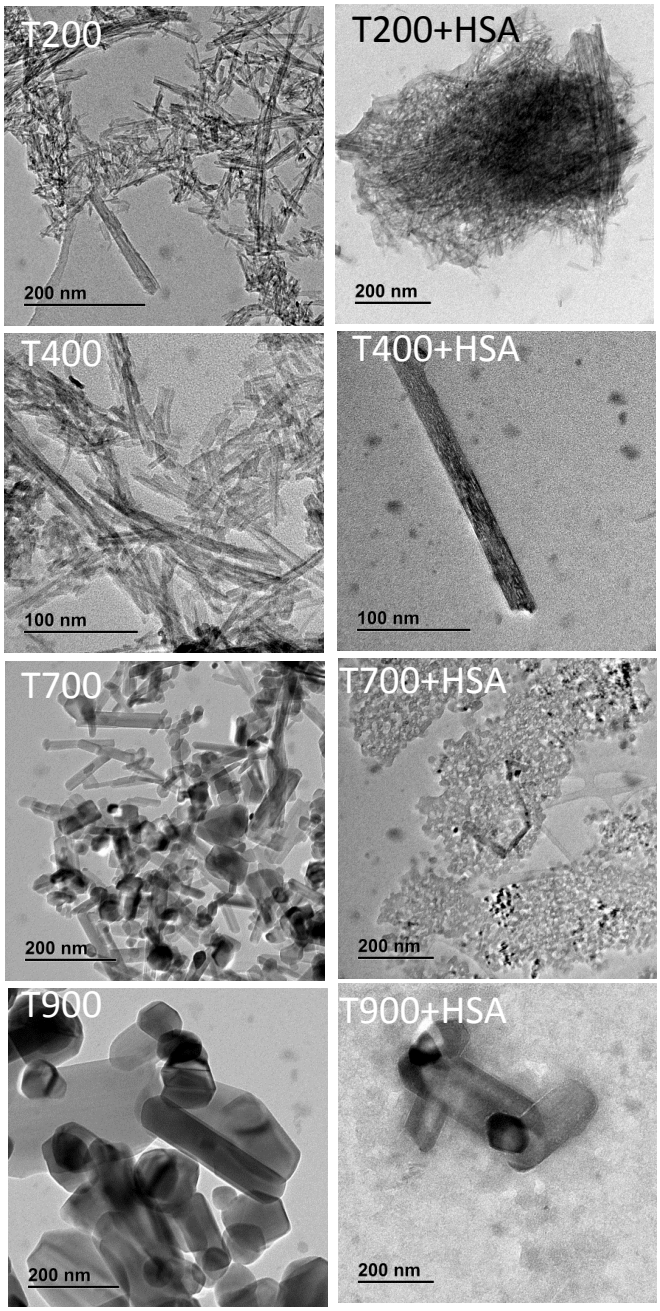

Figure 6-2: Transmission electron microscopy images of TiO_2 samples calcined at different temperatures (left) and the corresponding samples after mixing with a constant concentration of HSA showing the uniqueness of nanowire T400 sample which show little to no agglomeration with HSA.

The T400 sample is pure TiO_2 nanostructures annealed at 400 °C. In the T400 TEM image, the TiO_2 nanostructures change from being nanotubes to nanowires with very few nanotubes inter-spaced among them. Nanowires show very few agglomerations even under HSA at the chosen concentration. However, it will be seen later, that nanowires shows the lowest critical agglomeration dosage, meaning they have unique agglomeration characteristics with HSA. In the T700 and T900 samples, that the TiO_2 nanostructures become nanorods mixed with pyramid-like nanostructures. The average particle sizes increase from T700 to T900. When mixed with HSA, the T700 and T900 show variable agglomeration characteristics

6.2.2 Photoluminescence

From the absorption and emission characteristics of HSA, one observes that HSA absorbs photons peaking at a wavelength of about 280 nm (4.4 eV). Its emission, however peaks at around 355 nm (3.5 eV) in line with the Stoke's law of fluorescence which expects more energy input than the emitted output energy. It must be noted that there is a shoulder peak at 330 nm (3.8 eV) which corresponds to a secondary emission site in HSA Figure 6-3A. The proposed energy diagram of the absorption and emission process of the HSA is schematically illustrated in Figure 6-3B. The main peak at 355 nm suggests that there exists electron's band to band transition with a band gap of nearly 3.5 eV. These main and shoulder peaks may point to the energies of the two binding sites for any foreign molecules into the HSA molecule. In order to study the extent of interaction between TiO_2 nanostructures of varying shapes and the HSA, photoluminescence spectra were obtained for HSA of varying TiO_2 loadings. The spectra shown in Figure 6-4, illustrates that there was a reduction of the HSA emission peaks as the TiO_2 nanostructure concentration in HSA increases. At low concentrations of TiO_2, the decrement of the HSA emission intensity points to the encapsulation of TiO_2 in HSA rather than vice versa. Otherwise it would be the emission peaks of TiO_2 being quenched by HSA. The fact that the HSA emission peaks decrease leads one to conclude that there is energy transfer from HSA to TiO_2. Furthermore, the emission of the encapsulated TiO_2 is not evident in TiO_2

nanosheets and nanotubes as can be seen in Figure 6-4A and B, but becomes visible only at high TiO_2 concentrations for nanowires and nanorods Figure 6-4C and D.

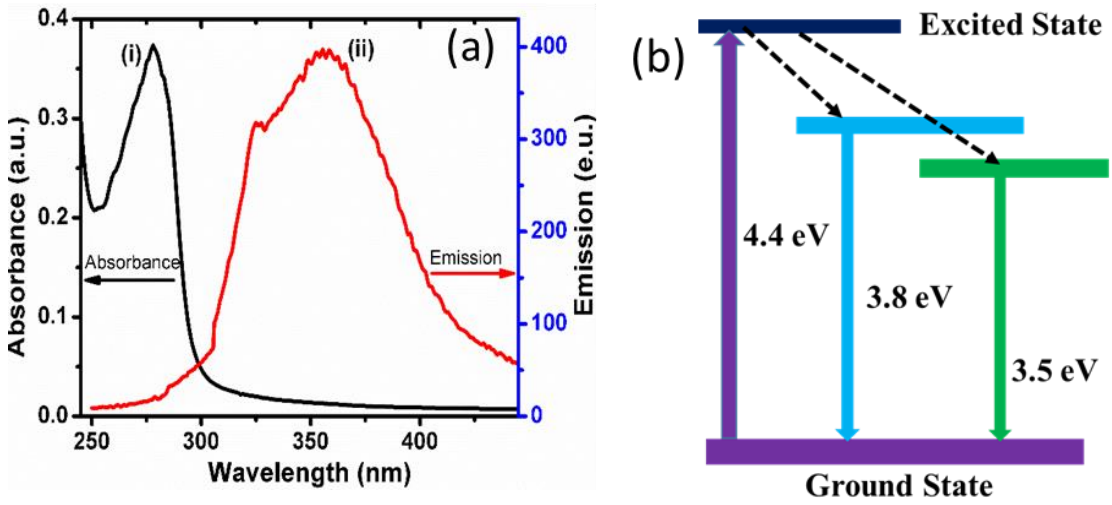

Figure 6-3: (A) Fluorescent spectra of HSA illustrating (i) the absorption and (ii) emission maxima and (B) the proposed energy diagram illustration the absorption for excitation to emission characteristic transitions

The TiO_2 emission peaks appear at much longer wavelengths or lower energies – mostly 415 nm (2.99 eV), 440 nm (2.82 eV) and 455 nm (2.73 eV) - than those displayed by HSA [355 nm (3.5 eV) and 330 nm (3.8 eV)]. Again this type absorption-emission protocol is in line with the Stoke's law of luminescence. The proposed energy diagram is given in Figure 6-4E. It is surprising that when TiO_2 nanostructures are encapsulated, their band-to-band transition peak at 2.99 eV (which is close to the band energy gap for bulk TiO_2 of 3.2 eV) is weaker in intensity than the defect levels presented here. The TiO_2 emission peak at 2.73 eV is stronger than the rest of the emission peaks instead.

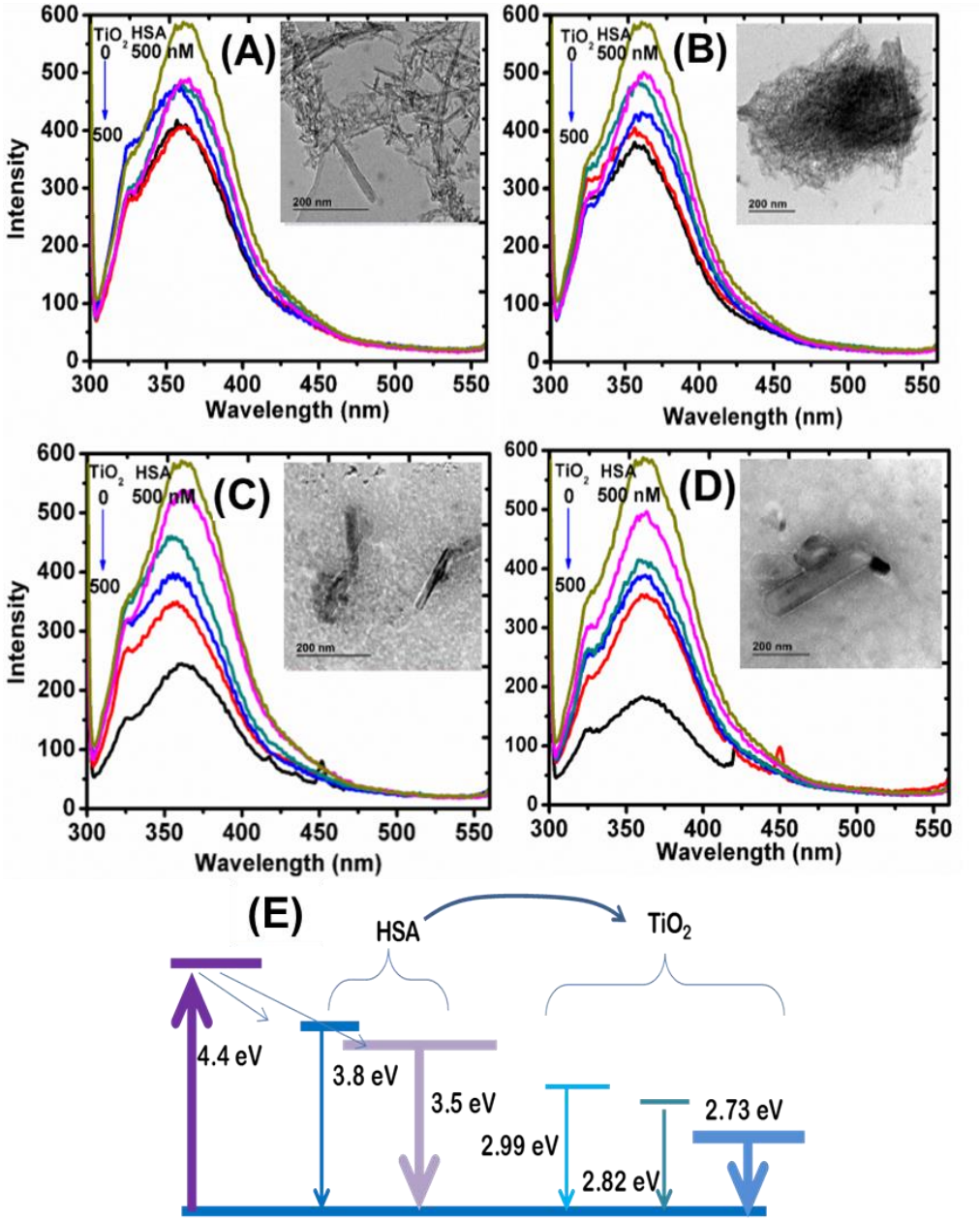

Figure 6-4: Emission spectra of HSA in presence of TiO_2 nanostructures of varying shapes (A) nanosheets (B) nanotubes (C) nanowires and (D) nanorods. The quenching of the emission peak for HSA as the concentration of TiO_2 increases shows that HSA transfers energy to TiO_2 whose emission is not evident in nanosheets and nanotubes but only shows up at high concentrations of TiO_2 in the shapes of nanowires and nanorods. The proposed energy diagram during the absorption-emission and energy-transfer processes is given in (E).

The binding interaction and the efficiency of energy transfer between colloidal TiO_2 and HSA was evaluated by the fluorescence method. The decrease in fluorescence emission spectra has been attributed to the energy transfer between HSA and the TiO_2 nanostructures of various shapes (Kathiravan and Renganathan 2008). This change was observed in all the TiO_2 materials used, however the trend is not exactly the same confirming that it is a surface dependent process. There are a few distinct mechanisms either with absorption or emission of photons by which energy can be transferred between a donor and an acceptor. Herein the quenching of the protein fluorescence has been analyzed by a mechanism of static quenching using the Stern−Volmer equation:

$$\frac{F_0}{F} = 1 + k_q \tau_0 [TiO_2] = 1 + K_{sv}[Q] \tag{8.1a}$$

$$\log\left(\frac{F_0 - F}{F}\right) = \log K_{sv} + n \log[Q] \tag{8.1b}$$

The k_q is the bimolecular quenching constant, which is a measurement of the efficiency of quenching, and [Q] is the quencher (TiO_2) concentration. Using the Stern−Volmer plot, F_0/F versus [TiO_2], one obtains a serious of plots which are summarized in Figure 6-5. It is worth mentioning that, while linear trends are expected, Figure 6-5A and B [pertaining to TiO_2 nanosheets and nanotubes wrapped in HSA respectively] are less linear than (C) and (D) [pertaining to TiO_2 nanowires and nanorods wrapped in HSA respectively]. This suggests that the energy transfer process from HSA to TiO_2 is more enhanced in TiO_2 shapes of nanowires and nanorods than in nanosheet and nanotubes.

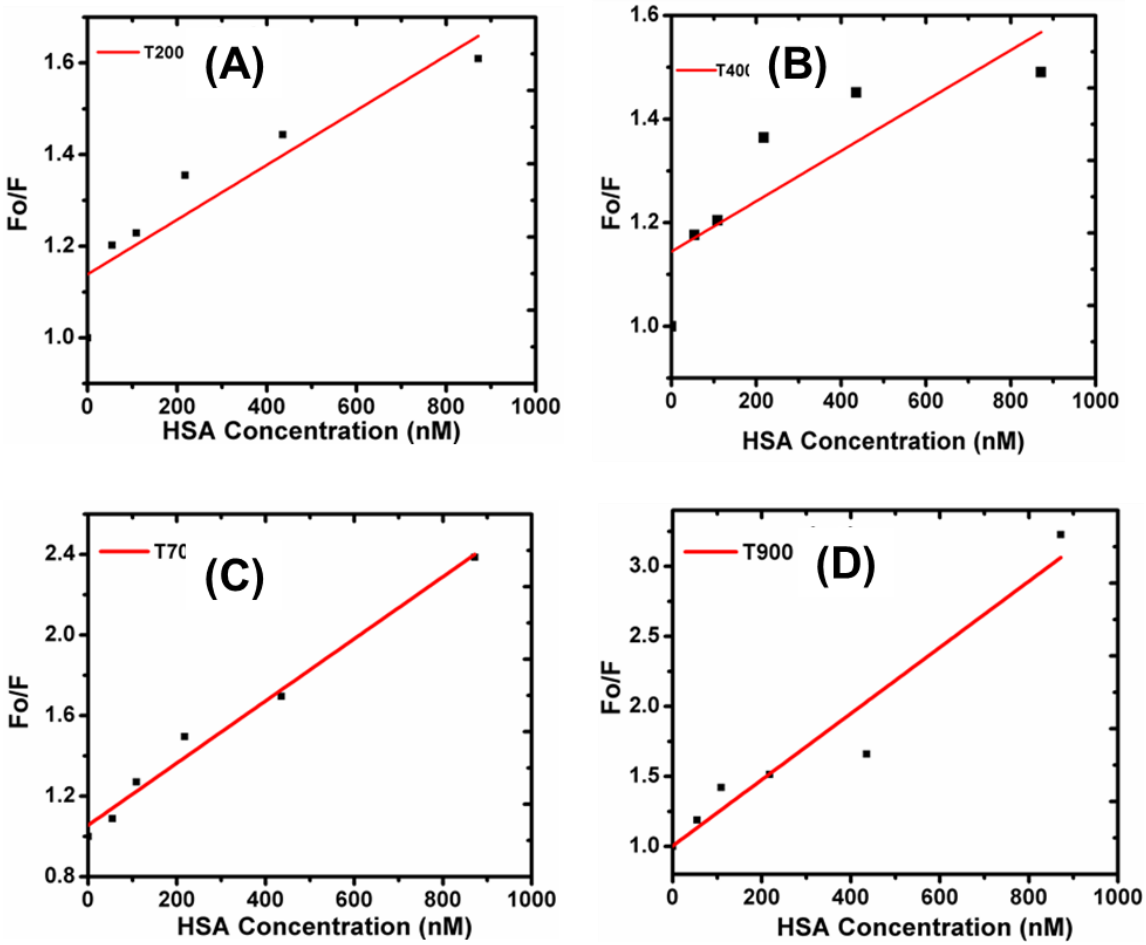

Figure 6-5: Photolumenescence quenching plots of trp (HSA) by (A) T200+HSA, (B) T400+HSA, (C) T700+HSA and (D) T900+HSA.

When the straight line equations in Equation 8.1 are fitted to the F/F_0 versus $[TiO_2]$ plots, slopes and intercepts are obtained which in turn aid in the calculation of the parameters: K_{sv} (which yield k_q and τ_0) and n, summarized in Table 6-1. Using the reported values for $\tau_0 = 5 \times 10^{-9}$ s, the respective values of K_{sv} for different HSA+TiO_2 material shapes were calculated to be 6.33×10^5, 5.10×10^5, 1.70×10^6, and 2.40×10^6 for T200+HSA, T400 +HSA, T700+HSA and T900+HSA bio-conjugate respectively, as shown in Table 6-1. The binding constant, K and the number of binding sites n, were determined from the

linear plots of Log ((Fo-F)/F) against Log[Q] where n is the slope and K is from the intercept.

Table 6-1 Stern-Volmer parameter from the analysis of photoluminescence quenching

TiO_2-HSA	**TiO_2 shape**	**Ksv/M^{-1}**	**T_0/s**	**k_q/ $M^{-1}s^{-1}$**	**n**	**K/M^{-1}**
T200+HSA	Nanosheets /Nanotubes	$6.33x10^5$	$5.00x10^{-9}$	$1.27x10^{14}$	0.41	197.7425
T400+HSA	Nanotubes /Nanowires	$5.10\ x10^5$	$5.00x10^{-9}$	$1.01x10^{14}$	0.47	171.20
T700+HSA	Nanowires /Nanorods	$1.70\ x10^6$	$5.00x10^{-9}$	$3.40x10^{14}$	0.93	679203.6
T900+HSA	Nanorods /bipyramids	$2.40\ x10^6$	$5.00x10^{-9}$	$4.80x10^{14}$	0.78	402.72

The significant drop in the PL intensity of TiO_2 spectra confirms the possible energy transfer from the Trp residue of serum albumin to TiO_2 material (Kathiravan and Renganathan 2008). From our previous study, specifically on the material properties, it was confirmed that the materials studied have wider energy band gap dependent on shape and size (Sikhwivhilu *et al.* 2012). Therefore, the excited state energy of serum albumin can be transferred to ground state of TiO_2 to yield stable bio-conjugate. Likewise, the electron in the HOMO can be easily excited to react with a biomolecule species at the Fermi level of TiO_2 (Liu, Wen and Zhao 2007; Kathiravan and Renganathan 2008; Ahmed *et al.* 2011). The PL signals are helpful in the determination of the recombination of photo induced electrons and gaps in TiO_2 as the PL intensity of HSA is reduced by energy transfer to TiO_2 (Liu, Wen and Zhao 2007).

6.2.3 ATR-IR spectroscopy and Raman spectroscopy

The typical FTIR and Raman spectroscopy results are presented in Figure 6-6. In Figure 6-6A are shown infrared spectra for pure T900 (rods/icosahedra) TiO_2 sample, pure

HSA and the HSA+T900 composite. HSA is much more infrared-active when compared to T900 in the range between 1400 cm^{-1} and 1800 cm^{-1} as one observes more intense peaks for HSA than T900. T900 only shows small peaks between 1650 cm^{-1} and 1700 cm^{-1}. The two amide bands –at 1550 cm^{-1} and 1650 cm^{-1} from HSA retained their resolution in the presence of nanomaterials, HSA loses a phonon at 1450 cm^{-1} when impregnated by T900 (TiO_2 nanorods/icosahedra) particles.

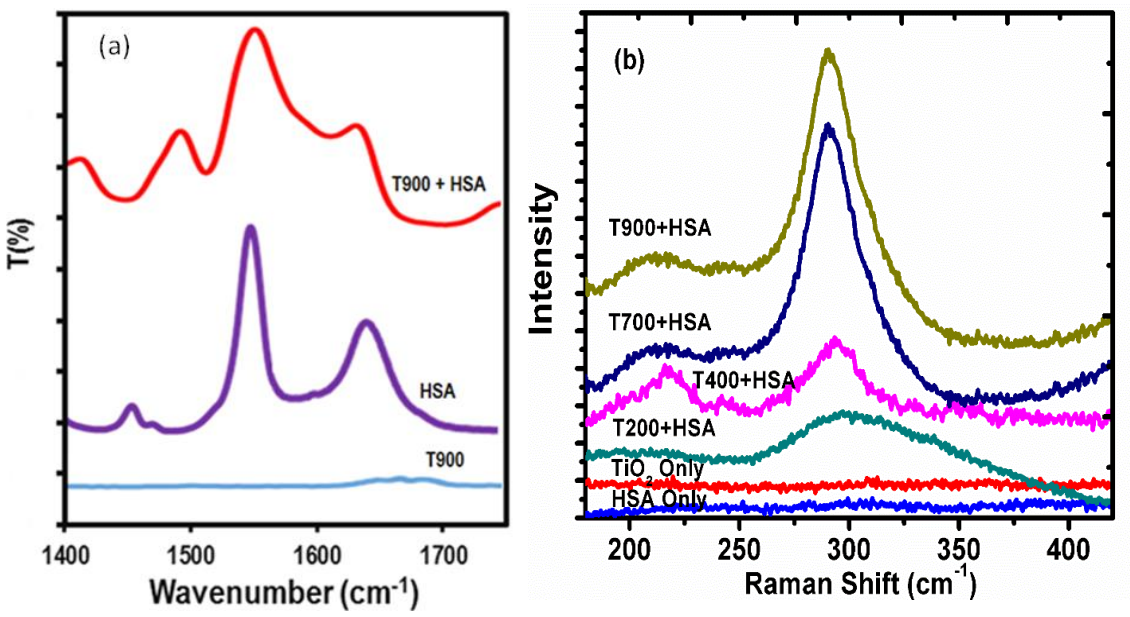

Figure 6-6: (A) ATR-IR spectra of pure, T900, pure HSA, and bioconjugates (TiO_2 + HSA) (B) Raman spectra of pure HSA, and bioconjugates (TiO_2 + HSA)

A new phonon arises at 1500 cm^{-1} which is exactly five times in vibrational frequency when compared to the Raman active band at 300 cm^{-1} in the forthcoming section of this chapter. This is possible the 5^{th} overtone of the Ti-amine or Ti-amide bond vibrations. There is a second new vibrational mode at 1400 cm^{-1} when HSA is wrapped around T900. This then is the second site where Ti binds itself in HSA. There was also a slight shift in the 1650 cm^{-1} phonon when the HSA is composited with TiO_2 which signifies structural delocalization of the HSA due to incorporation of TiO_2 rods and icosahedra. The

appearance of a shift of the amide I band at 1650 ± 5 cm^{-1} is attributed to the secondary structure of the adsorbed serum albumin looping which is also in agreement with the aggregation depicted by the DLS results in the forthcoming sections (Bouhekka and Bürgi 2012). In addition, the amine groups from protein amino acids appeared to bind possibly through a donor−acceptor bond at the Fermi level of material.

The Raman-active vibrational modes of the pure HSA, pure TiO_2 and various combinations of the two with varying shapes of nano-TiO_2 are given in Figure 6-6B. The analysis from Raman spectroscopy about the behaviour of protein in the presence of TiO_2 nanostructures is valuable for understanding the conformational changes in the various denaturation conditions. Specifically, in this work any denaturation is deemed to arise from the interaction with TiO_2 nanomaterials. We observed a significant increase in the Raman intensity band at ~300 cm^{-1} demonstrating the conformational disorder as the bio-corona is formed. Note that this 300 cm^{-1} phonon experiences consistent red-shifts as the TiO_2 shapes change from nano-sheets through to tubes, wires, and rods to icosahedra. This red-shifting could be due to heavier reduced mass of the TiO_2 shapes as the density increases from tubular to rod-like TiO_2 structures. This 300 cm^{-1} phonon is also about 5-times smaller than the new IR-active phonon in Figure 6-6A. As mentioned earlier, this 300 cm^{-1} Raman-active phonon could be the fundamental vibrational Ti-HSA mode whereas the 1500 cm^{-1} IR-active phonon could be the 5^{th} overtone of the same Ti-HSA vibrational mode. The adsorption of serum albumin on the metal oxide nanorods improved with the thermal modification of the surface meaning the surface energy transfer could increase (Silva-Bermudez, Rodil and Muhl 2011).

There also exist in the Raman spectra a second vibrational mode centered at around 200 cm^{-1}. This phonon suffers red-shifts as well as blue-shifts. The combination of red and blue shifts may signify the variation of both reduced mass of the TiO_2 shapes with the HSA as well as the binding spring constant on this binding site.

6.2.4 HSA agglomerate size distribution dependent on dosages of TiO_2

In order to determine the agglomerate sizes in TiO_2 composites with HSA with carrying concentration of each shape of TiO_2 nanostructures, the DLS which employs the Mie scattering theory to determine the particle size. The results of the agglomerate sizes are shown in Table 2 and the plot of agglomerate size against the concentration of the TiO_2 nanostructures is given in Figure 6-7.

One notes the profile of the data in Figure 6-7A shows that of the traditional s-curve or the sigmoid except for curve for TiO_2 nanowires/nanorods wrapped in HSA. There are several equations which can fit the s-curve which includes the Hill equation, the Dose-Response equation, the Weibull equation, and many others. Herein we have chosen to fit the TiO_2-dose-to-TiO_2+HSA- agglomerate data to the dose-response equation 8.2 given by:

$$S_{TiO2+HSA}(D) = S_0 + \frac{\left(S^{\max}_{TiO2+HSA} - S^{\min}_{TiO2+HSA}\right)}{1+10^{(\log D_0 - D)p}} \tag{8.2}$$

where $S_{TiO2+HSA}(D)$ is the size of the agglomerate of TiO_2+HSA dependent on the dose, D, of the TiO_2 nanostructures, S_0 is the size of HSA before addition of TiO_2 nanostructures, D_0 is the critical dose of the TiO_2 nanoparticles, $S_{TiO2+HSA}$ (max) or simply S_{max} is the maximum size that the composite can reach at high doses of TiO_2, $S_{TiO2+HSA}$(min) or simply S_{min} is the same as S_0 so that S_{max}-S_{min} or S_{max}-S_0 becomes the magnitude of the wrapping diameter of the TiO_2 in HSA and p is the Hill factor which describes.

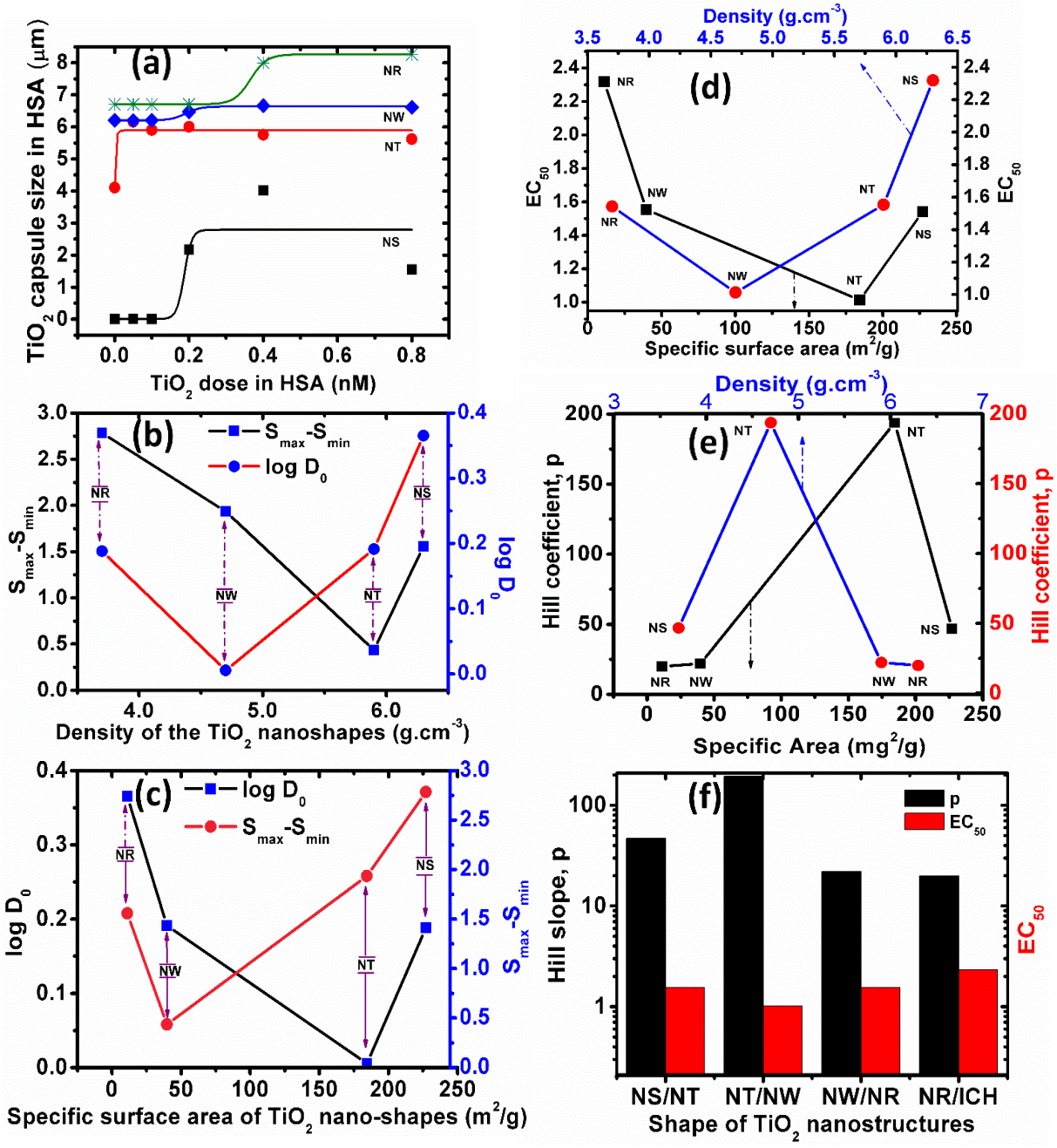

Figure 6-7: (a) Agglomeration induced by HSA on different morphologies of TiO_2 nanoparticles (NPs) as a function of the dosage; the S-shaped curve fitted on each data set is the dose-response equation whose correlation coefficients, R, are indicated next to each curve.

Table 6-2: Size distribution (in µm) of the TiO_2-HSA as the concentration of TiO_2 with different shapes is increased from 0.00 to 800 nM.

Type	**Agglomerate sizes of TiO_2@HSA for concentration of TiO_2 nanostructures/nM**						
	Conc. or Dose (nM)	0.000	0.0500	0.100	0.200	0.400	0.800
	Predominant TiO_2 shape						
T200+HSA	Nanosheets	0.0050	0.0080	0.0067	2.1751	4.0241	1.5571
T400+HSA	Nanotubes	0.0050	2.0584	1.8062	1.9059	1.6540	1.5197
T700+HSA	Nanowires	0.0032	0.0042	0.0079	0.2677	0.4645	0.4126
T900+HSA	Nanorods	0.0050	0.0048	0.0052	0.0058	1.2981	1.5629

Table 6-3 : summarizes the parameter from the fitting of Equation 2 to the data plotted in **Figure 6-7.**

	Specific area (m^2/g)	**Density (p/cm^3)**	**S_{min}**	**S_{max}**	**delS**	**logD_0**	**Hill coefficient, p**	**EC_{50}**
[TiO_2] in HSA								
S(T200 NSs + HSA)	227.1±11.3	3.7±0.05	0.0065±0.87	2.79±0.87	2.7841	0.19±7.88	46.70±31404.3	1.54
S(T400 NTs + HSA)	184.4±10.1	4.7±0.07	-0.14607	1.79±0.15	1.9349	0.00554	193.67	1.01
S(T700 NWs + HSA)	39.7±8.2	5.9±0.09	(3570±1.9)E-6	(438550±1.8)E-6	0.4350	0.19±0.0016	21.98±34.9	1.55
S(T900 NRs + HSA)	11.1±0.5	6.3±0.09	0.005	1.5629	1.5579	0.36±0.0011	19.87±0.61	2.32

NR: Nanorod, NS: Nanosheet, NT: Nanotube, NW: Nanowire

After fitting the dose –response equation to the data, calculations were performed on half maximal effective concentration (EC_{50}) which refers to the concentration of a drug, antibody or toxicant (in this case TiO_2 nanostructures) that induces a response halfway between the baseline, S_{min} and S_{max}, after a specified exposure time. It is commonly used as a measure of drug's potency.

The parameters (1) Hill coefficient, *p*, (2) EC_{50} and (3) $\Delta S = S_{max}\text{-}S_{min}$ and (4) log D_0 scale variously as the density and specific surface area of the toxicant, TiO_2. The density of the TiO_2 nanostructures as well as their specific surface area before mixing them with HSA were pre-determined by picnometry and BET respectively and these procedures have already been reported (Sikhwivhilu et al, 2012). The plots of log D_0 and ΔS versus specific area are given in Figure 6-7B and that of log D_0 and ΔS versus density are given in Figure 6-7C. One observes that log D_0 is generally inversely related to density of the TiO_2 nanostructures thus the lowest critical dose at which 50% of the maximum change in agglomeration Δ*S* takes is observed in nanotubes. Nanowires display the lowest agglomeration with HSA. This observation is corroborated by TEM observations in the previous section where nanowires were observed to segregate from HSA and appear isolated or agglomerated only to other nanowires. On the other hand, nanorods display the largest log D_0 whereas nanosheets present the largest agglomerates in HSA. The largest dose of TiO_2 for nanorods means there are not as toxic as nanowires.

Furthermore, in the case of the plot of EC_{50} versus specific surface area and versus density of the toxicant, one observes the lowest EC_{50} for nanowires followed by that of nanotubes. Nanorods and nanosheets show high values of EC_{50} as before. Since EC_{50}, by definition, is the dose responsible for 50% response or effect, this means that nanotubes and nanowires are more toxic than nanorods and nanosheets. In fact, nanotubes are at the top of the list and nanorods at the bottom. This is clearly demonstrated and supported by the Hill coefficient, p, graphs versus density and specific surface area in Figure 6-7E where nanotubes present the largest Hill coefficient value and nanorods present the lowest with nanowires and nanosheets appearing in between these extremes.

6.2.5 *In silico* interaction studies

In the primary steps of the docking studies the active pocket in HSA (PDB ID 1A06) was predicted using the cavity finding module of DS, based on the information present in the PDB database. The structure of HSA was prepared for docking using the "Prepare protein" module. This module cleans the protein and adds polar hydrogen into the suitable coordinate positions of the proteins using the CHARMM force field parameters. Thereafter, the nanostructure ligands were prepared and optimized using the "prepare ligand" module of DS. Specifically, the 4 nano-shapes of TiO_2 viz., nanorods, nanowires, nanosheets and nanotubes were docked in the active pocket of HSA and presented in Figures 8-11.

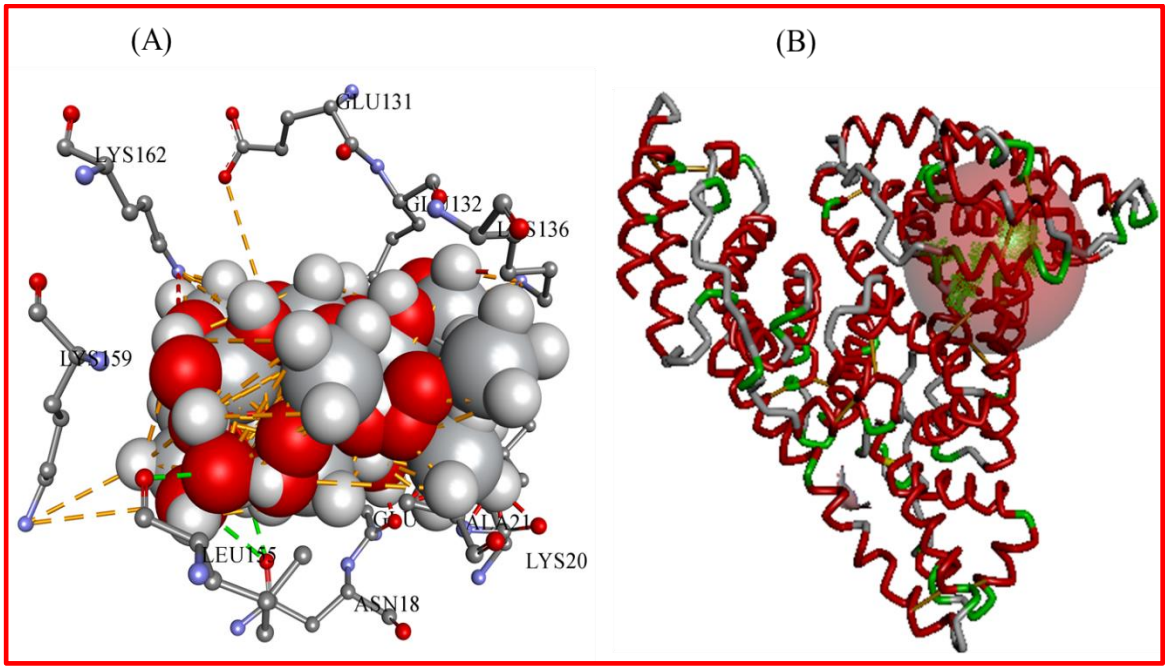

Figure 6-8: nanorod docked in the active pocket of HSA, (B) Binding site/s on HSA where docking took place.

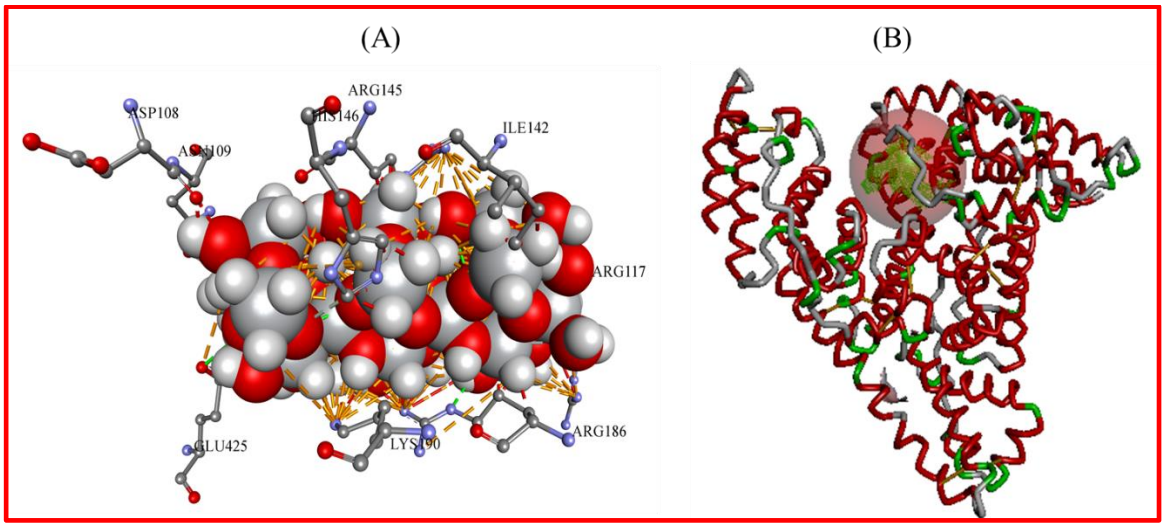

Figure 6-9: nanowire docked in the active pocket of HSA, (B) Binding site/s on HSA where docking took place.

The nanorods and nanowire showed comparable binding affinity values of -1.52 and -1.43 Kcal mol^{-1} respectively. Consequently, both these structures were oriented similarly in the active pockets of HSA (Figure 6-8 and Figure 6-9). Furthermore, the nanowire showed relatively greater binding energy of – 2.33 Kcal mol^{-1}, with a higher number of the interacting residues observed in the docked conformation of the nanowire. On the other hand, the nanotube showed highest binding energy of -2.85 Kcal mol^{-1}, with highest number of residues present in the interacting pose with the HSA Figure 6-11. These observations demonstrated that the nanotubes showed highest toxicity which can be accessed through the modes of their binding in the active sites of HSA.

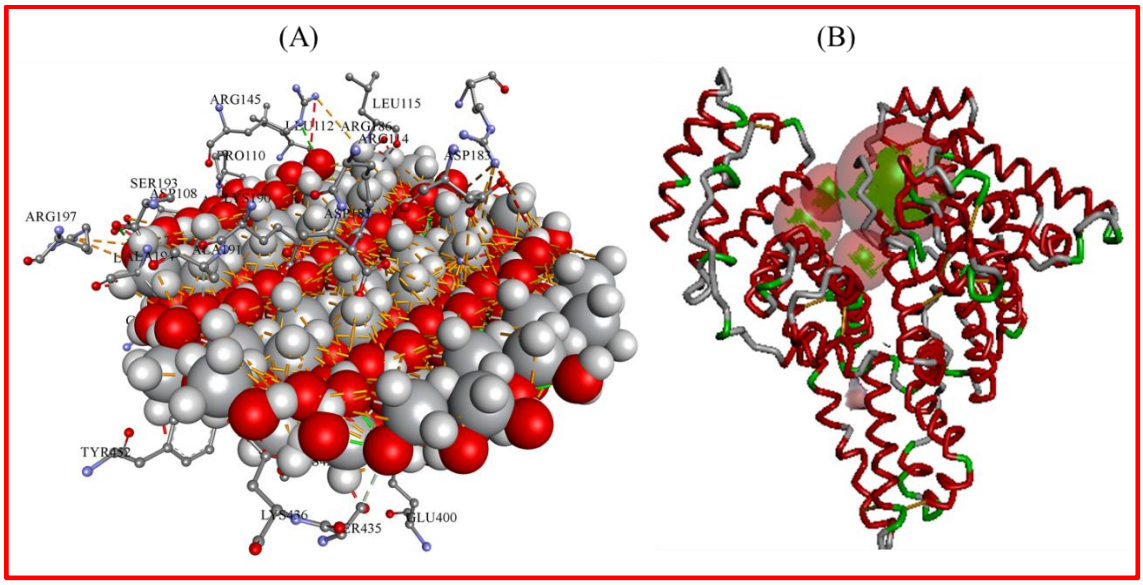

Figure 6-10: nanosheet docked in the active pocket of HSA, (B) Binding site/s on HSA where docking took place.

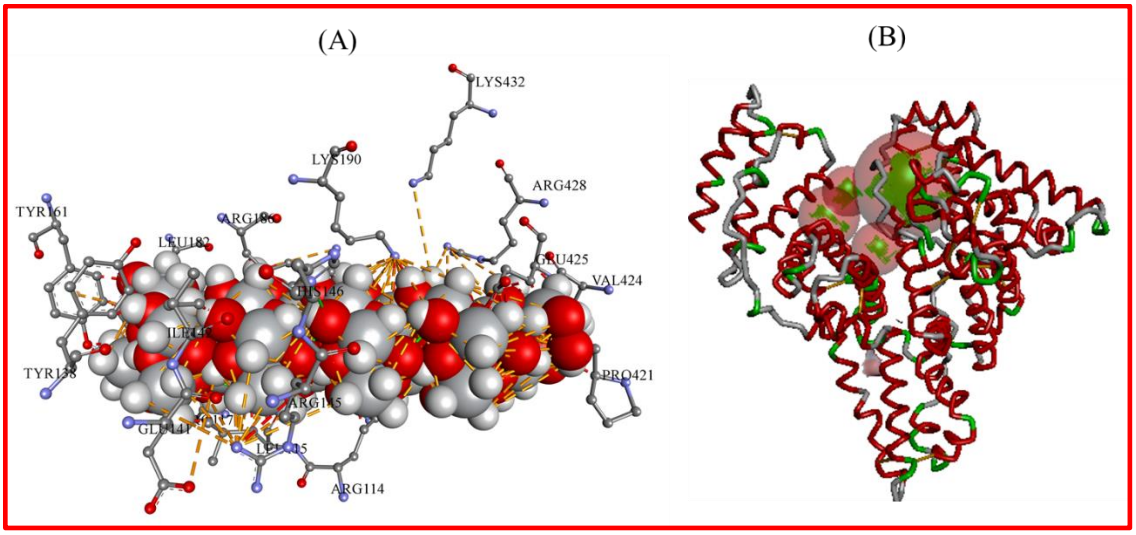

Figure 6-11: (A) nanotubes docked in the active pocket of HSA, (B) Binding site/s on HSA where docking took place.

6.3 Conclusions

The HSA has been allowed to interact with various nanoshapes of TiO_2 which includes: nanosheets, nanotubes, nanowires, and nanorods. Various concentrations of 0.2, 0.4, 0.6, 0.8 and 1 nM were employed in these pharmacokinetics studies. The characterization methods of TEM, SEM, PL, FTIR and Raman spectroscopy confirm that the HSA encapsulates the TiO_2 nanostructures with size of the encapsulation varying in a Sigmoid-type of curves with the dosage of TiO_2 nanostructures. The levels of encapsulation, S_{max}-S_{min}, the critical doses, log D_0 and the dose that leads to 50% effect, EC_{50}, and the Hill coefficient, p, are obtained from the fitting of the dose-response equation. The lowest Hill coefficient for nanotubes and the nanotubes display the highest p value suggesting that nanotubes are the most favorable shapes of the TiO_2 materials followed by nanowires. The degree of encapsulation is the lowest in these structures and they are seen leached outside of the HSA's encasement in TEM and confirmed by optical methods mentioned. Overall it was demonstrated that HSA has the propensity to encapsulate TiO_2 nanomaterials largely with varying critical doses dependent on the shape of the structures.

CHAPTER 7

7 Case Study 3: Biosynthesis of AgNPs and cytotoxicity studies

This chapter reports on the green synthesized and characterization of AgNPs followed by evaluation for antioxidant activity on ABTS and inhibitory effect on human embryonic kidney cells in a concentration dependent manner.

7.1 Methodology

7.1.1 Characterization of silver nanoparticles

The bio-reduction of Ag^+ ions in aqueous extract was monitored by UV–visible spectra while the corresponding morphology and size of the polymer and bio-stabilised AgNPs were measured using TEM. The hydrodynamic particle size of nanoparticle was determined using Zetasizer under conditions: temperature 25.0 °C, data collected at a count rate of 261.5 kcps for a duration of 60 s in 7 attenuations, while the measurement position was kept at 4.65 mm. The ATR spectra of nanoparticle powder were recorded at 4000 cm^{-1} to 400 cm^{-1}. X-ray diffraction study was carried out using a Bruker AXS D8 diffractometer with CuKα radiation (λ = 1.5418 Å) at 40 kV over a 2θ range from 20º to 80º at a scanning rate of 0.05 min^{-1}. Further confirmation of the conjugation was performed with Thermogravimetric Analyzer where samples were placed in a 10 μL alumina sample holder and then heated at a rate of 10 °C min^{-1}.

7.1.2 Cytotoxicity studies with MTT assay

Exponentially growing human embryonic kidney cells (HEK293T) were seeded in a 96-well micro-titer plate (cell count of 7000 cells per well). For checking cell proliferation, on the next day cells were treated with different concentrations (5–150 lM) of inhibitors. HEK293T without inhibitors was used as a positive control. At the end of 48 h incubation, the mixture was removed from the cells and after washing with PBS, 100 lL

fresh Dulbecco's modified Eagle's medium and 20 µL MTT (from 5 mg mL^{-1} stock) was added to each well. The plates were incubated further for 4 to 5 h at 37 ^{o}C. After the incubation period elapsed, the bulk of the residual medium was carefully removed, using a multichannel pipette, without disturbing the formazan crystals formed behind. Thereafter, 100 µL of DMSO (dimethyl sulphoxide) was added to each well for dissolving the formazan crystals. The plates were then agitated for 15–20 min on an orbital plate shaker, after which they were read immediately on the Titerplate reader (BioRad) at 570 nm. The relative percentage cell viabilities of the treated cells were calculated with reference to the control by comparing the viability.

7.1.3 Antioxidant Activity by ABTS

The radical scavenging activity of the biosynthesised nanoparticles was measured against stable free radicals of ABTS. Approximately 2.0 mM solution of ABTS was prepared in 0.75 mM, potassium persulfate, and allowed to stand for approximately 16 h in a dark environment. Thereafter, a series of colloidal nanoparticle solutions were separately mixed with 30 µl of 1.8 µM ABTS enzyme and then vortex mixed for 5 s followed by 30 min incubation at 25 °C to allow for the scavenging reaction to reach equilibrium before absorbance measurements were recorded at 734 nm.

7.1.4 Screening of phytochemical in *Iboza* riparia and *Ilex Mitis*

The plants used *Iboza* Riparia leaf and *Ilex Mitis* consists predominantly terpinoids and saponins have been used in the synthesis of AgNPs. Essential oils from the extracts are composed of hydrocarbons, terpenes and their oxygenated derivatives, terpenoids. Formation of higher molecular weight terpenes namely; hemiterpene, monoterpene, sesquiterpene, diterpene, and triterpene is through the 'head' to 'tail' linkage of isoprene units. The terpenes may form oxygenated derivatives with different functional groups like alcohol, ester, aldehyde, ether, ketones etc. while terpenoids can be hemiterpnoid, monoterpnoid, sesqiterpenoid, diterpenoid, triterpenoids (Evans, Evans and Trease 2002;

Patil Shriniwas and Kumbhar Subhash 2017). Plant surfactants are widely used in the synthesis of AgNPs as they contribute in the amalgamation of metal ions to NPs (Banerjee and Das 2013). Plant extracts contain surfactants, which enable the nanoparticle formation without any special reducing agent/capping agent. The role of surfactants is to act as capping agent preventing the growth and aggregation of nanoparticles.

7.2 Results and discussion

7.2.1 Morphology and particle size analysis

During the synthesis, color changes from yellow to orange/red/gray, depending on the reducing and capping agents used. The AgNPs prepared from *Iboza* Riparia extract demonstrated more aggregation (with gray color) in contrast to polymer based nanoparticles which were violet in color.

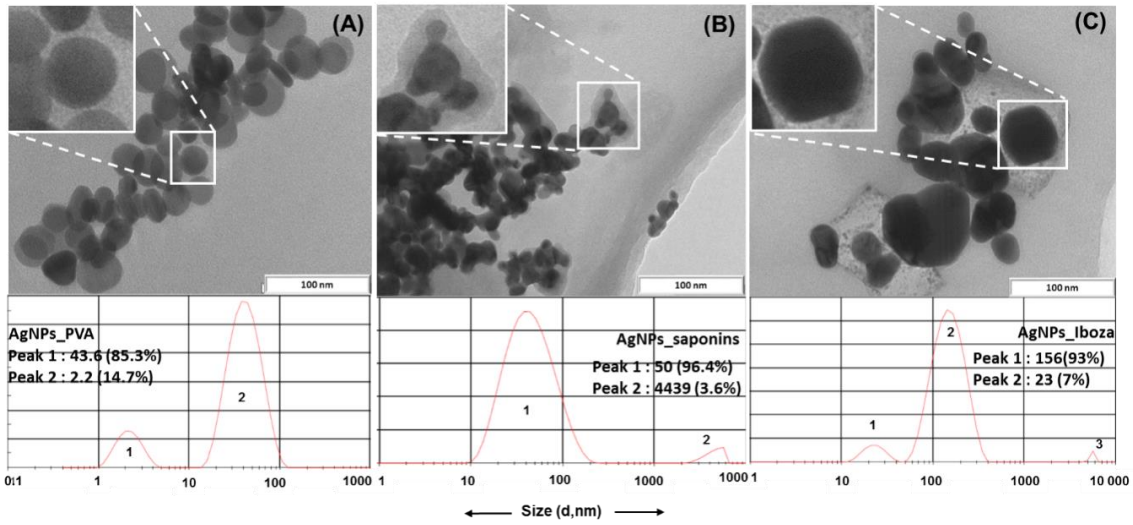

Figure 7-1: size distribution intensity of (A) *AgNPs-PVA*; (B) *AgNPs-SPNs*; (C) *AgNPs-DTPs*. Insert shows the TEM images of the corresponding particles prepared with *Image J*. Below is the hydrodynamic size distribution and intensity. #PVA Poly(vinyl alcohol): , SPN: saponin , DTPs diterpinoids

The TEM and DLS results suggested that the average diameter of AgNPs-PVA was 43.6 nm and conductivity of 0.11 mS while the intensity was 85.3 % as shown in Figure 7-1A. On the other hand, the *Ilex* Mitis and *Iboza* Riparia extracts (Figure 7-1B-C) produced AgNPs-*SPNs* and AgNPs-*DTPs* with an average size of 50 nm and 156 nm, while their respective intensities were 96.4 % and 93 %. In Figure 7-1B, we observed that NPs are generally small, however they are clustered due to the presence of the capping agent in the extract. Interestingly, there was a visible surface coating on the AgNPs-*SPNs* differing to the AgNPs-*DTPs* shown in Figure 7-1C. The AgNPs-DTPs was the largest with 156 nm and conductivity of 0.494 mS, this signifies poor reduction and capping of nanoparticles by diterpenes in contrast to saponins. Saponins produce nanoparticles that are much smaller with a conductivity of 0.39 mS because structurally they have more hydrophilic glycoside moieties combined with a lipophilic triterpene derivative (Hostettmann and Marston 1995). The significant difference in the conductivity results elucidates the electrical potential *difference between* the inner and outer surface of the dispersed phase in colloidal nanoparticles. This enables nanoparticles shown in Figure 7-1B to be much smaller and relatively stable. The capping agents themselves are being known to form the basis for biologically important compounds and having antimicrobial and anti-inflammatory properties. However, adjusting the morphology of nanoparticles is of key importance for utilizing their properties in biomedical applications. For this purpose, we use a capping agent or appropriate surfactant that affect the morphology of nanoparticles at ambient conditions. The surfactants contribute a vital role because of their ability to modify the chemical behavior of nanoparticles as discussed in section 2.1.

7.2.2 UV-Vis and ATR spectroscopy

In all experiments, the addition of plant extract of *Ilex* Mitis, *Iboza* Riparia and polymer into the beakers containing an aqueous solution of silver nitrate led to the change in the color of the solution to yellow to orange/red/gray, depending on the reducing and

capping agents used. The color change within reaction duration was due to excitation of surface plasmon vibrations in AgNPs (Veerasamy *et al.* 2011; Lee *et al.* 2016). The reduction of silver ions during the reaction was confirmed by ultraviolet–visible spectroscopy and showed maxima's at 508.3 nm, 413.2 nm and 405.9 nm for AgNPs-*PVA*, AgNPs-*SPNs* and AgNPs-*DTPs* respectively (see Figure 7-2A). These nanoparticles were allowed to stand for two months to assess their stability, interestingly they were found to be adequately stable as they retained their shape, size, color, and distribution coefficient.

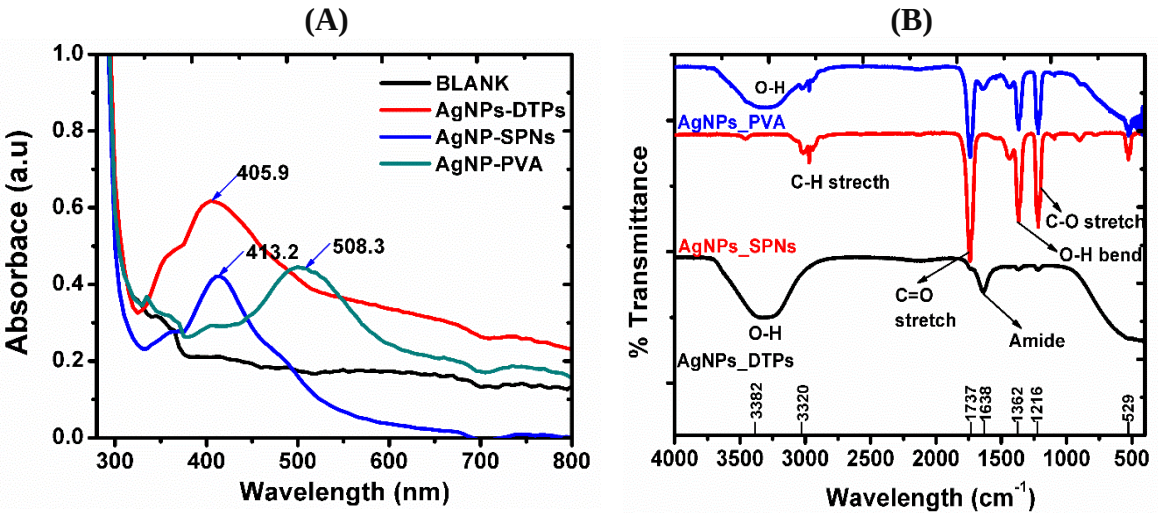

Figure 7-2: (A) UV-Vis spectra from 300 nm to 800 nm; (B) ATR spectra and (C) DSC thermogram of AgNPs-PVA; AgNPs-SPNs; AgNPs-*DTPs*

Further characterization was performed with ATR as illustrated in Figure 7-2B, which showed C-O stretch at 1216 cm^{-1} and O-H bend at 1362 cm^{-1} for all the samples – but it was significantly small for AgNPs-*DTPs*. There was also a very intense C=O peak at 1737 cm^{-1} which probably arise from the citrate used for the preparation of seed solution. Again this peak is much smaller in the case of AgNPs-*DTPs* although there is a dominance of α-pyrone compounds from the extract (Puyvelde *et al.* 1981). While a distinctive C=O stretch, amide band at 1638 cm^{-1} was observed for AgNPs-*DTPs*. It is well established in

the literature that amides can bind exceptionally strongly with AgNPs as confirmed by diminishing of the corresponding peak after the formation of NPs. On the other hand AgNPs-*SPNs* demonstrated the two intense C-O stretch at 1216 cm^{-1} and O-H bend at 1362 cm^{-1}. These intense bends attribute to their structures having more than one hydrophilic glycoside moieties combined with lipophilic triterpene derivatives. Ultimately the abundance of the C-O stretch arises from the connection of the glycoside moieties. Interestingly, these peaks were similar to those observed with AgNPs-*PVA*.

7.2.3 X-ray diffraction and thermal analysis

X-ray diffraction analysis was utilized to calculate the crystallite size of AgNPs. The XRD analysis of NPs synthesized using extracts exhibited typical diffraction peaks at 36.05º (100), 45.94º (200), 65.27º (220) and 76.14º (311) as shown in Figure 7-3A. The four planes of the fcc crystal structure of metallic silver exhibited well-defined characteristic diffraction peaks. The AgNPs formed using PVA also exhibited the same peaks, however the peaks at 65.27º (220) and 76.14º (311) showed much less intensity compared to AgNPs from the extract. The results obtained are in agreement with previous reports where plant extracts have been used for the synthesis of nanoparticles (Lee *et al.* 2016; Judith Vijaya *et al.* 2017). The sizes of the nanoparticle crystals calculated by the Debye-Scherrer equation were 44 nm (AgNPs-*PVA*), 156 nm (AgNPs-*SPNs*), 50 nm (AgNPs-*DTPs*), which are in good agreement with the sizes observed in TEM and DLS analysis. Peak broadening observed can be considered normal since the particles are less than 100 nm and the full-width at half maximum is consistent for each peak. However, there was a varying peak intensity for all the synthesized nanoparticles which is related to different sample quantities that were used for characterization.

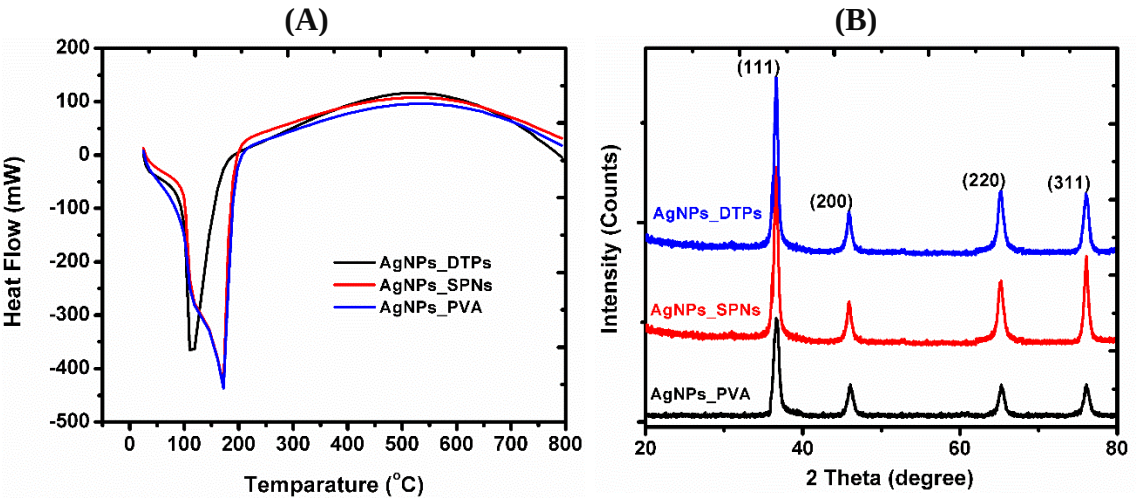

Figure 7-3: (A) DSC thermogram and (B) X-Ray Diffraction pattern of AgNPs-*PVA*, AgNPs-*SPNs* and AgNPs-*DTPs*

From the DSC results, there was no clear indication whether any of the conjugated NPs will undergo any deformation as the energetics of the process were more favorable beyond 171 ^{o}C of heat flow measured at 10 ^{o}C s^{-1}. Overall the, ATR and DSC results of AgNPs-*PVA*, AgNPs-*SPNs* and AgNPs-*DTPs* in Figure 7-2B and Figure 7-3A; are very similar in many ways and they correlate with the morphology and size distribution (see Figure 7-1).

7.2.4 Cytotoxicity studies on human embryonic kidney cells (HEK293T)

The leaf and stem extracts of *Iboza* Riparia have been reported previously to be active against *S. aureus* and several mycobacteria (Van Puyvelde *et al.* 1986; Van Puyvelde *et al.* 1994), but not for cytotoxicity against metabolically active or dividing cells (Vlietinck *et al.* 1995). Cytotoxicity studies of the AgNPs synthesized with PVA, *Ilex* Mitis and *Iboza* Riparia extracts were studied for MTT assay which has gained high attention in cell proliferation studies. MTT is a tetrazolium salt, which can be easily reduced to a colored formazan product with the help of reducing enzyme present only in metabolically active or dividing cells. The enzyme succinate dehydrogenase and cytochrome oxidase present in mitochondria of active cells that help in the reduction of

MTT. Thus under particular reduction conditions of MTT and subsequent formation of formazan is proportional to the number of viable or active cells present in the medium.

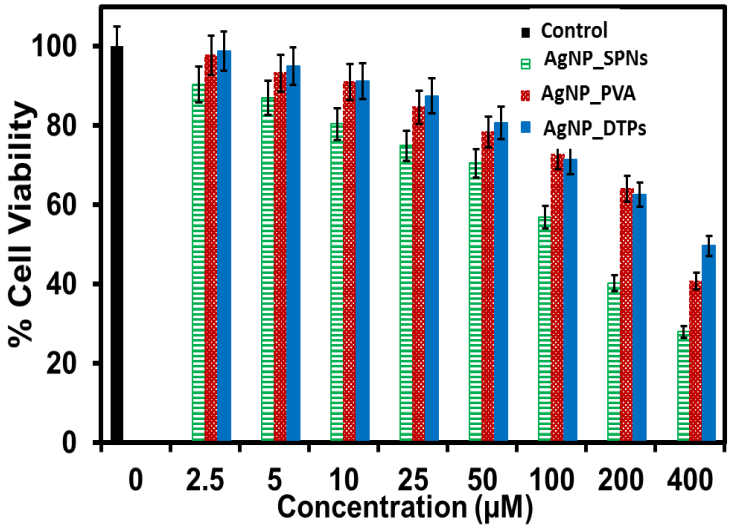

Figure 7-4: Antimicrobial activity (Zone of inhibition) of conjugated AgNPs against Extract. Values represent means and bars represent standard deviation

With the help of MTT-assay we have analysed the cytotoxicity and cell-proliferation inhibition activity of the three designed inhibitors (AgNPs-*SPNs*, AgNPs-*PVC* and AgNPs-*DTPs*) as shown in Figure 7-4. Using all the inhibitors at 100 µM, the viability of the cells were maintained at ~50%. However, at 200 µM, the viability of a cell in the presence of AgNPs-*PVA* inhibitor was found to be less than 50 % which is non-toxic to normal cells. Interestingly, AgNPs-*SPNs* and AGNPs-*DTPs* at 400 µM demonstrated the cell viability < 50%. Above this concentration, the reference and the tested inhibitors both became toxic to the normal cells. Overall, AgNPs-*DTPs* were found to be less toxic with 49.7 % cell viability, while AgNPs-*PVA* and AgNPs-*SPNs* had cell viability of 28.0 and 40.8 % respectively at 400 µM.

Recent reports have demonstrated extensively that by changing the stabilizing ligand on the surface of the nanoparticles we can actually be able to vary the cytotoxicity of the

particles making them user friendly for a variety of biological applications as the selected plants are used in traditional medicine against viral diseases.

7.2.5 ABTS antioxidant assay

The antioxidant activity information is also crucial, particularly for biosynthesized nanoparticles. For that reason, the antioxidant activity of the both AgNPs synthesized from *Iboza* Riparia leaf and *Ilex* Mitis extracts were studied on ABTS. ABTS is a suitable for antioxidant activity studies because it is relatively stable free radical but colorises in the presence of antioxidants (Mackerell, Feig and Brooks 2004). The free radical model treated with varying concentrations from 0.1-1.5 mL and absorbance due to the extent of activity reaction at 734 nm was recorded for colloidal AgNPs, along with the absorbance of pure ABTS (see Figure 7-5). The antioxidant activity of AgNPs-*SPNs*, AgNPs-*DTS* and AgNPs-*PVA* on ABTS* with λ_{max} at 734 nm as shown in the spectra.

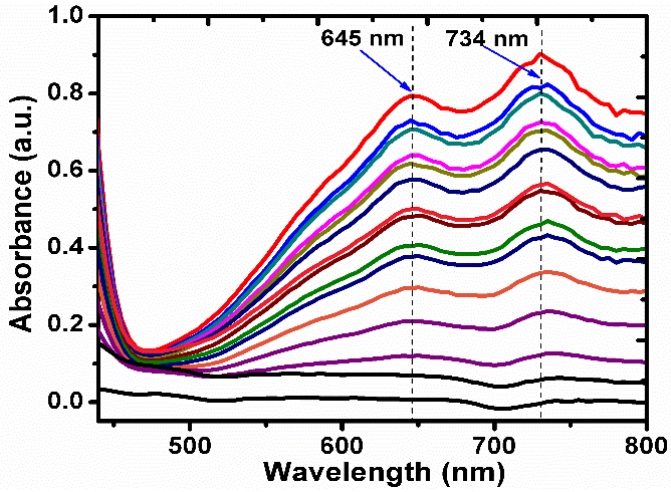

Figure 7-5: UV-Vis spectra of ABTS* after 30 min incubation with AgNPs-SPNs. Volume of nanoparticles was varied with increments of 20 µl keeping total volume at 1 mL.

The absorbance band reveals that AgNPs in the presence of phosphate buffer with the potential to dedicated hydrogen thus decreasing the intensity in the order AgNPs-*DTPs*> AgNPs-*PVA*>AgNPs-*SPNs*. The significant color change observed is one way to confirm that conjugated nanoparticles participate in the protonation possesses. Therefore, the scavenging efficiency of AgNPs-*SPNs,* AgNPs-*DTPs* were found to be 89.25 % in 0.20 mL and 96.62 % in 0.20 mL/0.05 mM.

7.3 Conclusions

The use of *Iboza* and *Ilex Mitis* extracts without any special reducing or capping agents produced nanoparticles that were stable. This was extended up to the level of cells that can arise from the abrupt increase in bacterial cell length as the functionalized nanoparticles are incorporated into the cells. Altogether the study elucidates the metal nanoparticle-bacteria interaction at the cellular level that can be utilized for beneficial biological application and if it significantly possesses potential to produce eco-toxicity, challenging the eco-friendly nature of nanoparticles. This will explore the potential possibilities of nontoxic nanomaterials, which can be prepared in a simple and cost-effective manner. These nanoparticles are potential candidates for suitable formulation of new types of bactericidal materials with good antioxidant activity.

CHAPTER 8

8 Case Study 4: Biosynthesis ZnONPs from jacaranda mimosifolia and it antibacterial assay

---

This chapter presents the green synthesis of zinc oxide nanoparticles with an average size of 9-12 nm using carica papaya seed extract. The composition of the extract was identified using gas chromatography-mass spectrometry. The major component was found to be oleic acid acting as an important capping agent for the stabilization of the nanoparticles. The prepared nanoparticles were characterized using X-ray diffraction, transmission electron microscopy, UV-Visible spectroscopy and fourier transform infrared spectroscopy. Thereafter, they were evaluated for bacterial activities against Escherichia coli and *Enterococcus faecium. In addition molecular simulation results on the adsorption of oleic acid on the surface of zinc oxide are presented.*

8.1 Methodology

8.1.2 Characterization of ZnONPs

Characterization of ZnONPs prepared as described in section 4.1.3.4, were characterized as follows. X-ray diffraction study was carried out using a Bruker AXS D8 diffractometer with CuKα radiation (λ = 1.5418 Å) at 40 kV over a 2θ range from 10^o to 70^o at a scanning rate of 0.05 min^{-1}. The size and morphology of the ZnONPs were investigated by HRTEM. The samples were dispersed in distilled water and ultrasonicated for 30 min before analysis. The absorption studies were carried out on a UV-Vis spectrophotometer. The colloidal solution of the sample was prepared by dissolving 1 mg of ZnO nanopowder in 50 mL ultra-pure deionized water and was run in the wavelength range 200-800 nm. FTIR spectra of ZnONPs samples and extract of *jacaranda mimosifolia* flowers were recorded in the range of 4000-500 cm^{-1} on Varian 800 FT-IR Scimitar Series supplied by SMM Instruments (Durban, SA).

To predict the composition of *jacaranda mimosifolia* flowers extract and a predominant capping agent, GC-MS analysis of the methanolic extract was carried out. 1.0 mg of the dried and powdered *jacaranda mimosifolia* flowers were dissolved in methanol and stirred for 30 min followed by filtering through 0.45 µm nylon filter. Finnigan MAT GCQ system with splitless injector mode was employed for the sample analysis. The injector temperature was set at 250 ^{o}C and ZB-5MS fused silica capillary column with dimensions 30 m x 0.25 mm x 1 µm was used. The carrier gas was helium with a flow rate of 1 mL min^{-1} and the amount of sample injected was 1 µL. The MS conditions are as follows, scan mode: full scan in EI mode (50 to 650 amu), transfer line temperature: 270 ^{o}C and ion source temperature: 200 ^{o}C. The identification of the compounds present in the *jacaranda mimosifolia* flowers extract was compared with the NIST library.

8.2 Results and Discussion

8.2.1 Characterization of ZnONPs

ZnONPs were formed via the simple method of alkali precipitation of zinc gluconate where the compounds present in the *jacaranda mimosifolia* flowers aqueous extract reduced the formed $Zn(OH)_2$ precursors. The schematic synthesis of ZnONPs is shown in Figure 8-1.

Figure 8-1: Schematic representation of synthesis of ZnONPs using *jacaranda mimosifolia* flower extract

The mechanism is explained on the basis that the biomolecules such as fatty acids, phenolic compounds, saponins, alkanoids, flavonoids present in the extract form complexing agents with the precursors which initially starts the process of nucleation forming reverse micelle and then further causing reduction and shaping of NPs (Crookes-Goodson, Slocik and Naik 2008; Gade *et al.* 2008; Sharma, Kanchi and Bisetty 2015). The GC-MS results reveal that 1, 6 dimethyldecahydronapthalene, oleic acid and citronellyl propionate are predominantly present in the *jacaranda mimosifolia* flowers extract. Based on the GC-MS, purity and fit values of 1, 6 dimethyldecahydronapthalene, oleic acid and citronellyl propionate, oleic acid was selected as a reducing and capping agent for the synthesis of ZnONPs. When zinc gluconate is dissolved in water, colorless

solution is formed due to the presence of $[Zn(H_2O)_6]^{2+}$ ions. The addition of NaOH produces white precipitates of ZnONPs in the core of a micelle. The capping agent acts as a stabilizing agent by adhering to the surface of NPs forming a protective layer and controls the particle size (Kumar and Rani 2013).

The microwave irradiations act as an efficient, environment friendly and economical heating method for the synthesis of NPs while maximizing the yield. The household microwave ovens also lead to the formation of metal and metal oxide NPs with good crystallinity and optical properties (Bhattacharjee, Ahmaruzzaman and Sinha 2014; Bhosale *et al.* 2015). The dielectric heating effect of microwaves is generated due to dipole moment interaction of the molecules and high frequency electromagnetic radiations. Since, water has a high dipole moment; it is the best solvent for the synthesis of NPs using microwaves (Baruwati, Polshettiwar and Varma 2010). As soon as an aqueous solution containing zinc gluconate, extracts, and NaOH are exposed to microwave heating, there is an enhancement in the reaction rate and nucleation thereby forming ZnO seeds. These seeds assemble together as clusters due to their high surface energy which grows rapidly to form NP aggregates (Wang *et al.* 2015).

The XRD analysis of ZnONPs synthesized using the extract exhibited typical diffraction peaks at 32.25^o (100), 34.90^o (002), 36.74^o (101), 47.99^o (102), 57.06^o (110) and 63.31^o (103) indexed to the crystalline ZnO wurtzite structure with P63mc space group whereas NPs formed without the use of extract exhibited peaks at 32.38^o (100), 35.08^o (002), 36.80^o (101), 48.12^o (102), 57.14^o (110) and 63.42^o (103), respectively as can be seen in Figure 8-2(Yoshio *et al.* 2001).

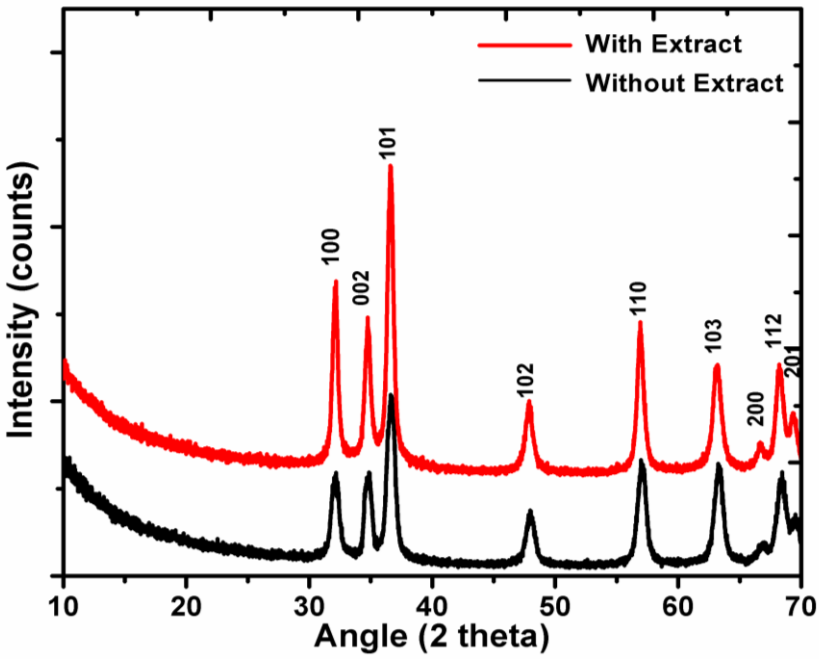

Figure 8-2: XRD diffraction pattern of ZnONPs with and without the use of extract

The lattice parameters for the hexagonal unit cell such as d-spacing (d), lattice constants (a, c) and unit cell volume (V) were calculated using the Lattice Geometry equation 8.1 (Suryanarayana and Norton 1998) and also summarized in Table 8-1:

$$\frac{1}{d^2} = \frac{4}{3}\frac{(h^2 + hk + k^2)}{a^2} + \frac{1^2}{C^2} \quad (8.1a)$$

$$a = \frac{\lambda}{3^{1/2}} \sin\theta (h2 + hk + k^2)^{1/2} \quad (8.1b)$$

$$V = 3^{1/2} a^2 \frac{C}{2} \quad (8.2)$$

Where, *h*, *k* and *l* are miller indices.

The calculated values of c/a ratio for ZnONPs Table 8-1 are close to the ideal value of 1.633 for ZnO hexagonal cell. The deviation from the ideal wurtzite crystal is probably due to lattice stability and ionicity (Morkoç and Özgür 2009). The morphology and size of the ZnONPs were demonstrated by HRTEM images. Figure 8-3A represents the

ZnONPs in the size range of 2-4 nm synthesized with *jacaranda mimosifolia* flower extract whereas Figure 8-3B shows the ZnONPs with an average diameter of 8-11 nm and spherical morphology prepared without the use of extract. The dark spots in the micrographs are the NPs clustered together due to their small size.

Table 8-1: Lattice parameters of ZnONPs synthesized using with and without *jacaranda mimosifolia* flowers extract

Sample	2θ	hkl	d-spacing (Å)	LP (Å)	UCV (Å^3)
ZnONPs (with Extract)	32.25^o	100	2.773	a = 3.205	45.73
	34.90^o	002	2.568	c = 5.141	
	36.74^o	101	2.443	c/a = 1.604	
ZnONPs (without extract)	32.28^o	100	2.770	a = 3.202	45.42
	35.08^o	002	2.555	c = 5.116	
	36.80^o	101	2.440	c/a = 1.598	

LP: Lattice parameters; UCV: Unit cell volume

The clear lattice fringe widths with the values of 0.24 nm and 0.26 nm in the HRTEM images (Figure 8-3) corresponds to 101 and 002 crystal planes and are indicative of the crystalline nature of ZnONPs.

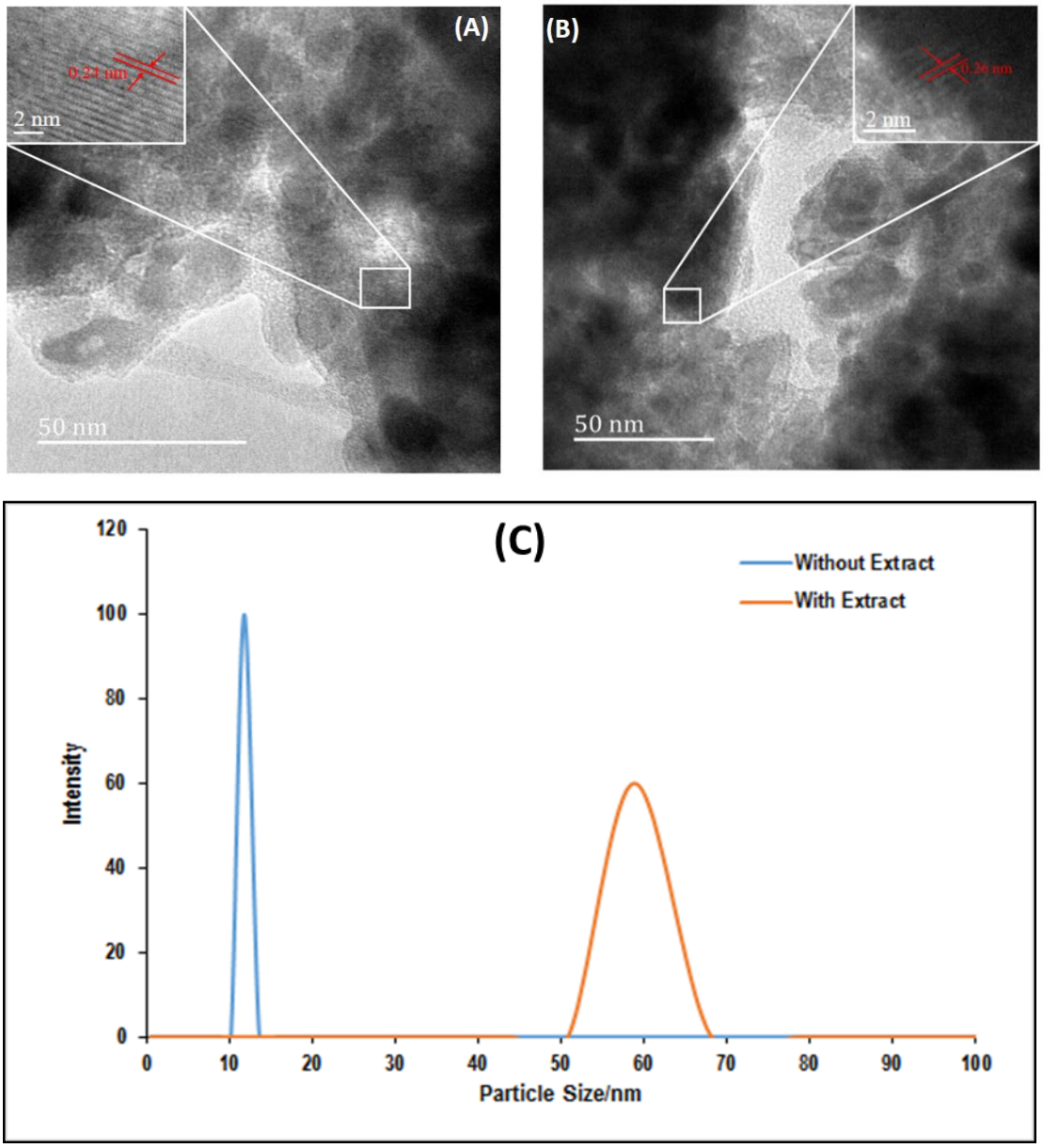

Figure 8-3: HRTEM micrographs of (A) ZnONPs with extract; (B) without extract (C) DLS of ZnONPs with and without the use of *jacaranda mimosifolia* flower extract

The semiconductor band structure of ZnONPs has been characterized via UV-Visible absorption spectroscopy. Figure 8-4 inset shows the UV-Vis spectra of with and

without extract mediated synthesized ZnONPs with the showing absorption peaks at 265.91 nm and 278.9 nm, respectively.

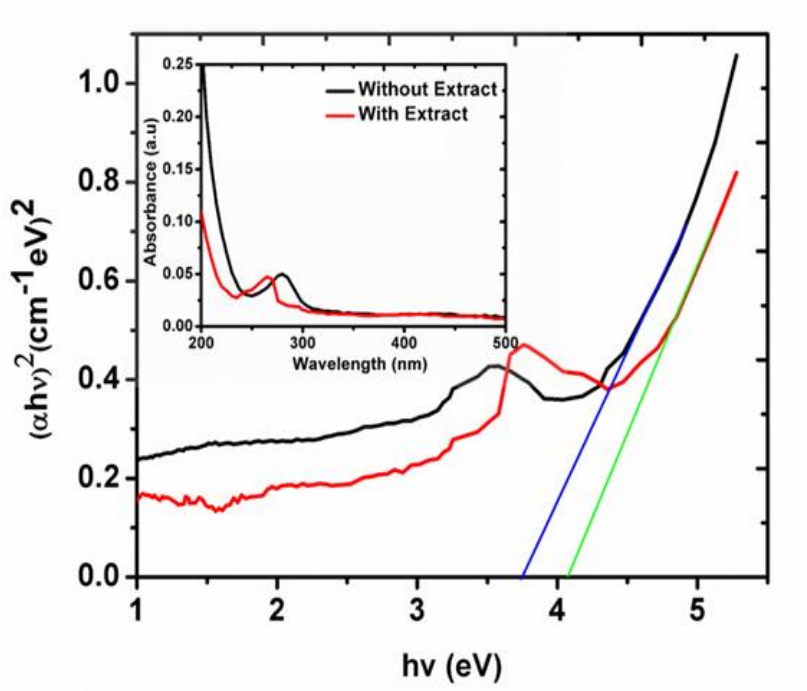

Figure 8-4: Tauc Plot of ZnONPs with and without the use of extract showing inset of UV-Vis spectra

The optical band gap for the ZnONPs was calculated using the Tauc expression given in equation 8.3(Tauc and Menth 1972),

$$(h\nu\alpha) = A(h\nu - E_g)^n \tag{8.3}$$

where, h is Planck's constant, ν is frequency of vibration, α is absorption coefficient, E_g band gap, A proportionality constant and n denotes the nature of sample transition. The direct band gap is found to be 4.07 eV and 3.74 eV for ZnONPs synthesized with and without extract, respectively resulting due to quantum confinement Figure 8-4. As the

particle size decreases, there is an increase in the energy gap of electronic transitions (Spanhel 2006) i.e., as the system becomes more confined, the energy separation between adjacent levels increases and also discrete energy levels arises at the band edges (Koole *et al.* 2014).

The FTIR analysis was employed to probe the role of biomolecules present in the extract for the formation of ZnONPs. As shown in Figure 8-5, the FTIR spectrum of extract exhibits a broad peak at 3373.12 cm^{-1} corresponding to O-H stretching vibration whereas the peaks at 2942.29 cm^{-1}, 2830.04 cm^{-1}, 1647.43 cm^{-1} and 1031.62 cm^{-1} correspond to C-H stretching, carbonyl group (C=O) and C-H bending, respectively.

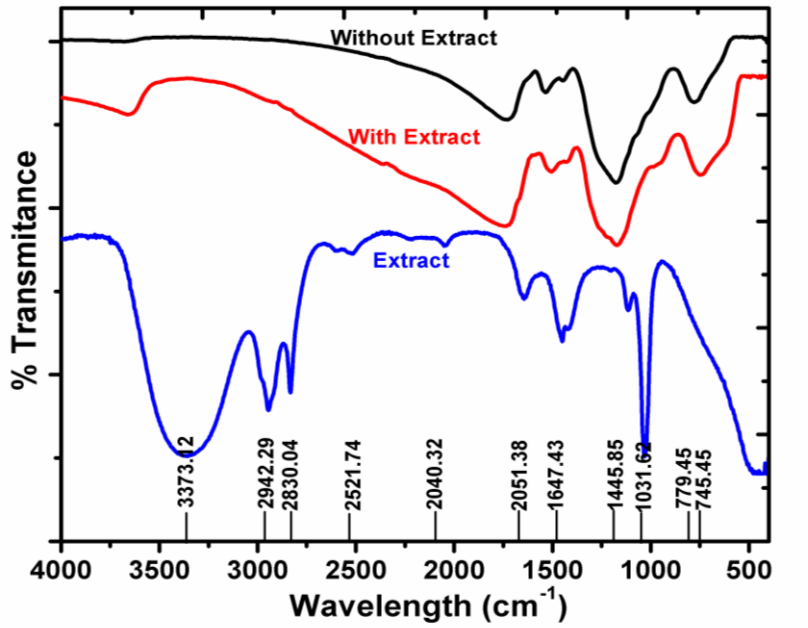

Figure 8-5: FTIR spectra of methanolic extract of *jacaranda mimosifolia* flower, ZnONPs of extract with the inset showing UV-Visible spectra

The peaks related to the following functional groups in the extract indicate the existence of different biomolecules; the major being oleic acid which was further

confirmed through GC-MS analysis. The spectra of ZnONPs synthesized using with and without extract shows Zn-O stretching peaks at 745.54 cm^{-1} and 779.45 cm^{-1}, respectively (Musat *et al.* 2014). There was disappearance of peaks corresponding to that of extract in the spectra of NPs. The weak peak around 1445.85 cm^{-1} in the case of the extract was broadened as seen in the spectra of NPs which could be attributed to C-H bending in methanol since the samples were prepared in methanol.

From the literature reports on the synthesis of metal oxide NPs with plant extract (Rajiv, Rajeshwari and Venckatesh 2013; Atarod, Nasrollahzadeh and Sajadi 2015; Nasrollahzadeh *et al.* 2015), it is evident that biomolecules play a pivotal role in the reduction of metal oxide salts and stabilization of NPs, but very few of them suggests that the biomolecules are involved in the process of formation of NPs. In this regard, GC-MS analysis of a methanolic extract of *jacaranda mimosifolia* flowers was carried out to identify the biomolecules present in the extract and to understand their impact on the morphology and size of NPs. Figure 8-6 illustrates the GC-MS chromatogram of the methanolic extract of the *jacaranda mimosifolia* flowers where different components were identified. In the retention time ranging from 15:03 to 20:03 min where the high intensity peaks were present, the following molecules were identified in the following order: 1, 6 dimethyldecahydronapthalene, oleic acid and citronellyl propionate. On the basis of purity fit, oleic acid was found to be the most significant capping agent molecule. Therefore, facet-specific binding adsorption sudies were carried out to comprehend its role as a capping agent which has been explained in the subsequent section.

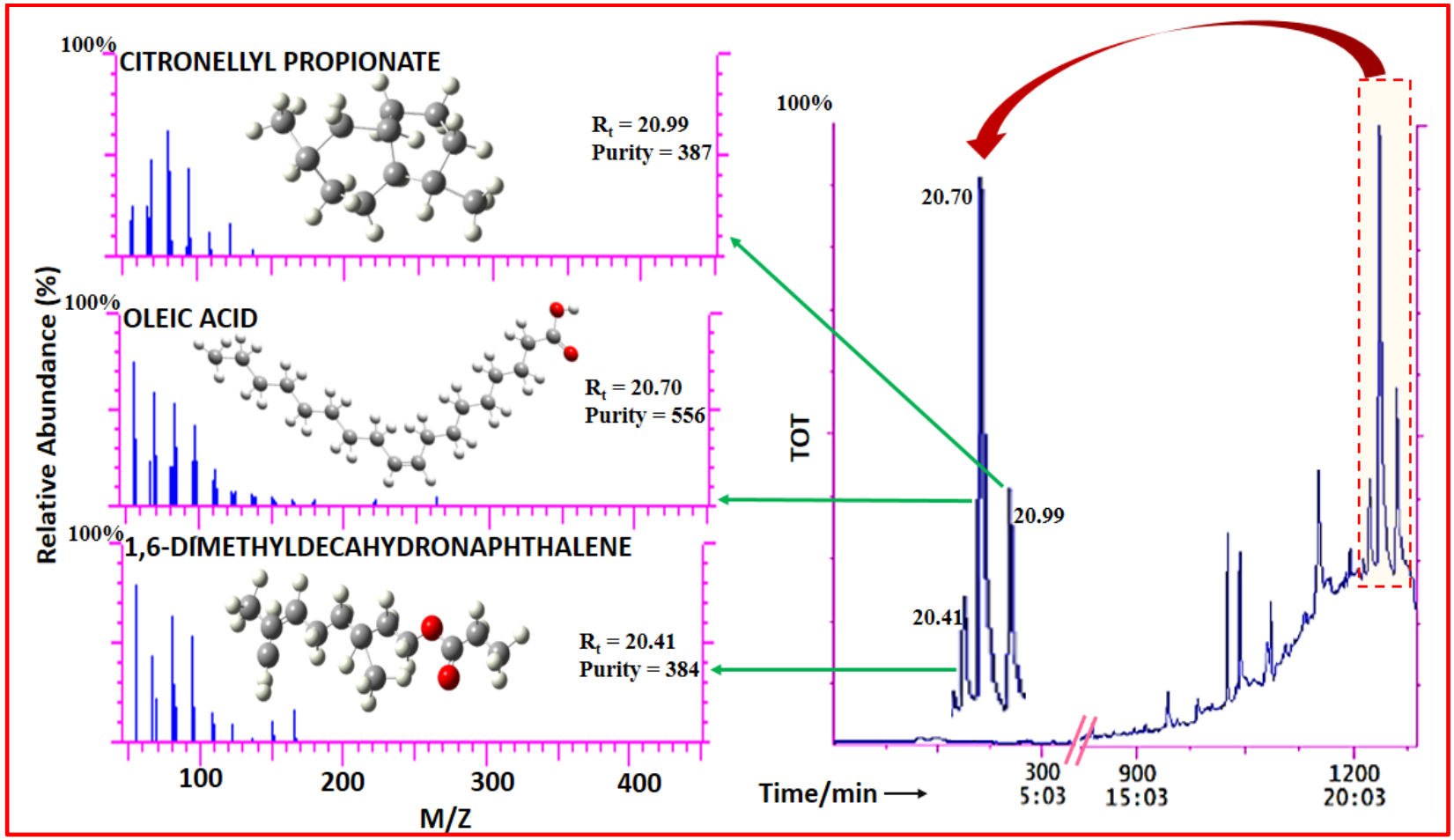

Figure 8-6: GC-MS chromatogram of methanolic extract of *jacaranda mimosifolia* flower

8.2.2 Bacterial assessment by standard plate count method

The viability of ZnONPs treated and untreated *E. coli* cultures were determined by standard plate count method that involves colony forming unit (CFU). The *E. coli* ATCC 25922 and *E. faecium* ATCC 35667 cells were grown to O.D of 0.6 at 600 nm (35±1 ^{o}C, 10^{6} CFU mL^{-1}), pelletized by centrifugation (4000 xg for 3 min at 4 ^{o}C), washed thrice by phosphate buffer saline (PBS, pH=7.4) and finally suspended into PBS containing varying concentrations (10, 25, 50, 75, 100 µg mL^{-1}) of NPs synthesized using *jacaranda mimosifolia* flowers extract and without extract. Bacterial culture in Luria Bertani (LB) broth without NPs served as negative control. The cells were grown for 120 min at 35±1 ^{o}C and were serially diluted in PBS. The dilutions were plated on LB agar plates. After overnight incubation at 37 °C, the number of CFU was counted manually. All the experiments were conducted in triplicate.

8.2.3 Antibacterial activity of synthesized ZnONPs

The antibacterial property of ZnONPs was analyzed by treating bacterial cultures with varying concentration of NPs ranging from 10 to 100 µg mL^{-1}. The CFU results revealed that as the concentration of ZnONPs increased, CFU count of gram negative (*E. coli*) and gram positive (*E. faecium*) bacterial cultures decreased. The ZnONPs prepared using extract and without extract exhibited antibacterial property can be seen in Figure 8-7. The percent viability of the ZnONPs exhibited stronger antibacterial activity against gram-positive *E. faecium* than against gram-negative *E. coli.* The results reported were in concurrence with previously published reports showing the antibacterial activity of ZnONPs (Pang *et al.* 2016). The important reason could be the difference in the cell wall structure of gram positive and gram-negative bacteria. The cell wall of gram-positive bacteria is normally composed of peptidoglycan which forms 80% of the cell wall. The remaining 10-20% of the cell wall is composed of teichoic acids, other proteins, and lipopolysaccharides which is the outer membrane. In the case of gram-negative bacteria, peptidoglycan forms 10% of the cell wall but the outer membrane is composed of 50%

lipopolysaccharides, 35% phospholipids and 15% lipoproteins. Thus, the outer membrane in gram-negative bacteria is tightly packed, hence, providing protection and sensitivity to antibacterial agents (Li *et al.* 2009). Moreover, the antibacterial activity depends on the size of NPs and also infectivity and sensitivity of different strains varies (Raghupathi, Koodali and Manna 2011). Therefore, ZnONPs synthesized using the extract of *jacaranda mimosifolia* flowers were in the range of 2-4 nm size as compared to NPs fabricated in the absence of extract (8-11 nm) and the *E. faecium* ATCC 35667 strain has been reported to be more pathogenic than *E. coli* ATCC 25922.

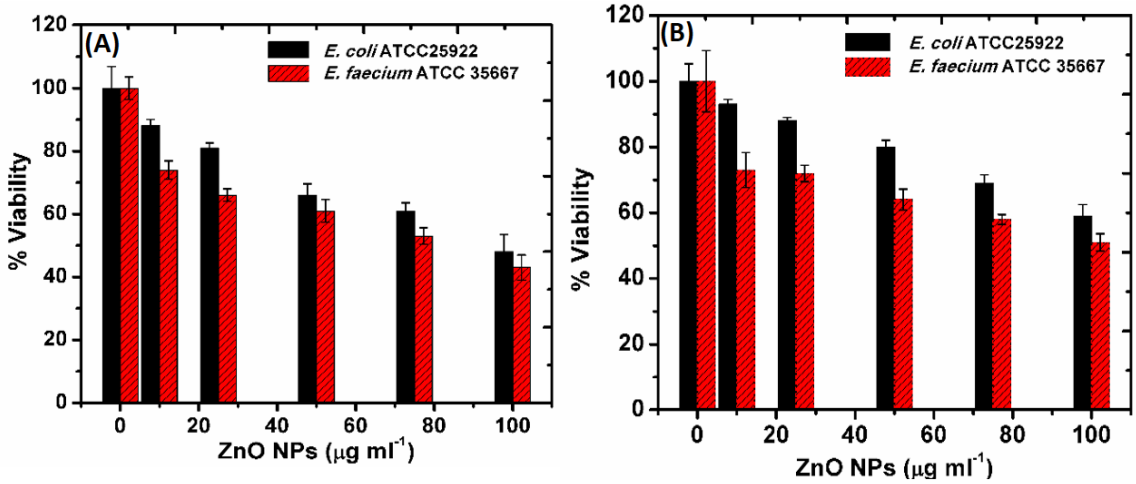

Figure 8-7: Viability of bacteria in the presence of (A) ZnONPs synthesized using extract, (B) ZnONPs synthesized without extract

When the bacterias were treated with 100 µg mL^{-1} of ZnONPs synthesized without extract, their viability was found to be 59% and 51% (Figure 8-7B), however when using NPs synthesized using *jacaranda mimosifolia* flowers extract, the percent viability was 48% and 43%, respectively (Figure 8-7A). The results indicated that the antimicrobial property of extract mediated synthesized ZnONPs was higher than that of the NPs synthesized without extract at higher concentrations (Figure 8-7A-B).

In addition, there was a statistically significant difference in cell viability at 100 µg mL^{-1} in *E.coli* and *E. faecium* when treated with ZnONPs using extract (p=0.0448). A similar trend was observed for concentrations 75, 50, and 25 µg mL^{-1} of NPs.

8.2.4 Adsorption of oleic acid on the surface of ZnONPs

Apart from many studies which focus on the quantum confinement effect of quantum dots such as ZnONPs, the surface chemistry is very significant in order to understand the physical and chemical properties of NPs. Consequently, the selective interaction of ZnONPs with capping agents such as oleic acid is critically vital to enhance biocompatibility and viability, making these nanomaterials a suitable candidate for applications involving biological studies. In this chapter, we therefore, employed molecular dynamics simulations to demonstrate that physical and chemical properties of ZnO nanocrystal are induced by surface chemistry which preferably leads to isotropic and anisotropic nanomaterials. The role of capping agent in defining the size and shape was studied by simulating three crystal lattice parameters as shown in Figure 8-8

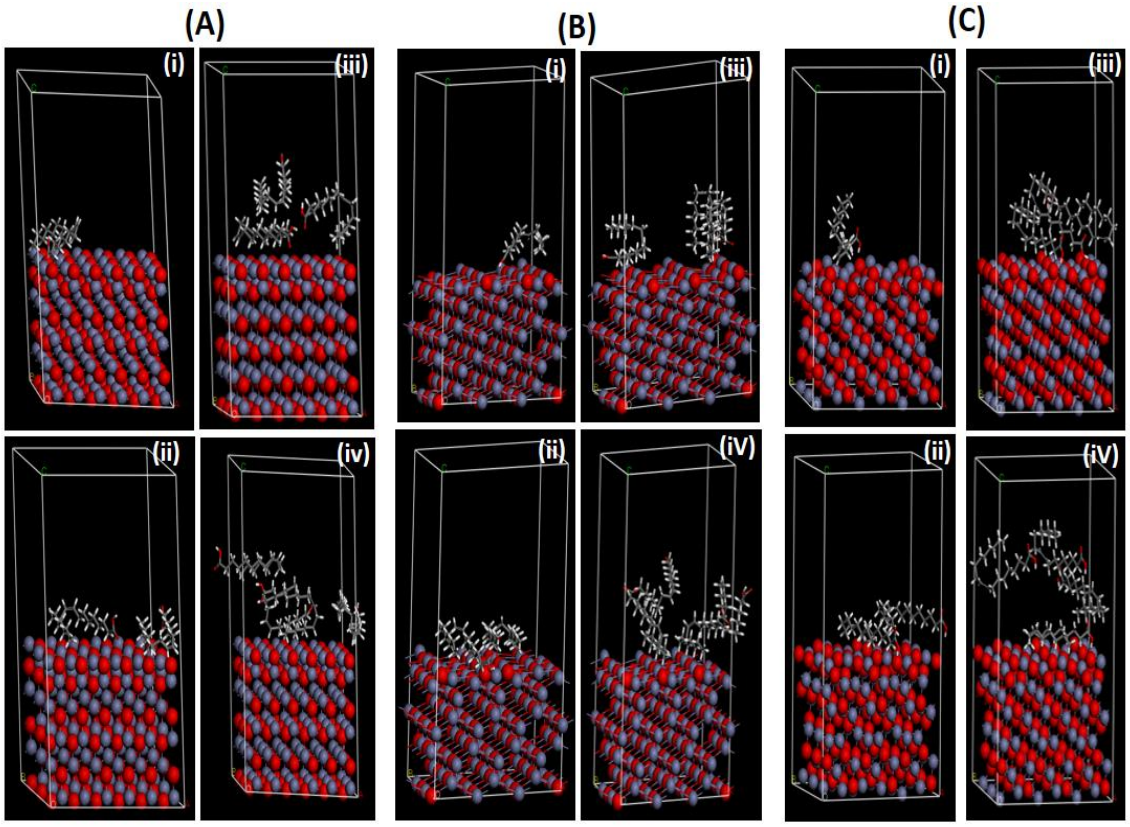

Figure 8-8: Adsorption of oleic acid molecules onto different surfaces (A) 002 (B) 100 and (C) 101 of ZnO clusters

It was demonstrated that ZnONPs have varied shape evolution and potentially different facets which lead to a facet-driven growth of ZnO to different shapes, thereby fine-tuning their optical properties. For many studies, facets such as (111) and (101) are highly studied because of their potential to drive the preferential growth of nanomaterial which is the main contributor of their varied optical properties (Chang and Waclawik 2014). In order to simulate the variation of the reaction parameters, three facets, (002), (100) and (101), were studied. It was demonstrated that as the concentration of oleic acid was increased, the strength of adsorption favored the (101) facet. The preferential passivation of (101) facet was evident from concentration profile shown in Figure 8-9C.

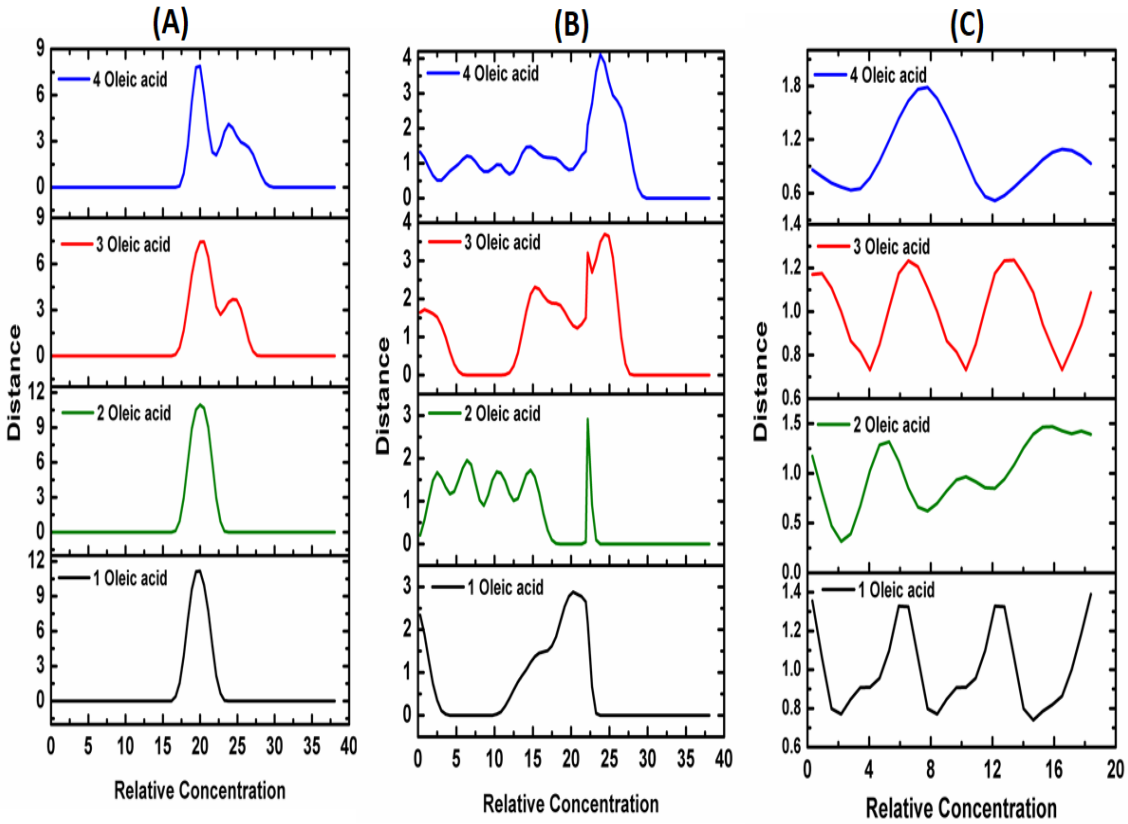

Figure 8-9: Concentration profile of oleic acid molecules adsorbed on (A) 002 (B) 100 (C) 101 facets of ZnO

In Figure 8-9, it can be seen that the average distance of oleic acid on the surface of ZnO cluster was located within the distance of an average of 1.4 Å as compared to other facets on which the oleic molecules were located on the varying distance of 4 and 9 Å for (100) and (002) facets, respectively. These results confirmed previous studies which indicated that the presence of oleic acid could drive the preferential growth of zinc oxide nanomaterials to nanorods array and other structures (McLaren *et al.* 2009).

The most favored model from Figure 8-8 was obtained by further calculating the interaction energy of each model. The interaction ($E_{interaction}$) was calculated using equation 8.4:

$$E_{interaction} = E_{complex} - (E_{ligand} + E_{surface}) \quad (8.4)$$

E_{compex} is the energy of the surface and oleic acid, E_{ligand} is the energy of the oleic acid and $E_{surface}$ is the energy of the surface (ZnO-100, ZnO-002 and ZnO-101) without ligands. The negative $E_{interaction}$ values indicate an attractive or strong oleic acid to ZnO interactions. The interaction energies of models depicted in Figure 8-8 were calculated using Eq. 4 as presented in Table 8-2. The interaction energies in Table 8-2 revealed that ZnO-101 has the highest interaction energy. The high interaction for ZnO-101 symbolizes that oleic acid binds stronger on the ZnO-101 surface than the other surfaces, with the interaction following the trend, ZnO-101, ZnO-002 and ZnO-100.

Table 8-2 Adsorption energy of oleic acid molecules on the facets of ZnO nanocluster

Facet	Adsorption energy (kcal/mol) of number of oleic acid molecules			
	1	2	3	4
100	-31.242	-65.724	-97.977	-121.28
002	-45.668	-92.127	-135.95	-167.62
101	-64.297	-128.69	-178.6	-221.92

Although, the interaction gives the general picture of the interaction of oleic acid with ZnO surface, this trend does not eliminate the fact that all surfaces can potentially interact with oleic acid but to the lesser extent than the 101 surface. This is merely an indication that more oleic acid molecules shall interact with 101 surfaces leaving the other surfaces (ZnO-002 and ZnO-100) with less number of oleic acid molecules. The concentration profiles of different facets of ZnO shown in Figure 8-9 are good indicators to probe the vicinity of functional groups on the surface of the metal oxide. The concentration profile proved that the affinity of the oleic acid is more pronounced on 101 facets, which is situated closer to the surface by about 1.4 Å. This selective adsorption was reported elsewhere to drive the rapid growth of ZnONPs to pencil-like nanorods (Wang and Lian 2014).

8.3 Conclusions

The results presented in the presented in this chapter demonstrates the biosynthesis of ZnONPs with a narrow size range of 2-4 nm using the extract of *jacaranda mimosifolia* flowers. The major finding was the presence of oleic acid as a capping agent in the synthesis of ZnONPs, identified by GC-MS and FTIR. The peaks corresponding to the oleic acid and ZnONPs were well depicted in the FTIR spectra as well. The capping agent, oelic acid was found to stabilise the resulting NPs. Furthermore, the other identified molecules like 1, 6 dimethyldecahydronapthalene and citronellyl propionate could also function as capping agents. The second major finding is the facet-specific binding of the oleic acid molecule on to the different surfaces of the ZnO. It was established on the basis of interaction energy and concentration profile that oleic acid preferred to adsorb onto (101) facet of ZnO as compared to the other (002) and (100) facets. This would lead to the understanding of the selective adsorption of molecules on to the surface of different NPs thereby driving into the formation of varied shapes and sizes. The oleic acid stabilized ZnONPs showed fairly good antibacterial activity against both gram-negative *E. coli* and gram-positive *E. faecium* bacteria. The antibacterial activity was pronounced in the case of gram positive bacteria (*E. faecium*) as the NPs could penetrate easily through the outer membrane due to the less compact nature as compared to that of gram-negative bacteria. The synthesis reported here is reproducible in short time, cost effective and environmentally safe as it makes use of an extract from the fallen waste *jacaranda mimosifolia* flowers for the first time.

CHAPTER 9

9 Case Study 5: Biosynthesis ZnONPs from papaya and electrochemical sensing of silymarin

---

This chapter reports on biosynthesized ZnONPs from carica papaya extract and demonstrates the electrochemical sensing of silymarin by integrating zinc oxide nanoparticles with multiwalled carbon nanotubes on the glassy carbon electrode. The electrochemical signals obtained from MWCNTs/ZnONPs/GCE were 2-fold higher than MWCNTs/GCE and bare GCE.

9.1 Methodology

9.1.1 Characterization of *carica papaya* extract and ZnONPs

Characterization of ZnONPs prepared as described in section 4.1.3.4, were characterized as follows. The XRD diffraction pattern and the HRTEM morphology of ZnONPs synthesized using carica papaya seed extract is shown in Figure 9 1. It can be noticed that ZnONPs exhibit characteristic peaks at 2θ value of 32.25°, 34.90°, 36.74°, 47.99°, 57.06° (Figure 9 1A) and 63.31° arising from the diffraction planes of (100), (002), (101), (102), (110), (103).

All these diffraction peaks have been indexed to the crystalline ZnO wurtzite structure with P63mc space group (Yoshio *et al.* 2001). No other peaks from the impurities such as $Zn(OH)_2$ or constituents of *carica papaya* seed extract were observed which indicates the formation of NPs with high purity. The lattice constants a and c were calculated to be 3.218 Å and 5.159 Å whereas c/a ratio value was 1.603 Å, close to the ideal value 1.633 Å for ZnO hexagonal cell structure using simplified lattice geometry equations 8.1 to 8.3 for the hexagonal lattice as: (Suryanarayana and Norton 1998). The calculated *c*/*a* value is usually smaller than the ideal values since the distances between cations and anions in the wurtzite crystal tends to be shorter due to ionicity (Hanada 2009).

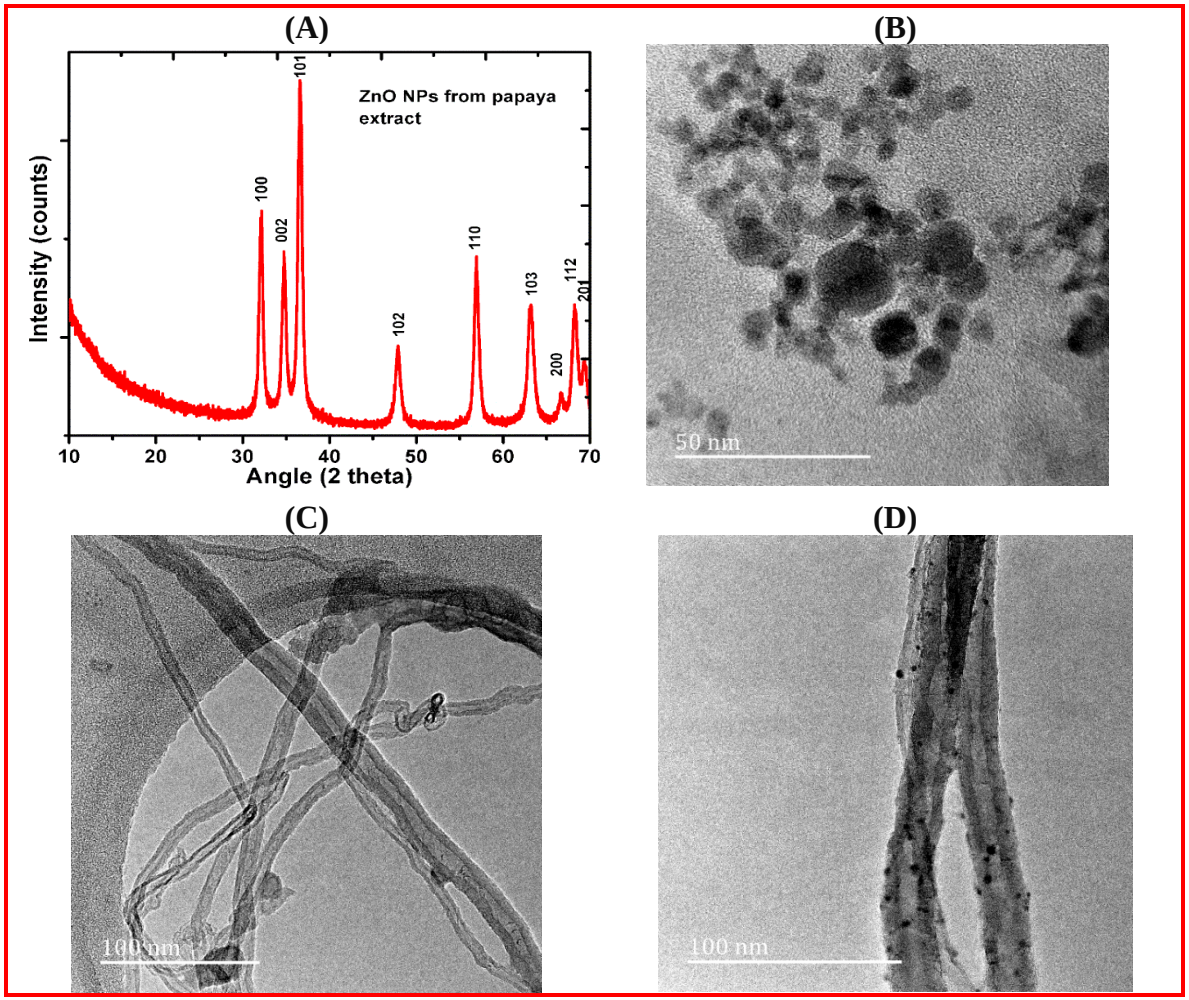
(A)
ZnO NPs from papaya extract
Intensity (counts)
Angle (2 theta)
100
002
101
102
110
103
200
112
201
10
20
30
40
50
60
70
(B)
50 nm
(C)
100 nm
(D)
100 nm

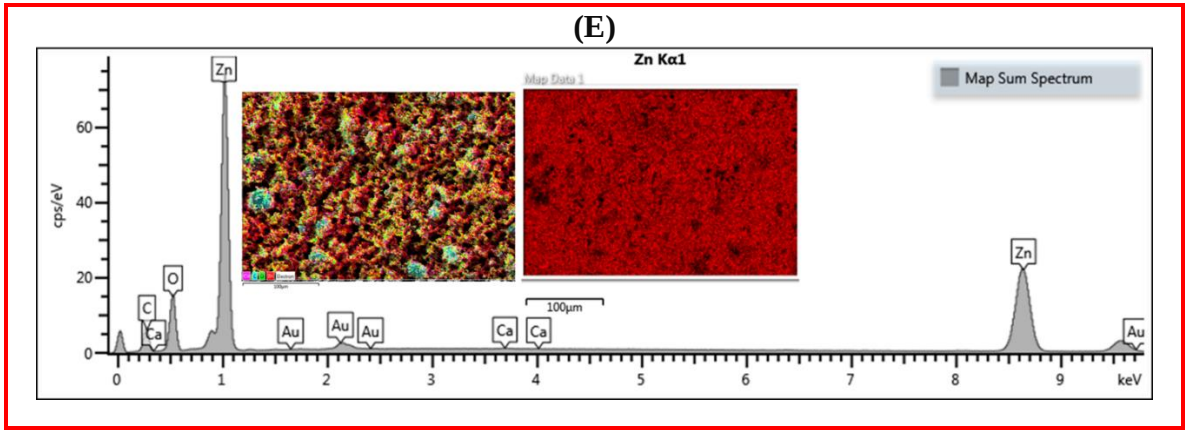

Figure 9-1: (A) XRD diffraction pattern of ZnONPs, (B) HRTEM of ZnONPs synthesized using *carica papaya* seed extract, (C) Bare MWCNTs, (D) MWCNTs modified with ZnONPs, (E) EDX mapping of MWCNTs modified with ZnONPs.

The *d*-spacing values calculated for all the peaks in the XRD pattern along with the full width half maximum (FWHM) have been tabulated in Table 9-1 as per to the literature report (Yoshio *et al.* 2001; Dinesh *et al.* 2014).

Table 9-1: Interplanar *d*-spacing from XRD and JCPDS with FWHM values.

Angle (2Theta) (XRD)	Reflection plane (*hkl*)	*d*-spacing (Å) (XRD)	*d*-spacing (Å) (JCPDS)	% contraction in *d*-spacing	FWHM (Degree)
32.11	100	2.7868	2.8136	0.9525	0.5483
34.77	002	2.5794	2.6024	0.8838	0.6091
36.60	101	2.4517	2.4751	0.9454	0.6067

48.03	102	1.8930	1.9105	0.9159	0.5234
56.93	110	1.6089	1.6244	0.9542	0.7142
63.18	103	1.4635	1.4768	0.9006	0.8284

169

170 The (101) diffraction peak in the XRD of ZnONPs is more intense compared to (100) and (002) peaks, which implies that the
171 preferential growth of NPs is in the (101) crystallographic plane. The average crystallite size of ZnONPs was calculated to be
172 14.76 nm using Debye-Scherrer equation 9.1 from the peak (101) width as (Prakash *et al.* 2015):

173 $$D = \frac{K\lambda}{\beta_{hkl}\, Cos\, \theta} \quad (9.1)$$

174 where, K is a constant equal to 0.9, λ is the wavelength of the incident X-ray, β is full width half maximum and θ is the Bragg's
175 angle. The calculated size is of an assumed diffracting domain. There exists a strong correlation between c/a ratio and u
176 parameter. As c/a ratio decreases, u value increases in such a way that the tetrahedral distances remain almost constant even
177 though there is distortion in the tetrahedral angles due to long-range polar interaction.
178 The bond length of Zn—O is given by equation 9.2:

179 $$L = [\frac{a^2}{3} + (\frac{1}{2} - u)^2 c^2]^{1/2} \quad (9.2)$$

180 where L is the bond length, a and c are lattice constants and u is the positional parameter in the wurtzite structure which is
181 defined by equation 9.3:

182 $$u = \frac{a^2}{3c^2} + 0.25 \quad (9.3)$$

The calculated Zn-O bond length is 1.959 Å, which is quite close and agrees with the ideal experimental value of 1.977 Å (Bindu and Thomas 2014). The HRTEM image depicts the spherical ZnONPs prepared from the *carica papaya* extract was in the size range of 4 to 8 nm (Figure 9-1B). The morphology in Figure 9-1C only shows the hollow inner tube of CNTs, whereas Figure 9-1D depicts the MWCNTs networks integrated with ZnONPs in a form of hybrid sheets. The strong π–π non-covalent interaction between the tubular structure of MWCNTs and the ZnONPs is driven by the hydrophobic surface thereby playing a crucial role towards the formation of *MWCNTs/ZnONPs* hybrid.

A more detailed analysis of the chemical composition of the *MWCNTs/ZnONPs* on GCE surface and the presence of zinc, oxygen and carbon by elemental mapping was studied with energy dispersive X-ray (EDX) as shown in Figure 9-1E. The presence of high concentration of zinc, oxygen and carbon revealed the uniform distribution of ZnONPs on MWCNTs.

The optical characterization of ZnONPs was recorded on UV-visible spectrophotometer. The UV-visible absorption spectrum with the inset of Tauc plot of ZnONPs synthesized using extract has been depicted in Figure 9-2A and the FTIR spectra of *carica papaya* seed extract and ZnONPs are presented in Figure 9-2B.

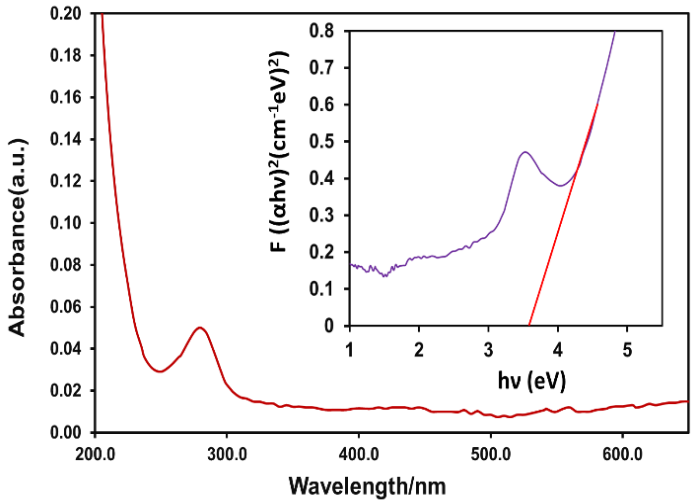

Figure 9-2(A) UV-visible absorption spectrum with the inset of Tauc plot of ZnONPs synthesized using extract

The optical band gap for the ZnONPs was calculated using equation 8.3 the expression proposed by Tauc and Menth (Tauc and Menth 1972). The absorption band of the synthesized ZnONPs was observed at 270.5 nm as compared to the absorption band of bulk ZnO (376 nm)(Debanath and Karmakar 2013). The value of optical band gap calculated using equation 8.3 was found to be 3.49 eV indicating the blue shift as a result of a decrease in particle size and quantum confinement shown in Figure 9-2A. This leads to the considerable change in the properties of NPs. Quantum confinement can be used to modify the band gap and ease charge transfer. It also enhances covalent bonding and electrostatic interaction which aids in the improved sensing of biomolecules (Mondal and Sharma 2016). To comprehend the role of capping agents played by the molecules present in the *carica papaya* seed extract in the synthesis of ZnONPs, FTIR and GC-MS analysis were carried out.

The FTIR shows two spectra; one of the *carica papaya* extract and other of the ZnONPs synthesized using extract. The spectrum of the extract in Figure 9-2B shows a broad peak at 3331 cm^{-1} due to adsorbed water O-H stretching of polyphenols.

The next band at 1639 cm^{-1} corresponds to surface hydroxyl group of H_2O molecule, the slender band at 1454 cm^{-1} due to the presence of tertiary alcohol (C-OH) group. The sharp absorption band at 1113 cm^{-1} represents the C-O stretching vibrations of carboxylic acids (-COOH). The small band at 783 cm^{-1} is due to C-Cl stretching of alkyl halides(Siripireddy and Mandal 2017).

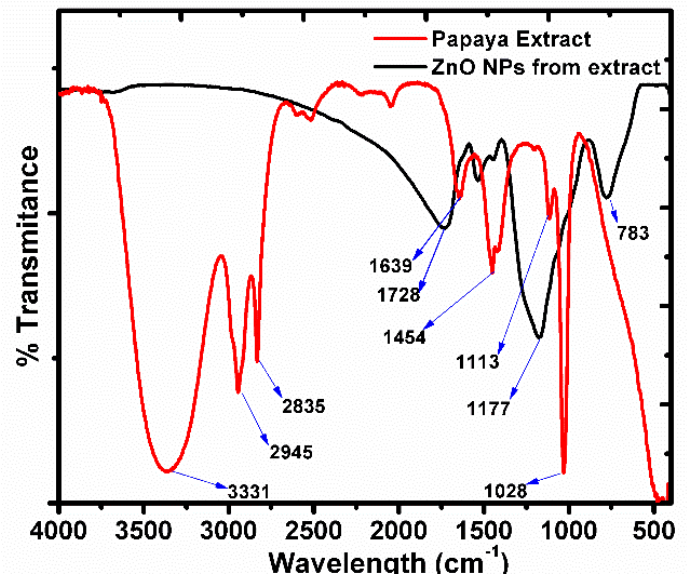

Figure 9-3: (B) FTIR spectra of *carica papaya* seed extract and ZnONPs

GC-MS analysis of the methanolic extract of *carica papaya* seeds was performed to understand which molecules, present in the extract, were responsible for directing the synthesis of ZnONPs

Figure **9-4**(A) GC-MS chromatograms of methanolic extract of *carica papaya* seeds containing (A) palmitic acid.

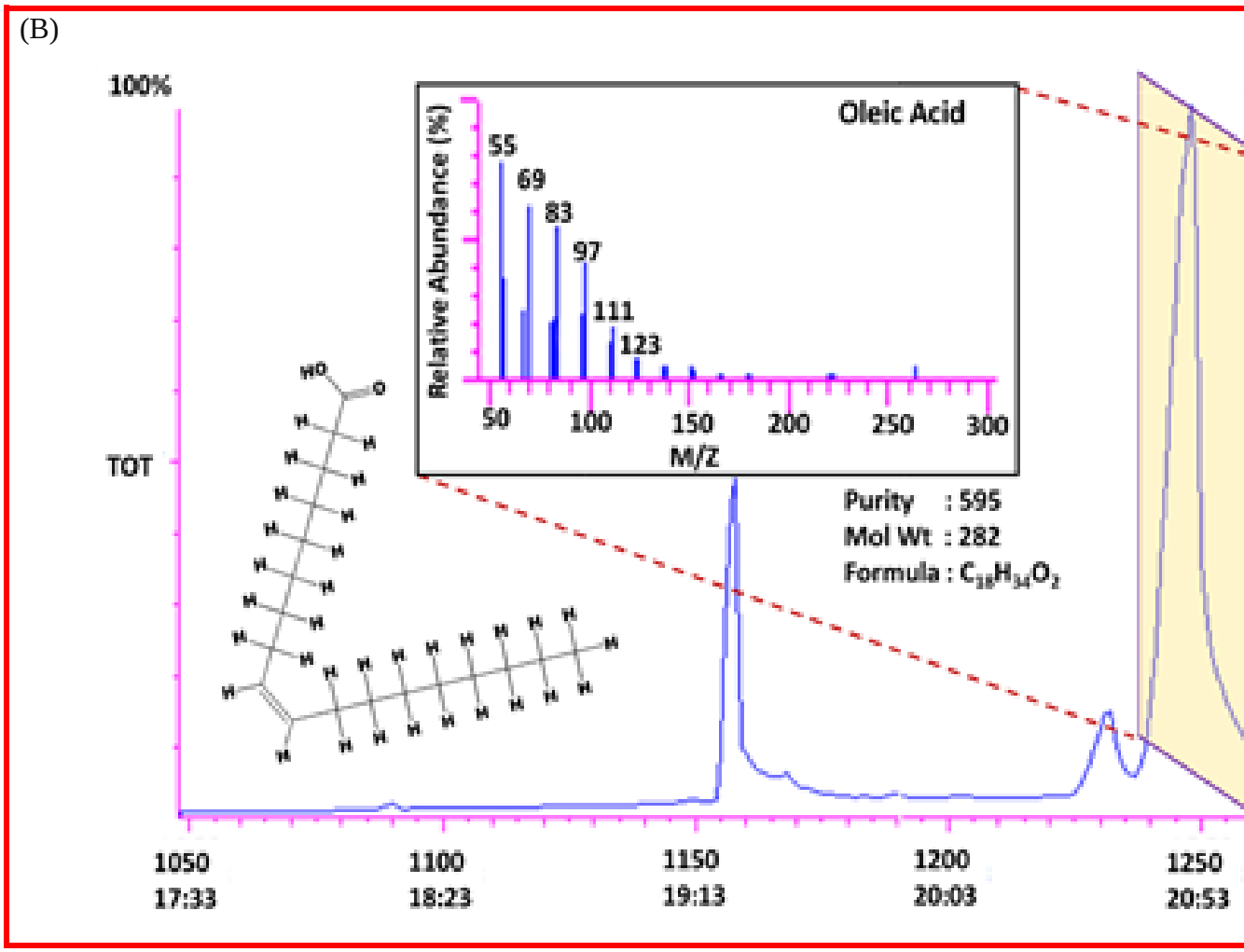

Figure 9-5. Two peaks were considered at different retention times, one at 19:13 min and the other at 20:53 min., since they were of high intensity compared to the other peaks in the GC-MS chromatogram. At the retention time of 19:13 min, palmitic acid was found to be present in major proportion whereas at 20:53 min, oleic acid was found to be in high proportion on the basis of purity fit. Among palmitic acid and oleic acid, it is noted that oleic acid has a purity index of 595 (the number of peaks that match those peaks in the spectrum in NIST library) whereas palmitic acid has purity index of 417. Based on purity index values of oleic acid and palmitic acid, it can be deduced that these two molecules were available to act as capping agents in the synthesis of ZnONPs (Kim *et al.* 2015;

Agrawal *et al.* 2017). The identified components in the methanolic extract of *carica papaya* seed extract have been tabulated in Table 9-2 and Appendix Table A4.

Table 9-2 Components detected in the methanolic seed extract of *carica papaya* by GC-MS.

RT (min)	Name (Molecular Formula)	Structure	Classification (Mol. Wt)
13:32	2-Methylbenzonitrile (C_8H_7N)	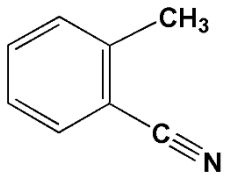	Aromatic nitrile (117)
14:44	4-Benzyloxybenzaldehyde ($C_{18}H_{12}O_2$)	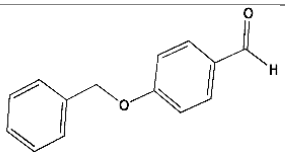	Aromatic aldehyde (212)
16:50	Linoleic acid ($C_{18}H_{32}O_2$)	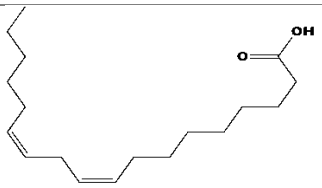	Fatty acid (280)
19:13	Palmitic acid ($C_{16}H_{32}O_2$)	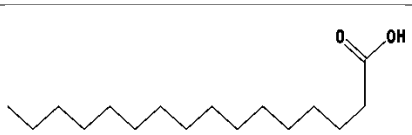	Fatty acid (256)
20:53	Oleic acid ($C_{18}H_{24}O_2$)	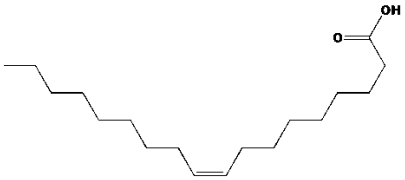	Fatty acid (282)

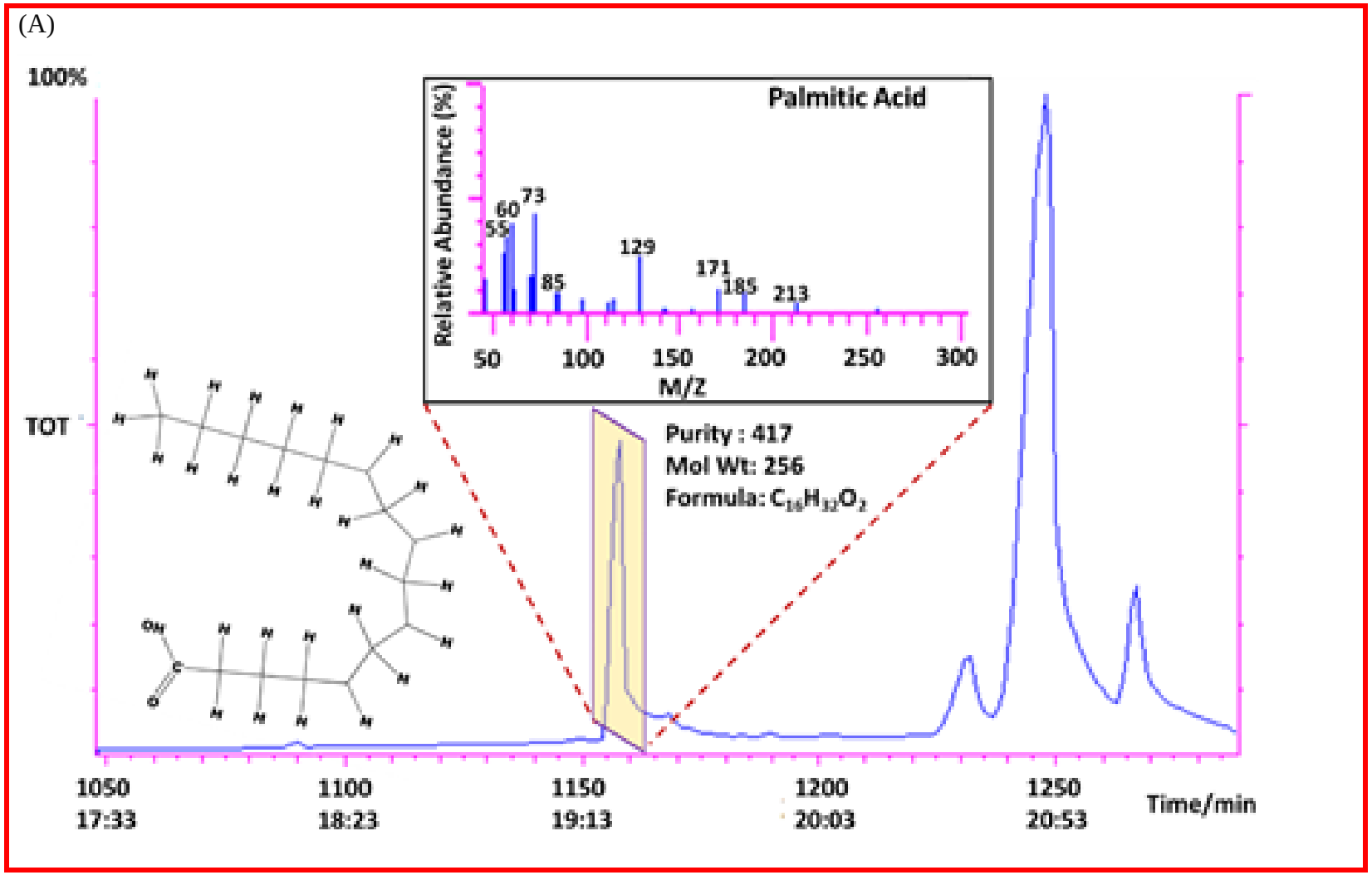

Figure 9-4(A) GC-MS chromatograms of methanolic extract of *carica papaya* seeds containing (A) palmitic acid.

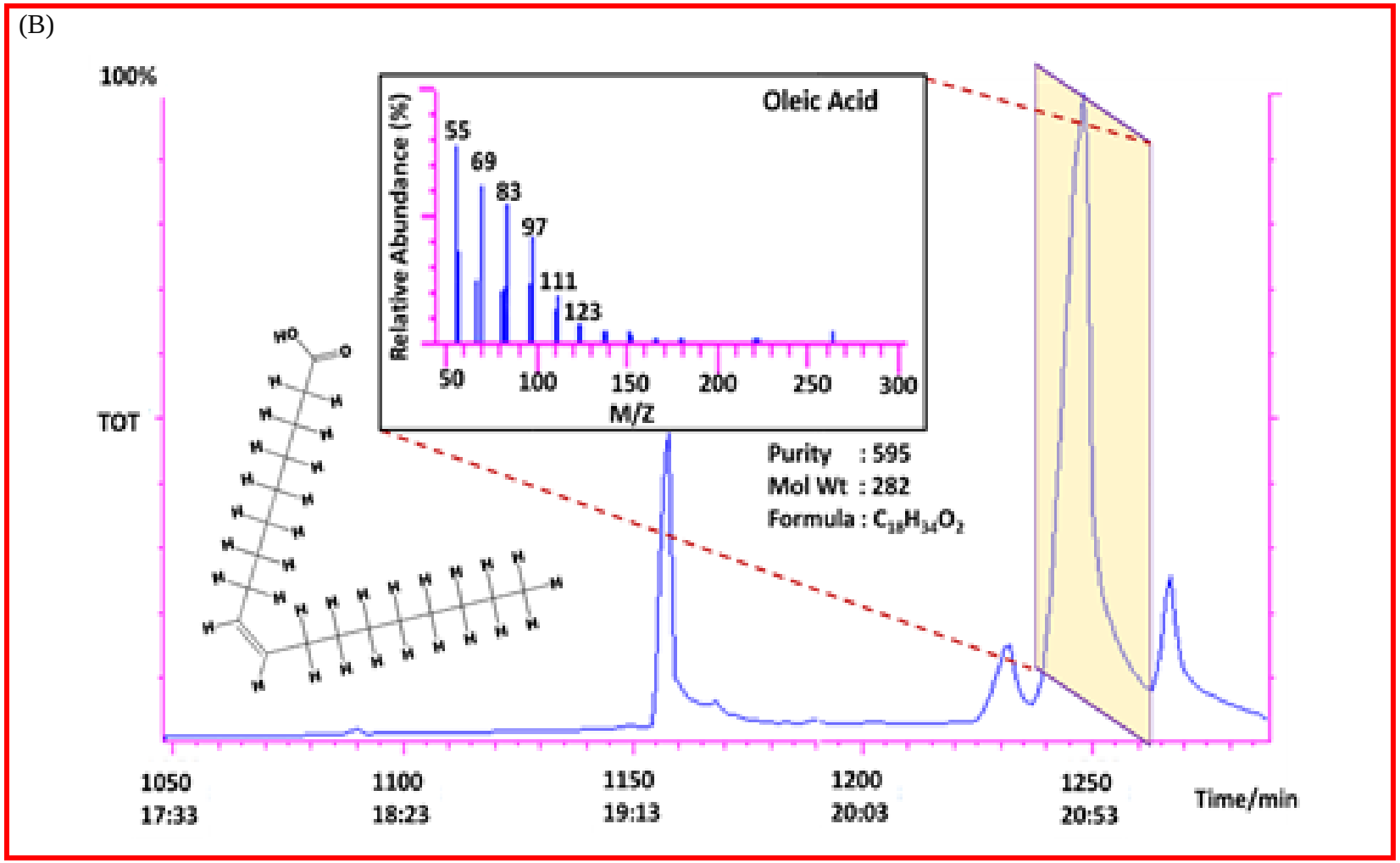

Figure 9-5 (B) GC-MS chromatograms of methanolic extract of *carica papaya* seeds containing oleic acid.

9.1.2 Electrochemical measurements

For electrode modification, the nanocomposite was prepared in a mass by mass ratio of 1:6 (MWCNTs: ZnONPs). The measurements were performed using GCE. The electrolyte used was phosphate buffer prepared by dissolving 0.800 g of NaH_2PO_4 with 5.201 g of Na_2HPO_4 in 500 mL of deionized water.

Silymarin is considered as practically insoluble in water with a poor solubility of 50 µg mL^{-1}, but soluble in ethanol, therefore, the three replicate samples were dissolved in 10 % ethanol (Shakeel *et al.* 2014; Onodera *et al.* 2016). The samples and standards were equilibrated by sonicating for 15 min prior to each measurement during which the potential was recorded at 0.18 ± 0.03 V.

9.2 Results and Discussion

9.2.1 Electrochemical sensing of silymarin

In general, for biosensor purpose, herein specific for the detection of silymarin, GCE is preferred over Au, Pt and other electrodes (Golabi and Noor-Mohammadi 1998). The GCE was modified with *MWCNTs/ZnONPs* composite and employed here as a working electrode for the silymarin sensing using the electroanalytical methods, which are square wave and cyclic voltammetric techniques. For more details, the first step is the evaluation of the voltammograms to identify the appropriate potential for silymarin detection. Afterwards, the identified potential used to measure the potential of various known concentrations of silymarin and plotting a current vs concentration calibration curve. This strategy enables us to determine the concentration of an unknown sample by analyzing the current at the identified potential. In Table 9-3**,** the summary of voltammograms obtained with bare GCE, *GCE/MWCNTs* and *GCE/MWCNTs/ZnONPs* were compared with regards to change in current and potential. Overall there was a significant improvement on the current response when *GCE/MWCNTs/ZnONPs* were used, indicating a much better surface area and electrical conductivity compared to the bare glassy carbon electrode. The MWCNTs also demonstrated to be an effective anchor

for ZnONPs as they possess good electrical conductivity and allows for electron transfer between the analytes and modified electrode surfaces. MWCNTs are essentially very long aspect ratio cylinders composed of layers of carbon atoms, enabling their interaction with surrounding molecules which can potentially translate to strong modulation of electrical conductance of CNTs, resulting in a large relative change in resistance, i.e., high sensitivity (Saleh Ahammad, Lee and Rahman 2009).

Table 9-3: Summary of electrochemical measurements of silymarin using bare GCE, *GCE-MWCNTs*, and *GCE/MWCNTs/ZnONPs*.

Peak	**Parameter**	**GCE**	***GCE/MWCNTs***	***GCE/MWCNTs/ZnONPs***
A1	E_{pa} (mV)	0.19	0.20	0.233
	i_{pa} (µA)	4.20	12.93	123.3
A2	E_{pa} (mV)	-	0.45	0.55
	i_{pa} (µA)	-	5.67	97.12
C1	E_{pc} (mV)	0.021	0.025	0.061
	i_{pc} (µA)	-3.04	-10.7	-112.4

The cyclic voltammogram (Figure 9-6A) showed that *GCE/MWCNTs/ZnONPs* is a suitable nanocomposite electrode to study redox reactions of silymarin molecules, as it is clearly displaying the redox mechanism. The cyclic voltammograms were recorded for the various concentrations ranging from 0.000 to 0.152 mg L^{-1} with an increment of 0.014 mg L^{-1}. For further silymarin sensing, the square wave voltammetry was used in the potential range 0.0 to 0.6 V vs Ag/AgCl.

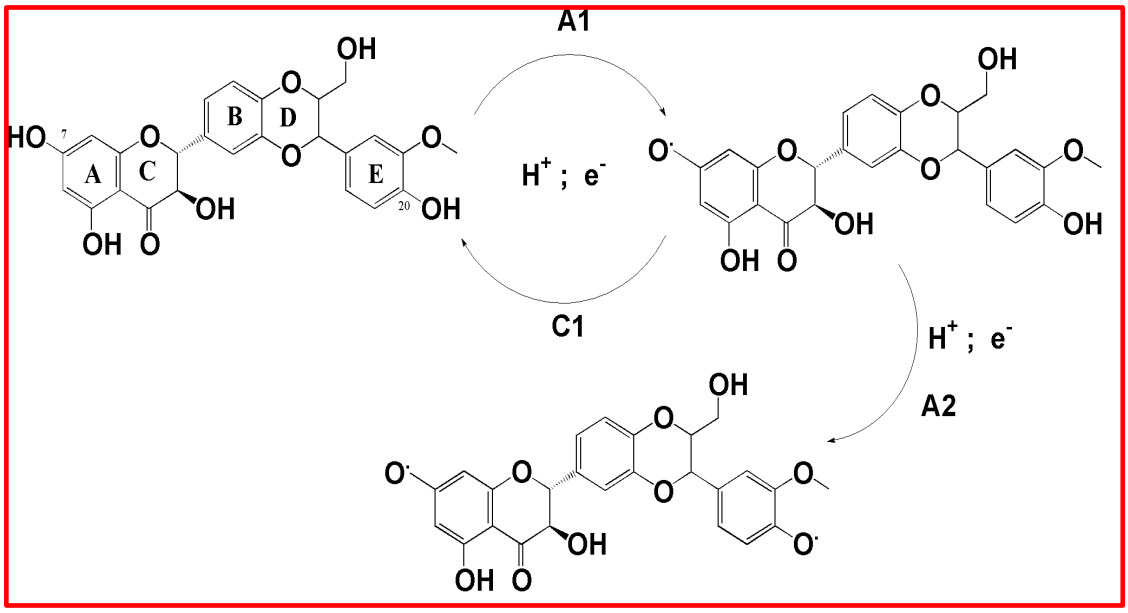

Scheme 9-1: Redox pathway of silymarin

The first oxidation peak A1 at 0.25 V was attributed to oxidation of the resorcinol group (Carbon number 7) *via* the transfer of electrons with the reversibility shown by a cathodic peak (C1) at 0.05 V (Scheme 9-1). The second oxidation peak, A2, at 0.55 V was attributed to the oxidation of *o*-methoxy-phenolic moiety (Carbon number 20) of the E ring of silymarin molecule. Both the oxidation peaks appeared to be stable as the concentration increases (Mpanza *et al.* 2014). In Figure 9-6B, the square wave measurements (SQW) showed a prominent anodic peak at 0.18 V vs Ag/AgCl for the oxidation of silymarin and, this peak becomes significant as the concentration increases from 0.014 to 0.152 mg L^{-1}. In both cyclic voltammograms and SQW the blank has been shown as a black line and it confirms that the redox peaks are arising from silymarin only. The SQW data was used for further calculating the low detection limit of 0.08 mg L^{-1} and linearity of the sensing analysis.

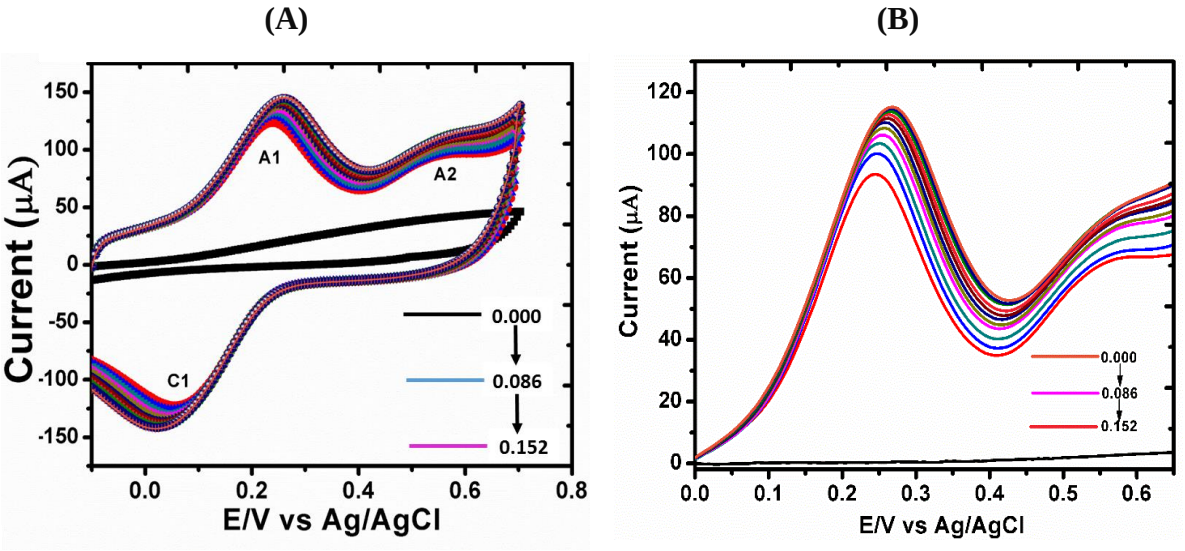

Figure 9-6: (A) Cyclic voltammograms at potential range -0.1 to 0.65 V for the silymarin concentration from 0.000 to 0.152 mg L^{-1} and Sweep rate: 0.02 V s^{-1}. (B) The square wave voltammogram showing change in current response for the silymarin concentration from 0.000 to 0.152 mg L^{-1} under measurement conditions: potential range 0.0 to 0.60 V, voltage step: 0.008 V; amplitude: 0.002 V; frequency: 5.000 Hz; sweep rate: 0.038 V s^{-1}

9.2.2 Optimization of pH and scan rate based on peak currents

Using the *GCE/MWCNTs/ZnONPs*, the impact of the change in pH in the detection of silymarin was evaluated from 2.5 to 8.0. The highest current response was obtained at pH 7.6 for the quantification of peak A1 and therefore, regarded as the optimum. Beyond pH 7.6 the current density corresponding to Cl dropped significantly indicating that the redox mechanisms corresponding to the resveratrol were not favored. With regards to the scan rate from 0.1 to 1.0 V s^{-1}, there was a steady improvement in the current response for silymarin in 0.1 M phosphate buffer of pH 7.6. The scan rate of 0.8 mV s^{-1}, was selected as optimum for *GCE/MWCNTs/ZnONPs* showing 123.3, 97.12 and 112.4 µA for peaks A1, A2 and C1, respectively. This was an indication of good catalytic activity of the *GCE/MWCNTs/ZnONPs.*

9.2.3 Reproducibility and repeatability of *GCE/MWCNTs/ZnONPs*

The reproducibility and repeatability of the *GCE/MWCNTs/ZnONPs* were determined. To examine the reproducibility of the developed technique, under the same conditions, three fabricated electrochemical sensors independently studied in a 0.2 mM silymarin solution. The electrodes of Pt, GC and Au, were functionalised with the composite of MWCNTs /ZnONPs by casting 40 µl dispersed in DMSO followed by oven drying at 60 ^{o}C for 20 min. The obtained RSD value of 1.92 % (n = 6) indicates that the results were reproducible using *GCE/MWCNTs/ZnONPs*. The repeatability was also investigated for 0.1 mg L^{-1} silymarin, using the same electrochemical sensor. The calculated RSD was found to be 2.31 % (n = 6). This shows the fair repeatability with *GCE/MWCNTs/ZnONPs* for silymarin detection in Milk Thistle tablets. The saturation point of the electrode was tested by doing 20 measurements of electrodes in comparison to other electrodes modified with the same nanocomposite. Using each electrode a standard solution of silymarin was electrochemically measured in triplicate with 10 additions and it was found that the current signal was decreasing in the following order Au> Pt> GCE. Although the electrodes have their linearity ranges the limits of detection (LODs) varied 28.6 µg L^{-1}, 22.1 µg L^{-1} and 14.8 µg L^{-1} for Au, Pt and GCE respectively. The results in Figure 9-7A depicts that all the electrodes show a non-linear fit in the following order GCE>Au>Pt. It was interesting to observe that Au electrode was more sensitive at low concentration; however it was susceptible to saturation in contrast to GCE. Overall all the electrodes were reusable after modification with the composite, the electrode were sonicated in DMSO to allow auto detachment of nanocomposite on the surface of the electrode. Based on the observation in Figure 9-7A- GCE was selected as the best electrode for the rest of the measurements. It reproducibility – Figure 9-7B was measured with five replicates for each of the seven modifications. The average current recorded with 0.117 mg L^{-1} was 3.98 ± 0.13 µA. Interestingly, for the measurements, the standard deviation was within 0.15 to 0.21 µA. This was a clear indication that GCE modified with *MWCNTs/ZnONPs* is suitable for redox evaluation of sylibins.

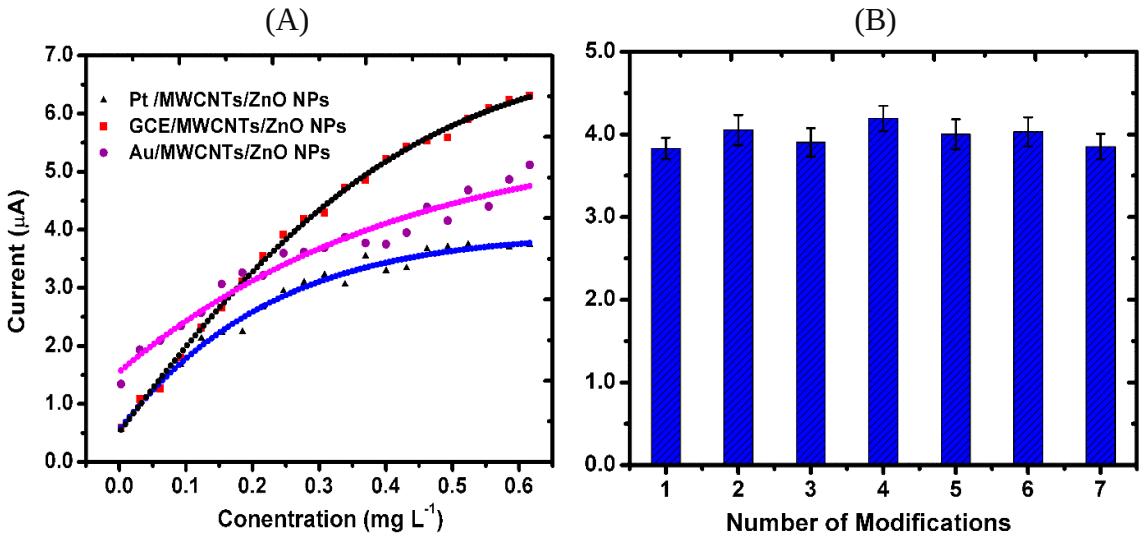

Figure 9-7: (A) Comparison of the three electrodes – Pt, GC and Au- modified with MWCNTs/ZnONPs composites. (B) GCE tested repeatability of 2.5 ppm for n = 7 using SQV method under conditions: voltage step: 0.008 V; amplitude: 0.002 V; frequency: 5.000 Hz; sweep rate: 0.038 V

9.2.4 Effect of interferences and selectivity on detection of silymarin

The selectivity of the present electrochemical sensor towards silymarin was evaluated by the simultaneous addition of some common organic and inorganic compounds. The interferents such as catechol (0.05 µg mL^{-1}) and their derivatives (urushiol, catecholamine, catechin) (0.05 µg mL^{-1}), 4-chlorophenol (0.05 µg mL^{-1}), dichlorophenol (0.05 µg mL^{-1}), trichlorophenol (0.05 µg mL^{-1}), pentachlorophenol (0.05 µg mL^{-1}), Na^{+} (0.05 µg mL^{-1}), Mg^{2+} (0.05 µg mL^{-1}), and K^{+} (0.05 µg mL^{-1}) were added to 0.15 µg mL^{-1} of standard silymarin solution and then current responses were measured. The obtained results revealed that there were no changes in the current response. The applied tolerance limit for the interference species at the maximum concentration resulted in a relative error of ±5%. However, 25-fold catechol derivatives and 10-fold 4-cholorophenol, dichlorophenol, trichlorophenol, pentachlorophenol, Na^{+}, Mg^{2+} and K^{+} had no effect on the detection of silymarin. Therefore, our results indicate that the developed electrochemical sensor, *GCE/MWCNTs/ZnONPs* has an excellent selectivity

for the detection of silymarin. The stability of the electrochemical sensor was evaluated by monitoring the current responses in 0.10 mg L^{-1} silymarin over a range of ten runs for three hours using the same coating, rinsing with de ionized water in between the measurements. The electrochemical sensor maintained 85.0 % of the original response, suggesting that the sensor retained its activity. The percentage recoveries of silymarin from the designed electrochemical sensor ranged from 85.0 to 98.30 %.

9.2.5 Analysis of calibration curve

Due to the appearance of the maximum oxidation peak around 0.18 V within the considered concentration range (Figure 9-6B), this potential was used for plotting the current vs concentration calibration curve. The calibration curve in the plot of current at 0.18 V versus concentration ranging from 0.014 to 0.152 mg L^{-1} is presented in Figure 9-8**.** The plot was further divided into three sections to identify the most linear part of the curve. The first calibration with five measurements data (N) gave regression equation of $I_p = 54.34 \pm 2.6C_i + 0.26 \pm 0.1\ \mu A$ with an R^2 of 0.9988 (part A in Figure 9-8) found to be the most linear followed by the second calibration with regression equation of $I_p = 23.38 \pm 1.4C_i + 2.41 \pm 0.1\ \mu A$ with an R^2 of 0.9854 (part B in Figure 9-8) while part C had $R^2 = 0.9517$.

Overall, in Figure 9-8**,** there is an increase in current with the increase in the whole concentration range from 0.015 to 0.137 mg L^{-1} and there is a convergence of current at the high concentration range from 0.137 to 0.15 mg L^{-1}. This is due to the fact that as the concentration of the analyte increases, the electrodes lose redox capability as a result of saturation of analyte on its surface (Thabani *et al.* 2014).

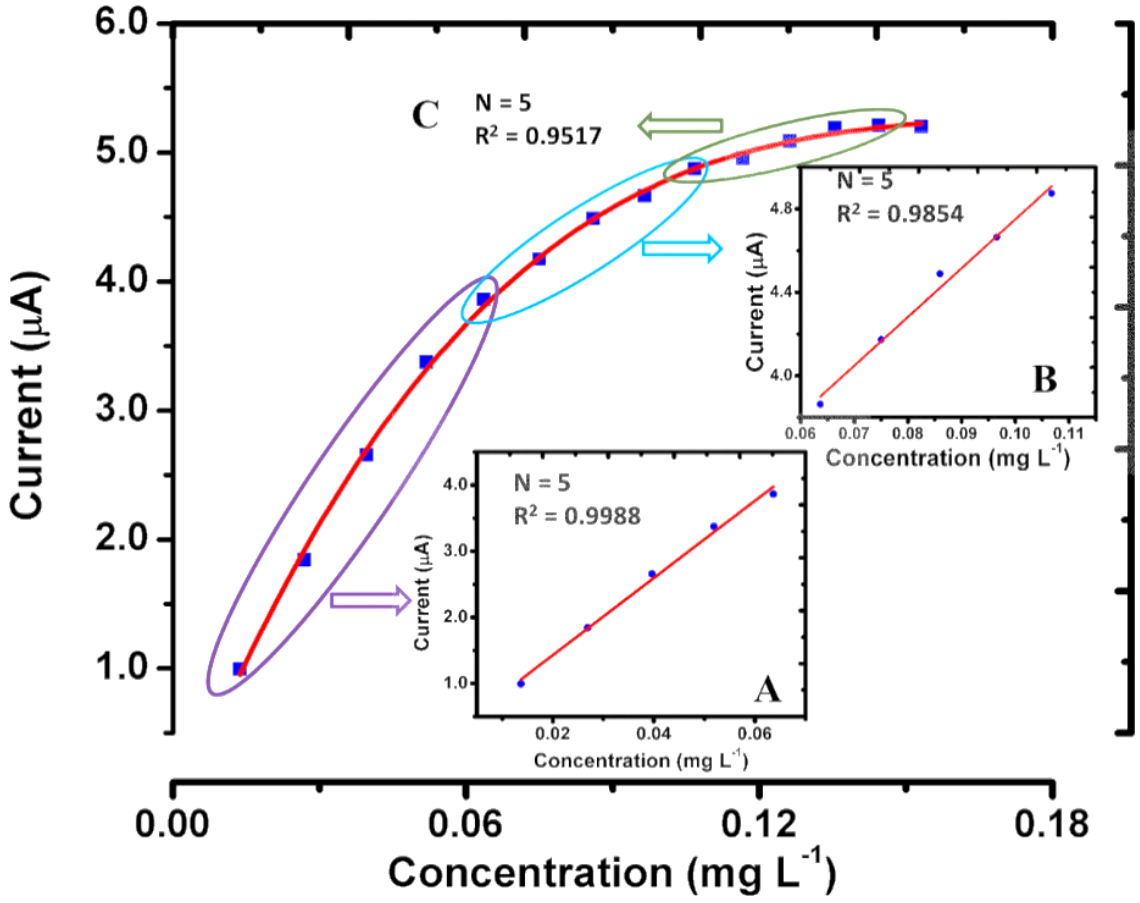

Figure 9-8: Calibration plot of current at 0.18 V against concentration ranging from 0.014 to 0.152 mg L^{-1}; Inset A depicts the first linear portion and the inset B is second linear portion

9.2.6 Commercial sample analysis

The crucial application of this work is to extend the implemented strategy towards analysis of silymarin concentration in commercial samples; namely, Milk Thistle tablet (GNC Herbal Plus, 160 mg of silymarin) samples. The tablet sample was finely ground and, thereafter, the accurately weighed 33.8 mg was dissolved in 50 mL of a 20% methanol solution. From the prepared sample solution, 2.5 µL was added into the electrochemical cell containing 30 mL of a buffer; this provides an equivalent concentration of 0.081 mg

L^{-1}. After electrochemical measurements, a current of 3.77 µA, corresponding to 0.062 mg L^{-1} concentration of silymarin was found using the calibration curve (Figure 9-8). We found 122 mg silymarin in the 160 mg quoted concentration of silymarin in the commercial Milk Thistle tablet, which is approximately 76% efficiency of detection using the developed MWCNTs/ZnONPs composite.

The efficiency of the method has been ascertained by comparing the results obtained from the applied SQW method and HPLC method reported in the literature. The data is presented in Table 9-4 below:

Table 9-4: Comparison of applied SQW method and HPLC method reported in literature

Analytical Parameters	**Applied SQW Method**	**HPLC Method (from literature)**	
Mean ± standard error	0.199	0.294	(Korany *et al.* 2017)
RSD%	1.92 (n=6)	0.665	(Korany *et al.* 2017)
R^2	0.9985	0.8919	(Kvasnička *et al.* 2003)
Recoveries	85-98.30%	99.58-100.20%	(Korany *et al.* 2017)

Since, concentration values lead to the calibration plot, R^2 values, recoveries and standard errors, we have chosen to compare the applied method with the reported HPLC method in the literature. The standard deviation error is less in the applied method, however, R^2 (linearity) is good in the applied SQW method in comparison to HPLC method. The R^2 value is one of the key parameters to predict the linear dynamic range within the concentration limits.

The percentage of recoveries are slightly lower compared to HPLC method as these values depend on the sample in which the content of silymarin varies. Therefore, it can be

concluded that the applied SQW method is comparable with the HPLC method reported in the literature.

9.3 Conclusions

We have reported a systematic eco-friendly protocol to produce oleic acid-stabilized ZnONPs using *carica papaya* seeds extract. This study proves that *carica papaya* seeds extract have the capacity to reduce zinc gluconate into ZnONPs and have advantages over other extracts since this fruit is easily available all over the world. The synthesized ZnONPs were integrated onto the MWCNTs to sense silymarin. The results showed that the current signals obtained from *GCE/MWCNT/ZnONPs* were 2-fold higher than *GCE/MWCNTs*. Therefore, these particles are expected to have extensive applications in the field of sensors. The present study gives an insight into the interaction of NPs with drug molecules and also the enhancement of electrochemical detection of the silymarin by the ZnONPs. The integration of experimental and computational results has not only helped to understand sensing at the molecular level but it can lead to the feasible design and optimization of methods based on the sensing of biomolecules in the presence of nanoparticles.

CHAPTER 10

10 Concluding remarks

The literature survey and the results from the case studies described in preceding chapters of this work, highlights the potential of using metal nanoparticles in various fields emphasizing an increasing need to produce them on an industrial scale and in stable formulations with environmentally friendly processes. Ultimately there are many efforts being made towards exploiting natural resources and implementing biological synthesis methods with proven advantages, such as being environmentally friendly, easy to scale up, and cost-effectiveness. The green production of nanoparticles using biological resources has also demonstrated great potential. The plants that have been successfully used for the biological synthesis of metal nanoparticles prompts the deeper exploration of biological nanofactories to meet the need for nanoproducts in various fields. Furthermore, the lack of knowledge of the chemical components responsible and the underlying mechanisms for the synthesis, action, and stabilization of biological nanoparticles, remain open challenges in taking advantage of plants and microorganisms for nanoparticle synthesis. The exact mechanism and the components responsible for plant-mediated synthetic nanoparticles remain to be elucidated. The colorimetric review revealed that there are much literature reports on the nanoparticles, specifically with functionalized colorimetric aptasensors. However the key challenge to their successful application is in transforming the aptamer-binding events into physically detectable signals.

CHAPTER 11

11 REFERENCES

Abdul Rahman, S., Saadun, R., Azmi, N. E., Ariffin, N., Abdullah, J., Yusof, N. A., Sidek, H. and Hajian, R. 2014. Label-Free Dengue Detection Utilizing PNA/DNA Hybridization Based on the Aggregation Process of Unmodified Gold Nanoparticles. *Journal of Nanomaterials*, 2014: 5.

Agrawal, N., Munjal, S., Ansari, Mohd Z. and Khare, N. 2017. Superhydrophobic palmitic acid modified ZnO nanoparticles. *Ceramics International*, 43 (16): 14271-14276.

Aherne, D., Ledwith, D. M., Gara, M. and Kelly, J. M. 2008. Optical Properties and Growth Aspects of Silver Nanoprisms Produced by a Highly Reproducible and Rapid Synthesis at Room Temperature. *Advanced Functional Materials*, 18 (14): 2005-2016.

Ahmed, M. H., Keyes, T. E., Byrne, J. A., Blackledge, C. W. and Hamilton, J. W. 2011. Adsorption and photocatalytic degradation of human serum albumin on TiO_2 and Ag–TiO_2 films. *Journal of Photochemistry and Photobiology A: Chemistry*, 222 (1): 123-131.

Ahmed, S., Annu, Manzoor, K. and Ikram, S. 2016a. Synthesis of Silver Nanoparticles Using Leaf Extract of Crotolaria retusa as Antimicrobial Green Catalyst. *Journal of Bionanoscience*, 10 (4): 282-287.

Ahmed, S., Annu, Zafeer, I. and Ikram, S. 2016b. One-Step Method for Formation of Silver Nanoparticles Using Withania somnifera Extract for Antimicrobial Activities. *Journal of Bionanoscience*, 10 (1): 47-53.

References

----------*o0o*----------

Ajitha, B., Kumar Reddy, Y. A., Reddy, P. S., Jeon, H.-J. and Ahn, C. W. 2016. Role of capping agents in controlling silver nanoparticles size, antibacterial activity and potential application as optical hydrogen peroxide sensor. *RSC Advances*, 6 (42): 36171-36179.

Akhil, K., Jayakumar, J., Gayathri, G. and Khan, S. S. 2016. Effect of various capping agents on photocatalytic, antibacterial and antibiofilm activities of ZnO nanoparticles. *Journal of Photochemistry and Photobiology B: Biology*, 160: 32-42.

Ali, M. S., Altaf, M. and Al-Lohedan, H. A. 2017. Green Synthesis of Biogenic Silver Nanoparticles Using Solanum Tuberosum Extract and Their Interaction With Human Serum Albumin: Evidence of "Corona" Formation Through a Multi-Spectroscopic and Molecular Docking Analysis. *J Photochem Photobiol B*, 173: 108-119.

Ambika, S. and Sundrarajan, M. 2015. Green biosynthesis of ZnO nanoparticles using Vitex negundo L. extract: Spectroscopic investigation of interaction between ZnO nanoparticles and human serum albumin. *Journal of Photochemistry and Photobiology B: Biology*, 149: 143-148.

Andrey, B., Arne, B., Alexander, W. and Andreas, W. 2014. Fabrication of ZnO Nanostructures. In: *Zinc Oxide Nanostructures*. Pan Stanford Publishing, 1-42. Available: http://dx.doi.org/10.1201/b15661-2 (Accessed 2015/10/13).

Antoine, T., Mishra, Y. K., Trigilio, J., Tiwari, V., Adelung, R. and Shukla, D. 2012. Prophylactic, therapeutic and neutralizing effects of zinc oxide tetrapod structures against herpes simplex virus type-2 infection. *Antiviral research*, 96 (3): 363-375.

Aryal, S., B.K.C, R., Dharmaraj, N., Bhattarai, N., Kim, C. H. and Kim, H. Y. 2006. Spectroscopic identification of SAu interaction in cysteine capped gold

nanoparticles. *Spectrochimica Acta Part A: Molecular and Biomolecular Spectroscopy*, 63 (1): 160-163.

Atarod, M., Nasrollahzadeh, M. and Sajadi, S. M. 2015. Green synthesis of a Cu/reduced graphene oxide/Fe3O4 nanocomposite using Euphorbia wallichii leaf extract and its application as a recyclable and heterogeneous catalyst for the reduction of 4-nitrophenol and rhodamine B. *RSC Advances*, 5 (111): 91532-91543.

Athilakshmi, J., Mohan, M. and Chand, D. K. 2013. Selective detection of cysteine/cystine using silver nanoparticles. *Tetrahedron Letters*, 54 (5): 427-430.

Baghizadeh, A., Ranjbar, S., Gupta, V. K., Asif, M., Pourseyedi, S., Karimi, M. J. and Mohammadinejad, R. 2015. Green synthesis of silver nanoparticles using seed extract of Calendula officinalis in liquid phase. *Journal of Molecular Liquids*, 207: 159-163.

Bai, X., Li, L., Liu, H., Tan, L., Liu, T. and Meng, X. 2015. Solvothermal Synthesis of ZnO Nanoparticles and Anti-Infection Application in Vivo. *ACS Applied Materials & Interfaces*, 7 (2): 1308-1317.

Balgobind, K., Kanchi, S., Sharma, D., Bisetty, K. and Sabela, M. I. 2016. Hybrid of ZnONPs/MWCNTs for electrochemical detection of aspartame in food and beverage samples. *Journal of Electroanalytical Chemistry*, 774: 51-57.

Balwe, S. G., Shinde, V. V., Rokade, A. A., Park, S. S. and Jeong, Y. T. 2017. Green synthesis and characterization of silver nanoparticles from extract of plant Radix Puerariae: An efficient and recyclable catalyst for the construction of pyrimido[1,2-b]indazole derivatives under solvent-free conditions. *Catalysis Communications*, 99: 121-126.

References

----------o0o----------

Banerjee, V. and Das, K. P. 2013. Interaction of silver nanoparticles with proteins: A characteristic protein concentration dependent profile of SPR signal. *Colloids and Surfaces B: Biointerfaces*, 111 (0): 71-79.

Baron, R., Zayats, M. and Willner, I. 2005. Dopamine-, l-DOPA-, Adrenaline-, and Noradrenaline-Induced Growth of Au Nanoparticles: Assays for the Detection of Neurotransmitters and of Tyrosinase Activity. *Analytical Chemistry*, 77 (6): 1566-1571.

Barth, U. v. and Hedin, L. 1972. A local exchange-correlation potential for the spin polarized case. i. *Journal of Physics C: Solid State Physics*, 5 (13): 1629.

Barui, A. K., Veeriah, V., Mukherjee, S., Manna, J., Patel, A. K., Patra, S., Pal, K., Murali, S., Rana, R. K., Chatterjee, S. and Patra, C. R. 2012. Zinc oxide nanoflowers make new blood vessels. *Nanoscale*, 4 (24): 7861-7869.

Baruwati, B., Polshettiwar, V. and Varma, R. S. 2010. Chapter 7 Microwave-assisted Synthesis of Nanomaterials in Aqueous Media. In: *Aqueous Microwave Assisted Chemistry*. The Royal Society of Chemistry, 176-216. Available: http://dx.doi.org/10.1039/9781849730990-00176 (Accessed

Basu, S., Jana, S., Pande, S. and Pal, T. 2008. Interaction of DNA bases with silver nanoparticles: Assembly quantified through SPRS and SERS. *Journal of Colloid and Interface Science*, 321 (2): 288-293.

Becke, A. D. 1988. A multicenter numerical integration scheme for polyatomic molecules. *The Journal of Chemical Physics*, 88 (4): 2547-2553.

Bhattacharjee, A., Ahmaruzzaman, M. and Sinha, T. 2014. Surfactant effects on the synthesis of durable tin-oxide nanoparticles and its exploitation as a recyclable

catalyst for the elimination of toxic dye: a green and efficient approach for wastewater treatment. *RSC Advances*, 4 (93): 51418-51429.

Bhosale, M. A., Chenna, D. R., Ahire, J. P. and Bhanage, B. M. 2015. Morphological study of microwave-assisted facile synthesis of gold nanoflowers/nanoparticles in aqueous medium and their catalytic application for reduction of p-nitrophenol to p-aminophenol. *RSC Advances*, 5 (65): 52817-52823.

Bilecka, I., Elser, P. and Niederberger, M. 2009. Kinetic and Thermodynamic Aspects in the Microwave-Assisted Synthesis of ZnO Nanoparticles in Benzyl Alcohol. *ACS Nano*, 3 (2): 467-477.

Bindu, P. and Thomas, S. 2014. Estimation of lattice strain in ZnO nanoparticles: X-ray peak profile analysis. *Journal of Theoretical and Applied Physics*, 8 (4): 123-134.

Bouhekka, A. and Bürgi, T. 2012. In situ ATR-IR spectroscopy study of adsorbed protein: Visible light denaturation of bovine serum albumin on TiO_2. *Applied Surface Science*, 261 (0): 369-374.

Brooks, B. R., Bruccoleri, R. E., Olafson, B. D., States, D. J., Swaminathan, S. and Karplus, M. 1983. CHARMM: A program for macromolecular energy, minimization, and dynamics calculations. *Journal of Computational Chemistry*, 4 (2): 187-217.

Brooks, B. R., Laidig, W. D., Saxe, P., Goddard, J. D., Yamaguchi, Y. and III, H. F. S. 1980. Analytic gradients from correlated wave functions via the two-particle density matrix and the unitary group approach. *The Journal of Chemical Physics*, 72 (8): 4652-4653.

References

----------o0o----------

Bunte, S. W. and Sun, H. 2000. Molecular Modeling of Energetic Materials: The Parameterization and Validation of Nitrate Esters in the COMPASS Force Field. *The Journal of Physical Chemistry B*, 104 (11): 2477-2489.

Cao, R., Li, B., Zhang, Y. and Zhang, Z. 2011. Naked-eye sensitive detection of nuclease activity using positively-charged gold nanoparticles as colorimetric probes. *Chemical Communications*, 47 (45): 12301-12303.

Cao, Y. C., Jin, R., Thaxton, C. S. and Mirkin, C. A. 2005. A two-color-change, nanoparticle-based method for DNA detection. *Talanta*, 67 (3): 449-455.

Catauro, M., Bollino, F., Papale, F., Marciano, S. and Pacifico, S. 2015. TiO_2/PCL hybrid materials synthesized via sol–gel technique for biomedical applications. *Materials Science and Engineering: C*, 47: 135-141.

Chang, J. and Waclawik, E. R. 2014. Colloidal semiconductor nanocrystals: controlled synthesis and surface chemistry in organic media. *RSC Advances*, 4 (45): 23505-23527.

Chen, A., Jiang, X., Zhang, W., Chen, G., Zhao, Y., Tunio, T. M., Liu, J., Lv, Z., Li, C. and Yang, S. 2013. High sensitive rapid visual detection of sulfadimethoxine by label-freeaptasensor. *Biosensors and Bioelectronics*, 42 (0): 419-425.

Chen, C.-K., Huang, C.-C. and Chang, H.-T. 2010. Label-free colorimetric detection of picomolar thrombin in blood plasma using a gold nanoparticle-based assay. *Biosensors and Bioelectronics*, 25 (8): 1922-1927.

Chen, S., Gao, H., Shen, W., Lu, C. and Yuan, Q. 2014. Colorimetric detection of cysteine using noncrosslinking aggregation of fluorosurfactant-capped silver nanoparticles. *Sensors and Actuators B: Chemical*, 190 (0): 673-678.

Chen, Y.-M., Yu, C.-J., Cheng, T.-L. and Tseng, W.-L. 2008. Colorimetric Detection of Lysozyme Based on Electrostatic Interaction with Human Serum Albumin-Modified Gold Nanoparticles. *Langmuir*, 24 (7): 3654-3660.

Chen, Z., Luo, S., Liu, C. and Cai, Q. 2009. Simple and sensitive colorimetric detection of cysteine based on ssDNA-stabilized gold nanoparticles. *Analytical and Bioanalytical Chemistry*, 395 (2): 489-494.

Chen, Z., Zhang, C., Zhou, T. and Ma, H. 2015. Gold nanoparticle based colorimetric probe for dopamine detection based on the interaction between dopamine and melamine. *Microchimica Acta*, 182 (5-6): 1003-1008.

Choi, Y., Ho, N.-H. and Tung, C.-H. 2007. Sensing Phosphatase Activity by Using Gold Nanoparticles. *Angewandte Chemie International Edition*, 46 (5): 707-709.

Chuang, Y.-J., Zhou, X., Pan, Z. and Turchi, C. 2009. A convenient method for synthesis of glyconanoparticles for colorimetric measuring carbohydrate–protein interactions. *Biochemical and Biophysical Research Communications*, 389 (1): 22-27.

Crookes-Goodson, W. J., Slocik, J. M. and Naik, R. R. 2008. Bio-directed synthesis and assembly of nanomaterials. *Chemical Society Reviews*, 37 (11): 2403-2412.

Debanath, M. K. and Karmakar, S. 2013. Study of blueshift of optical band gap in zinc oxide (ZnO) nanoparticles prepared by low-temperature wet chemical method. *Materials Letters*, 111: 116-119.

Dewar, M. J. S. 1983. Development and status of MINDO/3 and MNDO. *Journal of Molecular Structure*, 100: 41-50.

Dinesh, V. P., Biji, P., Ashok, A., Dhara, S. K., Kamruddin, M., Tyagi, A. K. and Raj, B. 2014. Plasmon-mediated, highly enhanced photocatalytic degradation of industrial

textile dyes using hybrid ZnO@Ag core-shell nanorods. *RSC Advances*, 4 (103): 58930-58940.

Dutta, P. P., Bordoloi, M., Gogoi, K., Roy, S., Narzary, B., Bhattacharyya, D. R., Mohapatra, P. K. and Mazumder, B. 2017. Antimalarial silver and gold nanoparticles: Green synthesis, characterization and in vitro study. *Biomedicine & Pharmacotherapy*, 91: 567-580.

Edeoga, H. O., Okwu, D. E. and Mbaebie, B. O. 2005. Phytochemical constituents of some Nigerian medicinal plants. *African Journal of Biotechology*, 4 (7): 685-688

Edison, T. N. J. I., Lee, Y. R. and Sethuraman, M. G. 2016. Green synthesis of silver nanoparticles using Terminalia cuneata and its catalytic action in reduction of direct yellow-12 dye. *Spectrochimica Acta Part A: Molecular and Biomolecular Spectroscopy*, 161: 122-129.

Elghanian, R., Storhoff, J. J., Mucic, R. C., Letsinger, R. L. and Mirkin, C. A. 1997. Selective Colorimetric Detection of Polynucleotides Based on the Distance-Dependent Optical Properties of Gold Nanoparticles. *Science*, 277 (5329): 1078-1081.

Ermer, O. 1976. Calculation of molecular properties using force fields. Applications in organic chemistry. In: Proceedings of *Bonding forces*. Berlin, Heidelberg, 1976//. Springer Berlin Heidelberg, 161-211.

Evans, W. C., Evans, D. and Trease, G. E. 2002. *Trease and Evans' pharmacognosy*. Edinburgh; New York: WB Saunders.

Famulok, M. and Mayer, G. 2006. Chemical biology: Aptamers in nanoland. *Nature*, 439 (7077): 666-669.

Fatimah, I. 2016. Green synthesis of silver nanoparticles using extract of Parkia speciosa Hassk pods assisted by microwave irradiation. *Journal of Advanced Research*, 7 (6): 961-969.

Feng, J.-J., Guo, H., Li, Y.-F., Wang, Y.-H., Chen, W.-Y. and Wang, A.-J. 2013. Single molecular functionalized gold nanoparticles for hydrogen-bonding recognition and colorimetric detection of dopamine with high sensitivity and selectivity. *ACS Applied Materials & Interfaces*, 5 (4): 1226-1231.

Gade, A. K., Bonde, P., Ingle, A. P., Marcato, P. D., Durán, N. and Rai, M. K. 2008. Exploitation of Aspergillus niger for Synthesis of Silver Nanoparticles. *Journal of Biobased Materials and Bioenergy*, 2 (3): 243-247.

Gairola, S., Naidoo, Y., Bhatt, A. and Nicholas, A. 2009. An investigation of the foliar trichomes of Tetradenia riparia (Hochst.) Codd [Lamiaceae]: An important medicinal plant of Southern Africa. *Flora - Morphology, Distribution, Functional Ecology of Plants*, 204 (4): 325-330.

Gallucci, M. N., Fraire, J. C., Maillard, A. P. V. F., Páez, P. L., Martínez, I. M. A., Miner, E. V. P., Coronado, E. A. and Dalmasso, P. R. 2017. Silver nanoparticles from leafy green extract of Belgian endive (Cichorium intybus L. var. sativus): Biosynthesis, characterization, and antibacterial activity. *Materials Letters*, 197: 98-101.

Gan, P. P., Ng, S. H., Huang, Y. and Li, S. F. 2012. Green synthesis of gold nanoparticles using palm oil mill effluent (POME): a low-cost and eco-friendly viable approach. *Bioresource Technology*, 113: 132-135.

Gao, H., Shen, W., Lu, C., Liang, H. and Yuan, Q. 2013. Surface plasmon resonance additivity of gold nanoparticles for colorimetric identification of cysteine and homocysteine in biological fluids. *Talanta*, 115 (0): 1-5.

References

----------*o0o*----------

Germain, V., Brioude, A., Ingert, D. and Pileni, M. P. 2005. Silver nanodisks: Size selection via centrifugation and optical properties. *Journal of Chemical Physics*, 122 (12): 124707.

Ghasemi, F., Hormozi-Nezhad, M. R. and Mahmoudi, M. A Colorimetric Sensor Array for Detection and Discrimination of Biothiols based on Aggregation of Gold Nanoparticles. *Analytica Chimica Acta*, (882): 58–67.

Ghasemi, F., Hormozi-Nezhad, M. R. and Mahmoudi, M. 2015a. A Colorimetric Sensor Array for Detection and Discrimination of Biothiols based on Aggregation of Gold Nanoparticles. *Analytica Chimica Acta*, doi:10.1016/j.aca.2015.04.011 (0)

Ghasemi, F., Hormozi-Nezhad, M. R. and Mahmoudi, M. 2015b. A Colorimetric Sensor Array for Detection and Discrimination of Biothiols based on Aggregation of Gold Nanoparticles. *Analytica Chimica Acta*, 882: 58–67.

Ghoshal, T., Biswas, S., Paul, M. and De, S. K. 2009. Synthesis of ZnO nanoparticles by solvothermal method and their ammonia sensing properties. *Journal of Nanoscience and Nanotechnology*, 9 (10): 5973-5980.

Golabi, S. M. and Noor-Mohammadi, F. 1998. Electrocatalytic oxidation of hydrazine at cobalt hexacyanoferrate- modified glassy carbon, Pt and Au electrodes. *Journal of Solid State Electrochemistry*, 2 (1): 30-37.

Guan, R., Kang, T., Lu, F., Zhang, Z., Shen, H. and Liu, M. 2012. Cytotoxicity, oxidative stress, and genotoxicity in human hepatocyte and embryonic kidney cells exposed to ZnO nanoparticles. *Nanoscale Research Letters*, 7 (1): 602.

Guarise, C., Pasquato, L., De Filippis, V. and Scrimin, P. 2006. Gold nanoparticles-based protease assay. *Proceedings of the National Academy of Sciences of the United States of America*, 103 (11): 3978-3982.

Gunalan, S., Sivaraj, R. and Rajendran, V. 2012. Green synthesized ZnO nanoparticles against bacterial and fungal pathogens. *Progress in Natural Science: Materials International*, 22 (6): 693-700.

Gunawan, C., Lim, M., Marquis, C. P. and Amal, R. 2014. Nanoparticle–protein corona complexes govern the biological fates and functions of nanoparticles. *Journal of Materials Chemistry B*, 2 (15): 2060-2083.

Guo, L., Zeng, S.-L., Zhang, Y., Li, P. and Liu, E. H. 2016. Comparative analysis of steroidal saponins in four Dioscoreae herbs by high performance liquid chromatography coupled with mass spectrometry. *Journal of Pharmaceutical and Biomedical Analysis*, 117: 91-98.

Hajizadeh, S., Farhadi, K., Forough, M. and Molaei, R. 2012. Silver nanoparticles in the presence of Ca2+ as a selective and sensitive probe for the colorimetric detection of cysteine. *Analytical Methods*, 4 (6): 1747-1752.

Han, C., Xu, K., Liu, Q., Liu, X. and Li, J. 2014. Colorimetric sensing of cysteine using label-free silver nanoparticles. *Sensors and Actuators B: Chemical*, 202 (0): 574-582.

Han, M. S., Lytton-Jean, A. K. R. and Mirkin, C. A. 2006. A Gold Nanoparticle Based Approach for Screening Triplex DNA Binders. *Journal of the American Chemical Society*, 128 (15): 4954-4955.

Hanada, T. 2009. Basic Properties of ZnO, GaN, and Related Materials. In: Yao, T. and Hong, S.-K. eds. *Oxide and Nitride Semiconductors: Processing, Properties, and Applications*. Berlin, Heidelberg: Springer Berlin Heidelberg, 1-19. Available: http://dx.doi.org/10.1007/978-3-540-88847-5_1 (Accessed

He, W., Kim, H.-K., Wamer, W. G., Melka, D., Callahan, J. H. and Yin, J.-J. 2014. Photogenerated Charge Carriers and Reactive Oxygen Species in ZnO/Au Hybrid Nanostructures with Enhanced Photocatalytic and Antibacterial Activity. *Journal of the American Chemical Society*, 136 (2): 750-757.

Hohenberg, P. and Kohn, W. 1964. Inhomogeneous Electron Gas. *Physical Review*, 136 (3B): B864-B871.

Horo, I., Masullo, M., Falco, A., Şenol, S. G., Piacente, S. and Alankuş-Çalışkan, Ö. 2015. New triterpene saponins from Phryna ortegioides. *Phytochemistry Letters*, 14: 39-44.

Hostettmann, K. and Marston, A. 1995. *Saponins*. Cambridge ;: Cambridge University Press.

Hu, J., Ni, P., Dai, H., Sun, Y., Wang, Y., jiang, s. and Li, Z. 2015. Aptamer-based colorimetric biosensing of abrin using catalytic gold nanoparticles. *Analyst*, 140: 3581-3586.

Huang, C.-C., Huang, Y.-F., Cao, Z., Tan, W. and Chang, H.-T. 2005. Aptamer-Modified Gold Nanoparticles for Colorimetric Determination of Platelet-Derived Growth Factors and Their Receptors. *Analytical Chemistry*, 77 (17): 5735-5741.

Huang, Y., Zhang, T., Zhou, H., Feng, Y., Fan, C., Chen, W., Crommen, J. and Jiang, Z. 2016. Fast separation of triterpenoid saponins using supercritical fluid chromatography coupled with single quadrupole mass spectrometry. *Journal of Pharmaceutical and Biomedical Analysis*, 121: 22-29.

Husen, A. and Siddiqi, K. S. 2014. Phytosynthesis of nanoparticles: concept, controversy and application. *Nanoscale Research Letters*, 9 (1): 229.

Janak, J. F., Moruzzi, V. L. and Williams, A. R. 1975. Ground-state thermomechanical properties of some cubic elements in the local-density formalism. *Physical Review B*, 12 (4): 1257-1261.

Johnsen, L. G., Skou, P. B., Khakimov, B. and Bro, R. 2017. Gas chromatography – mass spectrometry data processing made easy. *Journal of Chromatography A*, 1503 (Supplement C): 57-64.

Jongjinakool, S., Palasak, K., Bousod, N. and Teepoo, S. 2014. Gold Nanoparticles-based Colorimetric Sensor for Cysteine Detection. *Energy Procedia*, 56 (0): 10-18.

Joselin, J., Brintha, T. S. S., Florence, A. R. and Jeeva, S. 2013. Phytochemical evaluation of Bignoniaceae flowers. *Journal of Chemical & Pharmaceutical Research*, 5 (4): 106-111.

Judith Vijaya, J., Jayaprakash, N., Kombaiah, K., Kaviyarasu, K., John Kennedy, L., Jothi Ramalingam, R., Al Lohedan, H. A., Mohammed, M. A. V. and Maaza, M. 2017. Bioreduction potentials of dried root of Zingiber officinale for a simple green synthesis of silver nanoparticles: Antibacterial studies. *Journal of Photochemistry and Photobiology B: Biology*, 177: 62-68.

Kanjanawarut, R. and Su, X. 2009. Colorimetric Detection of DNA Using Unmodified Metallic Nanoparticles and Peptide Nucleic Acid Probes. *Analytical Chemistry*, 81 (15): 6122-6129.

Kathiravan, A. and Renganathan, R. 2008. Interaction of colloidal TiO_2 with bovine serum albumin: A fluorescence quenching study. *Colloids and Surfaces A: Physicochemical and Engineering Aspects*, 324 (1–3): 176-180.

Kerem, Z., German-Shashoua, H. and Yarden, O. 2005. Microwave-assisted extraction of bioactive saponins from chickpea (Cicer arietinum L). *Journal of the Science of Food and Agriculture*, 85 (3): 406-412.

Kim, K.-A., Cha, J.-R., Yun, S.-W. and Gong, M.-S. 2015. Preparation of Zinc Oxide Nanoparticles at Low Temperature Using New Organometallic Zinc Carbamate Precursor. *Bulletin of the Korean Chemical Society*, 36 (5): 1426-1432.

Kim, Y. S., Kim, J. H., Kim, I. A., Lee, S. J., Jurng, J. and Gu, M. B. 2010. A novel colorimetric aptasensor using gold nanoparticle for a highly sensitive and specific detection of oxytetracycline. *Biosensors and Bioelectronics*, 26 (4): 1644-1649.

Kirkpatrick, S., Gelatt, C. D. and Vecchi, M. P. 1983. Optimization by Simulated Annealing. *Science*, 220 (4598): 671-680.

Kohn, W. and Sham, L. J. 1965. Self-Consistent Equations Including Exchange and Correlation Effects. *Physical Review*, 140 (4A): A1133-A1138.

Koole, R., Groeneveld, E., Vanmaekelbergh, D., Meijerink, A. and Mello Donegá, C. 2014. Size Effects on Semiconductor Nanoparticles. In: de Mello Donegá, C. ed. *Nanoparticles: Workhorses of Nanoscience*. Berlin, Heidelberg: Springer Berlin Heidelberg, 13-51. Available: http://dx.doi.org/10.1007/978-3-662-44823-6_2 (Accessed

Korany, M. A., Haggag, R. S., Ragab, M. A. A. and Elmallah, O. A. 2017. A validated stability-indicating HPLC method for simultaneous determination of Silymarin and Curcumin in various dosage forms. *Arabian Journal of Chemistry*, 10 (Supplement 2): S1711-S1725.

Kuhnle, A., Linderoth, T. R., Hammer, B. and Besenbacher, F. 2002. Chiral recognition in dimerization of adsorbed cysteine observed by scanning tunnelling microscopy. *Nature*, 415 (6874): 891-893.

Kumar, H. and Rani, R. 2013. Structural and optical characterization of ZnO nanoparticles synthesized by microemulsion route. *International Letters of Chemistry, Physics and Astronomy*, 14: 26-36.

Kundu, S. 2013. Formation of self-assembled Ag nanoparticles on DNA chains with enhanced catalytic activity. *Physical Chemistry Chemical Physics*, 15 (33): 14107-14119.

Kvasnička, F., Bíba, B., Ševčík, R., Voldřich, M. and Krátká, J. 2003. Analysis of the active components of silymarin. *Journal of Chromatography A*, 990 (1): 239-245.

Kwon, Y. S., Ahmad Raston, N. H. and Gu, M. B. 2014. An ultra-sensitive colorimetric detection of tetracyclines using the shortest aptamer with highly enhanced affinity. *Chemical Communications*, 50 (1): 40-42.

Laberrigue, A. 1983. Experimental high-resolution electron microscopy by J. C. H. Spence. *Acta Crystallographica Section A*, 39 (3): 503-504.

Lakshmeesha, T. R., Sateesh, M. K., Prasad, B. D., Sharma, S. C., Kavyashree, D., Chandrasekhar, M. and Nagabhushana, H. 2014. Reactivity of Crystalline ZnO Superstructures against Fungi and Bacterial Pathogens: Synthesized Using Nerium oleander Leaf Extract. *Crystal Growth & Design*, 14 (8): 4068-4079.

Lakshmi Prasanna, V. and Vijayaraghavan, R. 2015. Insight into the Mechanism of Antibacterial Activity of ZnO: Surface Defects Mediated Reactive Oxygen Species Even in the Dark. *Langmuir*, 31 (33): 9155-9162.

Lee, C., Gaston, M. A., Weiss, A. A. and Zhang, P. 2013. Colorimetric viral detection based on sialic acid stabilized goldnanoparticles. *Biosensors and Bioelectronics*, 42 (0): 236-241.

Lee, C., Yang, W. and Parr, R. G. 1988. Development of the Colle-Salvetti correlation-energy formula into a functional of the electron density. *Physical Review B*, 37 (2): 785-789.

Lee, J.-H., Lim, J.-M., Velmurugan, P., Park, Y.-J., Park, Y.-J., Bang, K.-S. and Oh, B.-T. 2016. Photobiologic-mediated fabrication of silver nanoparticles with antibacterial activity. *Journal of Photochemistry and Photobiology B: Biology*, 162 (Supplement C): 93-99.

Lee, J.-S., Lytton-Jean, A. K. R., Hurst, S. J. and Mirkin, C. A. 2007. Silver Nanoparticle−Oligonucleotide Conjugates Based on DNA with Triple Cyclic Disulfide Moieties. *Nano Letters*, 7 (7): 2112-2115.

Lee, J.-S., Ulmann, P. A., Han, M. S. and Mirkin, C. A. 2008. A DNA−Gold Nanoparticle-Based Colorimetric Competition Assay for the Detection of Cysteine. *Nano Letters*, 8 (2): 529-533.

Lencina, C. L., Cardoso, M. C. d., Zancanaro, I., Gosmann, G., Pires, V. S., Sonnet, P., Guillaume, D. and Schenkel, E. P. 2011. Triterpenes and new saponins from Ilex chamaedryfolia: chemotaxonomic tool to ilex species differentiation. *Química Nova*, 34: 222-225.

Lepoitevin, M., Lemouel, M., Bechelany, M., Janot, J.-M. and Balme, S. 2015. Gold nanoparticles for the bare-eye based and spectrophotometric detection of proteins, polynucleotides and DNA. *Microchimica Acta*, 182 (5-6): 1223-1229.

Levy, M. 1979. Universal variational functionals of electron densities, first-order density matrices, and natural spin-orbitals and solution of the v-representability problem. *Proceedings of the National Academy of Sciences*, 76 (12): 6062-6065.

Li, H. and Rothberg, L. 2004. Colorimetric detection of DNA sequences based on electrostatic interactions with unmodified gold nanoparticles. *Proceedings of the National Academy of Sciences of the United States of America*, 101 (39): 14036-14039.

Li, L. and Li, B. 2009. Sensitive and selective detection of cysteine using gold nanoparticles as colorimetric probes. *Analyst*, 134 (7): 1361-1365.

Li, N., Ma, L., Wang, J., Zheng, L., Liu, J., Duan, Y., Liu, H., Zhao, X., Wang, S., Wang, H., Hong, F. and Xie, Y. 2010. Interaction Between Nano-Anatase TiO_2 and Liver DNA from Mice I*n Vivo*. *Nanoscale Research Letters*, 5 (1): 108-115.

Li, W., Pan, C., Hou, T., Wang, X. and Li, F. 2014. Selective and colorimetric detection of pyruvic acid using conformational switch of i-motif DNA and unmodified gold nanoparticles. *Analytical Methods*, 6 (6): 1645-1649.

Li, X., Xing, Y., Jiang, Y., Ding, Y. and Li, W. 2009. Antimicrobial activities of ZnO powder-coated PVC film to inactivate food pathogens. *International Journal of Food Science & Technology*, 44 (11): 2161-2168.

Lima, M., Fernandes, D., Silva, M., Baesso, M., Neto, A., de Morais, G., Nakamura, C., de Oliveira Caleare, A., Hechenleitner, A. and Pineda, E. 2014. Co-doped ZnO nanoparticles synthesized by an adapted sol–gel method: effects on the structural, optical, photocatalytic and antibacterial properties. *Journal of Sol-Gel Science and Technology*, 72 (2): 301-309.

Liming, S., Ningzhong, B., Kazumichi, Y., Kazunari, D., Arunava, G. and Craig, A. G. 2006. Direct synthesis of ZnO nanoparticles by a solution-free mechanochemical reaction. *Nanotechnology*, 17 (20): 5117.

Lindberg, H. K., Falck, G. C. M., Singh, R., Suhonen, S., Järventaus, H., Vanhala, E., Catalán, J., Farmer, P. B., Savolainen, K. M. and Norppa, H. 2013. Genotoxicity of short single-wall and multi-wall carbon nanotubes in human bronchial epithelial and mesothelial cells i*n vitro*. *Toxicology*, 313 (1): 24-37.

Liu, A., Zhang, Y., Chen, W., Wang, X. and Chen, F. 2013. Gold nanoparticle-based colorimetric detection of staphylococcal enterotoxin B using ssDNA aptamers. *European Food Research and Technology*, 237 (3): 323-329.

Liu, B., Wen, L. and Zhao, X. 2007. The photoluminescence spectroscopic study of anatase TiO_2 prepared by magnetron sputtering. *Materials Chemistry and Physics*, 106 (2–3): 350-353.

Liu, J., Bai, W., Niu, S., Zhu, C., Yang, S. and Chen, A. 2014. Highly sensitive colorimetric detection of 17[bgr]-estradiol using split DNA aptamers immobilized on unmodified gold nanoparticles. *Scientific Reports*, 4: 7571.

Liu, J. and Lu, Y. 2003. A Colorimetric Lead Biosensor Using DNAzyme-Directed Assembly of Gold Nanoparticles. *Journal of the American Chemical Society*, 125 (22): 6642-6643.

Liu, J. and Lu, Y. 2004. Colorimetric Biosensors Based on DNAzyme-Assembled Gold Nanoparticles. *Journal of Fluorescence*, 14 (4): 343-354.

Liu, J. and Lu, Y. 2006. Fast Colorimetric Sensing of Adenosine and Cocaine Based on a General Sensor Design Involving Aptamers and Nanoparticles. *Angewandte Chemie International Edition*, 45 (1): 90-94.

Liu, R., Liew, R., Zhou, J. and Xing, B. 2007. A Simple and Specific Assay for Real-Time Colorimetric Visualization of β-Lactamase Activity by Using Gold Nanoparticles. *Angewandte Chemie International Edition*, 46 (46): 8799-8803.

Liu, S., Zhang, Z. and Han, M. 2005. Gram-Scale Synthesis and Biofunctionalization of Silica-Coated Silver Nanoparticles for Fast Colorimetric DNA Detection. *Analytical Chemistry*, 77 (8): 2595-2600.

Logan, N., Sherif, A., Cross, A. J., Collins, S. N., Traynor, A., Bozec, L., Parkin, I. P. and Brett, P. 2015. TiO_2-coated CoCrMo: Improving the osteogenic differentiation and adhesion of mesenchymal stem cells in vitro. *Journal of Biomedical Materials Research Part A*, 103 (3): 1208-1217.

Lou, X., Xiao, Y., Wang, Y., Mao, H. and Zhao, J. 2009. Label-Free Colorimetric Screening of Nuclease Activity and Substrates by Using Unmodified Gold Nanoparticles. *ChemBioChem*, 10 (12): 1973-1977.

Lu, J.-m., Wang, Y.-f., Yan, H.-l., Lin, P., Gu, W. and Yu, J. 2016. Antidiabetic effect of total saponins from Polygonatum kingianum in streptozotocin-induced daibetic rats. *Journal of Ethnopharmacology*, 179: 291-300.

Lu, J., Ng, K. M. and Yang, S. 2008. Efficient, One-Step Mechanochemical Process for the Synthesis of ZnO Nanoparticles. *Industrial and Engineering Chemistry Research*, 47 (4): 1095-1101.

MacKerell, A. D., Bashford, D., Bellott, M., Dunbrack, R. L., Evanseck, J. D., Field, M. J., Fischer, S., Gao, J., Guo, H., Ha, S., Joseph-McCarthy, D., Kuchnir, L., Kuczera, K., Lau, F. T. K., Mattos, C., Michnick, S., Ngo, T., Nguyen, D. T., Prodhom, B., Reiher, W. E., Roux, B., Schlenkrich, M., Smith, J. C., Stote, R., Straub, J., Watanabe, M., Wiórkiewicz-Kuczera, J., Yin, D. and Karplus, M. 1998. All-Atom

Empirical Potential for Molecular Modeling and Dynamics Studies of Proteins. *The Journal of Physical Chemistry B*, 102 (18): 3586-3616.

Mackerell, A. D., Feig, M. and Brooks, C. L. 2004. Extending the treatment of backbone energetics in protein force fields: Limitations of gas-phase quantum mechanics in reproducing protein conformational distributions in molecular dynamics simulations. *Journal of Computational Chemistry*, 25 (11): 1400-1415.

Mancuso, M., Jiang, L., Cesarman, E. and Erickson, D. 2013. Multiplexed Colorimetric Detection of Kaposi's Sarcoma Associated Herpesvirus and Bartonella DNA using Gold and Silver Nanoparticles. *Nanoscale*, 5 (4): 1678-1686.

Mao, J., Lu, Y., Chang, N., Yang, J., Zhang, S. and Liu, Y. 2016. Multidimensional colorimetric sensor array for discrimination of proteins. *Biosensors and Bioelectronics*, 86: 56-61.

McLaren, A., Valdes-Solis, T., Li, G. and Tsang, S. C. 2009. Shape and Size Effects of ZnO Nanocrystals on Photocatalytic Activity. *Journal of the American Chemical Society*, 131 (35): 12540-12541.

Mehta, J., Van Dorst, B., Rouah-Martin, E., Herrebout, W., Scippo, M.-L., Blust, R. and Robbens, J. 2011. In vitro selection and characterization of DNA aptamers recognizing chloramphenicol. *Journal of Biotechnology*, 155 (4): 361-369.

Mei, Z., Chu, H., Chen, W., Xue, F., Liu, J., Xu, H., Zhang, R. and Zheng, L. 2013. Ultrasensitive one-step rapid visual detection of bisphenol A in water samples by label-free aptasensor. *Biosensors and Bioelectronics*, 39 (1): 26-30.

Meng, L., Jiang, A., Chen, R., Li, C.-z., Wang, L., Qu, Y., Wang, P., Zhao, Y. and Chen, C. 2013. Inhibitory effects of multiwall carbon nanotubes with high iron impurity

on viability and neuronal differentiation in cultured PC12 cells. *Toxicology,* 313 (1): 49-58.

Mikołajczyk-Bator, K., Błaszczyk, A., Czyżniejewski, M. and Kachlicki, P. 2016. Characterisation and identification of triterpene saponins in the roots of red beets (Beta vulgaris L.) using two HPLC–MS systems. *Food Chemistry*, 192: 979-990.

Mirkin, C. A., Letsinger, R. L., Mucic, R. C. and Storhoff, J. J. 1996. A DNA-based method for rationally assembling nanoparticles into macroscopic materials. *Nature*, 382 (6592): 607-609.

Mohammadi, S., Pourseyedi, S. and Amini, A. 2016. Green synthesis of silver nanoparticles with a long lasting stability using colloidal solution of cowpea seeds (Vigna sp. L). *Journal of Environmental Chemical Engineering*, 4 (2): 2023-2032.

Moldovan, B., David, L., Achim, M., Clichici, S. and Filip, G. A. 2016. A green approach to phytomediated synthesis of silver nanoparticles using Sambucus nigra L. fruits extract and their antioxidant activity. *Journal of Molecular Liquids*, 221: 271-278.

Mondal, K. and Sharma, A. 2016. Recent advances in electrospun metal-oxide nanofiber based interfaces for electrochemical biosensing. *RSC Advances*, 6 (97): 94595-94616.

Montazer, M. and Pakdel, E. 2011. Functionality of nano titanium dioxide on textiles with future aspects: Focus on wool. *Journal of Photochemistry and Photobiology C: Photochemistry Reviews*, 12 (4): 293-303.

Morkoç, H. and Özgür, Ü. 2009. General Properties of ZnO. In: *Zinc Oxide*. Wiley-VCH Verlag GmbH & Co. KGaA, 1-76. Available: http://dx.doi.org/10.1002/9783527623945.ch1 (Accessed

Morris, G. M., Huey, R., Lindstrom, W., Sanner, M. F., Belew, R. K., Goodsell, D. S. and Olson, A. J. 2009. AutoDock4 and AutoDockTools4: Automated docking with selective receptor flexibility. *J Comput Chem*, 30 (16): 2785-2791.

Mpanza, T., Sabela, M. I., Mathenjwa, S. S., Kanchi, S. and Bisetty, K. 2014. Electrochemical Determination of Capsaicin and Silymarin Using a Glassy Carbon Electrode Modified by Gold Nanoparticle Decorated Multiwalled Carbon Nanotubes. *Analytical Letters*, 47 (17): 2813-2828.

Musat, V., Tabacaru, A., Vasile, B. S. and Surdu, V.-A. 2014. Size-dependent photoluminescence of zinc oxide quantum dots through organosilane functionalization. *RSC Advances*, 4 (108): 63128-63136.

Narayanan, K. B. and Sakthivel, N. 2010. Biological synthesis of metal nanoparticles by microbes. *Advances in Colloid and Interface Science*, 156 (1): 1-13.

Nasrollahzadeh, M., Maham, M., Rostami-Vartooni, A., Bagherzadeh, M. and Sajadi, S. M. 2015. Barberry fruit extract assisted in situ green synthesis of Cu nanoparticles supported on a reduced graphene oxide-Fe3O4 nanocomposite as a magnetically separable and reusable catalyst for the O-arylation of phenols with aryl halides under ligand-free conditions. *RSC Advances*, 5 (79): 64769-64780.

Ndamane, Y., Kambizi, L., Songca, S. P. and Oluwafemi, O. S. 2013. Antibacterial effectiveness of Tetradenia riparia extract, a plant traditionally used in the Eastern Cape Province to treat diseases of the respiratory system. *Journal of medicinal plant research*, 7 (37): 2755-2760.

Neudert, G. and Klebe, G. 2011. DSX: a knowledge-based scoring function for the assessment of protein-ligand complexes. *J Chem Inf Model*, 51 (10): 2731-2745.

Newman, M. D., Stotland, M. and Ellis, J. I. 2009. The safety of nanosized particles in titanium dioxide– and zinc oxide–based sunscreens. *Journal of the American Academy of Dermatology*, 61 (4): 685-692.

Nymark, P., Catalán, J., Suhonen, S., Järventaus, H., Birkedal, R., Clausen, P. A., Jensen, K. A., Vippola, M., Savolainen, K. and Norppa, H. 2013. Genotoxicity of polyvinylpyrrolidone-coated silver nanoparticles in BEAS 2B cells. *Toxicology*, 313 (1): 38-48.

Oishi, J., Asami, Y., Mori, T., Kang, J.-H., Niidome, T. and Katayama, Y. 2008. Colorimetric Enzymatic Activity Assay Based on Noncrosslinking Aggregation of Gold Nanoparticles Induced by Adsorption of Substrate Peptides. *Biomacromolecules*, 9 (9): 2301-2308.

Okitsu, K., Mizukoshi, Y., Yamamoto, T. A., Maeda, Y. and Nagata, Y. 2007. Sonochemical synthesis of gold nanoparticles on chitosan. *Materials Letters*, 61 (16): 3429-3431.

Onodera, R., Hayashi, T., Nakamura, T., Aibe, K., Tahara, K. and Takeuchi, H. 2016. Preparation of silymarin nanocrystals using a novel high pressure crystallization technique and evaluation of its dissolution and absorption properties. *Asian Journal of Pharmaceutical Sciences*, 11 (1): 211-212.

Pang, B., Yan, J., Yao, L., Liu, H., Guan, J., Wang, H. and Liu, H. 2016. Preparation and characterization of antibacterial paper coated with sodium lignosulfonate stabilized ZnO nanoparticles. *RSC Advances*, 6 (12): 9753-9759.

Patil Shriniwas, P. and Kumbhar Subhash, T. 2017. Antioxidant, antibacterial and cytotoxic potential of silver nanoparticles synthesized using terpenes rich extract of Lantana camara L. leaves. *Biochemistry and Biophysics Reports*, 10 (Supplement C): 76-81.

Patra, S., Mukherjee, S., Barui, A. K., Ganguly, A., Sreedhar, B. and Patra, C. R. 2015. Green synthesis, characterization of gold and silver nanoparticles and their potential application for cancer therapeutics. *Materials Science and Engineering: C*, 53: 298-309.

Paul, I. E., Rajeshwari, A., Prathna, T. C., Raichur, A. M., Chandrasekaran, N. and Mukherjee, A. 2015. Colorimetric detection of melamine based on the size effect of AuNPs. *Analytical Methods*, 7 (4): 1453-1462.

Pavlov, V., Xiao, Y., Shlyahovsky, B. and Willner, I. 2004. Aptamer-Functionalized Au Nanoparticles for the Amplified Optical Detection of Thrombin. *Journal of the American Chemical Society*, 126 (38): 11768-11769.

Perdew, J. P. and Wang, Y. 1992. Accurate and simple analytic representation of the electron-gas correlation energy. *Physical Review B*, 45 (23): 13244-13249.

Pethakamsetty, L., Kothapenta, K., Nammi, H. R., Lakshmi Kalyani Ruddaraju, Kollu, P., Yoon, S. G. and Pammi, S. V. N. 2017. Green synthesis, characterization and antimicrobial activity of silver nanoparticles using methanolic root extracts of Diospyros sylvatica, . *Journal of Environmental Sciences*, 55: 157-163.

Pople, J. A., Krishnan, R., Schlegel, H. B. and Binkley, J. S. 1979. Derivative studies in hartree-fock and møller-plesset theories. *International Journal of Quantum Chemistry*, 16 (S13): 225-241.

Pople, J. A. and Nesbet, R. K. 1954. Self-Consistent Orbitals for Radicals. *The Journal of Chemical Physics*, 22 (3): 571-572.

Prakash, O., Gautam, P., Kumar, S., Singh, P., Dani, R. K., Bharty, M. K., Singh, N. K., Ghosh, A. K., Deckert, V. and Singh, R. K. 2015. Surface enhanced Raman

scattering investigation of two novel piperazine carbodithioic acids adsorbed on Ag and ZnO nanoparticles. *RSC Advances*, 5 (8): 5571-5579.

Pulay, P. 1969. Ab initio calculation of force constants and equilibrium geometries in polyatomic molecules. *Molecular Physics*, 17 (2): 197-204.

Puyvelde, L. V., Kimpe, N. D., Dubé, S., Chagnon-Dubé, M., Boily, Y., Borremans, F., Schamp, N. and Anteunis, M. J. O. 1981. 1′,2′-Dideacetylboronolide, an α-pyrone from Iboza riparia. *Phytochemistry*, 20 (12): 2753-2755.

Qian, Q., Deng, J., Wang, D., Yang, L., Yu, P. and Mao, L. 2012. Aspartic Acid-Promoted Highly Selective and Sensitive Colorimetric Sensing of Cysteine in Rat Brain. *Analytical Chemistry*, 84 (21): 9579-9584.

Ragavan, K. V., Selvakumar, L. S. and Thakur, M. S. 2013. Functionalized aptamers as nano-bioprobes for ultrasensitive detection of bisphenol-A. *Chemical Communications*, 49 (53): 5960-5962.

Raghupathi, K. R., Koodali, R. T. and Manna, A. C. 2011. Size-Dependent Bacterial Growth Inhibition and Mechanism of Antibacterial Activity of Zinc Oxide Nanoparticles. *Langmuir*, 27 (7): 4020-4028.

Rajiv, P., Rajeshwari, S. and Venckatesh, R. 2013. Bio-fabrication of zinc oxide nanoparticles using leaf extract of Parthenium hysterophorus L. and its size-dependent antifungal activity against plant fungal pathogens. *Spectrochim Acta A Mol Biomol Spectrosc*, 112: 384-387.

Ramakrishnan, S. K., Martin, M., Cloitre, T., Firlej, L. and Gergely, C. 2015. Design rules for metal binding biomolecules: understanding of amino acid adsorption on platinum crystallographic facets from density functional calculations. *Physical Chemistry Chemical Physics*, 17 (6): 4193-4198.

583 Ramesh, M., Anbuvannan, M. and Viruthagiri, G. 2015. Green synthesis of ZnO
584 nanoparticles using Solanum nigrum leaf extract and their antibacterial activity.
585 *Spectrochim Acta A Mol Biomol Spectrosc*, 136 Pt B: 864-870.

586 Ramimoghadam, D., Bin Hussein, M. Z. and Taufiq-Yap, Y. H. 2013. Hydrothermal
587 synthesis of zinc oxide nanoparticles using rice as soft biotemplate. *Chemistry*
588 *Central Journal*, 7: 136-136.

589 Raveendran, P., Fu, J. and Wallen, S. L. 2003. Completely "Green" Synthesis and
590 Stabilization of Metal Nanoparticles. *Journal of the American Chemical Society*,
591 125 (46): 13940-13941.

592 Ravichandran, V., Vasanthi, S., Shalini, S., Ali Shah, S. A. and Harish, R. 2016. Green
593 synthesis of silver nanoparticles using Atrocarpus altilis leaf extract and the study
594 of their antimicrobial and antioxidant activity. *Materials Letters*, 180: 264-267.

595 Ravindran, A., Mani, V., Chandrasekaran, N. and Mukherjee, A. 2011. Selective
596 colorimetric sensing of cysteine in aqueous solutions using silver nanoparticles in
597 the presence of Cr3+. *Talanta*, 85 (1): 533-540.

598 Ravindran, A., Singh, A., Raichur, A. M., Chandrasekaran, N. and Mukherjee, A. 2010.
599 Studies on interaction of colloidal Ag nanoparticles with Bovine Serum Albumin
600 (BSA). *Colloids and Surfaces B: Biointerfaces*, 76 (1): 32-37.

601 Rawat, K. and Kailasa, S. 2014. Visual detection of arginine, histidine and lysine using
602 quercetin-functionalized gold nanoparticles. *Microchimica Acta*, 181 (15-16):
603 1917-1929.

604 Ren, Y.-y., Yang, H., Wang, T. and Wang, C. 2016. Green synthesis and antimicrobial
605 activity of monodisperse silver nanoparticles synthesized using Ginkgo Biloba leaf
606 extract. *Physics Letters A*, 380 (45): 3773-3777.

Roothaan, C. C. J. 1951. New Developments in Molecular Orbital Theory. *Reviews of Modern Physics*, 23 (2): 69-89.

Rosi, N. L. and Mirkin, C. A. 2005. Nanostructures in Biodiagnostics. *Chemical Reviews*, 105 (4): 1547-1562.

Saleh Ahammad, A. J., Lee, J.-J. and Rahman, M. A. 2009. Electrochemical Sensors Based on Carbon Nanotubes. *Sensors (Basel, Switzerland)*, 9 (4): 2289-2319.

Sarreshtehdar Emrani, A., Danesh, N. M., Lavaee, P., Jalalian, S. H., Ramezani, M., Abnous, K. and Taghdisi, S. M. 2015. Sensitive and selective detection of digoxin based on fluorescence quenching and colorimetric aptasensors. *Analytical Methods*, 7: 3419-3424.

Sato, K., Hosokawa, K. and Maeda, M. 2003. Rapid Aggregation of Gold Nanoparticles Induced by Non-Cross-Linking DNA Hybridization. *Journal of the American Chemical Society*, 125 (27): 8102-8103.

Schofield, C. L., Haines, A. H., Field, R. A. and Russell, D. A. 2006. Silver and Gold Glyconanoparticles for Colorimetric Bioassays. *Langmuir*, 22 (15): 6707-6711.

Shakeel, F., Anwer, M. K., Shazly, G. A. and Jamil, S. 2014. Measurement and correlation of solubility of bioactive compound silymarin in five different green solvents at 298.15 K to 333.15 K. *Journal of Molecular Liquids*, 195: 255-258.

Shamaila, S., Khan Leghari Sajjad, A., Quart ul, A., Shaheen, S., Iqbal, A., Noor, S., Sughra, G. and Ali, U. 2017. A cost effective and eco-friendly green route for fabrication of efficient graphene nanosheets photocatalyst. *Journal of Environmental Chemical Engineering*, 5 (6): 5770-5776.

Shamaila, S., Sajjad, A. K. L., Ryma, N.-u.-A., Farooqi, S. A., Jabeen, N., Majeed, S. and Farooq, I. 2016. Advancements in nanoparticle fabrication by hazard free eco-friendly green routes. *Applied Materials Today*, 5 (Supplement C): 150-199.

Sharma, D., Kanchi, S. and Bisetty, K. 2015. Biogenic synthesis of nanoparticles: A review. *Arabian Journal of Chemistry*,

Sharma, D., Rajput, J., Kaith, B. S., Kaur, M. and Sharma, S. 2010. Synthesis of ZnO nanoparticles and study of their antibacterial and antifungal properties. *Thin Solid Films*, 519 (3): 1224-1229.

Sharma, D., Sabela, M. I., Kanchi, S., Bisetty, K., Skelton, A. A. and Honarparvar, B. 2018. Green synthesis, characterization and electrochemical sensing of silymarin by ZnO nanoparticles: Experimental and DFT studies. *Journal of Electroanalytical Chemistry*, 808 (Supplement C): 160-172.

Sharma, D., Sabela, M. I., Kanchi, S., Mdluli, P. S., Singh, G., Stenström, T. A. and Bisetty, K. 2016. Biosynthesis of ZnO nanoparticles using Jacaranda mimosifolia flowers extract: Synergistic antibacterial activity and molecular simulated facet specific adsorption studies. *Journal of Photochemistry and Photobiology B: Biology*, 162 (Supplement C): 199-207.

Sharma, D., Sharma, S., Kaith, B. S., Rajput, J. and Kaur, M. 2011. Synthesis of ZnO nanoparticles using surfactant free in-air and microwave method. *Applied Surface Science*, 257 (22): 9661-9672.

Sharma, H. S., Ali, S. F., Hussain, S. M., Schlager, J. J. and Sharma, A. 2009. Influence of Engineered Nanoparticles from Metals on the Blood-Brain Barrier Permeability, Cerebral Blood Flow, Brain Edema and Neurotoxicity. An Experimental Study in the Rat and Mice Using Biochemical and Morphological Approaches. *Journal of Nanoscience and Nanotechnology*, 9 (8): 5055-5072.

Shen, Q., Nie, Z., Guo, M., Zhong, C.-J., Lin, B., Li, W. and Yao, S. 2009. Simple and rapid colorimetric sensing of enzymatic cleavage and oxidative damage of single-stranded DNA with unmodified gold nanoparticles as indicator. *Chemical Communications*, (8): 929-931.

Siddhartha, S. and Debabrata, D. 2010. Label-free colorimetric estimation of proteins using nanoparticles of silver. *Nano-Micro Letters*, 2 (2): 164-168.

Sikhwivhilu, L. M., Mpelane, S., Mwakikunga, B. W. and Sinha Ray, S. 2012. Photoluminescence and Hydrogen Gas-Sensing Properties of Titanium Dioxide Nanostructures Synthesized by Hydrothermal Treatments. *ACS Applied Materials & Interfaces*, 4 (3): 1656-1665.

Silva-Bermudez, P., Rodil, S. E. and Muhl, S. 2011. Albumin adsorption on oxide thin films studied by spectroscopic ellipsometry. *Applied Surface Science*, 258 (5): 1711-1718.

Siripireddy, B. and Mandal, B. K. 2017. Facile green synthesis of zinc oxide nanoparticles by Eucalyptus globulus and their photocatalytic and antioxidant activity. *Advanced Powder Technology*, 28 (3): 785-797.

Slater, J. C. 1951. A Simplification of the Hartree-Fock Method. *Physical Review*, 81 (3): 385-390.

Slater, J. C. 1972. Statistical Exchange-Correlation in the Self-Consistent Field. In: Löwdin, P.-O. ed. *Advances in Quantum Chemistry*. Academic Press, 1-92. Available: http://www.sciencedirect.com/science/article/pii/S0065327608605419 (Accessed

Søndergaard, M., Bøjesen, E. D., Christensen, M. and Iversen, B. B. 2011. Size and Morphology Dependence of ZnO Nanoparticles Synthesized by a Fast Continuous Flow Hydrothermal Method. *Crystal Growth & Design*, 11 (9): 4027-4033.

Song, B., Liu, J., Feng, X., Wei, L. and Shao, L. 2015. A review on potential neurotoxicity of titanium dioxide nanoparticles. *Nanoscale Research Letters*, 10: 342.

Song, G., Chen, C., Ren, J. and Qu, X. 2009. A Simple, Universal Colorimetric Assay for Endonuclease/Methyltransferase Activity and Inhibition Based on an Enzyme-Responsive Nanoparticle System. *ACS Nano*, 3 (5): 1183-1189.

Song, G., Xu, C. and Li, B. 2015. Visual chiral recognition of mandelic acid enantiomers with l-tartaric acid-capped gold nanoparticles as colorimetric probes. *Sensors and Actuators B: Chemical*, 215: 504-509.

Song, K.-M., Cho, M., Jo, H., Min, K., Jeon, S. H., Kim, T., Han, M. S., Ku, J. K. and Ban, C. 2011. Gold nanoparticle-based colorimetric detection of kanamycin using a DNA aptamer. *Analytical Biochemistry*, 415 (2): 175-181.

Song, K.-M., Jeong, E., Jeon, W., Cho, M. and Ban, C. 2012. Aptasensor for ampicillin using gold nanoparticle based dual fluorescence–colorimetric methods. *Analytical and Bioanalytical Chemistry*, 402 (6): 2153-2161.

Spanhel, L. 2006. Colloidal ZnO nanostructures and functional coatings: A survey. *Journal of Sol-Gel Science and Technology*, 39 (1): 7-24.

Stashenko, E. and Martínez, J. R. 2014. Gas Chromatography-Mass Spectrometry. In: Guo, D. X. ed. *Advances in Gas Chromatography*. InTech. Available: https://www.intechopen.com/books/advances-in-gas-chromatography/gas-chromatography-mass-spectrometry (Accessed

Storhoff, J. J., Elghanian, R., Mucic, R. C., Mirkin, C. A. and Letsinger, R. L. 1998. One-Pot Colorimetric Differentiation of Polynucleotides with Single Base Imperfections Using Gold Nanoparticle Probes. *Journal of the American Chemical Society*, 120 (9): 1959-1964.

Su, H., Sun, B., Chen, L., Xu, Z. and Ai, S. 2012. Colorimetric sensing of dopamine based on the aggregation of gold nanoparticles induced by copper ions. *Analytical Methods*, 4 (12): 3981-3986.

Sun, X., Li, Q., Jiang, J. and Mao, Y. 2014. Morphology-tunable synthesis of ZnO nanoforest and its photoelectrochemical performance. *Nanoscale*, 6 (15): 8769-8780.

Sun, Y., Zhao, H., Boussouar, I., Zhang, F., Tian, D. and Li, H. 2015. Highly sensitive chiral sensing by calix[4]arene-modified silver nanoparticles via dynamic light scattering. *Sensors and Actuators B: Chemical*, 216: 235-239.

Sundrarajan, M., Ambika, S. and Bharathi, K. 2015. Plant-extract mediated synthesis of ZnO nanoparticles using Pongamia pinnata and their activity against pathogenic bacteria. *Advanced Powder Technology*, 26 (5): 1294-1299.

Suryanarayana, C. and Norton, M. G. 1998. Crystal Structure Determination. II: Hexagonal Structures. In: *X-Ray Diffraction: A Practical Approach*. Boston, MA: Springer US, 125-152. Available: http://dx.doi.org/10.1007/978-1-4899-0148-4_5 (Accessed

Tamuly, C., Saikia, I., Hazarika, M., Bordoloi, M., Hussain, N., Das, M. R. and Deka, K. 2015. Bio-derived ZnO nanoflower: a highly efficient catalyst for the synthesis of chalcone derivatives. *RSC Advances*, 5 (12): 8604-8608.

Taton, T. A., Mirkin, C. A. and Letsinger, R. L. 2000. Scanometric DNA Array Detection with Nanoparticle Probes. *Science*, 289 (5485): 1757-1760.

Tauc, J. and Menth, A. 1972. States in the gap. *Journal of Non-Crystalline Solids*, 8–10: 569-585.

Thabani, M., Myalowenkosi, S., Sanele, M., Suvardhan, K. and Krishna, B. 2014. Electrochemical Determination of Capsaicin and Silymarin Using a Glassy Carbon Electrode Modified by Gold Nanoparticle Decorated Multiwalled Carbon Nanotubes. *Analytical Letters*, 47 (17): 2813-2828.

Tiwari, N., Rathore, A. , Prabhune, A. and Kulkarni, S. 2010. Gold Nanoparticles for Colorimetric detection of hydrolysis of antibiotics by penicillin G acylase. *Advances in Bioscience and Biotechnology*, 1, : 322-329.

Tokareva, I. and Hutter, E. 2004. Hybridization of Oligonucleotide-Modified Silver and Gold Nanoparticles in Aqueous Dispersions and on Gold Films. *Journal of the American Chemical Society*, 126 (48): 15784-15789.

Tsai, C.-S., Yu, T.-B. and Chen, C.-T. 2005. Gold nanoparticle-based competitive colorimetric assay for detection of protein-protein interactions. *Chemical Communications*, (34): 4273-4275.

Uehara, N., Fujita, M. and Shimizu, T. 2009. Colorimetric Assay of Aminopeptidase N Activity Based on Inhibition of the Disassembly of Gold Nano-composites Conjugated with a Thermo-responsive Copolymer. *Analytical Sciences*, 25 (2): 267-273.

Van Puyvelde, L., Dube, S., Uwimana, E., Uwera, C., Dommisse, R. A., Esmans, E. L., Van Schoor, O. and Vlietinck, A. J. 1979. New α-pyrones from Iboza riparia. *Phytochemistry*, 18 (7): 1215-1218.

Van Puyvelde, L., Ntawukiliyayo, J. D., Portaels, F. and Hakizamungu, E. 1994. *In vitro* inhibition of mycobacteria by Rwandese medicinal plants. *Phytotherapy Research*, 8 (2): 65-69.

Van Puyvelde, L., Nyirankuliza, S., Panebianco, R., Boily, Y., Geizer, I., Sebikali, B., De Kimpe, N. and Schamp, N. 1986. Active principles of Tetradenia riparia. I. Antimicrobial activity of 8(14),15-sandaracopimaradiene-7α,18-diol. *Journal of Ethnopharmacology*, 17 (3): 269-275.

Vanommeslaeghe, K., Hatcher, E., Acharya, C., Kundu, S., Zhong, S., Shim, J., Darian, E., Guvench, O., Lopes, P., Vorobyov, I. and Mackerell, A. D., Jr. 2010. CHARMM general force field: A force field for drug-like molecules compatible with the CHARMM all-atom additive biological force fields. *J Comput Chem*, 31 (4): 671-690.

Veerasamy, R., Xin, T. Z., Gunasagaran, S., Xiang, T. F. W., Yang, E. F. C., Jeyakumar, N. and Dhanaraj, S. A. 2011. Biosynthesis of silver nanoparticles using mangosteen leaf extract and evaluation of their antimicrobial activities. *Journal of Saudi Chemical Society*, 15 (2): 113-120.

Venugopal, K., Ahmad, H., Manikandan, E., Arul, T. K., Kavitha, K., Moodley, M. K., Rajagopal, K., Balabhaskar, R. and Bhaskar, M. 2017. The impact of anticancer activity upon Beta vulgaris extract mediated biosynthesized silver nanoparticles (ag-NPs) against human breast (MCF-7), lung (A549) and pharynx (Hep-2) cancer cell lines,. *Journal of Photochemistry & Photobiology, B: Biology*, 173 99-107.

Vlietinck, A. J., Van Hoof, L., Totté, J., Lasure, A., Berghe, D. V., Rwangabo, P. C. and Mvukiyumwami, J. 1995. Screening of hundred Rwandese medicinal plants for antimicrobial and antiviral properties. *Journal of Ethnopharmacology*, 46 (1): 31-47.

Vosko, S. H., Wilk, L. and Nusair, M. 1980. Accurate spin-dependent electron liquid correlation energies for local spin density calculations: a critical analysis. *Canadian Journal of Physics*, 58 (8): 1200-1211.

Wang, A.-J., Liao, Q.-C., Feng, J.-J., Zhang, P.-P., Li, A.-Q. and Wang, J.-J. 2012. Apple pectin-mediated green synthesis of hollow double-caged peanut-like ZnO hierarchical superstructures and photocatalytic applications. *CrystEngComm*, 14 (1): 256-263.

Wang, F., Wu, Y., Zhan, S., He, L., Zhi, W., Zhou, X. and Zhou, P. 2013. A Simple and Sensitive Colorimetric Detection of Silver Ions Based on Cationic Polymer-Directed AuNPs Aggregation. *Australian Journal of Chemistry*, 66 (1): 113-118.

Wang, H. and Lian, Y. 2014. A mechanistic study of oleic acid-mediated solvothermal shape controllable preparation of zinc oxide nanostructures. *Journal of Alloys and Compounds*, 594: 141-147.

Wang, J., Deng, X., Zhang, F., Chen, D. and Ding, W. 2014. ZnO nanoparticle-induced oxidative stress triggers apoptosis by activating JNK signaling pathway in cultured primary astrocytes. *Nanoscale Research Letters*, 9 (1): 117-117.

Wang, L., Liu, X., Hu, X., Song, S. and Fan, C. 2006a. Unmodified gold nanoparticles as a colorimetric probe for potassium DNA aptamers. *Chemical Communications*, (36): 3780-3782.

Wang, M., Gu, X., Zhang, G., Zhang, D. and Zhu, D. 2009. Continuous Colorimetric Assay for Acetylcholinesterase and Inhibitor Screening with Gold Nanoparticles. *Langmuir*, 25 (4): 2504-2507.

Wang, X., Tian, J., Fei, C., Lv, L., Wang, Y. and Cao, G. 2015. Rapid construction of TiO2 aggregates using microwave assisted synthesis and its application for dye-sensitized solar cells. *RSC Advances*, 5 (12): 8622-8629.

Wang, Z., Lévy, R., Fernig, D. G. and Brust, M. 2006b. Kinase-Catalyzed Modification of Gold Nanoparticles: A New Approach to Colorimetric Kinase Activity Screening. *Journal of the American Chemical Society*, 128 (7): 2214-2215.

Waseda, Y., Matsubara, E. and Shinoda, K. 2011. Fundamental Properties of X-rays. In: Waseda, Y., Matsubara, E. and Shinoda, K. eds. *X-Ray Diffraction Crystallography: Introduction, Examples and Solved Problems*. Berlin, Heidelberg: Springer Berlin Heidelberg, 1-20. Available: https://doi.org/10.1007/978-3-642-16635-8_1 (Accessed

Watanabe, S., Yoshida, K., Shinkawa, K., Kumagawa, D. and Seguchi, H. 2010. Thioglucose-stabilized gold nanoparticles as a novel platform for colorimetric bioassay based on nanoparticle aggregation. *Colloids and Surfaces B: Biointerfaces*, 81 (2): 570-577.

Wei, H., Chen, C., Han, B. and Wang, E. 2008. Enzyme Colorimetric Assay Using Unmodified Silver Nanoparticles. *Analytical Chemistry*, 80 (18): 7051-7055.

Wei, H., Li, B., Li, J., Wang, E. and Dong, S. 2007. Simple and sensitive aptamer-based colorimetric sensing of protein using unmodified gold nanoparticle probes. *Chemical Communications*, (36): 3735-3737.

Weir, A., Westerhoff, P., Fabricius, L., Hristovski, K. and von Goetz, N. 2012. Titanium Dioxide Nanoparticles in Food and Personal Care Products. *Environmental Science & Technology*, 46 (4): 2242-2250.

Wiener, J. J. M. and Politzer, P. 1998. Comparison of various density functional methods for computing bond dissociation energies. *Journal of Molecular Structure: THEOCHEM*, 427 (1): 171-174.

Winkler, D. A., Mombelli, E., Pietroiusti, A., Tran, L., Worth, A., Fadeel, B. and McCall, M. J. 2013. Applying quantitative structure–activity relationship approaches to nanotoxicology: Current status and future potential. *Toxicology*, 313 (1): 15-23.

Wu, S., Li, D., Wang, J., Zhao, Y., Dong, S. and Wang, X. 2017. Gold nanoparticles dissolution based colorimetric method for highly sensitive detection of organophosphate pesticides. *Sensors and Actuators B: Chemical*, 238: 427-433.

Wu, Z.-S., Zhang, S.-B., Guo, M.-M., Chen, C.-R., Shen, G.-L. and Yu, R.-Q. 2007. Homogeneous, unmodified gold nanoparticle-based colorimetric assay of hydrogen peroxide. *Analytica Chimica Acta*, 584 (1): 122-128.

Xia, F., Zuo, X., Yang, R., Xiao, Y., Kang, D., Vallée-Bélisle, A., Gong, X., Yuen, J. D., Hsu, B. B. Y., Heeger, A. J. and Plaxco, K. W. 2010. Colorimetric detection of DNA, small molecules, proteins, and ions using unmodified gold nanoparticles and conjugated polyelectrolytes. *Proceedings of the National Academy of Sciences*, 107 (24): 10837-10841.

Xie, X., Xu, W., Li, T. and Liu, X. 2011. Colorimetric Detection of HIV-1 Ribonuclease H Activity by Gold Nanoparticles. *Small*, 7 (10): 1393-1396.

Xie, X., Xu, W. and Liu, X. 2012. Improving Colorimetric Assays through Protein Enzyme-Assisted Gold Nanoparticle Amplification. *Accounts of Chemical Research*, 45 (9): 1511-1520.

Xu, P., Wang, R., Ouyang, J. and Chen, B. 2015. A new strategy for TiO(2) whiskers mediated multi-mode cancer treatment. *Nanoscale Research Letters*, 10: 94.

Xu, X., Han, M. S. and Mirkin, C. A. 2007. A Gold-Nanoparticle-Based Real-Time Colorimetric Screening Method for Endonuclease Activity and Inhibition. *Angewandte Chemie*, 119 (19): 3538-3540.

Xu, X., Wang, J., Yang, F., Jiao, K. and Yang, X. 2009. Label-Free Colorimetric Detection of Small Molecules Utilizing DNA Oligonucleotides and Silver Nanoparticles. *Small*, 5 (23): 2669-2672.

Xue, W., Zhang, G. and Zhang, D. 2011. A sensitive colorimetric label-free assay for trypsin and inhibitor screening with gold nanoparticles. *Analyst*, 136 (15): 3136-3141.

Yang, C., Wang, Y., Marty, J.-L. and Yang, X. 2011. Aptamer-based colorimetric biosensing of Ochratoxin A using unmodified gold nanoparticles indicator. *Biosensors and Bioelectronics*, 26 (5): 2724-2727.

Yoshio, K., Onodera, A., Satoh, H., Sakagami, N. and Yamashita, H. 2001. Crystal structure of ZnO:Li at 293 K and 19 K by x-ray diffraction. *Ferroelectrics*, 264 (1): 133-138.

Yue, J., Chen, Z., E, Y., Chen, L., Zhang, J., Song, Y. and Zhai, Y. 2014. Preparation TiO_2 core-shell nanospheres and application as efficiency drug detection sensor. *Nanoscale Research Letters*, 9 (1): 465.

Zelnik, R., Rabenhorst, E., Matida, A. K., Gottlieb, H. E., Lavie, D. and Panizza, S. 1978. Ibozol, a new diterpenoid from Iboza riparia. *Phytochemistry*, 17 (10): 1795-1797.

Zeng, Z., Mizukami, S. and Kikuchi, K. 2012. Simple and Real-Time Colorimetric Assay for Glycosidases Activity Using Functionalized Gold Nanoparticles and Its Application for Inhibitor Screening. *Analytical Chemistry*, 84 (21): 9089-9095.

Zhan, Y., Liu, R., Wang, W., Li, J., Ou Yang, X. and Zhang, Y. 2016. Total saponins isolated from Radix et Rhizoma Leonticis suppresses tumor cells growth by regulation of PI3K/Akt/mTOR and p38 MAPK pathways. *Environmental Toxicology and Pharmacology*, 41: 39-44.

Zhang, L., Xu, C., Liu, C. and Li, B. 2014. Visual chiral recognition of tryptophan enantiomers using unmodified gold nanoparticles as colorimetric probes. *Analytica Chimica Acta*, 809 (0): 123-127.

Zhang, X., Servos, M. R. and Liu, J. 2012a. Fast pH-assisted functionalization of silver nanoparticles with monothiolated DNA. *Chem. Comm.*, 48 (81): 10114-10116.

Zhang, X., Servos, M. R. and Liu, J. 2012b. Fast pH-assisted functionalization of silver nanoparticles with monothiolated DNA. *Chemical Communications*, 48 (81): 10114-10116.

Zhang, Y., Jiang, J., Li, M., Gao, P., Zhou, Y., Zhang, G., Shuang, S. and Dong, C. 2016. Colorimetric sensor for cysteine in human urine based on novel gold nanoparticles. *Talanta*, 161: 520-527.

Zhang, Y., Li, B. and Xu, C. 2010. Visual detection of ascorbic acid via alkyne-azide click reaction using gold nanoparticles as a colorimetric probe. *Analyst*, 135 (7): 1579-1584.

Zhang, Y. L., Yang, Y., Zhao, J. H., Tan, R. Q., Cui, P. and Song, W. J. 2009. Preparation of ZnO nanoparticles by a surfactant-assisted complex sol–gel method using zinc nitrate. *Journal of Sol-Gel Science and Technology*, 51 (2): 198-203.

Zhao, W., Chiuman, W., Brook, M. A. and Li, Y. 2007a. Simple and Rapid Colorimetric Biosensors Based on DNA Aptamer and Noncrosslinking Gold Nanoparticle Aggregation. *ChemBioChem*, 8 (7): 727-731.

Zhao, W., Chiuman, W., Lam, J. C. F., Brook, M. A. and Li, Y. 2007b. Simple and rapid colorimetric enzyme sensing assays using non-crosslinking gold nanoparticle aggregation. *Chemical Communications*, (36): 3729-3731.

Zhao, W., Lam, J. C. F., Chiuman, W., Brook, M. A. and Li, Y. 2008. Enzymatic Cleavage of Nucleic Acids on Gold Nanoparticles: A Generic Platform for Facile Colorimetric Biosensors. *Small*, 4 (6): 810-816.

Zhao, X., Liu, R., Teng, Y. and Liu, X. 2011. The interaction between Ag+ and bovine serum albumin: A spectroscopic investigation. *Science of The Total Environment*, 409 (5): 892-897.

Zheng, Y., Wang, Y. and Yang, X. 2011. Aptamer-based colorimetric biosensing of dopamine using unmodified gold nanoparticles. *Sensors and Actuators B: Chemical*, 156 (1): 95-99.

Ziegler, T. 1991. Approximate density functional theory as a practical tool in molecular energetics and dynamics. *Chemical Reviews*, 91 (5): 651-667.

----------*o0o*----------

905 **APPENDIX 1**

906 **Table A1**: Literature review table on green synthesis of AgNPs

Green Material	Size (nm)	Morphology	Applications	Citation
 Solanum tuberosum	16 ± 2	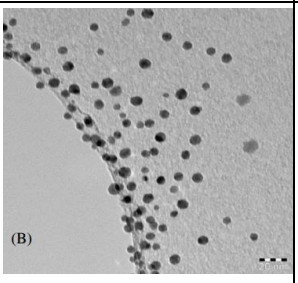	Drug delivery	(Ali, Altaf and Al-Lohedan 2017)
 Radix Puerariae	35	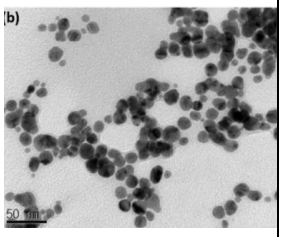	Catalysis	(Balwe *et al.* 2017)
 Syzygium jambos	10	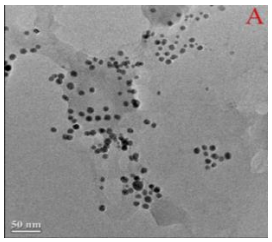	Antimalarial	(Dutta *et al.* 2017)
 Diospyros sylvatica	10	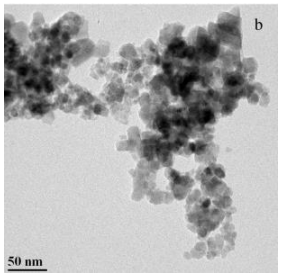	Antimicrobial activity	(Pethakamsetty *et al.* 2017)

907

Appendix 1

----------o0o----------

908 **Table A1:** continues….

Green Material	Size (nm)	Morphology	Applications	Citation
 Beta vulgaris	20	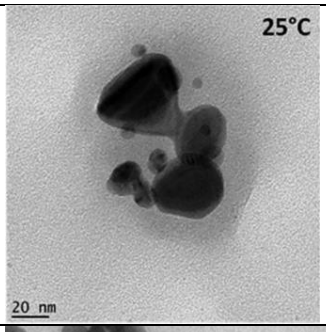	Anticancer	(Venugopal *et al.* 2017)
 Sambucus nigra L	26	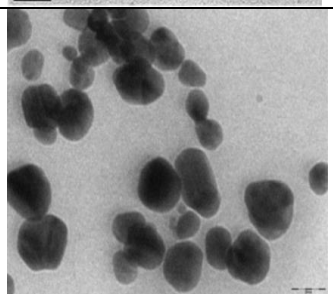	Antioxidant activity	(Moldovan *et al.* 2016)
 Vigna sp. L seeds	24	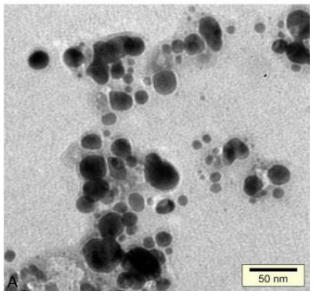	-	(Mohammadi, Pourseyedi and Amini 2016)
 Cichorium intybus L. var. sativus	64	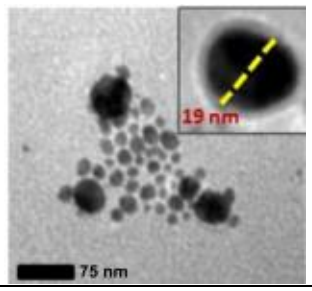	Antibacterial activity	(Gallucci *et al.* 2017)
 Terminalia cuneata	25	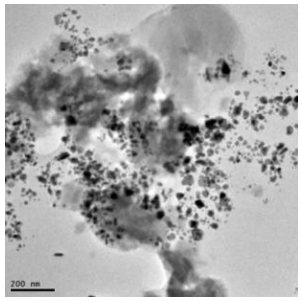	Catalytic activity	(Edison, Lee and Sethuraman 2016)

Appendix 1

----------o0o----------

Table A1: continues….

Green Material	Size (nm)	Morphology	Applications	Citation
 Atrocarpus altilis	38	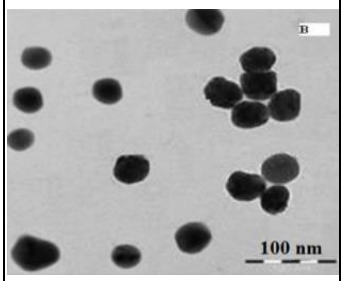	Biomedicine, Water treatment or purification, and Nanobiotechnology	(Ravichandran *et al.* 2016)
 Parkia speciosa Hassk pods	50	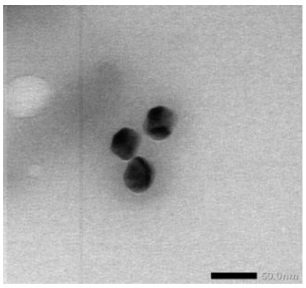	Antibacterial activity	(Fatimah 2016)
 Ginkgo Biloba leaf	16	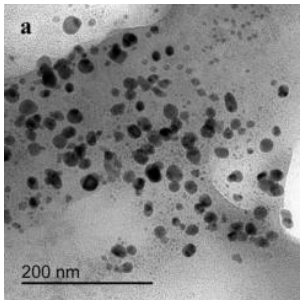	Antimicrobial activity	(Ren *et al.* 2016)
 Calendula officinalis	10	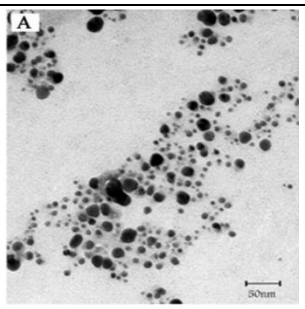	-	(Baghizadeh *et al.* 2015)

Appendix 1

----------o0o----------

Table A1: continues….

Green Material	Size (nm)	Morphology	Applications	Citation
 Butea monosperma leaf	80	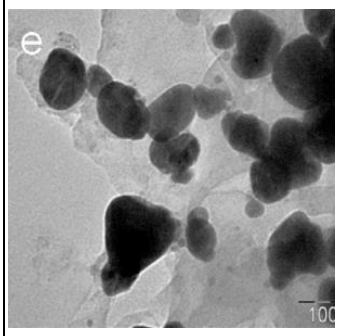	Anticancer	(Patra *et al.* 2015)
 Azadirachta indica leaf	5	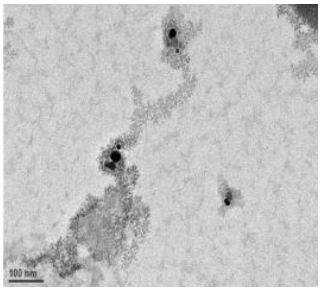	Antimicrobial activity	(Ahmed *et al.* 2016a)

----------o0o----------

APPENDIX 2

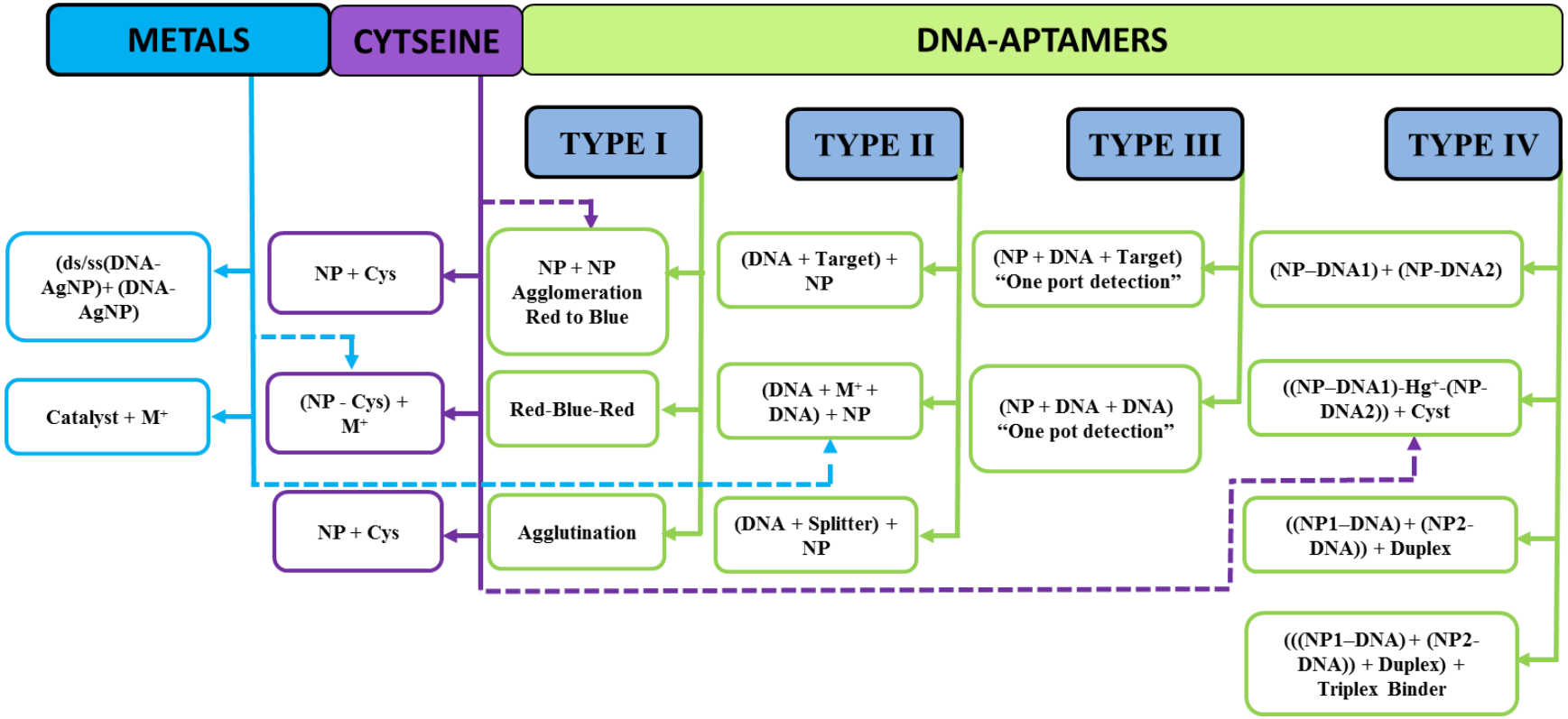

Figure A1: Possible colorimetric detection approaches for metals, ligands and macromolecules.

Appendix 2

----------*o0o*----------

Table A2.1: Biomolecule-sensing based on AuNPs or AgNPs aggregation.

Nanoparticle (size)	**Analyte/s**	**Sample/s**	**Functionalization**	**Analytical performance**	**Ref**
AuNPs Monodisperse	Bisphenol-A	Urine and water samples	Aptamer–AuNPs	LOD: 0.01 pg mL^{-1} LDR: 10 000 to 0.1 pg mL^{-1}	(Ragavan, Selvakumar and Thakur 2013)
AuNPs (40–50 nm) Monodisperse	Concanavalin A	Lectin (jack beans)	Thioglucose-AuNPs	LOD: 9 nM LDR: 10–100 nM (R^2 = 0.983)	(Watanabe *et al.* 2010)
AuNPs (12.33 nm) Monodisperse	Maltose, mannose, glucose, lactose and D-mannopentaose	Carbohydrate-AuNPs	Carbohydrate–protein interactions	NR	(Chuang *et al.* 2009)
AuNPs (15, 20, and 2.5 nm) Monodisperse	Cysteine, glutathione and glutathione disulfide	Blood/serum	Citrate-AuNPs: 15 nm CTAB-AuNPs: 20 nm $NaBH_4$-coated AuNPs: 2.5 nm	LDR: cysteine, NR LDR: glutathione: 10–100 and 200–800 µM LDR: glutathione disulfide 10–300 and 400–800 µM LOD: cysteine <0.5 LOD: glutathione 10 µM LOD: glutathione disulfide 10 µM	(Ghasemi, Hormozi-Nezhad and Mahmoudi 2015b)
AuNPs (~13 nm) Monodisperse	Dopamine	Interferent: ascorbic acid	AuNPs induced by copper ions	LOD: 30 nM LDR 1: 33 nM to 100 nM LDR 2: 0.1 µM to 4.5 µM	(Zhang, Li and Xu 2010)
AuNPs (15 nm) Monodisperse	Dopamine (DA)	Spiked serum	DA inhibits melamine-induced AuNP aggregation	LOD: 33 nM LDR: 33 nM to 3.33 mM	(Chen *et al.* 2015)

Appendix 2

----------*o0o*----------

Table 2.1; Continues

Nanoparticle (size)	**Analyte/s**	**Sample/s**	**Functionalization**	**Analytical performance**	**Ref**
AuNPs (13 nm) Monodisperse	Dopamine	Common interferents, such as 3,4-dihydroxyphenylalanine (DOPA), catechol, 3,4-dihydroxyphenylacetic acid (DOPAC), homovanillic acid (HVA), epinephrine (EP) and ascorbic acid (AA).	The aptamer conformational change could facilitate salt-induced AuNP aggregation 58-mer dopamine-binding aptamer (DBA)	LOD: 360 nM LDR: 0.54 -5.4 μM	(Zheng, Wang and Yang 2011)
AuNPs ±15 nm Multi-dispersed	Dopamine (DA)	Human urine, human serum	DA-induced aggregation of 4-amino-3-hydrazino-5-mercapto-1,2,4-triazol (AHMT) –AuNPs through hydrogen-bonding interactions	LOD: 70 nM LDR: 0.2–1.1 μM	(Feng *et al.* 2013)
AuNPs Monodisperse	Dopamine (DA)	Human serum	DA colorimetric sensing based on AuNP aggregation induced by copper ions	LOD: 200 nM LDR: 0.5–10 μM	(Su *et al.* 2012)
AgNPs (NR) Monodisperse	Coralyne	Selectivity test against intercalating ligands, ethidium bromide (EB) and daunomycin (DM)	Homoadenine-AgNPs, label-free colorimetric detection of small molecules using DNA oligonucleotides and AgNPs	LOD: 0.25 coralyne molecules/adenine base	(Xu *et al.* 2009)
AgNPs (5–15 nm) Multi-disperse	4-nitroaniline (4-NA)	self-assembled AgNPs on DNA	4-NA reduction to para-phenylenediamine		(Kundu 2013)

Appendix 2

----------*o0o*----------

Table 2.1; Continues

Nanoparticle (size)	Analyte/s	Sample/s	Functionalization	Analytical performance	Ref
AgNPs (12 ± 2 nm) Multi-disperse	Adenine, guanine, cytosine, thymine	NR	Strength of interactions between the fundamental chemical components of DNA and AgNP surfaces	NR	(Basu *et al.* 2008)
AuNPs (13 nm) Multi-disperse	Ampicillin	ssDNA aptamer-AuNPs	Colorimetric assay of ampicillin using specific aptamers	LOD: 5 ng mL^{-1}	(Song *et al.* 2012)
AuNPs	Oxytetracycline	Tetracyclines (TCs) as counter targets	Ultrasensitive colorimetric detection of oxytetracycline using shortened aptamer	LOD: 0.1 nM	(Kwon, Ahmad Raston and Gu 2014)
AuNPs (13 nm)	Oxytetracycline	Aptamer-AuNPs	Aptamer-specific colorimetric assay	LOD: 25 nM LDR: 25 nM to 1 µM	(Kim *et al.* 2010)
AuNPs (18 nm) Monodisperse	Bisphenol a	Water samples	AuNP aggregation by competitive binding of bisphenol A and aptamer	LOD: 0.1 ngmL^{-1}	(Mei *et al.* 2013)
AuNPs (13 nm) Multi-disperse	Ochratoxin A	Standards	Aggregation occurs as random coil structures to compact rigid antiparallel G-quadruplexes	LDR: 20 to 625 nM LOD: 20 nM	(Yang *et al.* 2011)
AuNPs (13 nm) Monodisperse	Cysteine	Amino acids, glutathione, thioglycolic acid and mercaptoethyl alcohol	2:1 cysteine/Cu^{2+} complex	LOD: 10 nM	(Li and Li 2009)
AuNPs (13 nm) Monodisperse	Ascorbic acid	Fruit juices	Alkyne–azide click reaction	LOD: 3.0 nM	(Zhang, Li and Xu 2010)

Appendix 2

----------*o0o*----------

Table 2.1; Continues

Nanoparticle (size)	Analyte/s	Sample/s	Functionalization	Analytical performance	Ref
AuNPs (NR) Monodisperse	Cysteine	19 amino acids	ssDNA-AuNPs	LOD: 100 nM LDR: 0.1 to 5 μM	(Chen *et al.* 2009)
AuNPs (20.1±1.8 nm) Multi-disperse	Influenza B/Victoria, influenza B/Yamagata	Virus dilution (hemagglutination assay titer, 512)	Sialic acid-AuNPs	LOD: 0.09 vol%. upper limit of linearity 2.5 vol %	(Lee *et al.* 2013)
AuNPs (13 nm) Monodisperse	Tryptophan enantiomers	D/L enantiomers	AuNPs	LOD: 0.1 μM	(Zhang *et al.* 2014)
AuNPs (~11.89 nm) Mono-disperse	Arginine, histidine, lysine	Urine samples	Quercetin-AuNPs	LOD: 0.04, 0.03, and 0.02 μM. LDR: 2.5–1,250 μM (Arg) and 1–1,000 μM (His and Lys),	(Rawat and Kailasa 2014)
AuNPs-I (15 nm) AuNPs-II (30 nm) AuNPs-III (40 nm) Multi-disperse	Melamine	Pre-treated milk	Citrate-AuNPs	AuNPs-I (2.37 x10^{-8} M) AuNPs-II (3.3 x 10^{-8} M) AuNPs-III (8.9 x 10^{-8} M)	(Paul *et al.* 2015)
AgNPs (NR) Mono-disperse	Cysteine	Various metals	2:1 cysteine/Ca^{2+} complex	LOD: 83 nM LDR: 0.25 – 10 μM	(Hajizadeh *et al.* 2012)
AgNPs (10 – 15 nm) Multi-disperse	Cysteine	10 mM of nine amino acids	2:1 cysteine/Cr^{3+} complex	LOD: 1 nM	(Ravindran *et al.* 2011)

Appendix 2

----------*o0o*----------

Table 2.1; Continues

Nanoparticle (size)	Analyte/s	Sample/s	Functionalization	Analytical performance	Ref
AgNPs (10-20 nm) Multi-disperse	Dopamine, L-DOPA, noradrenaline adrenaline	Tyrosinase	AgNPs	LOD: dopamine, L-DOPA and noradrenaline 2.5 µM adrenaline 20 µM tyrosinase activity~10 units (~100 μg mL^{-1})	(Baron, Zayats and Willner 2005)
AuNPs (~ 13 nm) Multi-disperse	Kanamycin	Other antibiotics: streptomycin, sulfadimethoxine and ampicillin	ssDNA aptamer-AuNPs	LOD: 10 nM	(Song *et al.* 2011)
AuNPs (~ 13 nm) Mono-disperse	Sulfadimethoxine (SDM)	NR	AuNPs	LDR: 50 ng mL^{-1} to 1.0 µg mL^{-1} LOD: 50 ng mL^{-1}	(Chen *et al.* 2013)
AuNPs (~15 nm) Multi-disperse	Penicillin G	Different penicillins	CTAB-AuNPs	LOD: 0.007 mg mL^{-1}	(Tiwari 2010)
AuNPs (20 nm) Mono-disperse	Cysteine	19 essential amino acids	DNA-AuNPs	LOD: 100 nM LDR: 100 nM – 2 µM	(Lee *et al.* 2008)
AuNPs (13 nm) Multi-disperse	Adenosine	inosine, guanosine, and cytosine	aptamer-OD-AuNPs	LOD: 10 µM	(Zhao *et al.* 2007a)
AuNPs (13 nm) Mono-disperse	Adenosine and caffeine	Other nucleosides	Aptamers	LOD: 0.3 mM	(Liu and Lu 2006)

Appendix 2

----------*o0o*----------

Table 2.1; Continues

Nanoparticle (size)	**Analyte/s**	**Sample/s**	**Functionalization**	**Analytical performance**	**Ref**
AuNPs (15 nm) Mono-disperse	Digitoxin	Rat serum	AuNPs	LOD: 571 pM	(Sarreshtehdar Emrani *et al.* 2015)
AuNPs (10.8-13.1 nm) Multi-disperse	Cysteine	Interferents: Na^{+}, Cu^{2+}, Cl^{+} and urea	AuNPs	LDR: 0.1 to 0.6 ppm LOD: 0.01ppm	(Jongjinakool *et al.* 2014)
AgNPs (5 – 20 nm) Multi-disperse	Cysteine/cystine	Other amino acids	AgNPs	LDR: 25–250 µM LOD: 2.5 ppm	(Athilakshmi, Mohan and Chand 2013)
AgNPs (8 nm) Mono-disperse	Cysteine and homocysteine	Human urine and plasma samples	Non-ionic fluorosurfactant-AuNPs,	LOD: 0.4 µM.	(Gao *et al.* 2013)
AgNPs (8±1.6nm) Multi-disperse	Cysteine	Human urine and plasma samples	Fluorosurfactant-AgNPs	LOD: 0.05 µM. LDR: 1.5–6.0 µM	(Chen *et al.* 2014)
AgNPs (9.5±2.0 nm) Multi-disperse	Cysteine	Serum and artificial cerebrospinal fluid	AgNPs and Ca^{2+}	LDR: 0.1–1000 µM LOD: 0.1 µM	(Han *et al.* 2014)
AuNPs (20.0±1.4) nm Multi-disperse	Cysteine	Human urine	Pectinase-protected AuNPs	LDR: $4.85x10^{-6}$ to 302 µM and 3.25 to 0.103 mM LOD: $4.6x10^{-9}$ M.	(Zhang *et al.* 2016)
AuNPs (13 nm) Monodisperse	Cysteine	Brain microdialysate (sample), lactate, ascorbic acid and glucose (interferents)	Cysteine-AuNPs	LDR: 0.166 to 1.67 µM LOD: 0.1 µM	(Qian *et al.* 2012)

Appendix 2

----------*o0o*----------

Table 2.1; Continues

Nanoparticle (size)	Analyte/s	Sample/s	Functionalization	Analytical performance	Ref
AuNPs (13 nm) Monodisperse	Pyruvic acid	Interferents: lactic acid (LA), ascorbic acid (AA) and glucose.	AuNPs	LDR: 5.6 µM to 168.0 µM LOD: 3.0 µM	(Li *et al.* 2014)
AuNPs (13 nm) Monodisperse	Sulfadimethoxine (SDM), kanamycin (KAN) and adenosine (ADE)	Mixture of KAN, SDM and ADE	Aptamer of KAN, SDM and ADE (1:1:1 mixture).	NR	(Liu *et al.* 2014)
AuNPs (13 nm) Monodisperse	17β-estradiol	Intereferents: methanol, diethylstilbestrol, bisphenol A, 19-nortestosterone, estroil, estrone	AuNPs	LOD: 0.1 ng mL^{-1}	(Liu *et al.* 2014)
AuNPs (20 nm) Monodisperse	Caffeine	ATP and target-doped blood serum	AuNPs	LOD: 1.25 µM	(Xia *et al.* 2010)
AuNPs (13 nm) Monodisperse	Parathion	Sea and tap water	Parathion inhibits AChE-induced aggregation of AuNPs	LDR: 15 to 65 ppb and 140 to 1000 ppb LOD: 0.7 ppb (2.4 nM)	(Wu *et al.* 2017)

CTAB: cetyl trimethyl ammonium bromide; OD: oligonucleotides; SDM: sulfadimethoxine; KAN: kanamycin; ADE: adenosine; AChE: acetylcholinesterase, Cyt C: cytochrome c.; LDR: linear dynamic range; LOD: limit of detection

Appendix 2

----------*o0o*----------

Table A2.2: DNA/protein sensing based on AuNP aggregation

Nanoparticle (size)	Analyte/Target	Functionalization	Analytical application	Analytical performance	Ref.
AuNPs (13 nm) and AgNPs (10 -20 nm) Monodisperse	DNA3 complementary DNA	DNA1-AuNPs DNA2-AgNPs	Complementary DNA recognition	NR	(Zhang, Servos and Liu 2012b)
AuNPs (12.33 nm) Monodisperse	Maltose > mannose > glucose > lactose > MAN5.	Carbohydrates-AuNPs	carbohydrate–lectin interactions	NR	(Chuang *et al.* 2009)
AuNPs (13-nm) Monodisperse	Lysozyme	HSA-AuNPs	Colorimetric detection	LOD: 50 nM.	(Chen *et al.* 2008)
AgNPs (10-15 nm) Monodisperse	Globular proteins (BSA and IgG)	AgNPs	Concentration-dependent particle agglutination	LOD: 10 to 80 μg mL^{-1}	(Siddhartha and Debabrata 2010)
AuNPs and AgNPs Monodisperse	Specific DNA sequence	AuNPs and AgNPs	Detection of DNA through nucleic acids (PNA) hybridization	LOD: DNA/PNA ratio of 0.05	(Kanjanawarut and Su 2009)
AuNPs (50 nm) Multidisperse	Con A	p-Aminophenyl-D-mannose-AuNPs	Carbohydrate–lectin system	LOD: 9.0 nM (R^2 = 0.983) LDR: 10-100 nM	(Watanabe *et al.* 2010)
AuNPs Multidisperse	PDGFs and PDGFR	Apt-AuNPs	Protein analysis and cancer diagnosis	-2.5-10 and 10-20 nM, respectively, for 0.42 nM Apt-AuNPs -25-75 and 75-200 nM, respectively, for 8.4 nM Apt-AuNPs.	(Huang *et al.* 2005)
AuNPs (32 nm) Monodisperse	Con A binding partners	Mannopyranoside-encapsulated gold nanoparticles (Man-AuNPs)	Competitive colorimetric assay for ConA binding partners through protein–protein interactions	NR	(Tsai, Yu and Chen 2005)

Appendix 2

----------*o0o*----------

Nanoparticle (size)	Analyte/Target	Functionalization	Analytical application	Analytical performance	Ref.
AuNPs (13 nm) Monodisperse	24-bp polynucleotide target	AuNPs capped with 3¢- and 5¢ (alkanethiol) oligonucleotides	Hybridization of the target with the probes		(Storhoff *et al.* 1998)
AuNPs (20 nm) Monodisperse	H_2N-Cys-Tyr(PO_3^{2-})-Arg-OH	AuNPs	Sensing phosphatase activity of alkaline phosphatase	54: 3.4 uM of peptide : alkaline phosphate	(Choi, Ho and Tung 2007)
AuNPs (15 nm) Monodisperse	Bla molecules	AuNPs	β-Lactamase activity Identification of Bla molecules and screening for Bla inhibitors	60 pM	(Liu *et al.* 2007)
AgNPs (31 nm) Multidisperse	AgNP-oligonucleotide conjugates	DNA-AgNPs	Hybridization of two complementary DNA-AgNPs	NR	(Lee *et al.* 2007)
AuNPs (13 nm) Monodisperse	Single-stranded DNA cleavage	AuNPs	Enzymatic cleavage and oxidative damage of single-stranded DNA	NR	(Shen *et al.* 2009)
AuNPs (14 nm) Monodisperse	HIV-1 ribonuclease H	AuNPs	Colorimetric detection of HIV-1 ribonuclease H activity by AuNPs	27 units mL^{-1}	(Xie *et al.* 2011)
AuNPs (13 nm) Monodisperse	Tyrosin	AuNPs	Crosslinking/ aggregation of Au-NPs based on trypsin-catalyzed hydrolysis of Arg6	1.6 ng mL^{-1}	(Xue, Zhang and Zhang 2011)
AuNPs Monodisperse	Methyltransferase activity	DNA-AuNPs	Colorimetric assay for endonuclease/ methyltransferase activity and inhibition	NR	(Song *et al.* 2009)
AuNPs (13 nm) Monodisperse		DNA-modified AuNPs	Enzymatic cleavage of nucleic acids, colorimetric biosensors	0.5 units mL^{-1}	(Zhao *et al.* 2008)
AuNPs (13 nm) Monodisperse	Thrombin	Aptamer-AuNPs	Colorimetric assay based on the aptamer folding and unfolding	LDR: 0 to 167 nM LOD: 0.83 nM	(Wei *et al.* 2007)
AuNPs (20 nm) Monodisperse	Thrombin	AuNPs	G-quadruplex structure folding	LOD: 10 nM	(Xia *et al.* 2010)

Appendix 2

----------*o0o*----------

Nanoparticle (size)	**Analyte/Target**	**Functionalization**	**Analytical application**	**Analytical performance**	**Ref.**
AuNPs (NR)	Triplex DNA binders: BePI or CORA	Aptamer-AuNPs	Screening triplex DNA binders	NR	(Han, Lytton-Jean and Mirkin 2006)
AuNPs (13.3±1.2 nm) Multidisperse	Thrombin	Fibrinogen-AuNPs (56 nm)	Colorimetric assay for blood plasma	LOD: 0.04 pM LDR: 0.1 to 10 pM	(Chen, Huang and Chang 2010)
AgNPs (NR) Multidisperse	CIAP and PKA	AgNPs	Adenosine phosphorylation and dephosphorylation	LOD: CIAP: 1.0 unit mL^{-1} PKA: 0.022 unit mL^{-1}	(Wei *et al.* 2008)
AuNPs (~ 12.74 nm) Monodisperse	staphylococcal enterotoxin B	AuNPs	Colorimetric assay based on aggregation in the absence of the aptamer	LDR: 10 to 50 ng mL^{-1} LOD : 10 ng mL^{-1}	(Liu *et al.* 2013)
AuNPs (NR) Multidisperse	Aminopeptidase N	Gold nano-composites conjugated with a thermo-responsive copolymer	Activity based on inhibition of the disassembly of Gold nano-composites	AR: 20 to 50 U L^{-1}	(Uehara, Fujita and Shimizu 2009)
AuNPs (15.1 nm) Multidisperse	β-galactosidase and β-glucosidase	Gal-Lip-AuNPs and Glc-Lip-AuNPs	Glycosidase inhibitor screening	LODs: β-galactosidase 9.2 nM and β-glucosidase 22.3 nM at 20°C	(Zeng, Mizukami and Kikuchi 2012)
AuNPs (26 nm) Monodisperse	ADA	AuNPs	Nucleotide-dependent aggregation	LOD: 0.8227 U L^{-1}	(Zeng, Mizukami and Kikuchi 2012)
AuNPs (13 nm) Monodisperse	Endonuclease	DNA-AuNPs with duplex interconnection	Endonuclease activity and inhibition	NR	(Xu, Han and Mirkin 2007)
AuNPs (13 nm) Monodisperse	Biotin (biotinylation)	Peptide-AuNPs and avidin-AuNPs	Kinase-catalyzed substrate biotinylation	NR	(Wang *et al.* 2006b)
AuNPs (20 nm) Multidisperse	Protein kinase A,	AuNPs	Kinase activity based on the coagulating ability of a cationic substrate peptide and its phosphorylation	NR	(Oishi *et al.* 2008)

Appendix 2

----------*o0o*----------

Nanoparticle (size)	**Analyte/Target**	**Functionalization**	**Analytical application**	**Analytical performance**	**Ref.**
AuNPs (NR) Multidisperse	Acetylcholinesterase	Citrate-AuNPs	AChE-catalyzed hydrolysis of acetylthiocholine	0.6 mU mL^{-1}	(Wang *et al.* 2009)
AuNPs (16 nm) AgNPs (16 nm) Monodisperse	Con A	Mannose AuNPs Mannose-AgNPs	Con A induced aggregation	Mannose -AuNPs LOD: 0.04 µM LDR: 0.04-0.10 µM Mannose-AgNPs: LDR: 0.08 – 0.26 µM LOD: 0.1µM	(Schofield *et al.* 2006)
AuNPs (15 nm) AgNPs (20 nm) Monodisperse	Kaposi's sarcoma associated herpesvirus and Bartonella DNA	Oligonunucleotides-AuNPs Oligonunucleotides-AgNPs	Aggregation reaction with multi-color changes	LOD: 1 nM	(Mancuso *et al.* 2013)
AgNPs (10-15 nm) Multidisperse	BSA and immunoglobulins	AgNPs	Nanoparticle agglutination	LOD: 10 -80 µg mL^{-1}	(Siddhartha and Debabrata 2010)
AuNPs (21 nm) Monodisperse	polyA, polyC, polyU, polyI, BSA, lysozyme, dsDNA,ssDNA	AuNPs	Aggregation due to self-assembly (discrimination and detection)	LOD: Protein ~100 pM Homopolynuclotide ~10 pM	(Lepoitevin *et al.* 2015)
AuNPs (13.2 nm) Monodisperse	Dengue virus	AuNPs	PNA/DNA hybridization	LOD: 0.12 μM	(Abdul Rahman *et al.* 2014)
AuNPs (~13 nm) Monodisperse	ssDNA and dsDNA	AuNPs	DNA sequences based on electrostatic interactions	AR: 100 fmol	(Li and Rothberg 2004)
AuNPs (13 nm) Monodisperse	Abrin	Catalytic AuNPs	Peroxidase-like activity	LDR: 0.2 to 17.5 nM LOD: 0.05 nM	(Hu *et al.* 2015)
AuNPs (13 nm) Monodisperse	Lipase	Tween 20-GNPs	Enzyme-regulated AuNP aggregation	LOD: 0.028 mg mL^{-1} LDR: 0.15 to 1.80 mg mL^{-1}	(Sun *et al.* 2015)

Appendix 2

----------o0o----------

Nanoparticle (size)	**Analyte/Target**	**Functionalization**	**Analytical application**	**Analytical performance**	**Ref.**
AuNPs (50 nm) Multidisperse	Native proteins	DNA-AuNPs	50% human urine	Cluster analysis	(Mao *et al.* 2016)

NR: Not Reported; CIAP: Calf Intestine Alkaline Phosphatase; HSA-AuNPs : Human serum albumin-modified gold nanoparticles, PKA: Protein Kinase A; SEB: Staphylococcal enterotoxin B; LOD: Limit of detection; AR: Activity Range; PDGFs : Platelet-derived growth factors; PDGFR : platelet- derived growth factor receptors,, Con A: Concanavalin A; Man-AuNPs: Mannopyranoside- encapsulated gold nanoparticles; Gal: β-galactosidase and Glc: β-glucosidase; ADA: Adenosine Deaminase; AChE: Acetylcholinesterase, KSHV: Kaposi's sarcoma associated herpesvirus; BePI: benzo[e]pyridoindole; CORA: coralyne, BSA: Bovine serum albumin: PNA: peptide nucleic acid; LDR: linear dynamic range; LOD: limit of detection.

APPENDIX 3

Table A3.1a: Absorption spectroscopy data and colorimetric observations obtained with AgNP10 for the Lys, BSA and ssDNA at 0.1, 1.0 and 10 µg ml^{-1}

NaCl (mM)	Lys	BSA	ssDNA
10	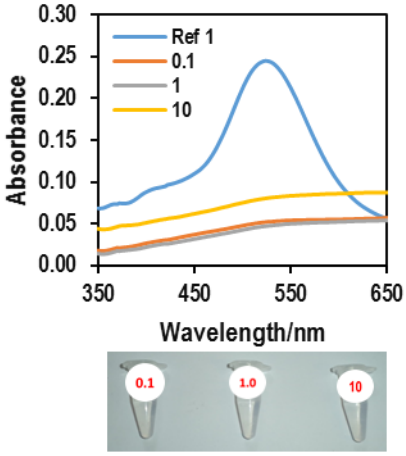	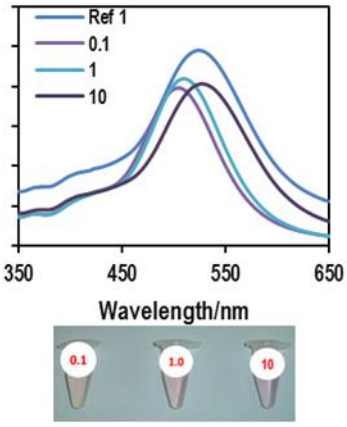	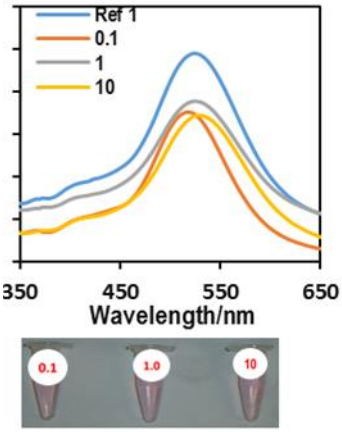
50	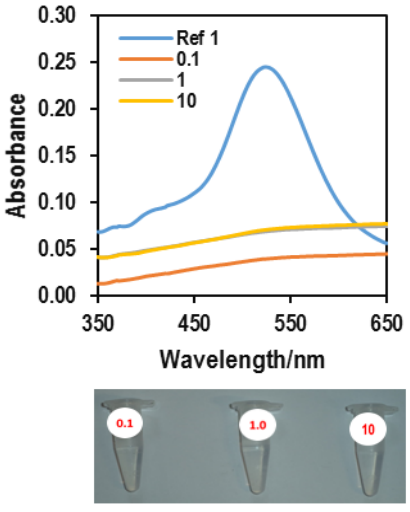	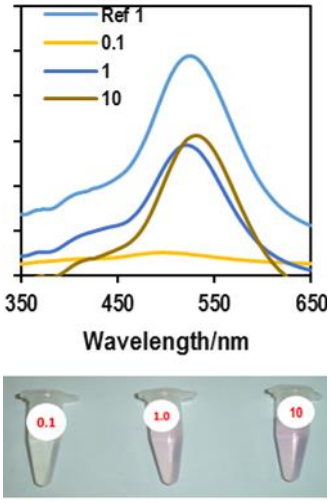	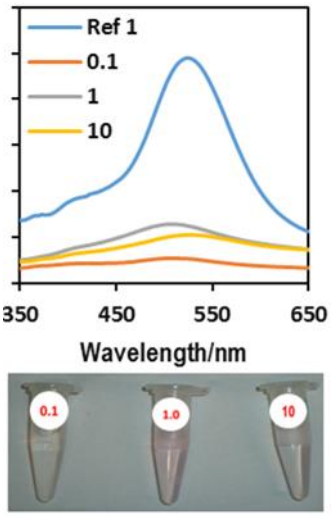
100	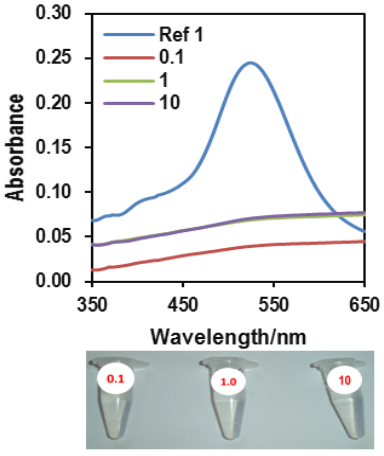	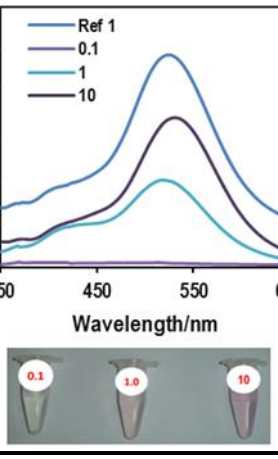	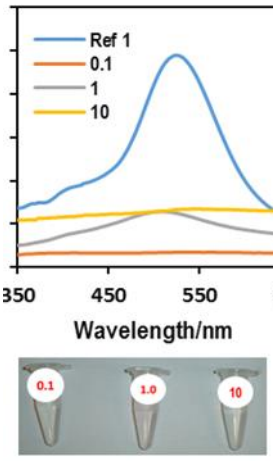

----------*o0o*----------

Table A3.1b: Absorption spectroscopy data and colorimetric observations obtained with AgNP50 for the Lys, BSA and ssDNA at 0.1, 1.0 and 10 µg ml^{-1}

NaCl/mM	Lys	BSA	ssDNA
10	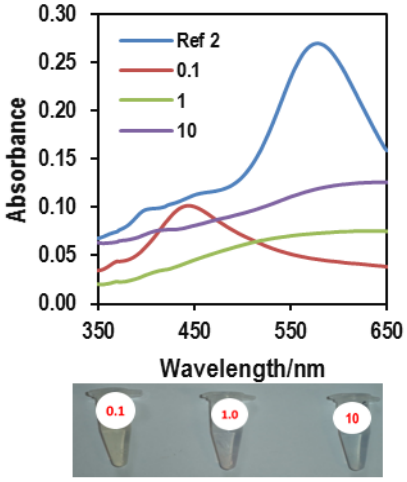	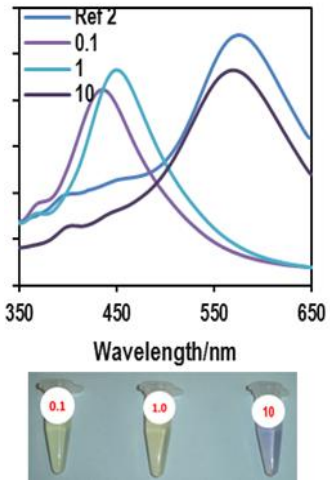	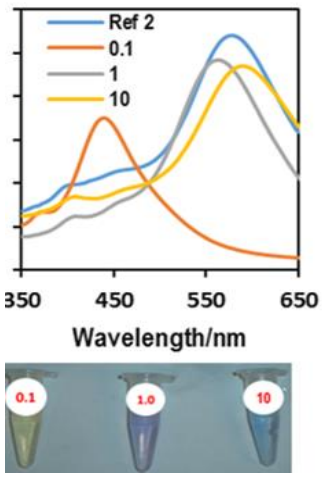
50	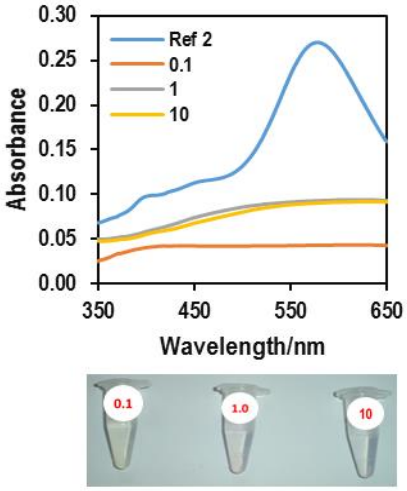	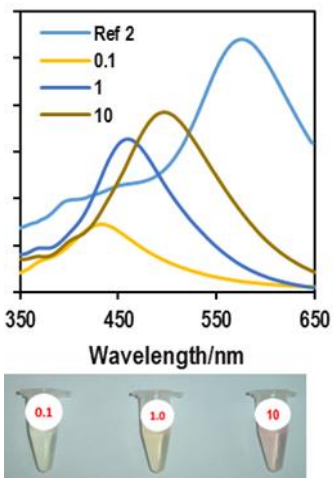	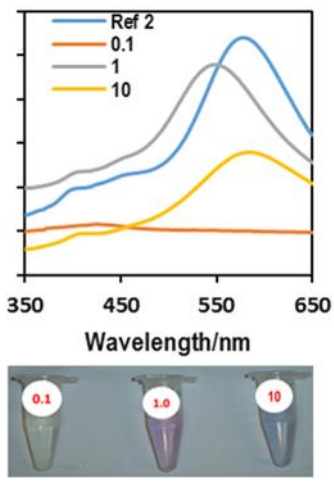
100	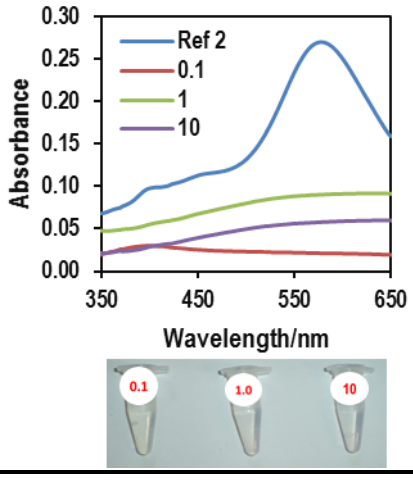	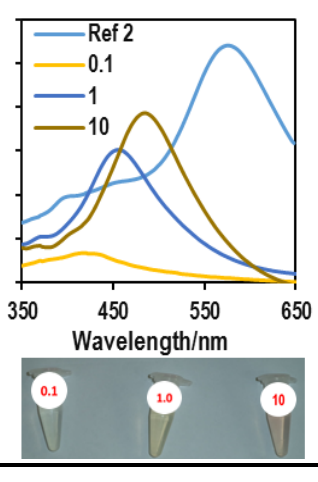	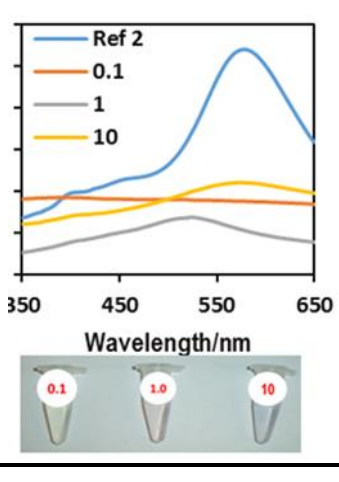

----------*o0o*----------

Table A3.2a. Absorbance spectroscopy data and colorimetric observations obtained with AgNP10 for the dsDNA from salmon, herring and calf at 0.1, 1.0 and 10 µg ml^{-1}

NaCl/mM	Salmon	Herring	Calf
10	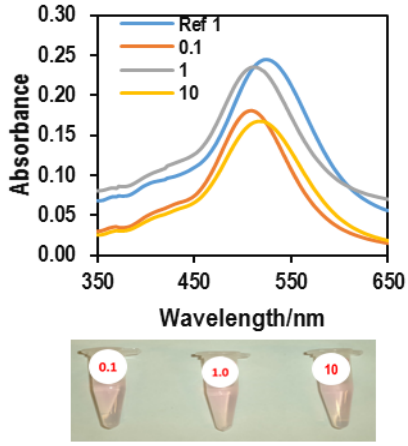	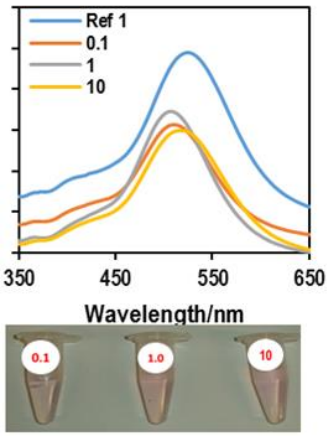	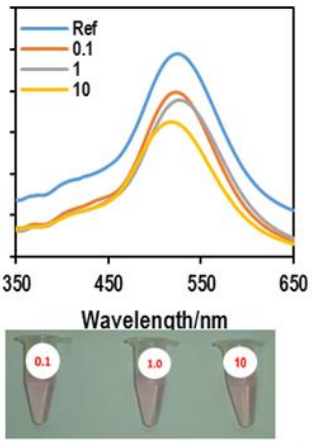
50	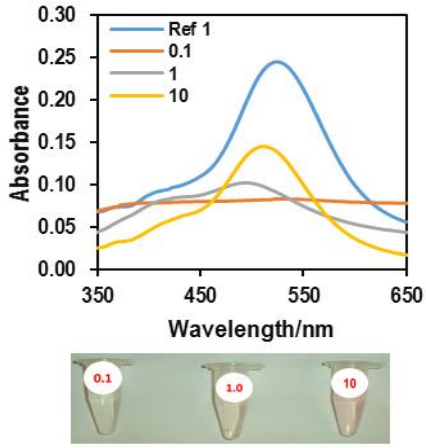	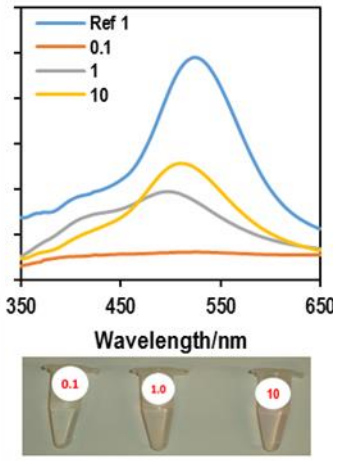	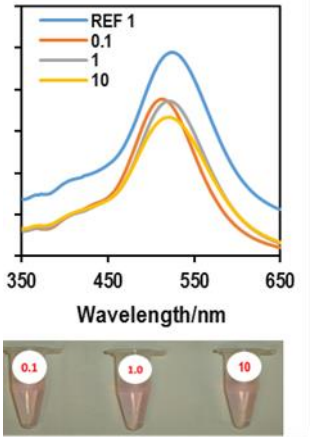
100	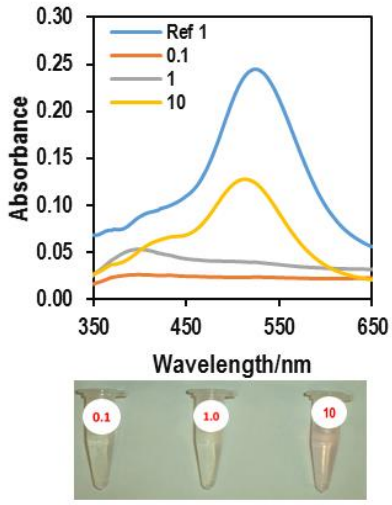	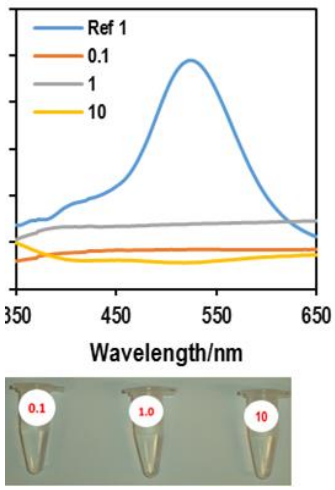	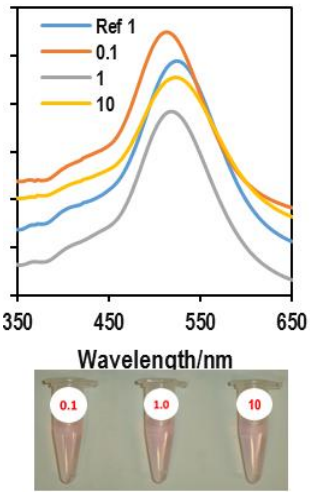

----------*o0o*----------

Table A3.2b. Absorbance spectroscopy data and colorimetric observations obtained with AgNP50 for the dsDNA from salmon, herring and calf at 0.1, 1.0 and 10 µg ml^{-1}

NaCl/mM	Salmon	Herring	Calf
10	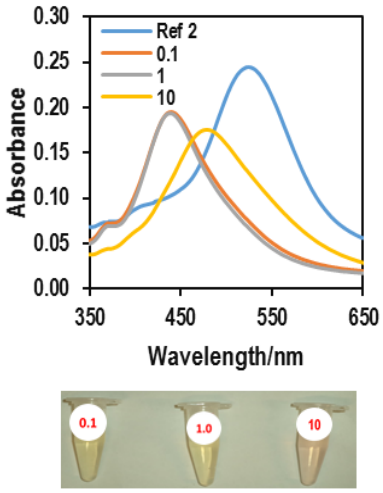	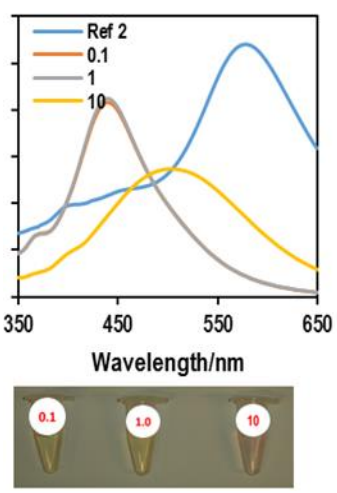	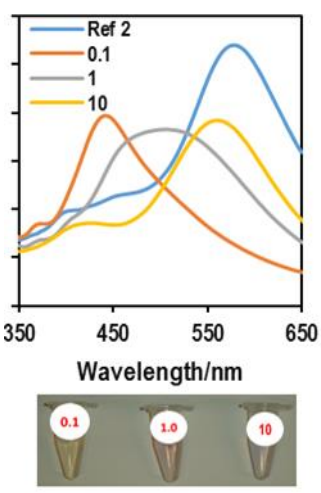
50	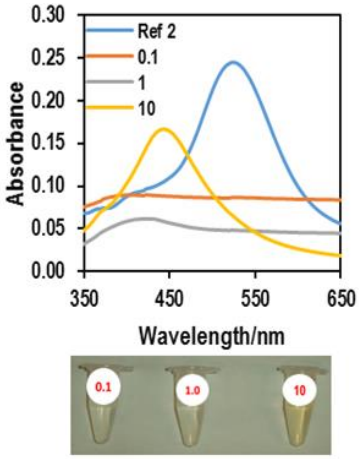	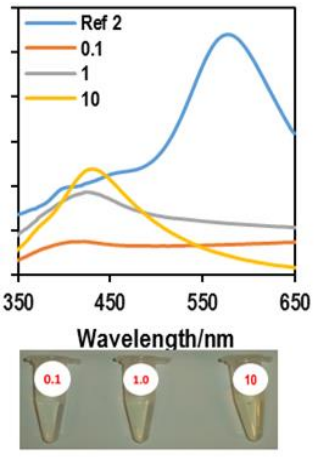	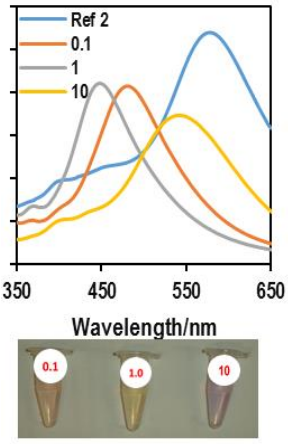
100	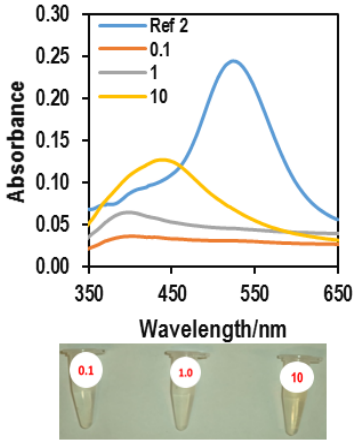	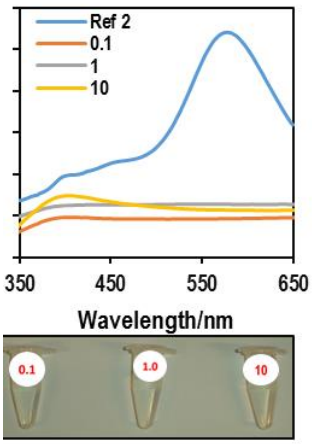	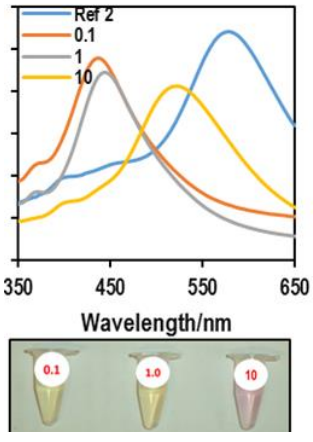

----------*o0o*----------

Table A3.3a. Absorbance spectroscopy data and colorimetric observations obtained with AgNP10 for the polynucleotides at 0.1, 1.0 and 10 µg ml^{-1}

NaCl/mM	poly A	polyC	polyU
10	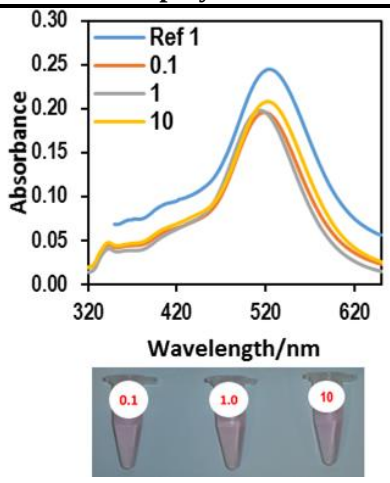	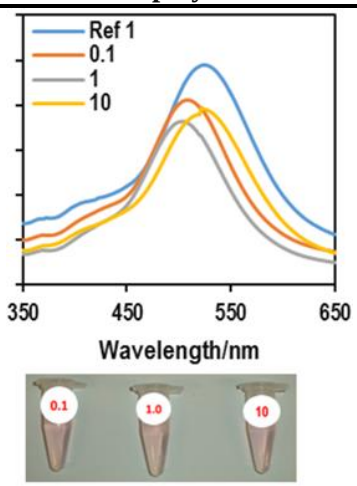	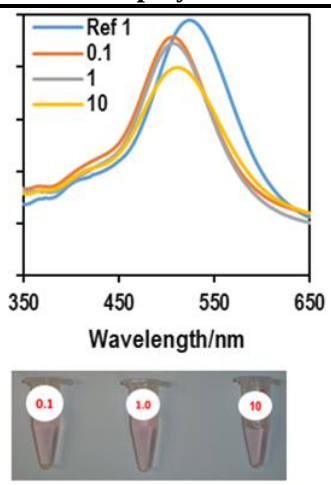
50	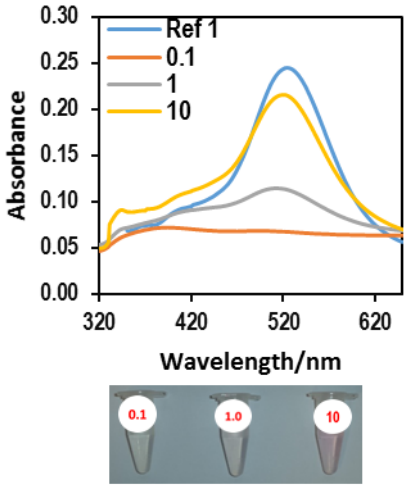	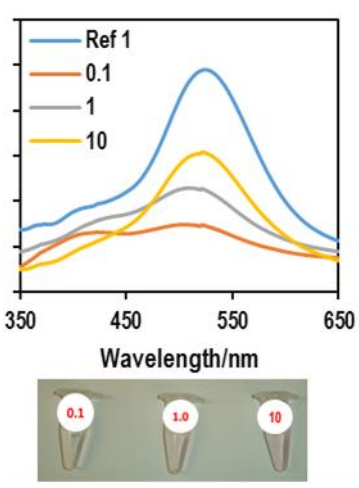	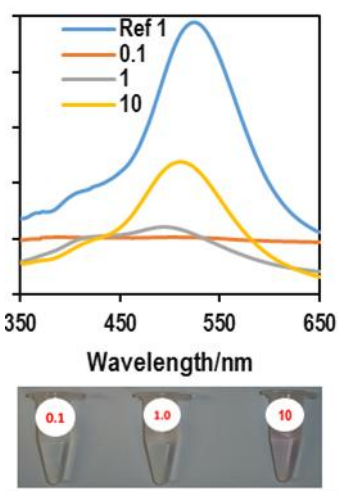
100	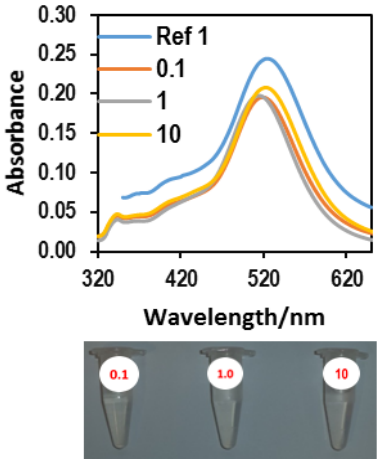	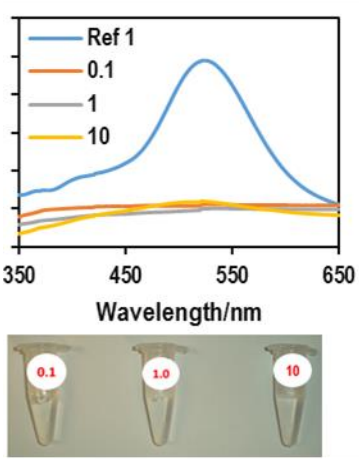	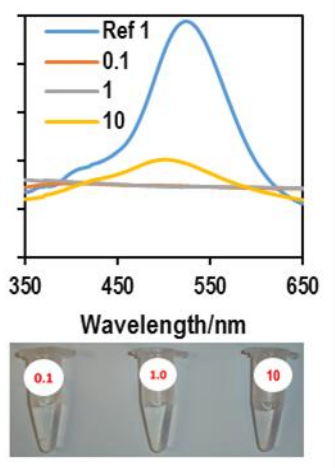

----------*o0o*----------

Table A3.3b. Absorbance spectroscopy data and colorimetric observations obtained with AgNP50 for the polynucleotides at 0.1, 1.0 and 10 µg ml^{-1}

NaCl/mM	polyA	polyC	polyU
10	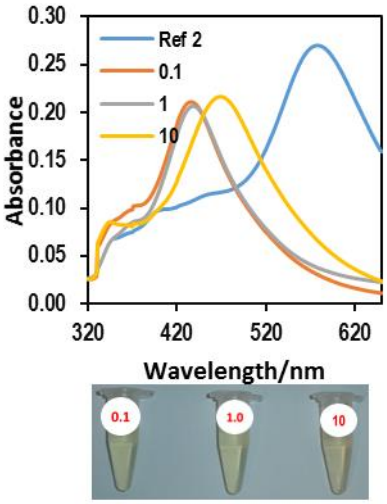	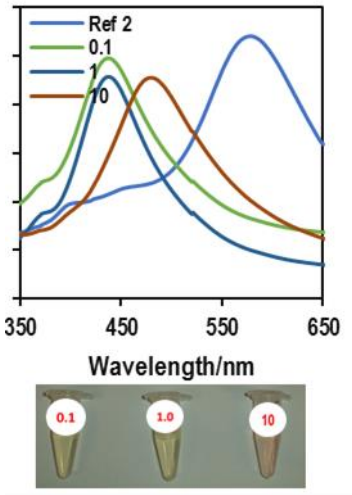	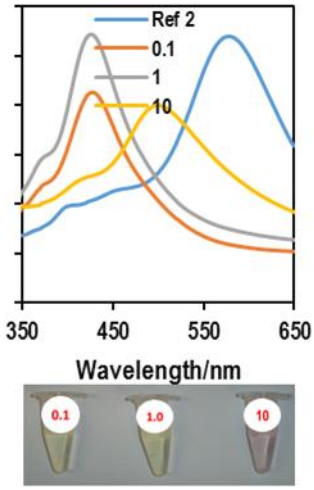
50	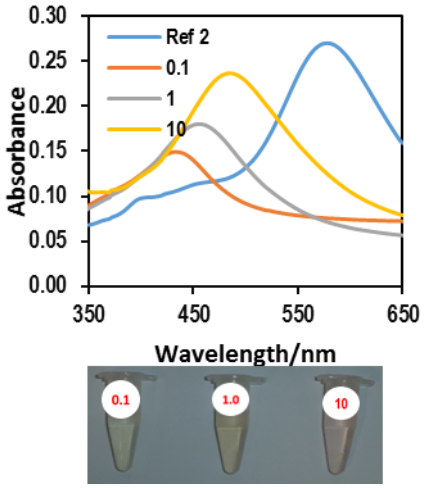	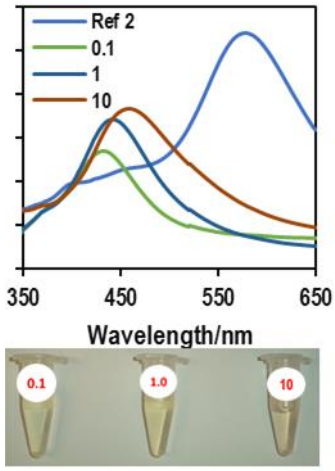	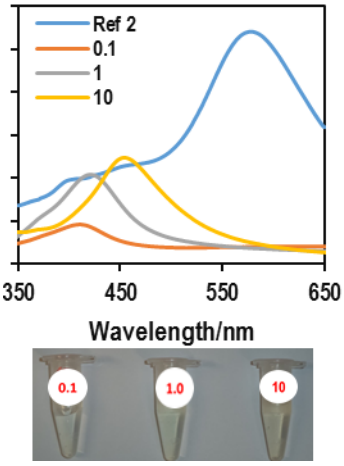
100	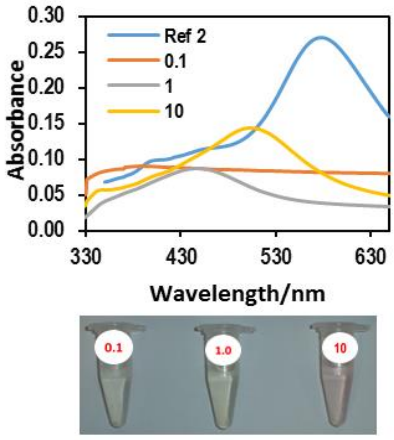	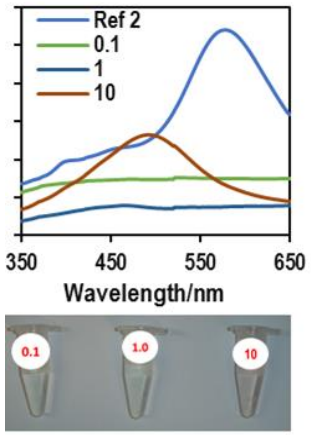	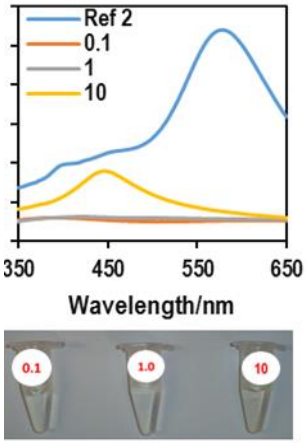

Appendix **3**

----------*o0o*----------

Table A3.4: Summary of absorbance spectroscopy data in relation to the corresponding colorimetric observations

		AgNP10						AgNP50					
		NaCl 10 mM		NaCl 50 mM		NaCl 100 mM		NaCl 10 mM		NaCl 50 mM		NaCl 100 mM	
BioMolecule/μg ml^{-1}		**λ/nm**	**Color**	**λ/nm**	**Color**	**λ/nm**	**Color**	**λ/nm**	**Color**	**λ/nm**	**Color**	**λ/nm**	**Color**
BSA	0.1	498	4	500	1	518	1	436	2	434	2	424	2
	1.0	512	4	526	5	522	4	450	2	462	3	454	3
	10	528	5	530	5	530	5	570	7	498	4	486	4
ssDNA	0.1	522	5	526	1	524	1	440	2	432	2	516	2
	1.0	524	5	526	5	504	4	564	7	552	7	520	4
	10	528	5	508	7	540	1	584	5	576	7	574	7
dsDNA calf	0.1	524	5	526	5	536	5	442	2	452	4	432	2
	1.0	528	5	518	5	530	5	496	5	488	3	442	3
	10	520	5	516	5	494	5	546	7	546	7	520	5
dsDNA her	0.1	508	5	534	1	406	1	448	2	406	1	390	1
	1.0	512	5	506	4	398	1	448	3	420	1	396	1
	10	518	5	526	4	460	1	514	5	434	2	394	1
dsDNA sal	0.1	512	4	528	1	390	1	440	2	446	1	396	1
	1.0	514	4	500	1	398	1	440	2	416	2	400	1
	10	516	4	516	4	520	4	484	4	390	2	446	2
Poly A	0.1	453	2	504	1	492	1	508	2	424	2	450	1
	1.0	453	2	521	1	513	1	519	2	467	3	452	2
	10	477	2	528	4	510	1	527	3	497	4	506	4
Poly C	0.1	515	5	510	1	511	1	442	2	436	1	493	1
	1.0	505	5	516	1	0.0	1	442	2	441	2	465	1
	10	524	5	527	4	0.0	1	489	4	463	3	0.0	3
Poly U	0.1	508	5	505	1	525	1	432	2	416	1	0.00	1
	1.0	514	5	496	1	593	1	432	2	418	1	506	1
	10	519.	5	518	3	507	1	508	5	467	1	450	1

----------*o0o*----------

APPENDIX 4

Table A4.1 Classification of molecules on the basis of GC chromatogram of methanolic extract of *jacaranda mimosifolia* flower.

INFORMATION DETAILS	CHROMATOGRAPHS
1, 6 dimethyldecahydro-napthalene Purity : 384 Fit : 895 Mol. Wt. : 166 Formula : $C_{12}H_{22}$	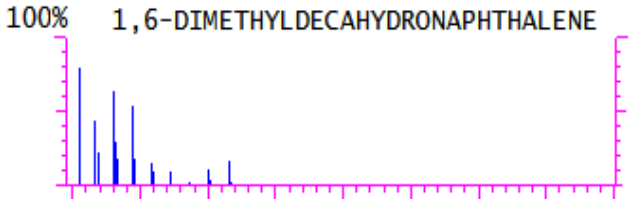
Oleic acid Purity : 559 Fit : 864 Mol. Wt. : 282 Formula : $C_{18}H_{34}O_2$	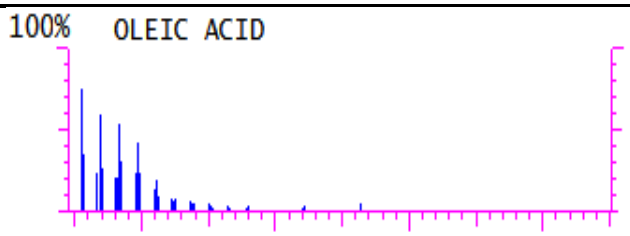
Citronellyl propionate Purity : 387 Fit : 855 Mol. Wt. : 212 Formula : $C_{13}H_{24}O_2$	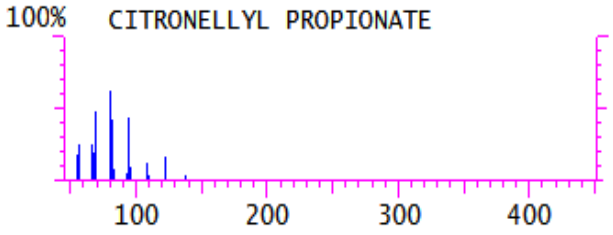

Appendix 4

----------*o0o*----------

Table A4.2 Classification of molecules on the basis of GC chromatogram of methanolic extract of *jacaranda mimosifolia* flower.

INFORMATION DETAILS	CHROMATOGRAPHS
1, 6 dimethyldecahydro-napthalene Purity : 384 Fit : 895 Mol. Wt. : 166 Formula : $C_{12}H_{22}$	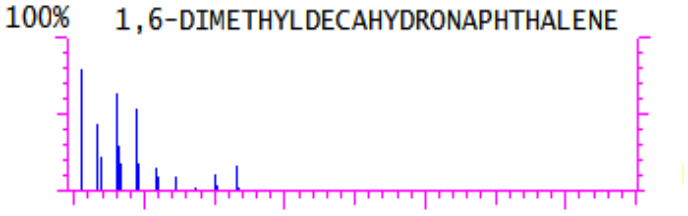
Oleic acid Purity : 559 Fit : 864 Mol. Wt. : 282 Formula : $C_{18}H_{34}O_2$	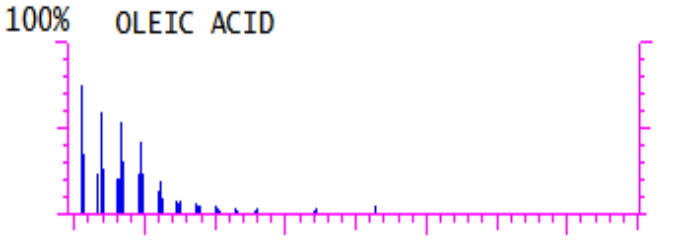
Citronellyl propionate Purity : 387 Fit : 855 Mol. Wt. : 212 Formula : $C_{13}H_{24}O_2$	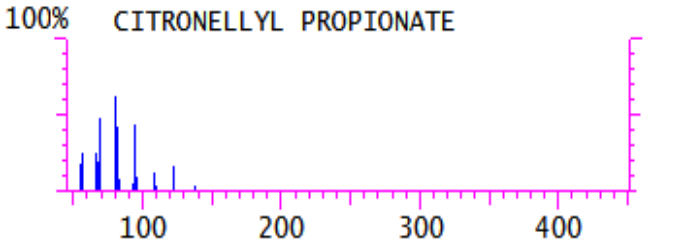

----------*o0o*----------

PUBLICATIONS

ADVANCED ENGINEERING MATERIALS
www.aem-journal.com

A Review of Gold and Silver Nanoparticle-Based Colorimetric Sensing Assays

Myalowenkosi Sabela, Sebastien Balme, Mikhael Bechelany,* Jean-Marc Janot, and Krishna Bisetty*

The nanoparticle colorimetric-based methods have been extensively used for rapid detection, however there are few limitations which can be kept under control or avoided by understanding the crucial parameters involved in these reactions. This review addresses the main parameters that influence colorimetric-based methods and provides a rational classification of the current approaches, by focusing particularly on gold nanoparticles (AuNPs) and silver nanoparticles (AgNPs). The AgNP and AuNP-based colorimetric assays can be very efficient and sensitive especially for biomolecule identification and for metal ion detection in environmental screening. Specifically, this review highlights the detection of metal ions through their coordination with nanoparticle stabilizing ligands. The review also addresses various approaches based on label-free aptasensors to better understand their role as smart colorimetric sensing devices.

1. Introduction

The term *nanoparticle* (NP) defines any small object (from 1 to 100 nm) that behaves as a unit concerning its transport and properties. Indeed, as their properties change in function of their size, particles can be classified based on their diameter. Thus, ultrafine particles (or NPs) are particles with a diameter between 1 and 100 nm, whereas fine particles have a diameter between 100 and 2500 nm. For tailored applications, NPs can be capped with a variety of different anionic and cationic ligands, from displaceable small molecules to polymer coatings. The choice of capping ligand depends on the NPs used that can range from conductive inks to biomedical tools.

Among the known nanoparticles, gold and silver NPs (AuNPs and AgNPs) have been widely studied because of their unique optical, electrical, and photothermal properties. AuNPs and AgNPs show unique optical features in well-dispersed solutions, depending on their level of aggregation which is mostly determined by their specific surface plasmon resonance (SPR) profiles.[1] Metal-noble NPs are small enough to confine their electrons and produce quantum effects. This is a key parameter for naked-eye colorimetric sensing applications, because modifications of their surface charge are transformed into a visible color change. Furthermore, NPs also have a very high extinction coefficient that depends mainly on their size, shape, and inter-particle distance. Such properties enable them to compete with analytical techniques, like absorbance or fluorescence spectroscopy. Colorimetric-based assays have been developed by exploiting the color changes associated with the aggregation of metal-noble NPs.[2] Due to their adaptability, high sensitivity, low cost, and versatility (**Figure 1**), AgNP- and AuNP-based assays have been used for the detection of metal ions,[3] small molecules,[3b,f,4] proteins,[3f,4z,5] deoxyribonucleic acid DNA,[3f,5i,6] and enzymes.[5a,6g,7] AuNPs are often used as sensing elements to develop sensitive, selective, simple, and label-free colorimetric assays.[7h,8] Consequently, NP used as detection agents could be considered as a sort of "litmus test" for target molecules.[5i,9]

Although analytical methods, such as high-performance liquid chromatography, electrophoresis, voltammetry, and fluorescence spectroscopy, are the preferred approaches for the detection of various macromolecules, sensitive, fast, and high-throughput screening methods are still required.[4x] NP-based colorimetric methods are quick and user-friendly detection approaches that take advantage of various chemical mechanisms. For instance, such methods can be used for the rapid detection of influenza viruses through the binding between the influenza virus envelope protein hemagglutinin and sialic acid-stabilized AuNPs,[10] or for high-throughput screening of endonuclease inhibitors.[7e]

In this review, the colorimetric approaches that allows for the naked-eye detection of color changes through ultraviolet-visible (UV-Vis) absorption spectroscopy without fluorescence detection methods are addressed. Specifically, aptamer-based applications for the detection of metal ions, small ligands and biological macromolecules will be described. Accordingly, the methods have been subdivided on the analytes and the NP's surface modifications and not on the basis of the used NPs, as the

Dr. S. Balme, Dr. M. Bechelany, Dr. J.-M. Janot
Institut Européen des Membranes, UMR 5635, Université de Montpellier CNRS, ENSCM, Place Eugène Bataillon, F-34095 Montpellier cedex 5, France
E-mail: sebastien.balme@umontpellier.fr; mikhael.bechelany@umontpellier.fr
M. Sabela, Prof. K. Bisetty
Department of Chemistry, Durban University of Technology, P.O Box 1334, Durban 4000, South Africa

DOI: 10.1002/adem.201700270

Sébastien Balme has obtained his PhD in physical-chemistry in 2005 at Montpellier 2 University on "proteins surface interaction by time resolved confocal fluorescence spectroscopy." He went then for post-doc to Geneva University in physical chemistry department to work on "SPME fiber modification for specific detection of phytosterol in complex matrix." Since 2007, he held an assistant professor position in physical-chemistry at Montpellier 2 university. His research activities are focused on the electrolyte transport through biomimetic nanopore, the interaction of (bio)macromolecule (and dye) with nanostructured material and the confinement effects.

Mikhael Bechelany (born in March 1979) obtained his PhD in Materials Chemistry from the University of Lyon (France) in 2006. Then, he worked as a post-doc at EMPA (Switzerland). In 2010, he became a Scientist (CR) at CNRS. His current research interest in the European Institute of Membranes (UMR CNRS 5635) in Montpellier (France) focuses on novel synthesis methods for metals and ceramics nanomaterials like Atomic Layer Deposition (ALD), electrodeposition, electrospinning, 3D printing, and/or on the nanostructuring using natural lithography (nanospheres, 2D materials and/or membranes). His research efforts include the design of nanostructured membranes for health, environment, and renewable energy.

colorimetric performances of AgNPs or AuNPs are very similar. The applications involving aqueous/water-soluble stabilized NPs with no solid surface arrays, such as glass will be highlighted. To ensure that all key possibilities are fully explored, the different sections herein have been divided as follows: detection of metals, small molecule (cysteine, dopamine), and oligonucleotides (cross-linking).

2. Gold and Silver NP Synthesis, Morphology, and Properties

The most commonly used methods for the synthesis of AgNPs and AuNPs involve reducing AgCl or $AgNO_3$ and $HAuCl_4$ with sodium citrate and sodium borohydride. The AuNP mixture is boiled with vigorous stirring in a round bottom flask fitted with a reflux condenser for approximately 10 min. Color change from yellow to wine red is observed within a few seconds.[4s,z,11] The AuNP solution concentration can be calculated following Beer's law, using the extinction coefficient of $2.7 \times 10^8\ M^{-1}\ cm^{-1}$ at $\lambda = 520$ nm.[12] For AgNPs, 1% tri-sodium citrate is added to 0.3 mM silver nitrate solution, and the mixture stirred for 5 min. After a drop-by-drop addition of 1 mM sodium borohydride solution in the dark, the resulting mixture is stirred at room temperature for 2 h. The bright yellow AgNPs are then filtered through a Millipore syringe (0.45 nm) to remove the precipitate.[4t] NPs are then characterized by diffusion light scattering (DLS) to calculate their hydrodynamic radius in solution, or by transmission electron microscopy (TEM) to describe their morphology (**Figure 2**).

For colorimetric assays, AgNPs have some advantages compared with AuNPs. Specifically, AgNP extinction coefficients are higher than those of AuNPs of the same average size,[7h] but with AuNPs being more popular. This could be explained by the fact that AgNPs functionalization usually leads to their chemical degradation and thereafter the AgNP surface can be easily oxidized, thus reducing their stability.[4f,7h,14] Indeed, Manuco et al.[15] reported that AuNPs are stable for more than 1 month at

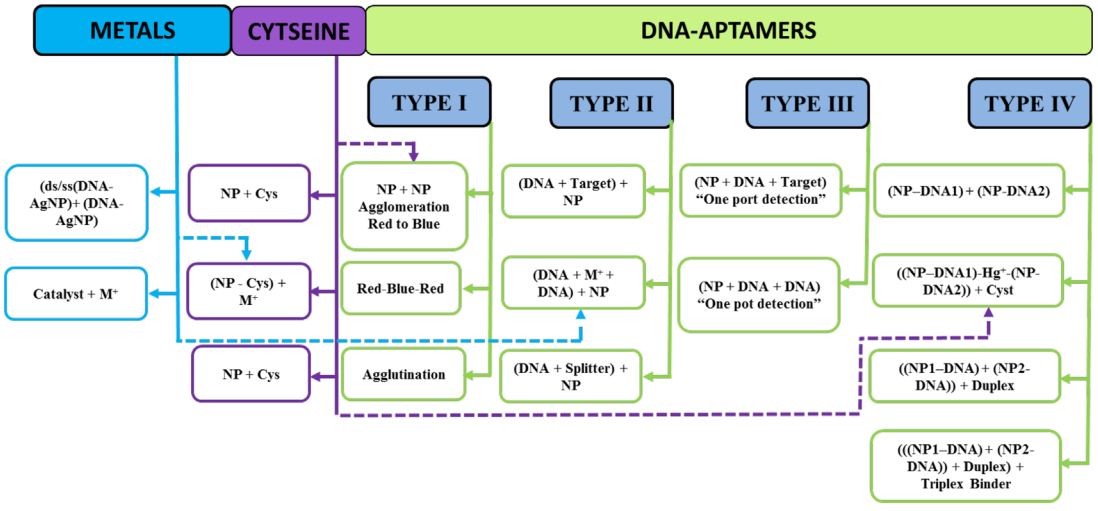

Figure 1. Possible colorimetric detection approaches for metals, ligands, and macromolecules.

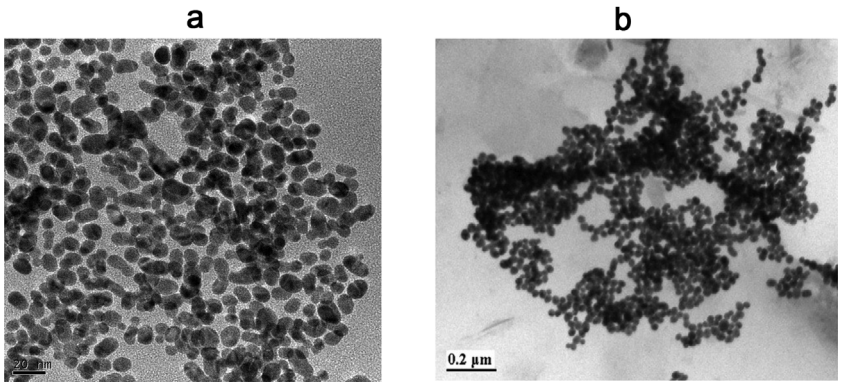

Figure 2. TEM images of a) 13 nm citrate-capped AuNPs from wine-red solution[4s] and of b) guanine-induced AgNP aggregates.[13]

room temperature, whereas AgNPs only for about two weeks. This difference could be linked to the different reaction constants of thiolated gold and silver. The high extinction coefficients and distance-dependent optical properties of AuNPs accounts for the high sensitivity of AuNP-based colorimetric assays. Moreover, color changes can be easily observed by the naked eye, thus making them attractive for DNA-related colorimetric assays.[4c,k,6b,7h,8] The DNA adsorption kinetics by AgNPs are slower than those by AuNPs and they cannot be accelerated by adding salt at neutral pH. This unique property of the specific molecular recognition of DNA-related colorimetric assays accounts for the difficulty of attaching DNA to AgNPs at neutral pH.[16]

Similarly, AgNPs are good candidates as optical sensors because they display distance-dependent optical properties.[4f,17] Their stability can be improved by producing Ag/Au core-shell NPs that retains the Ag core optical properties. However, oligonucleotide-modified Ag/Au alloy particles are not as stable as oligonucleotide-modified core-shell particles and irreversibly aggregate in comparable conditions.[17b] Furthermore, nanoparticles, such as nanorods, prisms, bipyramid of materials, have different SPR wavelengths.[15] For this reason, sensing platforms based on AuNPs optical properties in combination with the molecular recognition of ligands, such as alkyl thiols, antibodies, nucleic acids, and proteins, are active areas of research.[3d] Mirkin's group developed aptamer-based colorimetric assays for macromolecules using the more stable AuNPs, despite AgNPs having a greater extinction coefficient.[6c,18]

NP colloidal stability can be adjusted by modifying the surface charges that affects electrostatic stabilization, and NP aggregation can be induced through loss (or screening) of surface charges. Basically, when AgNPs and AuNPs are exposed to light, they oscillate the electromagnetic field of light. This induces a collective coherent oscillation of conduction band electrons, giving rise to SPR. The SPR band intensity and wavelength depend on the factors that affect the electron charge density on the particle surface. According to Mie's theory, these factors include the metal type, particle size, shape, structure, composition, and dielectric constant of the surrounding medium.[19] Thus, unmodified AuNPs are red while AgNPs are blue or maroon due to their specific and size-dependent SPR absorption. Addition of salt triggers electrostatic repulsion between negatively-charged NPs and antiparticle changes, resulting in NPs aggregation and, consequently, specific color, and wavelength changes.[3e,4t,6a,13] Hence, by monitoring the changes in absorbance, it is possible to understand the characteristics of the enhanced scattering effect in aggregated NPs compared with non-aggregated NPs.[10] Consequently, the band gap energies can also be used to improve the knowledge on NPs sensing and catalytic properties.[20] The SPR profile is characteristic of the NP surface modification by small molecules, metal ions and biomacromolecules.[21]

3. Detection of Metals Ions (Aggregation Induced by Interparticle Cross-Linking)

AgNPs and AuNPs colorimetric changes are due to the particle surface modification and aggregation. This can be achieved by NPs aggregation induced by interparticle bond formation (crosslinking aggregation) or by modifying colloidal stabilization (non-crosslinking aggregation).[7a,22] In the non-crosslinking system, aggregation is driven by the London/van der Waals attractive forces between NPs.[7a] Therefore, the presence of specific functional groups, such as hydroxyl (–OH), carboxyl (–COOH), and amine ($–NH_2$), on the NPs surface plays a critical role in aggregation. By modulating the strength of the NPs intermolecular ion and surface chemistry, this method can be improved.[23] For example, highly charged nucleotides or uncharged nucleosides can bind to citrate-capped AuNPs with the displacement of weakly bound citrate ions through metal–ligand interactions. This can increase AuNPs stabilization or trigger their aggregation, respectively, through gain or loss of surface charges.[7a]

Recently, colorimetric measurements based on metal-induced aggregation of small molecules (for instance, cysteine, dopamine), peptides, and DNA-functionalized NPs have received considerable attention.[3b,c,4i,11c] Indeed, aggregation results in changes in the inter-particle distances, leading to a shift of the SPR absorption band of AgNPs to a longer wavelength.[4t] These cross-linking aggregation-based approaches have been used for the detection of metal ions (**Table 1**). Hajizadeh et al.[3c] described the development of a sensitive and selective colorimetric assay based on the interaction between cysteine, sodium dodecyl sulfate (SDS)-capped AgNPs, and calcium ions. In the presence

Table 1. Detection of metal ions.

Nanoparticle	Analyte	Sample/intereferent	Functionalization	Analytical performance	Ref
AuNPs	Mercury Hg^{2+}	River water and tap water	Citrate-AuNPs + 2, 2'-bipyridyl (Bipy)	LOD: 38 nM LDR: 0.2–2.0 μM	[24]
AuNPs (20 nm)	Mercury Hg^{2+}	Target-doped blood serum	AuNPs and conjugated polyelectrolyte	LOD: 50 μM	[3f]
AuNPs (12 nm)	H_2O_2	Interferent solutions at different concentration	Citrate-AuNPs	LOD: 1.3 μM LDR: 1.3–41 μM	[4a]
AuNPs (17 ± 2 nm)	Cr^{3+}	Tap water and underground water	Mercaptosuccinic acid-AuNPs	LOD: 0.6 μM LDR: 0.6–1.4 μM	[11a]
AuNPs (13 nm)	Ag^{+}	Bimetallic conjugate mixtures	Au–PolyT and Ag–PolyA	LODs: 86.8 nM	[14]
AuNPs (13 nm)	Pb^{2+}	Divalent metal ions	DNAzyme–AuNPs	LOD: 0.1–4 μM	[3a]
AuNPs (13 nm)	Pb^{2+}	RNA-cleaving DNA enzyme	Aptamer–AuNPs	LDR: 0.020–200 μM LODs: 10 μM	[7i]
AuNPs (10 nm)	Pb^{2+}, Pd^{2+}, Hg^{2+}, Pt^{2+}	Standard solutions	Peptide-AuNPs	LODs: nM/ppb range	[3d]
AuNPs (3.5 nm)	K^{+}	Monovalent cations (Li^{+}, Na^{+}, Rb^{+}, NH^{4+}) and bivalent (Ca^{2+} and Mg^{2+})	Aptamer–AuNPs	LOD: 1.0 mM	[3e]
AuNPs (13 nm)	SCN^{-}: thiocyanate	Tap water and common ions	Citrate-AuNPs	LOD: 140 nM	[4s]
AgNPs (9.5 ± 2.0 nm)	Ca^{2+}	Serum and artificial cerebrospinal fluid	AgNPs and cysteine	LOD: 0.1 mM	[4t]

LDR, linear dynamic range; LOD, limit of detection.

of calcium ions and NaCl, AgNPs aggregation was induced, leading to a yellow-to-red color change[3c] (**Figure 3**). Mukherjee and co-workers[3b] used a similar approach for cysteine detection with AgNPs in the presence of Cr^{3+}. As in the case for colorimetric assays in which a ligand is used for complexation, these approaches ultimately are effective for detection of both ligands and metal ions. For instance, in the presence of Cu^{2+}, ascorbic acid rapidly induces AuNPs aggregation as a result of the Cu^{+}-catalyzed 1,3-dipolar cycloaddition of azides and alkynes (click reaction). Thus, the AuNPs solution color changed and this was observed by naked eye for LOD of 3 nM.[4i]

Enzymes, such as deoxyribozymes (DNAzymes) with high specificity for metal ions can form blue aggregates with AuNPs, have also been used for the detection of metal ions. Specifically, Pb^{2+} induces NPs aggregation, thus maintaining the color of the original solution.[3a]

Peptide-based AuNPs also have been used as colorimetric sensors for metal ions. For example, in the Flg-A3 fusion peptide, the N-terminal Flg (-Asp-Tyr-Lys-Asp-Asp-Asp-Asp-Lys-) includes charged, and aromatic residues involved in metal ion complexation, whereas the A3 peptide (-Ala-Tyr-Ser-Ser-Gly-Pro-Ala-Pro-Pro-Met-Pro-Pro-Phe-) binds to gold surfaces. This led to an overall negative charge (pI = 3.9) that prevents NPs aggregation by repulsive forces.[3d] Interestingly, after addition into the solution of peptide-AuNPs, the colorimetric response of each metal ion (Co^{2+}, Hg^{2+}, Pb^{2+}, Pd^{4+} and Pt^{2+}) was different and reproducible and occurs within 1 min[3d] (**Figure 4**).

This indicates that peptides are versatile ligands and their complexation with metal ions is driven through interaction of the peptide backbone with their amino acid side chains. Modifications in the peptide sequences could affect the metal speciation and coordination geometry.[3a,d] The limitation of the peptide-NP colorimetric sensor is that DNAzyme activity in the presence of NPs solution should be minimal.

4. Detection of Small Molecules: Cysteine, Dopamine

This section focuses on small molecules such as analytes and colorimetric substrates (**Table 2**), particularly cysteine and dopamine, because they have been extensively studied.

Cysteine has been employed as a common strategy for the detection of metals, but it also can be quantified by colorimetric assays. Metal ions are used as cross-linking agents for cysteine-AuNP or – AgNP pairs to induce NP aggregation and the consequent red to blue color change of the NP solution is observed. The degree of aggregation depends on the cysteine concentration and the average AuNPs diameter in the presence of different cysteine concentrations. In such colorimetric assays, organic molecules bind to the Au/AgNPs surface via their amine ($-NH_2$) (blue) or thiol ($-SH$) (yellow) terminal groups (**Figure 5**).

Ligands with the $C_6H_8O_6$ formula, without $-NH_2$ or $-SH$ functional groups, preferably bind to the AuNPs surface, and are highly unlikely to induce AuNPs aggregation.[4i,u,32]

The thiol groups of cysteine interact with the surface of colloidal AuNPs or AgNPs via chemisorption-type interactions; however, cysteine can complex with metal ions, such as Pb^{2+}, Zn^{2+}, Cu^{2+},[4i,11c] Ca^{2+},[3c,4t] Cr^{3+},[3b] at a ratio of two cysteines for each metal ion.[10,11c] In the presence of metal ions, cysteines can induce AgNP and AuNP aggregation with a color change from yellow to purple and blue to red, respectively.[3b,c,4u,11c] These assays are based on the NP distance-dependent optical

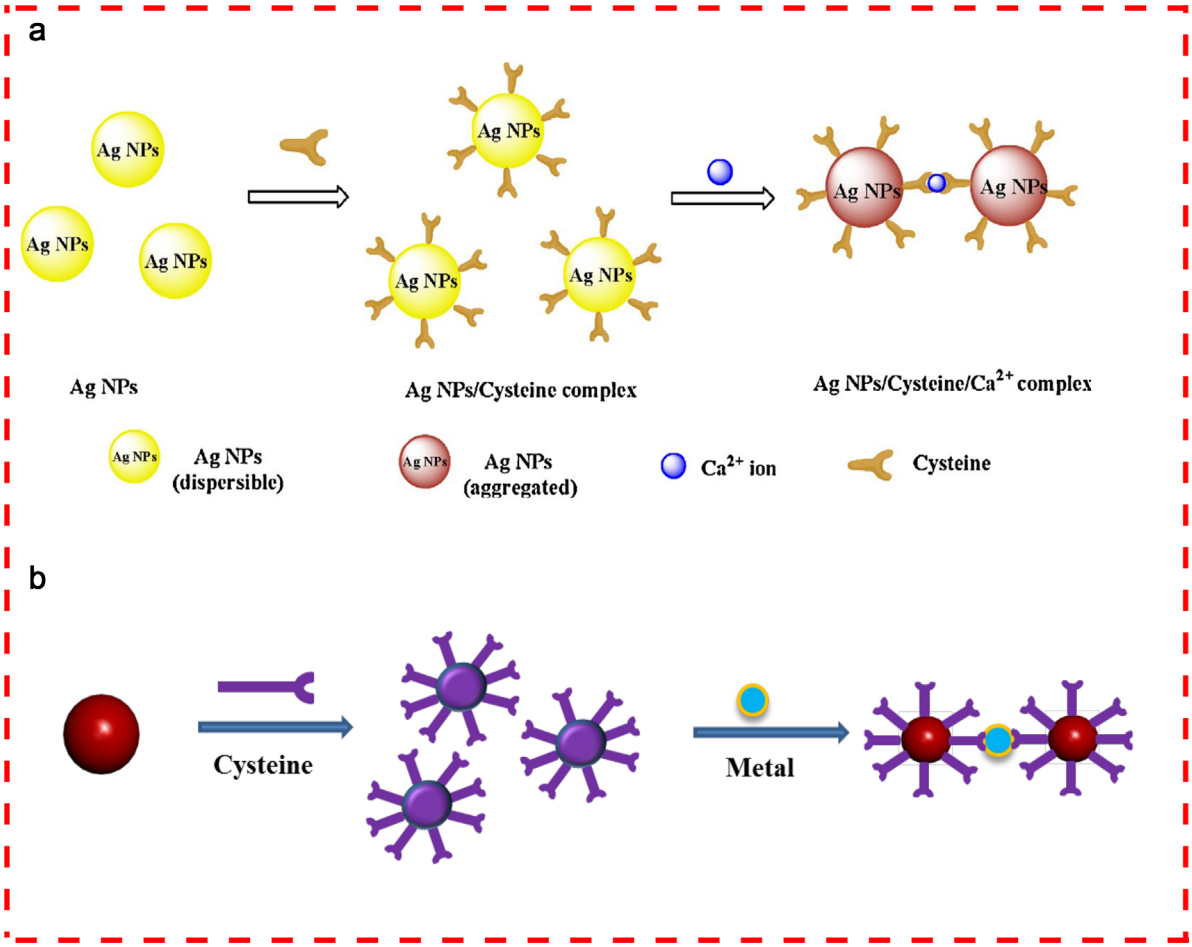

Figure 3. Schematic illustration of the strategy for cysteine detection using a) AgNPs and b) AuNPs. The simultaneous presence of cysteine molecules and Ca^{2+} ions that act as a "glue" to link two neighboring NP-cysteine complexes results in NP cross-linking. Reproduced with permission from.[3c]

properties after coordination, as confirmed by the change in the zeta potential from −30.7 mV for pure AgNPs to −19.63 mV after interaction with cysteine and Cr^{3+}.[3b] Specifically, Hajizadeh et al.[3c] reported that cysteine can rapidly induce AgNP aggregation (yellow-to-red color change) in the presence of Ca^{2+} and 10 mM NaCl, leading to a decrease in electrostatic repulsion and faster aggregation. Cysteine concentration can be determined also by using AuNPs and a UV-Vis spectrometer with a LOD of 10 nM (1.2 ng mL^{-1}).[11c] The ratio between absorption at 524 and absorption at 396 nm (A_{524}/A_{396}) is linear with a cysteine concentration range from 0.25 to 10 mM ($R^2 = 0.993$) with a LOD of 83 nM.[3c] Jongjinakool and co-workers detected cysteine in a concentration range from 0.1 to 0.6 ppm with a LOD of 0.01 ppm.[4u] In Figure 5b–c, a multi-component mixtures demonstrated that cysteine and homocysteine were identified based on the different SPR wavelengths induced by aggregation of non-ionic fluoro-surfactant-functionalized AuNPs upon addition of a mixture of the amino acids. The absorbance changes due to AuNPs aggregation induced by cysteine and homocysteine increase the individual absorbance values (LDR from 0.5 to 4.5 μM for cysteine and LOD (S/N = 3) of 0.4 μM for homocysteine).[4o]

When dopamine (DA) and Cu^{2+} solutions are mixed, the amine group directly coordinates with Cu^{2+} without nitrogen atoms bonded to the gold surface.[4i] The LOD for DA is 30 nM with, differently from cysteine-based methods, a linear calibration curve for two concentration ranges (3.3×10^{-8}–1.0×10^{-7} M and 3.0×10^{-7}–4.5×10^{-6} M) with correlation coefficients of 0.9981 and 0.9979, respectively.[4i] Likewise, addition of 5 mM Cu^{2+} improves the colorimetric probe to a LOD of 200 nM.[29] AuNPs also can be used for the quantitative colorimetric detection of neurotransmitters that mediate the generation and growth of AuNPs, with a LOD of 2.5 μM for dopamine, L-DOPA and noradrenaline, and of 20 μM for adrenaline.[4b] The metal ion-Au/AgNPs interaction is mainly a coulombic interaction and its strength is directly related to the molecular structure and charged groups. Therefore, selectivity can be improved by working on these two parameters.[4r] For instance, researchers highlighted the excellent selectivity of AuNP-based colorimetric assays for cysteine compared with other biomolecules, such as thioglycolic acid and mercaptoethyl alcohol,[11c] glutathione[11b,c] glutathione disulfide,[11b] aspartic acid, and glutamic acid.[23] Moreover, selectivity changes also when using cysteine derivatives, namely glycine, dipeptide Cys-Gly, cysteamine, mercaptopropionic acid,

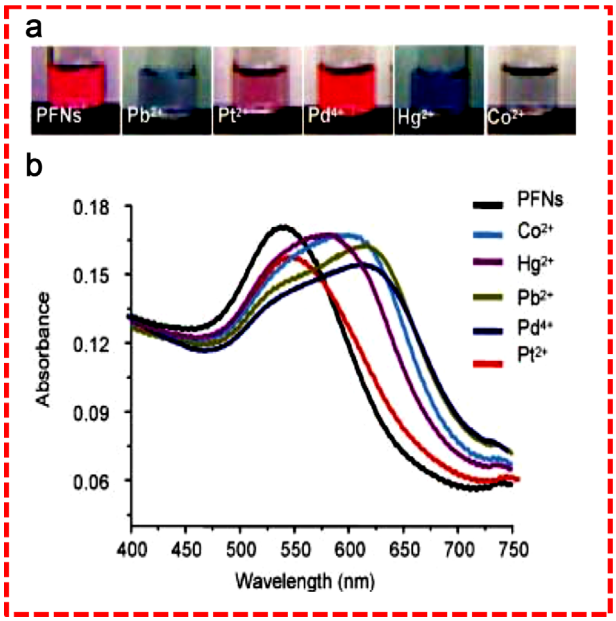

Figure 4. Colorimetric response of peptide-AuNPs to metal ions. a) Optical microscopy images of peptide-AuNP solutions (10 mM in Au atoms) after exposure to 10 mM of different metal salts. b) Corresponding UV/Vis spectra of peptide-AuNPs in the presence of the different metal ions.[3d] PFNs, peptide-AuNPs without metal ions.

S-protected (S-methyl-L-cysteine), N-protected (N-acetylcysteine), and O-protected cysteine (L-cysteine methylester hydrochloride), as indicated by the color change from yellow to pink and peak broadening.[4m] Therefore, it is imperative to investigate the detection of sulfur-containing amino acids compared with other standard amino acids.[4m] Chen et al.[4e] used 19 naturally occurring amino acids, but they could not improve the colorimetric response of cysteine.

Another strategy for cysteine detection is based on the observation that when cysteine is added to AuNPs/ssDNA, the ssDNA molecules that stabilize AuNPs against salt-induced aggregation are displayed spontaneously by cysteine encapsulation on the AuNPs surfaces, via an Au–S bond.[4e] The salt-induced aggregations result in a characteristic AuNPs color change from red to blue.[4e,m] According to Chen et al.[4e] this approach is not feasible with other amino acids (**Figure 6**a).

In this system, the A_{640}/A_{525} ratio is linearly dependent on the cysteine concentration (from 0.1 to 5.0 μM with LOD of 100 nM).[4e] Differently from methods that require AuNPs modification, this approach is simple and fast, but it requires specific links between the biomolecules and AuNPs to allow ssDNA displacement from the NPs surface. On the other hand, Mirkin's group developed a cysteine detection assay where two sets of AuNPs probes are functionalized with different oligonucleotide sequences (probe **A**: 5′ HS-C10-A10-**T**-A10 3′; probe **B**: 5′ HS-C10-T10-**T**-T10 3′) and rapidly form aggregates upon combination through the thymidine–thymidine (T–T) mismatches complexed with Hg^{2+} with LODs as low as a 100 nM (Figure 6b).[4d] Comparison of the two methods (ssDNA-AuNPs and mismatch assay) highlights that they rely on the distance-dependent optical properties of AuNPs, the sharp melting transition of oligonucleotide-AuNPs aggregates, and the very selective coordination of Hg^{2+} with cysteine during which the purple-to-red color change occurs.[4d,e] However, proteins with one free cysteine residue, such as human serum albumin, can spontaneously attach to AuNPs surfaces through Au–S bond formation.[2] These studies demonstrate that the presence of negatively-charged carboxyl groups in the cross-linkers remains essential to induce AuNPs aggregation through ion pair interactions between amino groups present in cysteines and carboxyl groups in the cross-linkers.[4m,23] On comparison of the dopamine- and cysteine-based methods it was evident that functional groups present on the surface also plays a key role in metal detection.

4.1. Recognition of Chiral Molecules

Stereochemistry plays a central role in molecular recognition and interactions. Indeed, the molecule's chemical and biological properties depends not only on the nature of their constituent atoms, but also on their position in space.[32b] Currently, chiral molecules are mostly separated with techniques like capillary electrophoresis, high-performance liquid, and gas chromatography. Nanoparticles allow for the easy detection of chiral molecules by the naked eye. For instance, the color of the AuNPs solution changes from red to blue in the presence of D-tryptophan (LOD of 0.1 μM and LDR of 0.2–10 μM), but not of L-tryptophan.[4y] Interestingly, AuNPs can selectively adsorb D-tryptophan, and therefore, L-tryptophan molecules can easily be separated by simple centrifugation of the tryptophan/AuNP solution.[4y] The infrared spectra confirms the D-tryptophan absorption to AuNPs by disappearance of the NH (NH3 +) stretching absorption peaks (3078 and 3038 cm^{-1}), leaving the carboxylic group (–COOH) and nitrogen atom of the indole ring free for further coordination. This distinctive feature allows for binding of one Cu^{2+} ion to two tryptophan molecules by coordination with the COOH and nitrogen atom of the indole ring, hence allowing for recognition.[4y] Another reported visual differentiation is between the D- and L-forms of mandelic acid (MA) was based on their chirality toward 13 nm l-tartaric acid-capped AuNPs. The L-MA solution changes the red colour of l-TA-capped AuNPs to a bare-eye observable blue, while d-MA does not trigger any color changes.[33] The AgNPs capped with a novel chiral R-mandelic acid-derived calix[4]arene (R-MAC4), for it good optical and structural properties. These self-assembled NPs were used to recognize the N-Fmoc-d/l-aspartic acid (d/l-FAA).[34]

4.2. Detection of Macromolecules

Nanoparticles can be easily modified by replacing surface-adsorbed weak ligands (e.g., negatively charged citrate ions) with thiolated macromolecules that are difficult to displace due to their strong binding to the surface.

Xue and co-workers described citrate-AuNP-based assays for trypsin and arginine residues screening (**Figure 7**). The aggregation of negatively charged citrate-capped AuNPs in the presence of a peptide composed of six arginine residues (Arg_6)

Table 2. Biomolecule-sensing based on AuNPs or AgNPs aggregation.

Nanoparticle [size]	Analyte/s	Sample/s	Functionalization	Analytical performance	Ref
AuNPs Monodisperse	Bisphenol-A	Urine and water samples	Aptamer–AuNPs	LOD: 0.01 pg mL^{-1} LDR: 10 000–0.1 pg mL^{-1}	[4ab]
AuNPs (40–50 nm) Monodisperse	Concanavalin A	Lectin (jack beans)	Thioglucose-AuNPs	LOD: 9 nM LDR: 10–100 nM ($R^2 = 0.983$)	[25]
AuNPs (12.33 nm) Monodisperse	Maltose, mannose, glucose, lactose and D-mannopentaose	Carbohydrate-AuNPs	Carbohydrate–protein interactions	NR	[26]
AuNPs (15, 20, and 2.5 nm) Monodisperse	Cysteine, glutathione and glutathione disulfide	Blood/serum	Citrate-AuNPs: 15 nm CTAB-AuNPs: 20 nm $NaBH_4$-coated AuNPs: 2.5 nm	LDR: cysteine, NR LDR: glutathione: 10–100 and 200–800 μM LDR: glutathione disulfide 10–300 and 400–800 μM LOD: cysteine <0.5 LOD: glutathione 10 μM LOD: glutathione disulfide 10 μM	[11b]
AuNPs (≈13 nm) Monodisperse	Dopamine	Interferent: ascorbic acid	AuNPs induced by copper ions	LOD: 30 nM LDR 1: 33–100 nM LDR 2: 0.1–4.5 μM	[4i]
AuNPs (15 nm) Monodisperse	Dopamine (DA)	Spiked serum	DA inhibits melamine-induced AuNP aggregation	LOD: 33 nM LDR: 33–3.33 mM	[12]
AuNPs (13 nm) Monodisperse	Dopamine	Common interferents, such as 3,4-dihydroxyphenylalanine (DOPA), catechol, 3,4-dihydroxyphenylacetic acid (DOPAC), homovanillic acid (HVA), epinephrine (EP) and ascorbic acid (AA).	The aptamer conformational change could facilitate salt-induced AuNP aggregation 58-mer dopamine-binding aptamer (DBA)	LOD: 360 nM LDR: 0.54–5.4 μM	[27]
AuNPs ±15 nm Multi-dispersed	Dopamine (DA)	Human urine, human serum	DA-induced aggregation of 4-amino-3-hydrazino-5-mercapto-1,2,4-triazol (AHMT) −AuNPs through hydrogen-bonding interactions	LOD: 70 nM LDR: 0.2–1.1 μM	[28]
AuNPs Monodisperse	Dopamine (DA)	Human serum	DA colorimetric sensing based on AuNP aggregation induced by copper ions	LOD: 200 nM LDR: 0.5–10 μM	[29]
AgNPs (NR) Monodisperse	Coralyne	Selectivity test against intercalating ligands, ethidium bromide (EB) and daunomycin (DM)	Homoadenine-AgNPs, label-free colorimetric detection of small molecules using DNA oligonucleotides and AgNPs	LOD: 0.25 coralyne molecules/adenine base	[4f]
AgNPs (5–15 nm) Multi-disperse	4-nitroaniline (4-NA)	self-assembled AgNPs on DNA	4-NA reduction to para-phenylenediamine		[20]
AgNPs (12 ± 2 nm) Multi-disperse	Adenine, guanine, cytosine, thymine	NR	Strength of interactions between the fundamental chemical components of DNA and AgNP surfaces	NR	[13]
AuNPs (13 nm) Multi-disperse	Ampicillin	ssDNA aptamer-AuNPs	Colorimetric assay of ampicillin using specific aptamers	LOD: 5 ng mL^{-1}	[4l]
AuNPs	Oxytetracycline	Tetracyclines (TCs) as counter targets	Ultrasensitive colorimetric detection of oxytetracycline using shortened aptamer	LOD: 0.1 nM	[4v]
AuNPs (13 nm)	Oxytetracycline	Aptamer-AuNPs	Aptamer-specific colorimetric assay	LOD: 25 nM LDR: 25–1 μM	[4g]
AuNPs (18 nm) Monodisperse	Bisphenol a	Water samples	AuNP aggregation by competitive binding of bisphenol A and aptamer	LOD: 0.1 ng mL^{-1}	[4q]
AuNPs (13 nm) Multi-disperse	Ochratoxin A	Standards	Aggregation occurs as random coil structures to compact rigid antiparallel G-quadruplexes	LDR: 20–625 nM LOD: 20 nM	[4k]
AuNPs (13 nm) Monodisperse	Cysteine	Amino acids, glutathione, thioglycolic acid and mercaptoethyl alcohol	2:1 cysteine/Cu^{2+} complex	LOD: 10 nM	[11c]
AuNPs (13 nm) Monodisperse	Ascorbic acid	Fruit juices	Alkyne–azide click reaction	LOD: 3.0 nM	[4i]

(*Continued*)

Table 2. (*Continued*)

Nanoparticle [size]	Analyte/s	Sample/s	Functionalization	Analytical performance	Ref
AuNPs (NR) Monodisperse	Cysteine	19 amino acids	ssDNA-AuNPs	LOD: 100 nM LDR: 0.1–5 μM	[4e]
AuNPs (20.1 ± 1.8 nm) Multi-disperse	Influenza B/Victoria, influenza B/Yamagata	Virus dilution (hemagglutination assay titer, 512)	Sialic acid-AuNPs	LOD: 0.09 vol% upper limit of linearity 2.5 vol%	[10]
AuNPs (13 nm) Monodisperse	Tryptophan enantiomers	D/L enantiomers	AuNPs	LOD: 0.1 μM	[4y]
AuNPs (≈11.89 nm) Mono-disperse	Arginine, histidine, lysine	Urine samples	Quercetin-AuNPs	LOD: 0.04, 0.03, and 0.02 μM. LDR: 2.5–1,250 μM (Arg) and 1–1,000 μM (His and Lys),	[30]
AuNPs-I (15 nm) AuNPs-II (30 nm) AuNPs-III (40 nm) Multi-disperse	Melamine	Pre-treated milk	Citrate-AuNPs	AuNPs-I (2.37×10^{-8} M) AuNPs-II (3.3×10^{-8} M) AuNPs-III (8.9×10^{-8} M)	[4z]
AgNPs (NR) Mono-disperse	Cysteine	Various metals	2:1 cysteine/Ca^{2+} complex	LOD: 83 nM LDR: 0.25–10 μM	[3c]
AgNPs (10–15 nm) Multi-disperse	Cysteine	10 mM of nine amino acids	2:1 cysteine/Cr^{3+} complex	LOD: 1 nM	[3b]
AgNPs (10–20 nm) Multi-disperse	Dopamine, L-DOPA, noradrenaline adrenaline	Tyrosinase	AgNPs	LOD: dopamine, L-DOPA and noradrenaline 2.5 μM adrenaline 20 μM tyrosinase activity ≈ 10 U (≈100 μg mL^{-1})	[4b]
AuNPs (≈13 nm) Multi-disperse	Kanamycin	Other antibiotics: streptomycin, sulfadimethoxine and ampicillin	ssDNA aptamer-AuNPs	LOD: 10 nM	[4j]
AuNPs (≈13 nm) Mono-disperse	Sulfadimethoxine (SDM)	NR	AuNPs	LDR: 50 ng mL^{-1} to 1.0 μg mL^{-1} LOD: 50 ng mL^{-1}	[4n]
AuNPs (≈15 nm) Multi-disperse	Penicillin G	Different penicillins	CTAB-AuNPs	LOD: 0.007 mg mL^{-1}	[7m]
AuNPs (20 nm) Mono-disperse	Cysteine	19 essential amino acids	DNA-AuNPs	LOD: 100 nM LDR: 100 nM–2 μM	[4d]
AuNPs (13 nm) Multi-disperse	Adenosine	inosine, guanosine, and cytosine	Aptamer-OD-AuNPs	LOD: 10 μM	[31]
AuNPs (13 nm) Mono-disperse	Adenosine and caffeine	Other nucleosides	Aptamers	LOD: 0.3 mM	[4c]
AuNPs (15 nm) Mono-disperse	Digitoxin	Rat serum	AuNPs	LOD: 571 pM	[4aa]
AuNPs (10.8–13.1 nm) Multi-disperse	Cysteine	Interferents: Na^{+}, Cu^{2+}, Cl^{+} and urea	AuNPs	LDR: 0.1–0.6 ppm LOD: 0.01 ppm	[4u]
AgNPs (5–20 nm) Multi-disperse	Cysteine/cystine	Other amino acids	AgNPs	LDR: 25–250 μM LOD: 2.5 ppm	[4m]
AgNPs (8 nm) Mono-disperse	Cysteine and homocysteine	Human urine and plasma samples	Non-ionic fluorosurfactant-AuNPs,	LOD: 0.4 μM.	[4o]
AgNPs (8 ± 1.6 nm) Multi-disperse	Cysteine	Human urine and plasma samples	Fluorosurfactant-AgNPs	LOD: 0.05 μM LDR: 1.5–6.0 μM	[4r]
AgNPs (9.5 ± 2.0 nm) Multi-disperse	Cysteine	Serum and artificial cerebrospinal fluid	AgNPs and Ca^{2+}	LDR: 0.1–1000 μM LOD: 0.1 μM	[4t]
AuNPs (20.0 ± 1.4 nm) Multi-disperse	Cysteine	Human urine	Pectinase-protected AuNPs	LDR: 4.85×10^{-6} to 302 μM and 3.25–0.103 mM LOD: 4.6×10^{-9} M	[4ac]
AuNPs (13 nm) Monodisperse	Cysteine	Brain microdialysate (sample), lactate, ascorbic acid and glucose (interferents)	Cysteine-AuNPs	LDR: 0.166–1.67 μM LOD: 0.1 μM	[23]

(*Continued*)

Table 2. (*Continued*)

Nanoparticle [size]	Analyte/s	Sample/s	Functionalization	Analytical performance	Ref
AuNPs (13 nm) Monodisperse	Pyruvic acid	Interferents: lactic acid (LA), ascorbic acid (AA) and glucose.	AuNPs	LDR: 5.6–168.0 μM LOD: 3.0 μM	[4w]
AuNPs (13 nm) Monodisperse	Sulfadimethoxine (SDM), kanamycin (KAN) and adenosine (ADE)	Mixture of KAN, SDM and ADE	Aptamer of KAN, SDM and ADE (1:1:1 mixture)	NR	[4x]
AuNPs (13 nm) Monodisperse	17β-estradiol	Intereferents: methanol, diethylstilbestrol, bisphenol A, 19- nortestosterone, estroil, estrone	AuNPs	LOD: 0.1 ng mL^{-1}	[4x]
AuNPs (20 nm) Monodisperse	Caffeine	ATP and target-doped blood serum	AuNPs	LOD: 1.25 μM	[3f]
AuNPs (13 nm) Monodisperse	Parathion	Sea and tap water	Parathion inhibits AChE-induced aggregation of AuNPs	LDR: 15–65 ppb and 140–1000 ppb LOD: 0.7 ppb (2.4 nM)	[4ad]

CTAB: cetyl trimethyl ammonium bromide; OD: oligonucleotides; SDM: sulfadimethoxine; KAN: kanamycin; ADE: adenosine; AChE: acetylcholinesterase, Cyt C: cytochrome c.; LDR: linear dynamic range; LOD: limit of detection.

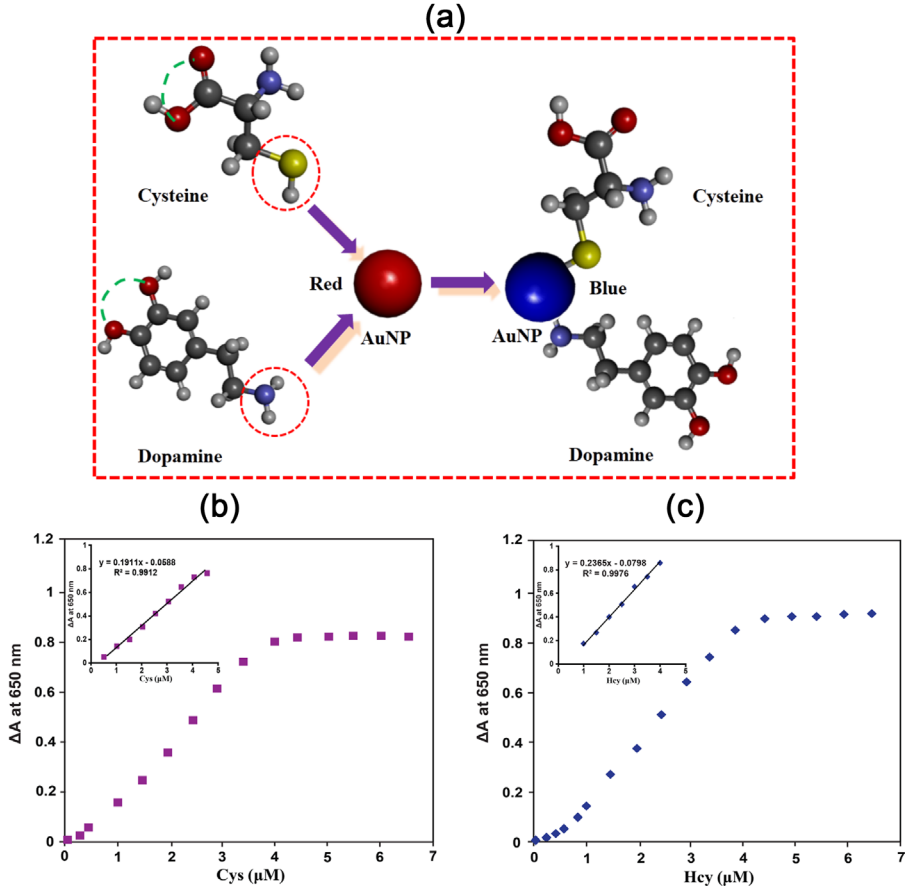

Figure 5. a) Chemisorption model for cysteine and dopamine on the AuNP surface. The solution color changes from red to blue in the presence of cysteine or dopamine. b) and c) shows linear relationship of nonionic fluorosurfactant-capped gold nanoparticles versus Cys and Hcy 650 nm. The linear range for Cys was 0.5–4.5 μM, and for Hcy was 1.0–4.0 μM. Conditions: pH 6.5, 100 mM NaCl, 30 s incubation period at 50 °C.

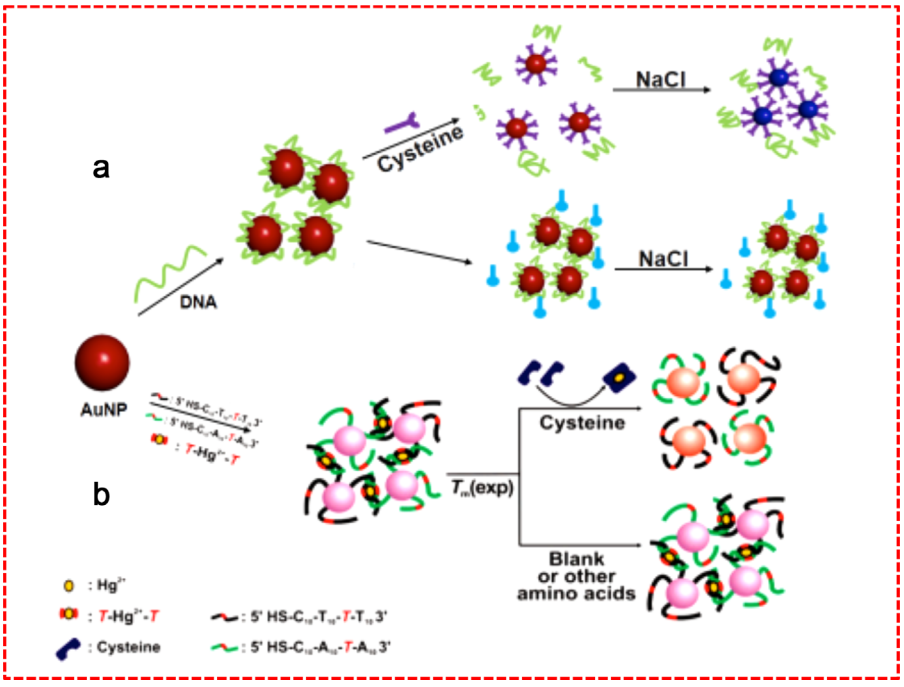

Figure 6. a) In the presence of cysteine, the ssDNAs is displayed by cysteine on AuNPs surface resulting in AuNP aggregation, and in a color change from red to blue upon addition of NaCl. Other amino acids do not lead to a color change due to the absence of thiol groups.[4e] b) Cysteine colorimetric detection using AuNPs probes that contain T-T mismatches complexed with Hg^{2+}: competitive approach in which cysteine can displace Hg^{2+}.[4d]

occurred mainly through electrostatic interactions, and led to a red-shift of the usual SPR profile.[35] However, when the Arg_6 peptide was hydrolyzed into fragments upon trypsin addition in the solution, the electrostatic interactions between AuNPs and arginine residues were weakened and, therefore, neither AuNPs aggregation nor SPR shift was observed.

Moreover, Arg_6 hydrolysis catalyzed by trypsin is retarded if trypsin inhibitors are present in the solution. This feature was used to develop a label-free assay for trypsin (LOD: 1.6 ng mL^{-1}) and Arg_6 residues screening with AuNPs.[35] Similarly, interaction of citrate-AuNPs with fibrinogen to form fibrinogen–AuNPs through electrostatic and hydrophobic interactions was used for the detection of thrombin (LOD: 0.04 pM and LDR: 0.1–10 pM; $R^2 = 0.96$).[7l] Although the mechanism of detection was the same, the molecular interactions was different. Indeed, fibrinogen was adsorbed on NPs before the addition of thrombin.[7l] Conversely, trypsin interacts with Arg_6 before the NPs addition into the system.[35] Detection of thrombin has been improved by the use of catalytic enlargement as shown in **Figure 8**.[5a]

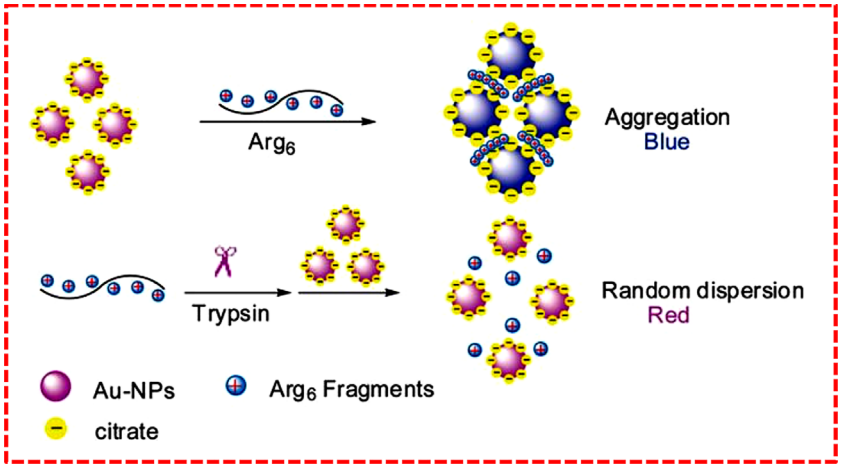

Figure 7. Colorimetric assay for trypsin by using AuNP crosslinking/aggregation based on trypsin-catalyzed hydrolysis of Arg_6 for random dispersion of citrate capped AuNPs. Reproduced with permission from.[35]

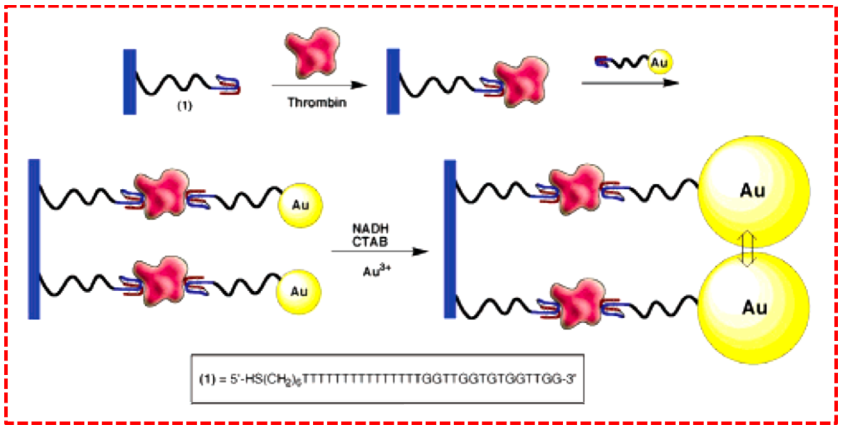

Figure 8. Amplified thrombin detection on surfaces by catalytic enlargement of thrombin-aptamer-functionalized Au–NPs.[5a] As the concentration of thrombin increases, the surface loading of bound thrombin is higher, resulting in a number of Au NP seeds for enlargement.

Specifically, upon aptamer-AuNPs reaction with thrombin, AuNPs aggregate. But in the presence of other proteins (200 nM BSA or human IgG antibodies), the aptamer-AuNPs does not precipitate implying that the precipitation originates from the specific interaction between aptamer and thrombin (LOD: 20 nM).[5a]

Similarly, Chen's group evaluated the possibility of using mannopyranoside-encapsulated AuNPs/concanavalin (Man-AuNPs/Con A) complexes for a competitive colorimetric assay for ten proteins. However, only thyroglobulin, *bandeiraea simplicifolia* lectin I (BS-I), soybean agglutinin (SBA), and *maackia amurensis* (MAL) significantly modified the absorption spectrum of Man-AuNPs/Con A complexes.[5b] In contrast to the method proposed by Xue et al.,[35] where upon the introduction of thrombin in the fibrin–AuNP solutions, catalyzes the polymerization of the free and conjugated fibrinogen species to form insoluble fibrillar fibrin–AuNP agglutinates.[71] Finally, Guarise et al.[36] exploited the fact that, compared with the native peptide substrates, protease-cleaved peptides do not induce NPs aggregation (and thus the color of the solution does not change) to detect two proteases (thrombin and lethal factor).

Quercetin-AuNPs have been used as a colorimetric probe for the detection of amino acids, such as arginine (Arg), histidine (His), and lysine (Lys). Indeed, quercetin-AuNPs aggregation caused by amino acids leads to a color change from red to blue.[30] In optimal conditions, a linear relationship exists between the absorption ratios at different wavelengths (A_{702}/

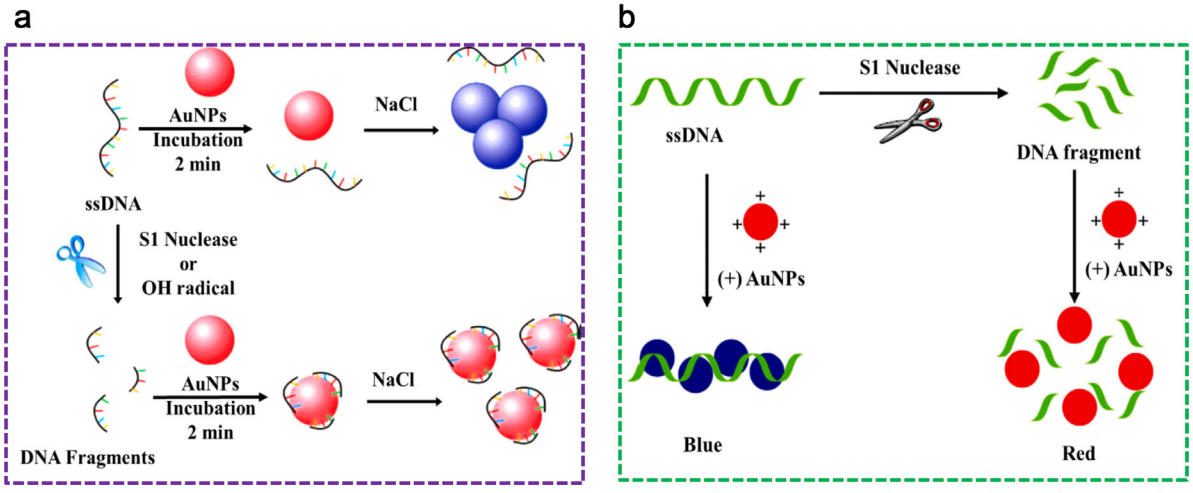

Figure 9. Schematic representation of AuNP-based colorimetric strategies for ssDNA cleavage assays. a) Salt-induced NP aggregation before and after ssDNA cleavage by the S1 nuclease or OH radicals. Reproduced with permission from.[6g] b) Nuclease activity assay using positively charged AuNPs and polyanionic ssDNA ((+)AuNPs). Reproduced with permission from.[7n]

A_{525} for Arg, A_{693}/A_{525} for His, and A_{745}/A_{525} nm for Lys) and the concentration ranges (from 1.25 to 2.50 μM for Arg; from 1 to 1,00 μM for His and Lys), with LOD values of 0.04, 0.03, and 0.02 μM, respectively, at pH 5.0.[30] Siddhartha and Debabrata[5h] reported that protein estimation is within a LOD of 10–80 $\mu g\,mL^{-1}$ using unmodified AgNPs.

Lately, the sequence-length-dependent adsorption of ssDNA on AuNPs has been investigated for colorimetric nuclease assays and measurement of oxidative DNA damage.[6g] Based on ssDNA adsorption rate on citrate-AuNPs, it can be hypothesized that incubation with AuNPs for a specific period of time can lead to differential adsorption of short and long ssDNA. Consequently, the stability of the ssDNA–AuNPs complex in the presence of salt could be influenced by the ssDNA length.[6g] The confirmation of this hypothesis led to the development of colorimetric assays taking advantage of ssDNA length to improve adsorption. For example, when ssDNA is cleaved by the S1 nuclease or −OH radicals in small fragments, these shorter ssDNA can be rapidly adsorbed on AuNPs and significantly enhance the negative charge density on each AuNP surface for the same time of incubation (**Figure 9**a).

Basically, charging the NPs surface increases the electrostatic repulsion between the ssDNA–AuNPs complexes enough to inhibit NP aggregation at the same salt concentration, and the solution color does not change. Thus, DNA cleavage can be directly visualized by naked eye.[6g] Charge interaction between positively charged AuNPs and polyanionic ssDNA leads to AuNPs aggregation that can be monitored by the color change from red to blue (Figure 9b).[7n] However, in the presence of the S1 nuclease, the ssDNA substrate is cleaved into small fragments, and the AuNPs solution remains red. Thus, the nuclease activity can be easily monitored by naked eye or with a simple colorimetric reader.[7n] In this case, the exocyclic amino group of nucleotides is the main cause of nucleotide-dependent aggregation because cysteamine-capped AuNPs are positively-charged at pH 3.6 (with a pKa of 10.75), leading to efficient electrostatic interactions with the negatively charged DNA. These results complement each other because during S1 enzymatic activity, ssDNA is degraded into smaller fragments that cannot induce aggregation.[6g,7n]

Additionally, the non-crosslinking AuNPs aggregation induced by the loss of surface charges also is exploited for enzymatic activity testing and screening for potential inhibitors.[7a] This approach has been extended to the serotype I-specific detection of dengue virus DNA. In the absence of the DNA target solution, peptide nucleic acids (PNA) induce AuNPs aggregation with a red-to-purple color change and the appearance of a second absorbance peak at 650 nm due to the AuNPs surface coating by PNA.[37] Likewise, sialic acid-reduced and −stabilized AuNPs ($d = 20.17 \pm 1.8$ nm) can be used for the colorimetric detection of influenza viruses.[10] The discrimination of such molecules can also be standardized using chemometric techniques including hierarchical cluster analysis and principal component analysis. This approah was used to accurately classified and measure the array response of cysteine, gluthatione, glutathione disulfide, and interferences without any misclassification.[38]

5. DNA-Functionalized Nanoparticles (Aptasensors)

This is the most fascinating area of NP-based colorimetric assays. Much attention has been focused on aptamers (i.e., ssDNAs and oligopeptides with high binding affinity and selectivity for target molecules) as powerful biological macromolecules (**Table 3**). Particularly, the aptamer advantages compared with antibodies, such as possibility of chemical synthesis and modification and lower immunogenic response, contribute to their potential.[4j] They are generally selected in vitro by using the systematic evolution of ligands by exponential enrichment (SELEX) technique and random-sequence nucleic acid libraries.[4j,l,p,v,x,39] This allows selecting, the highest binding aptamer(s). Then, aptamers can be capped with thiol groups that bind to two AuNPs.[6c,9,18] The principle of colorimetric sensing based on aptamers to detect specific DNA sequences was introduced about a decade ago and is now a key tool in biodiagnostics.[9,18] Since then, other aptamer-based sensors have been developed for the detection of metal ions, small molecules,[4d,e] and proteins.[5c,g,7d]

The development of DNA-aptamer-based colorimetric assays by Mirkin's group was inspired by the fact that the steps necessary for NPs+ modification with ligands can be tedious or time-consuming and relatively expensive.[6c,18,47] NPs stabilized by ssDNA aptamers do not aggregate with the addition of salt only.[3e,4c] Conversely, in the presence of the target/analyte, the aptamer is folded because it binds to the target while desorbing from the NPs surface, which leads to NPs aggregation and colorimetric changes. Ideally, folded aptamers or dsDNAs should hardly adsorb onto the NPs. This is related to the higher structure rigidity and high proton density inside dsDNA.[3e,4g,x,6e] Indeed, ssDNAs cannot hybridize with each other to form dsDNAs. Thus, their strategy is based on the observation that unmodified AuNPs and AgNPs can differentiate between ssDNA and dsDNA, mainly due to the higher structure rigidity of the latter.[3e,4n,6e] However, not only the strands but also their lengths contribute to NP stabilization. For instance, Chen and co-workers tested ssDNAs of different length (18nt: 5′ TAG AAT ACT CCC CCAGGT 3′); 24nt: 5′ GGT TGG TCA GAT TCA GTG GGT TAG 3′, and 30nt: 5′ AAA CCC CCC TGC TAAAAC CCC AAA CCC 3′) for AuNP stabilization and consequently for detection and sensitivity. They found that the longer ssDNAs have a better stabilization effect because at the same molar concentration, longer ssDNAs have more monomeric deoxynucleotide units. Moreover, it is difficult for cysteine to replace highly stable DNA-protected AuNPs.[4e] DNA bases possess higher affinity toward gold than silver via coordination between Au and nitrogen atoms (thus favoring DNA adsorption). However, the negatively charged surfaces of AuNPs electrostatically repel DNA phosphate backbones (reducing DNA adsorption).[3e] The key challenge to their successful application is in transforming the aptamer-binding events into physically detectable signals.[4c]

The development of the nanotechnology for NPs functionalization with DNA and the biotechnology for the in vitro selection of target-specific nucleic acids offer a unique opportunity for designing colorimetric biosensors.[7c,17a] The

Table 3. DNA/protein sensing based on AuNP aggregation.

Nanoparticle [size]	Analyte/Target	Functionalization	Analytical application	Analytical performance	Ref.
AuNPs (13 nm) and AgNPs (10–20 nm) Monodisperse	DNA3 complementary DNA	DNA1-AuNPs DNA2-AgNPs	Complementary DNA recognition	NR	[16]
AuNPs (12.33 nm) Monodisperse	Maltose>mannose>glucose>lactose>MAN5.	Carbohydrates-AuNPs	carbohydrate–lectin interactions	NR	[26]
AuNPs (13-nm) Monodisperse	Lysozyme	HSA-AuNPs	Colorimetric detection	LOD: 50 nM	[7f]
AgNPs (10–15 nm) Monodisperse	Globular proteins (BSA and IgG)	AgNPs	Concentration-dependent particle agglutination	LOD: 10–80 $\mu g\,mL^{-1}$	[5h]
AuNPs and AgNPs Monodisperse	Specific DNA sequence	AuNPs and AgNPs	Detection of DNA through nucleic acids (PNA) hybridization	LOD: DNA/PNA ratio of 0.05	[6a]
AuNPs (50 nm) Multidisperse	Con A	p-Aminophenyl-D-mannose-AuNPs	Carbohydrate–lectin system	LOD: 9.0 nM ($R^2 = 0.983$) LDR: 10–100 nM	[25]
AuNPs Multidisperse	PDGFs and PDGFR	Apt-AuNPs	Protein analysis and cancer diagnosis	–2.5–10 and 10–20 nM, respectively, for 0.42 nM Apt-AuNPs –25–75 and 75–200 nM, respectively, for 8.4 nM Apt-AuNPs.	[5c]
AuNPs (32 nm) Monodisperse	Con A binding partners	Mannopyranoside-encapsulated gold nanoparticles (Man-AuNPs)	Competitive colorimetric assay for ConA binding partners through protein–protein interactions	NR	[5b]
AuNPs (13 nm) Monodisperse	24-bp polynucleotide target	AuNPs capped with 3¢- and 5¢ (alkanethiol) oligonucleotides	Hybridization of the target with the probes		[6c]
AuNPs (20 nm) Monodisperse	H_2N-Cys-Tyr(PO_3^{2-})-Arg-OH	AuNPs	Sensing phosphatase activity of alkaline phosphatase	54: 3.4 μM of peptide: alkaline phosphate	[40]
AuNPs (15 nm) Monodisperse	Bla molecules	AuNPs	β-Lactamase activity Identification of Bla molecules and screening for Bla inhibitors	60 pM	[41]
AgNPs (31 nm) Multidisperse	AgNP-oligonucleotide conjugates	DNA-AgNPs	Hybridization of two complementary DNA-AgNPs	NR	[17a]
AuNPs (13 nm) Monodisperse	Single-stranded DNA cleavage	AuNPs	Enzymatic cleavage and oxidative damage of single-stranded DNA	NR	[6g]
AuNPs (14 nm) Monodisperse	HIV-1 ribonuclease H	AuNPs	Colorimetric detection of HIV-1 ribonuclease H activity by AuNPs	27 $U\,mL^{-1}$	[7o]
AuNPs (13 nm) Monodisperse	Tyrosin	AuNPs	Crosslinking/aggregation of Au-NPs based on trypsin-catalyzed hydrolysis of Arg6	1.6 $ng\,mL^{-1}$	[35]
AuNPs Monodisperse	Methyltransferase activity	DNA-AuNPs	Colorimetric assay for endonuclease/methyltransferase activity and inhibition	NR	[7k]
AuNPs (13 nm) Monodisperse		DNA-modified AuNPs	Enzymatic cleavage of nucleic acids, colorimetric biosensors	0.5 $U\,mL^{-1}$	[7i]
AuNPs (13 nm) Monodisperse	Thrombin	Aptamer-AuNPs	Colorimetric assay based on the aptamer folding and unfolding	LDR: 0–167 nM LOD: 0.83 nM	[5g]
AuNPs (20 nm) Monodisperse	Thrombin	AuNPs	G-quadruplex structure folding	LOD: 10 nM	[3f]
AuNPs (NR)	Triplex DNA binders: BePI or CORA	Aptamer-AuNPs	Screening triplex DNA binders	NR	[42]
AuNPs (13.3 ± 1.2 nm) Multidisperse	Thrombin	Fibrinogen-AuNPs (56 nm)	Colorimetric assay for blood plasma	LOD: 0.04 pM LDR: 0.1–0 pM	[7l]

(*Continued*)

Table 3. (*Continued*)

Nanoparticle [size]	Analyte/Target	Functionalization	Analytical application	Analytical performance	Ref.
AgNPs (NR) Multidisperse	CIAP and PKA	AgNPs	Adenosine phosphorylation and dephosphorylation	LOD: CIAP: 1.0 U mL^{-1} PKA: 0.022 U mL^{-1}	[7h]
AuNPs (≈12.74 nm) Monodisperse	staphylococcal enterotoxin B	AuNPs	Colorimetric assay based on aggregation in the absence of the aptamer	LDR: 10–50 ng mL^{-1} LOD: 10 ng mL^{-1}	[4p]
AuNPs (NR) Multidisperse	Aminopeptidase N	Gold nano-composites conjugated with a thermo-responsive copolymer	Activity based on inhibition of the disassembly of Gold nano-composites	AR: 20–50 U L^{-1}	[43]
AuNPs (15.1 nm) Multidisperse	β-galactosidase and β-glucosidase	Gal-Lip-AuNPs and Glc-Lip-AuNPs	Glycosidase inhibitor screening	LODs: β-galactosidase 9.2 nM and β-glucosidase 22.3 nM at 20 °C	[44]
AuNPs (26 nm) Monodisperse	ADA	AuNPs	Nucleotide-dependent aggregation	LOD: 0.8227 U L^{-1}	[8]
AuNPs (13 nm) Monodisperse+	Endonuclease	DNA-AuNPs with duplex interconnection	Endonuclease activity and inhibition	NR	[7e]
AuNPs (13 nm) Monodisperse	Biotin (biotinylation)	Peptide-AuNPs and avidin-AuNPs	Kinase-catalyzed substrate biotinylation	NR	[7d]
AuNPs (20 nm) Multidisperse	Protein kinase A,	AuNPs	Kinase activity based on the coagulating ability of a cationic substrate peptide and its phosphorylation	NR	[7g]
AuNPs (NR) Multidisperse	Acetylcholinesterase	Citrate-AuNPs	AChE-catalyzed hydrolysis of acetylthiocholine	0.6 mU mL^{-1}	[45]
AuNPs (16 nm) AgNPs (16 nm) Monodisperse	Con A	Mannose AuNPs Mannose-AgNPs	Con A induced aggregation	Mannose −AuNPs LOD: 0.04 μM LDR: 0.04–0.10 μM Mannose-AgNPs: LDR: 0.08–0.26 μM LOD: 0.1 μM	[2]
AuNPs (15 nm) AgNPs (20 nm) Monodisperse	Kaposi's sarcoma associated herpesvirus and Bartonella DNA	Oligonunucleotides-AuNPs Oligonunucleotides-AgNPs	Aggregation reaction with multi-color changes	LOD: 1 nM	[15]
AgNPs (10–15 nm) Multidisperse	BSA and immunoglobulins	AgNPs	Nanoparticle agglutination	LOD: 10–80 μg mL^{-1}	[5h]
AuNPs (21 nm) Monodisperse	polyA, polyC, polyU, polyI, BSA, lysozyme, dsDNA,ssDNA	AuNPs	Aggregation due to self-assembly (discrimination and detection)	LOD: Protein ≈100 pM Homopolynuclotide ≈10 pM	[5i]
AuNPs (13.2 nm) Monodisperse	Dengue virus	AuNPs	PNA/DNA hybridization	LOD: 0.12 μM	[37]
AuNPs (≈13 nm) Monodisperse	ssDNA and dsDNA	AuNPs	DNA sequences based on electrostatic interactions	AR: 100 fmol	[6e]
AuNPs (13 nm) Monodisperse	Abrin	Catalytic AuNPs	Peroxidase-like activity	LDR: 0.2–17.5 nM LOD: 0.05 nM	[46]
AuNPs (13 nm) Monodisperse	Lipase	Tween 20-GNPs	Enzyme-regulated AuNP aggregation	LOD: 0.028 mg mL^{-1} LDR: 0.15–1.80 mg mL^{-1}	[7p]
AuNPs (50 nm) Multidisperse	Native proteins	DNA-AuNPs	50% human urine	Cluster analysis	[5j]

NR: Not Reported; CIAP: Calf Intestine Alkaline Phosphatase; HSA-AuNPs: Human serum albumin-modified gold nanoparticles, PKA: Protein Kinase A; SEB: Staphylococcal enterotoxin B; LOD: Limit of detection; AR: Activity Range; PDGFs: Platelet-derived growth factors; PDGFR: platelet- derived growth factor receptors, Con A: Concanavalin A; Man-AuNPs: Mannopyranoside- encapsulated gold nanoparticles; Gal: β-galactosidase and Glc: β-glucosidase; ADA: Adenosine Deaminase; AChE: Acetylcholinesterase, KSHV: Kaposi's sarcoma associated herpesvirus; BePI: benzo[e]pyridoindole; CORA: coralyne, BSA: Bovine serum albumin: PNA: peptide nucleic acid; LDR: linear dynamic range; LOD: limit of detection.

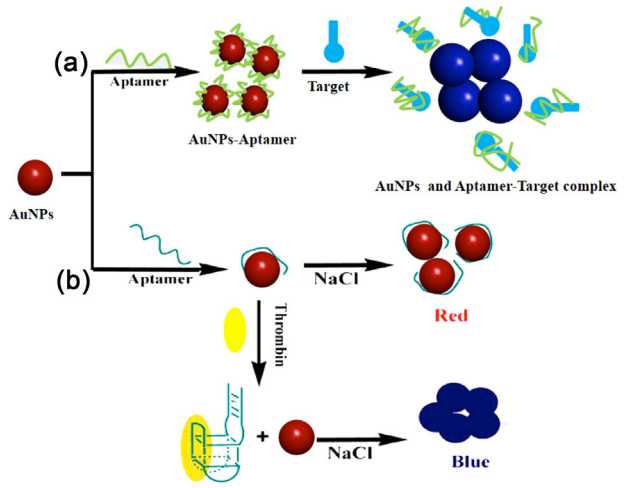

Figure 10. Schematic representation of Type I colorimetric aptasensors for detection a) small[4q,4aa] and b) large molecular targets.[5g]

four types of DNA aptamer-based colorimetric approaches are highlighted below:

5.1. Type I: Aptamers Adsorbed on Nanoparticles

Type I aptasensors includes two common steps: (i) adsorption of the DNA unit onto the NPs surface and (ii) recognition of the target molecule by the DNA strands while serving as an optical sensing element. DNA adsorption on NPs surface is favored by the high charge density and stability provided by the aptamer[4f] (**Figure 10**). This is a crucial step because the selectivity of the targeting molecule must be retained during adsorption onto NPs, especially when the aptamer is designed for qualitative assays.[4f] The aptamer conjugation constant is stronger than that of antibodies and that of non-specific adsorption between aptamer and NPs.[4q] With these conditions in mind, Xu and co-workers[4f] used unmodified DNA and AgNPs to detect ligands binding to homoadenine, by monitoring the color change from yellow to brown due to AgNP aggregation after salt addition. When coralyne binds to the homoadenine sequence in the aptamer, the aptamer is removed from the AgNP surface and AgNP can aggregate. The A_{550}/A_{397} ratio shows a good linear correlation with coralyne concentrations between 0.0 and 10 mM with a LOD of 0.3 mM.[4f] Using a similar strategy, DNA–AuNPs/AgNPs were used to detect several targets, such as bisphenol A (LOD: 0.1 ng mL^{-1}[4q] and LOD: 0.01 pg mL^{-1}[4ab]), digoxin (LOD: 571 pM),[4aa] oxytetracycline (OTC) (LOD: 25 nM),[4g] thrombin, (LOD: 0.83 nM),[5g] kanamycin (LOD: 25 nM),[4j] OTC (LOD: 0.1 nM), ampicillin (LOD: 5 ng mL^{-1}),[4l] staphylococcal enterotoxin B (LOD: 10 ng mL^{-1}),[4p] and pyruvic acid (LOD: 3.0 μM).[4w]

It is acknowledged that for many type I aptamers, addition of the target/ligand induces the aptamer release from the NP surface and consequently the color change as the salt tolerance decreased by NPs.[4f,q,aa,48] Two groups reported an intriguing observation using a similar approach.[4c,49] When aptamers are added to NPs, their interaction via hybridization leads to NP aggregation and consequently to the color change from red to blue. Addition of the target molecule (e.g., adenosine) to the aptamer-NP solution induces a dramatic conformational change of the aptamer structure that leads to the dissociation of the NP network and to a new color change (blue to red).[4c,49]

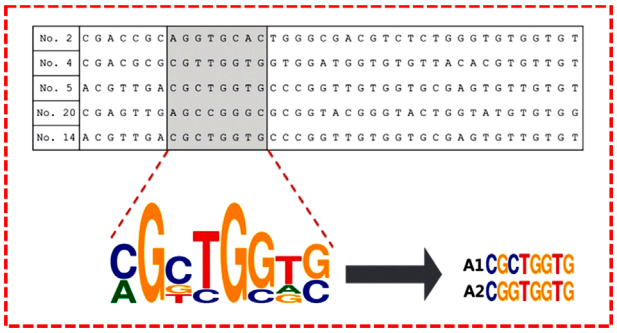

Figure 11. Truncation process after analysis of the sequences of the original five 76-mer aptamers that bind to oxytetracycline, 20–8 mer.[4v]

AuNPs have also been used by Dong's group[5g] to understand the conformational changes of thrombin-binding aptamers (TBA) when they are removed from the AuNP colloidal solution in the presence or not of thrombin. Addition of 100 mL of 0.5 M NaCl causes a quick color change (red to purple) in the solution with thrombin, but not in that with only TBA. Due to the color change, the TBA conformation modification from unfolded to G-quadruplex/duplex formation could be directly monitored by naked eye, thus allowing the easy detection of thrombin (Figure 10b).[5g] Likewise, the addition of enough salt could be used to inhibit the repulsion between unmodified negatively charged AuNPs and result in their aggregation and in the corresponding red-to-blue color change. As previously reported, there is stronger coordination interaction between the nitrogen atoms of unfolded ssDNA and AuNPs than electrostatic repulsion between the negatively charged phosphate backbone and the negatively charged AuNPs.[5g] Conversely, the relatively rigid structure of dsDNA or folded ssDNA (e.g., G-quadruplexes) prevents the exposure of the DNA bases to AuNPs and the high density of negative charges increases the repulsion between DNA and AuNPs. However, aggregation of DNA-functionalized AuNPs can be induced also by hybridization of target DNA that does not cross-link the NPs. A conceivable disadvantage of this non-crosslinking system, compared with the crosslinking system, is the consumption of target DNA.[48]

Recently, a viable approach to overcome the limitations of type I aptamers due to the DNA length was reported. Briefly, the design of shortened aptamers is mainly based on selecting nucleotide bases characterized by high homogeneity in accordance with their conserved regions.[4l,v] Shortened aptamers that contain common regions have approximately the same binding affinity as the original. For instance, based on the conserved sequences with high homogeneity of the original five 76-mer aptamers, A1 and A2 (8-mer sequences) were successfully obtained and still exhibited high affinity and specificity for tetracycline (TC)[4v] (**Figure 11**).

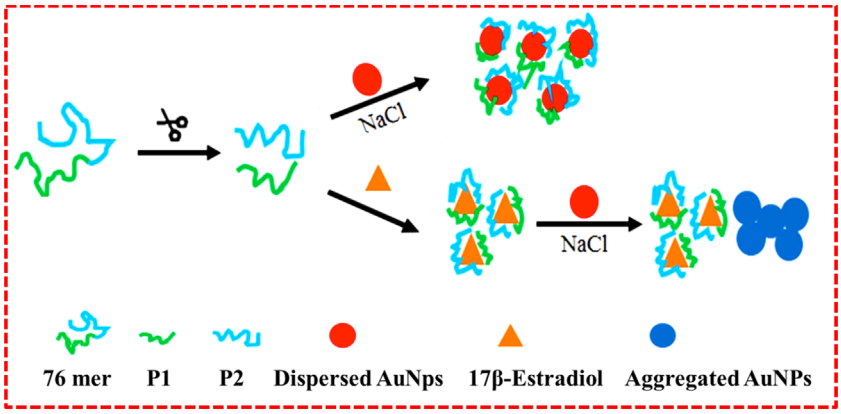

Figure 12. Schematic illustration of an AuNP-based colorimetric aptasensor to detect 17β-estradiol using split aptamers. Reproduced from.[4x] Split aptamers binds irreversibly to the target analyte.

Although only the original stacking pocket and six additional specific bases are present in A1 and A2, they display higher binding affinity (K_d 1.067 nM for TC). The LOD of A2 for oxytetracycline (OTC) was 0.1 nM, which is about 500-fold better than that of the original 76-mer aptamer, and the color change can be detected in the presence of 10 nM OTC.[4v] Similarly, based on their common sequence and predicted structure, Changill Ban's group[4l] shortened three 90-mer ssDNA aptamers that specifically bind to ampicillin to obtain AMP4 (21-mer 5′-CACGGCATGGTG GGCGTCGTG-3′), AMP17 (19-mer 5′-GCGGGCGGTTGTATAGCGG-3′), and AMP18 (21-mer 5′ TTAGTTGGGGTTCAGTTGG-3′).[4l] Comparison of AMP17, AMP4 and AMP18 (at concentrations of 100, 150, and 200 mM, respectively) showed that ampicillin can be detected at concentrations as low as 5 ng mL^{-1} using the AuNP-based dual fluorescence–colorimetric method and in a milk sample at 10 ng mL^{-1}.[4l]

Thus, the results by Song et al.[4v] and Kwon et al.[4l] illustrate and confirm that using aptamers harboring only the binding site/active site sequence can further improve their selective features.

Importantly, the target must not react or crosslink with NPs. Moreover, the ratio between NPs and aptamer could affect the final sensitivity. Too many aptamers in the sensing system reduce the sensitivity, while too few decrease, the stability of the sensing systems.[4q] One of the primary challenges of Type I approaches relies on the different binding affinities of ssDNA and dsDNA toward unmodified NPs. However, the important feature is that negatively charged ssDNA sequences can effectively stabilize NPs against salt-induced aggregation, providing a convenient route for colorimetric assays without NP surface biomodification.

5.2. Type II: Aptamer-Target Adsorbed on Nanoparticles

Type II aptamers also include two common steps: (i) aptamer linkage to the target molecule to form a complex, and (ii) aptamer-target complex adsorption to the NP surface. With Type II approaches, it is always wise to check the interaction of the pure aptamer with NPs (Type I) because the system may follow a similar mechanism.[4c,50] Ideally, aptamer adsorption onto the NP surface should not lead to NP aggregation (and thus color change) after addition of high salt concentration. In the presence of the target, the aptamers should bind in competition with AuNPs, resulting in a color change in the presence of salts. A typical Type II system has been used by Chen et al. for sulfadimethoxine (SDM) detection using unmodified AuNPs. In optimal conditions (pH 8, 0.2 mM of aptamer and 2 M of salt), the LDR was 50 ng mL^{-1} to 1 mg mL^{-1} and the LOD was 50 ng mL^{-1}.[4n]

Upon addition of SDM, the conformation of the SDM-binding aptamer changes from a random coil structure to a more folded rigid structure that promotes the detachment of the adsorbed aptamers from AuNPs and results in the subsequent AuNP aggregation after salt addition. This leads to a color change from red to purple-blue that can be easily observed by naked eye,[4n] Recently, Liu et al. assessed whether aptamer truncation could improve the sensitivity also in Type II aptamers[4x] (**Figure 12**). Briefly, the long (76-mer) aptamer specific for 17β-estradiol was split in two shorter sequences (P1 and P2) that still retain the original aptamer affinity and specificity, but with 10-fold higher LODs. Indeed, 17 β-estradiol could be detected with a LDR from 0.1 to 105 ng mL^{-1}.[4x] The authors hypothesized that this increased sensitivity is caused by the lower aptamer adsorption concentration and lower affinity for AuNPs of the shorter ssDNA sequences.[4v,x] Likewise, Xie et al.[7o] developed an assay in which incubation of a RNA-DNA duplex with the HIV-1 reverse transcriptase (RT) leads to the production of ssDNAs and ssRNAs that can form a charged protecting layer on the AuNPs surface and consequently, to NP stabilization at a precisely defined salt concentration. In the absence of RT, the selected RNA–DNA duplex remains intact, and the unprotected AuNPs aggregate in the presence of salt with a concomitant change in color.

Wang et al.[3e] used K^+ as a target because it stabilizes ssDNA, thus facilitating the formation of G-tetrads within 4 min. AuNPs incubated with G-tetrads changes color (red-to-purple) like unmodified AuNPs, suggesting that the G-tetrad structure is not significantly adsorbed onto AuNPs.[3e] The presented assay,

which uses C-rich (5′-CCTCCCTCCTTTTCC ACCCACC-3′) oligonucleotide aptamers, cationic polymers, and AuNPs, provides a platform for the detection of other ions and molecules[3g] (**Figure 13**). For instance, in the presence of Ag+, the two oligonucleotide form a tightly bound complex with a C–Ag^+–C notation and change conformation, from a random coil to a hairpin structure with a stronger π–π* transition of the bases with deoxyribose. The resulting C–Ag^+–C complex poorly interacts with a cationic polymer known as Poly (diallyldimethylammonium chloride) (PDDA) and subsequently the polymer aggregates AuNPs through electrostatic interactions, with a color change from wine red to blue.[3g] In the absence of Ag^+, the positively charged polymer can electrostatically interact with ssDNA and destroy the charge balance, leading to induction of AuNP aggregation (LOD of 48.6 nM and LDR from 100 to 1000 nM for Ag^+). Together, the results by Wang et al.[3e,g] are in agreement with the hypothesis that unstructured DNA oligonucleotides strongly adsorb onto the NP surface and prevent salt-induced NP aggregation.

Recently, Zhang et al.[7p] demonstrated that AuNPs possess peroxidase-like activity that can catalyze 3, 3, 5, 5-tetramethylbenzidine (TMB) in the presence of H_2O_2. AuNP peroxidase-like activity can be improved by surface activation with target-specific aptamers. However, by increasing the concentration of abrin (i.e., the target), AuNP peroxidase-like activity decreases and the aptamer is desorbed from the AuNP surface, resulting in a decrease of AuNP catalytic activity. The LDR for the current analytical system ranges from 0.2 to 17.5 nM with LOD of 0.05 nM.[7p]

Comparison of Type I and Type II systems shows that aptamer-NP complexes are preferentially formed in Type I and aptamer-target complexes in type II systems. It is reasonable to expect less sensitivity from Type I systems because the colorimetric changes are related to the aptamer detachment from the NP surface. The amount of aptamer removed will depend on the amount of target. On the other hand, Type II systems are limited by the fact that the aptamer is expected to retain its adsorption properties after complexation with the target. This suggests that if it is folded during target binding, it should be flexible enough to facilitate colorimetric changes. Overall it all depends on the aptamer capability because we would prefer induced aggregation in the absence of the aptamer.

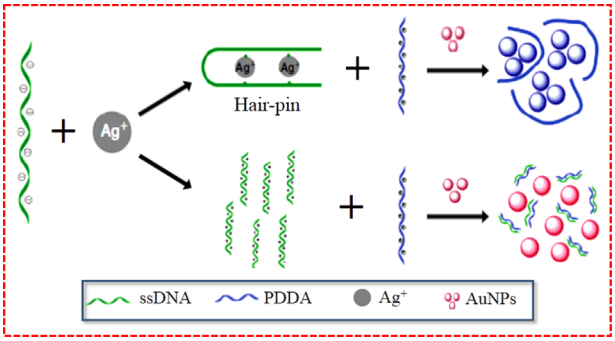

Figure 13. Schematic description of the colorimetric lead biosensor for Ag^+ detection based on AuNP aggregation induced by PDDA and Ag^+ aptamers.[3g]

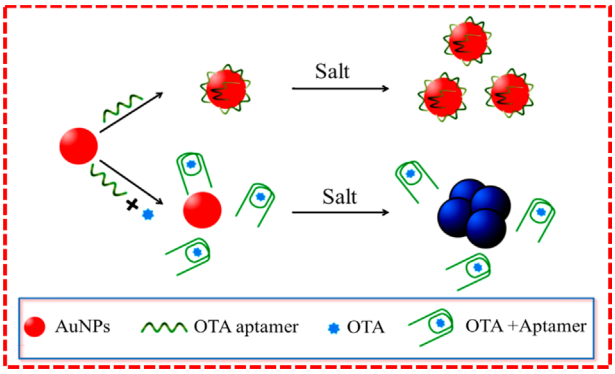

Figure 14. *One-pot detection system of* ochratoxin A (OTA). The target is bound to the aptamer and upon salt addition, AuNP aggregation can be detected by the solution color change.[4k]

5.3. Type III: Competition in "One-Pot Detection Systems"

Type III approaches are an intermediate between Type I and Type II systems because the aptamer and the target (or targets) interacts in the presence of NPs, and therefore, this approach is often referred to as *"one-pot detection systems."* Sometimes, more than one class of aptamers are used to stabilize NPs.[4x] Yang and co-workers[4k] described a *"one-pot detection system"* for ochratoxin A (OTA) where phosphate buffered saline (PBS), Mg^{2+}, OTA, and the aptamer are mixed with AuNPs that can undergo salt-induced aggregation within 5 min[4k] (**Figure 14**).

Although the method is different, the authors hypothesized that "the duly formed G-quadruplex structure could not protect AuNPs against salt-induced aggregation, and thus the color change from red to blue could be observed by the naked eye," as previously proposed by Wei et al.[5g] and Wang et al.[3e] for Type I and Type II detection systems. Interestingly the LOD is 20 nM, while the LDR from 20 to 625 nM.[4k] The major limitation of the Type III approach is that there is more than one source of electrostatic interactions that could change the solution color. For instance, if the metal is in excess, it will also contribute to the electrostatic interactions, and this can only be prevented by having ssDNA in excess. Therefore selectivity is a major limiting factor for this approach.

5.4. Type IV: Multiplex Aptasensors

In this section, the systems that use more than one aptamer based on the previously described structure-switching strategies are described. In homogeneous multiplex aptasensors, more than one class of aptamer is used to stabilize NPs for detection of single or several targets [4x]. Several approaches are based on the likelihood that the target DNA molecules with one nucleotide mismatch have different melting temperatures, and therefore they can be distinguished by NPs disassociation based on temperature.[6b,c,f,7e,17a,50] A typical example of such a DNA sensor was reported by Mirkin and co-workers,[18] in which the target DNA molecules triggered AuNPs aggregation by hybridizing two complementary DNA strands on the AuNPs.

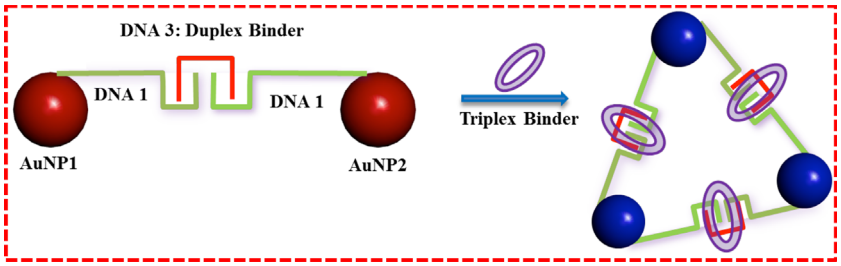

Figure 15. Representation of the structure and color change of nano-assemblies in the presence of a triplex binding agent at room temperature.[42]

Another assay includes AuNPs of different sizes (AuNP1 and AuNP2) that are functionalized with non-complementary DNAs (3′ or 5′ pyrimidine-rich thiol-modified oligonucleotides) (**Figure 15**). Functionalized AuNP1 and AuNP2 are then cross-linked with another complementary DNA to form non-aggregating duplexes.[42] Introduction of a triplex binding agent induces triplex formation through base hydrogen bonds and consequently, reversible NP aggregation that result in a red-to-blue color change.[42] Analysis of the aggregate melting properties in terms of cooperative binding theories suggests a lower DNA surface coverage on AgNPs functionalized with 12 mer-thiolated homo-oligonucleotides containing only adenine (AgNPs/ST) than that on AuNPs functionalized with 12 mer-thiolated homo-oligonucleotides containing only thymine (AuNPs/ST), while exhibiting changes that are significantly different from those of AuNPs upon hybridization.[51]

Interestingly, Sato et al.[48] demonstrated that ssDNA–AuNPs have different stability against salt-induced aggregation in the presence of complementary DNA, although there is no triplex binder.[48] Using a similar assay format, Zhao et al. configured oligonucleotide-modified AuNPs duplexes with a short complementary oligonucleotide. Upon addition of adenosine (the target), the aptamer switches its structure from a DNA duplex to an aptamer/target complex, because the aptamer preferentially binds to the target molecule.[7b] Importantly, the aptamer on NP surfaces must retain its switching capability.[7b,18,42,48] Erickson's group[15] developed a multiplexed one-pot detection system for Kaposi's sarcoma-associated herpesvirus (KSHV) and Bartonella using both AuNPs and AgNPs. Specifically, when the Bartonella-targeted DNA (BA-DNA) is introduced in the solution, AgNPs aggregate and the solution turns pink, more dependent on the SRP characteristics of non-aggregated AuNPs. When KSHV-DNA was introduced, AuNP aggregate and the solution changes to a murky yellow-orange color, more dependent on AgNP aggregation.[15] The multi-color change tuning of AuNPs and AgNPs gave LODs down to 1 and 2 nM, respectively.[15]

Niu et al.[4x] used more than one class of aptamers to stabilize AuNPs (Type I). Specifically, a kanamycin-specific aptamer (750 nM), a sulfadimethoxine-specific aptamer (250 nM) and an adenosine-specific aptamer (500 nM) are mixed (1:1:1 volume ratio) and adsorbed directly onto the surface of unmodified AuNPs by electrostatic interaction. Upon addition of any of the three targets, the conformation of the corresponding aptamer changes from a random coil structure to a rigid folded structure that cannot adsorb and stabilize AuNPs.[4x] Although this looks more like a type III system, more than one aptamer is present and the reaction does not proceed sequentially.

Ultimately, multiplex systems are not straight forward because multiplex detection largely depends on the concentration of each aptamer and the buffer used for the aptamer reaction with its target.[4x] Moreover, all the aptamers in solution can be adsorbed onto the NP surface; however, the level of adsorption also depends on the neighboring aptamers. For this reason, the use of aptamers with short sequences gives better adsorption yields. It has been shown that changing the length of the ssDNA sequences yields different particle dispersion profiles on unmodified AuNPs, and that short DNA sequences might improve the colloidal stability against salt-induced aggregation.[4l,v,6e] Most importantly, the aptamer on the NP surface must retain its switching capability and for this reason the switching capability of the structures with aptamers is a key factor that determine the LOD of the assay.[7b]

The multiplex type of aptamers has proven to be useful for enzyme activity and inhibitor assays.

5.5. Nanoparticle-Based Enzyme Assays

NPs can be used also to improve colorimetric assays of enzymes.[52] In these systems, the substrate for the target enzyme should also be a suitable NP stabilizer. For instance, it should be stable at high salt concentration (approximately 100 mM). Moreover, a charged molecule that can provide electrostatic and steric stabilization is likely to yield better selectivity. The strong interaction between amino groups and AuNPs surfaces has been well confirmed and the bond energy is comparable to that of a thiol–Au bond. The rapid aggregation induced by the non-crosslinking process is a useful approach for enzyme inhibition-based colorimetric screening, as shown by several studies using assays that rely on polymeric aggregates of DNA-functionalized AuNPs (DNA–AuNPs) with DNA-duplex interconnections.[7e,j,k] Mirkin's group functionalized two separate batches of 13-nm AuNPs with two different thiol-modified oligonucleotide strands (DNA-1: 5′-CTCCCTAATAACAATTTA TAACTATTCCTA-A10-SH-3′, and DNA-2: 5′-TAGGAATAGTTA TAAATTGTTATTAGGGAG-A10- SH-3′) (blue and red ribbons, respectively, in **Figure 16**).[7e]

The endonuclease (DNase I) degrades the DNA-duplex interconnections and NPs are released, thus generating a red color[7e] (Figure 16). In the presence of inhibitors, the DNase 1 activity is decreased and the aggregates are strongly hydrolyzed

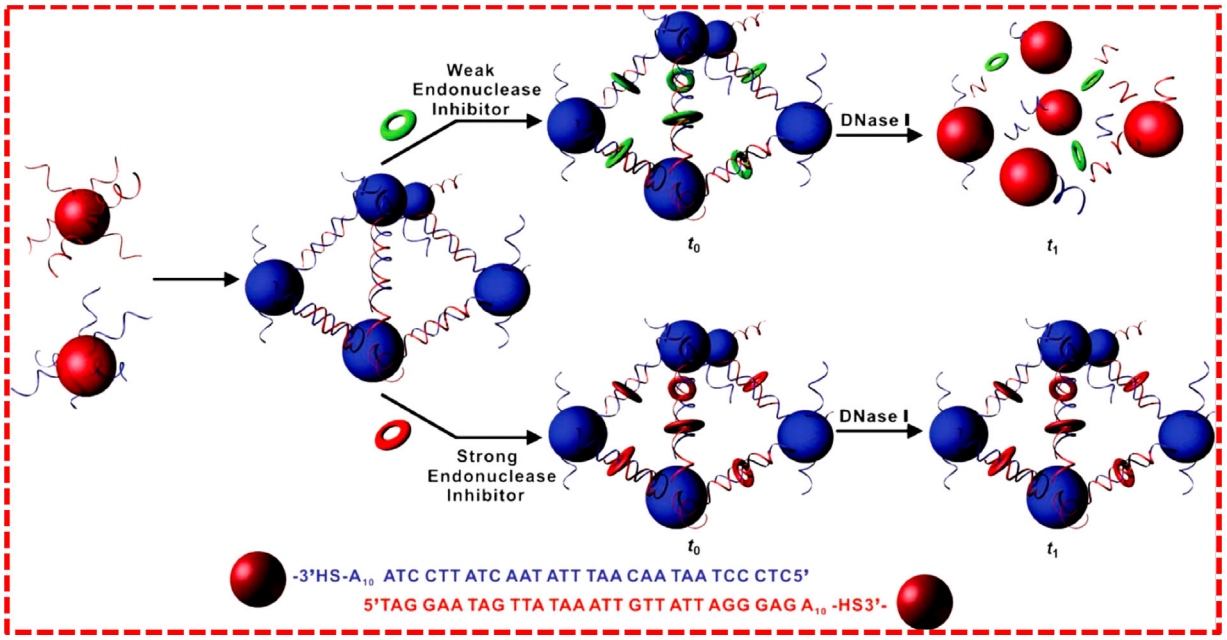

Figure 16. Aggregation and dissociation of the DNA-AuNPs probe used in the colorimetric screening of endonuclease inhibitors. The probe consists of spherical AuNPs functionalized with two complimentary oligonucleotides (blue and red ribbons). Individual NPs (red) aggregate into a cross-linked network of NPs (blue) through hybridization of their oligonucleotide chains. Upon addition of DNase I, the aggregates remain intact longer in the presence of a strong endonuclease inhibitor.[7e]

(T_H) . Consequently, the time required for the color change is much longer. Most importantly, strong inhibitors (in contrast to weak inhibitors) hinder DNase I activity to such an extent that the color change is no longer possible.[7e] In their method, endonucleases cleaves dsDNA in the absence of inhibitors and cross-linked AuNPs can separate into single AuNP molecules, as indicated by the instant color change, from blue to red. With this approach, the inhibitor performance can be directly evaluated. Similar observations were made using a system that includes a single type of DNA–AuNPs probe and an appropriate oligonucleotide linker that can hybridize with the DNA probe. The linker was designed to contain a self-complementary region that can form a duplex structure with a base-pair overlap that contains the recognition sites and overhanging 3′-ends[7k] (**Figure 17**). Significant color change is observed when the endonuclease (DNA methyltransferase, DNA MTase) degrades the DNA duplex.[7k]

Although highly selective and more sensitive than conventional methods, this visual inspection assay is limited for the preparation of probes by functionalizing two separate AuNP batches with two different thiol-modified oligonucleotide strands. On the other hand, this approach can be used for most endonucleases by simply changing the recognition sequence in the linker DNA.[7k] For instance, similar assays were used for assessing adenosine triphosphate (ATP) dephosphorylation by calf intestine alkaline phosphatase (CIAP) and peptide phosphorylation by protein kinase A (PKA). ATP can protect AgNPs from salt-induced aggregation only in the absence of enzymes. Phosphorylation and dephosphorylation can be readily detected by the color change of AgNPs (CIAP LOD: 1 U mL^{-1}, and PKA LOD: 0.022 U mL^{-1}).[7h] Zhao and co-workers took advantage of the non-crosslinking AuNPs aggregation phenomenon to develop a simple colorimetric assay for monitoring an enzymatic dephosphorylation reaction, where ATP is converted into adenosine by CIAP.[7a] AuNPs capped by adenosine 5′-monophosphate (AMP), adenosine 5′-diphosphate (ADP), or adenosine 5′-triphosphate (ATP) are progressively more stable than bare AuNPs, but their stability gradually decreases (and thus the color of the solution) with the dephosphorylation process.[7a] Likewise, Choi et al.[40] described an alkaline phosphatase assay based on AuNPs aggregation.[40] To develop an adenosine deaminase assay, Zhang and co-workers[8] hypothesized that the interaction between adenosine amino group and AuNPs surface will displace the weakly bound citrate ions from the AuNPs surface and diminish the stability of citrate-capped AuNPs, resulting in the aggregation of AuNPs in the presence of NaCl and a corresponding red to blue color change. Adenosine, guanosine, and cytidine (molecules that contain amino groups) strongly interact with AuNPs, causing aggregation. Conversely, inosine, thymidine, and uridine have negligible effects on AuNPs stability, therefore the solution remains red because of the stronger electrostatic repulsion between negatively-charged AuNPs. Xinhui et al.[7j] described a suitable method for nucleases, such as the S1 nuclease. In the presence of nucleases and their substrates, unmodified AuNPs are stabilized by dNMPs at high salt concentration and the solution remains red. Conversely, in the absence of nucleases or substrates, the unmodified AuNP solution turns blue at high salt concentration due to aggregate formation.[7j]

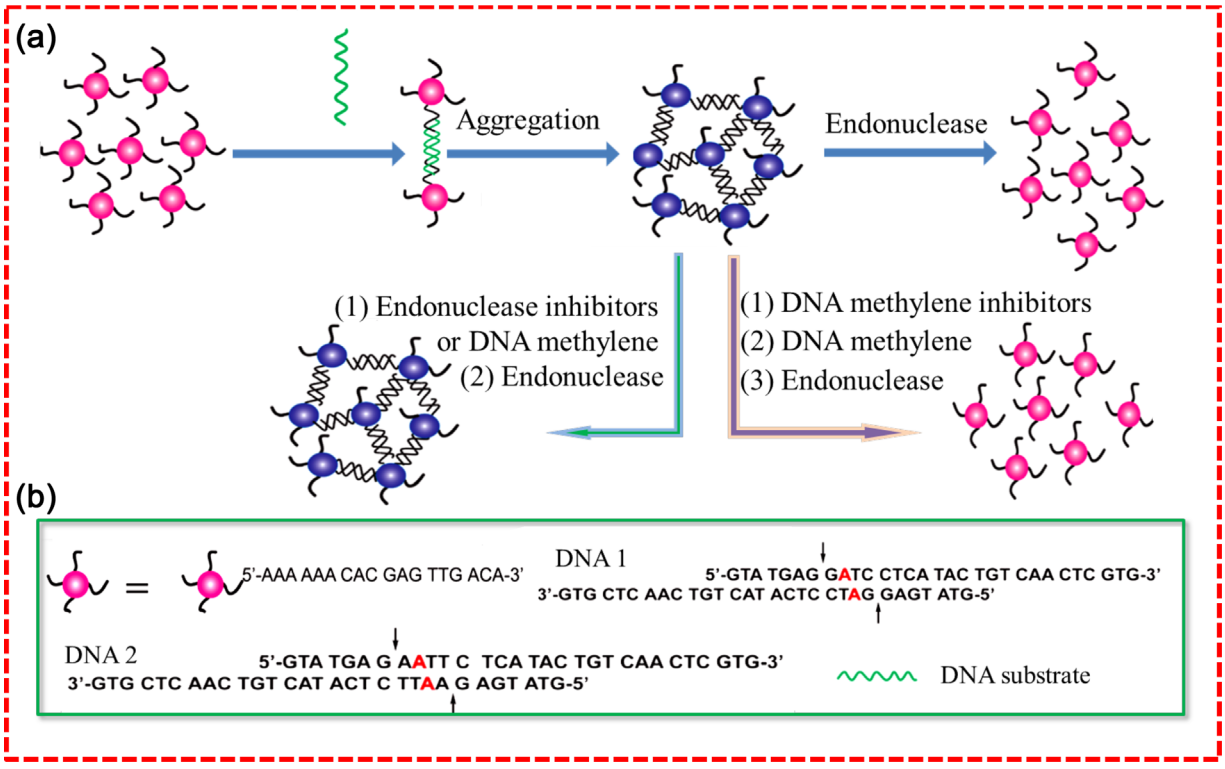

Figure 17. a) Schematic representation of the assay to assess endonuclease and methyltransferase activity and inhibition. b) Sequences of the DNA probe, DNA-1 (recognition site for the DpnII/Dam MTase) and DNA-2 (recognition site for the EcoRI/EcoRI MTase). The arrows show the cleavage sites, and the red letters indicate the methylation sites.[7k]

Xu and co-workers[7d] developed a colorimetric assay to screen for inhibitors of several kinases with the same type of NPs (**Figure 18**). The method takes advantage of peptide-capped NPs, in which 10% of peptide ligands carry an extension that is the substrate for a specific kinase (PKA or calmodulin-dependent kinase II, CaM KII). Using γ-biotin-ATP as a co-substrate, the kinase reaction results in substrate-AuNP biotinylation.

When biotinylated substrate-AuNPs are mixed with avidin-AuNPs, they immediately aggregate due to the specific binding between avidin and biotin.[7d] Similarly, Wei et al.[7h] reported that in the absence of the kinase, or in the presence of an efficient inhibitor, no observable color change occurs after addition of avidin-modified NPs, and the solutions are indefinitely stable without showing signs of aggregation.[7d] Furthermore, a hydrolysis-based colorimetric assay for acetylcholinesterase (AChE) was developed based on the finding that AChE can catalyze acetylthiocholine hydrolysis into thiocholine.[45] AChE and acetylthiocoline are added in the AuNP solution, the generated thiocholine can take the place of citrate on the AuNP surface, promoting NP aggregation and a change of color from red to gray. Addition also of the AChE inhibitor tacrine (1,2,3,4-tetrahydroacridin-9-amine) leads to less AuNP aggregation and a slower color change.[45] Uehara et al.[43] reported that gold nanocomposites conjugated with a thermo-responsive copolymer can be used in a colorimetric assay to quantify the activity of aminopeptidase N (APN). By heating the solution, the assembled gold nanocomposites disassemble and the solution color change from blue, purple to red. This process is inhibited by cysteine, therefore the enzymatic decomposition of cysteinylglycine into cysteine and glycine by APN can be monitored.[43]

Tiwari et al.[7m] hypothesized that particles could be used for the detection of the hydrolytic activity of penicillin G acylase (PGA) on penicillin G. This hydrolysis reaction leads to a shift in the surface plasmon band of AuNPs from 527 to 545 nm accompanied by a solution color change from red to blue. The presence of 0.007 mg mL^{-1} PGA can be detected. The enzyme is known to hinder the salt-induced NP aggregation. Xie and co-workers[7o] found that DNA–RNA duplexes cannot stabilize unmodified NPs at a certain salt concentration, a typical type II approach. However, addition of the active HIV-1 RNase H enzyme leads to the specific cleavage of RNA strands into RNA fragments and ssDNAs that can stabilize NPs against salt-induced aggregation. In an assay for glycosidases based on self-immolative elimination to release amines, functionalized trigger-AuNPs aggregate by electrostatic attraction upon cleavage of the trigger. The assay gives LODs for β-galactosidase (Gal) and β-glucosidase (Glc) of 9.2 and 22.3 nM, respectively, at 20 min, and they improve slightly over time.[44] The functionalized AuNPs (2.0 nM), which were capped with the enzyme substrate ligand Gal-Lip (or Glc-Lip) and lipoic acid at a ratio of 1:1, showed a typical SPR peak at 521 nm (i.e., a red shift of 2 nm compared with citrate-AuNPs) and good stability in PBS. The respective addition of Gal or Glc caused a time-dependent decrease of the peak absorbance induced by NP aggregation that could be observed by naked eye.

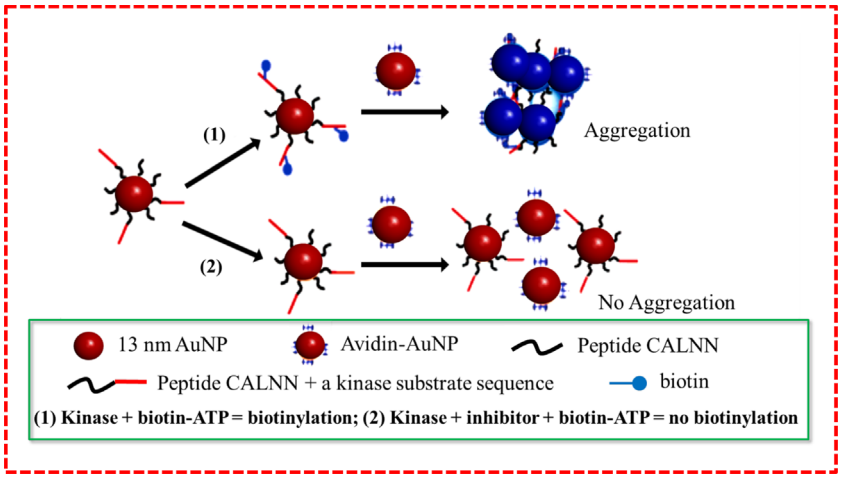

Figure 18. Schematic representation of phosphorylation/biotinylation of substrate-NPs followed by addition of avidin-modified NPs, in the presence and absence of a kinase inhibitor.[7d]

Two different systems (the DNA endonuclease DNase I and the Pb^{2+}-dependent RNA-cleaving DNA enzyme 8–17) were chosen to demonstrate the utility of an assay for the detection of metal ions and enzyme activities based on rapid NP aggregation driven by van der Waals attraction[7i] (**Figure 19**).

The authors reasoned that the removal from the NP surface of DNA strands, which serve as electrostatic and steric stabilizers at relatively high salt concentrations (e.g., 40 mM $MgCl_2$), should result in AuNPs destabilization and aggregation, a process driven by van der Waals attraction.[7i] Indeed, addition of 100 mM Pb^{2+} generated a rapid red-to-purple color change at room temperature.[7i]

AuNPs generation induced by neurotransmitters can be used to analyze the activity of tyrosinase, an enzyme that catalyzes the O_2-induced hydroxylation of tyrosine to L-DOPA.[4b] As tyrosinase concentration increases, the SPR bands of NPs are intensified and slightly blue-shifted, suggesting that larger particles are formed, and small Au nanoclusters enlarged.[4b] This system can be used for the sensitive detection of dopamine, L-DOPA, and noradrenaline (LOD of 2.5 μM) and adrenaline (0.2 μM) that act as active reducing agents for Au–NP generation of Au–NPs.[4b]

Colorimetric aptasensors for the quantitative analysis of abrin using catalytic AuNPs were reported for the first time by Zhang et al. and Wu et al. The AuNP peroxidase-like activity can catalyze 3, 3, 5, 5-tetramethylbenzidine (TMB) formation in the presence of H_2O_2, leading to a color change.[4a,7p] Particularly, Song et al.[7k] quote the work by Mirkin's group[7e] and say that the rest of the methods eliminate the binder use of different DNAs to obtain functionalized-NP1 and functionalized-NP2. However, such method requires cumbersome preparation of modified NPs and the formation of crosslinked NPs. Thus, it is not suitable for high-throughput screening.

Crosslinking also offers a unique selectivity in reversibility of NP aggregation, where analytes dissociate the cross-linker and re-disperse the NP aggregates to their original color. For instance, Lu and co-workers described detection assays for Pb^{2+}, adenosine, and cocaine where DNA molecules with a single RNA linkage serve as cross-linkers that bring complementary DNA-AuNPs into aggregates. The DNA enzyme catalyzes the specific hydrolytic cleavage of the substrate strand that disrupts the NP assembly, changing the color from purple to red and thus indicating the presence of Pb^{2+}.[3a,7c]

Zhao and co-workers[7a] speculated that if the substrate and product of an enzymatic reaction affect differently AuNP stability by changing their electrophoretic properties, such a reaction can be monitored colorimetrically and the enzymatic activity can therefore be determined.

6. Core-Shell Nanoparticles and Ratios

Core–shell nanoparticles (CSNs) are a class of nanostructured materials that have recently received increased attention owing to their interesting properties and broad range of applications in catalysis, biology, materials chemistry, and sensors. By rationally tuning the cores as well as the shells of such materials (ratios), a range of core–shell nanoparticles can be produced. In this review, the combination of gold and silver enhancement, an electron-dense deposits that can be read by a simple colorimetric array workstation.[6d] However, Cao et al.[17b] stated that AgNPs cannot be effectively passivated by alkylthiol-modified-oligonucleotides using the protocols for modifying AuNPs, because they irreversibly aggregate when heated in a solution with 0.05 M NaCl, the concentration needed for DNA hybridization. For this reason, an Au shell can be grown on AgNP, forming a particle with an Au outer surface (3.1 ± 0.6 Å). This surface can be easily modified with alkylthiol-oligonucleotides and indefinitely suspended in high salt solutions. Ag/Au core-shell NPs retain the optical properties of the silver core, but have optical properties different from pure AuNPs, thus providing another "color" option for 30-mer DNA target-directed colorimetric detection.[6f,17b]

By taking advantage of their reversible aggregation and melting nature, oligonucleotide-modified $Ag@SiO_2$ nanoprobes can be prepared by using 5′ TCT-CAA-CTC-GTA-(CH_2)

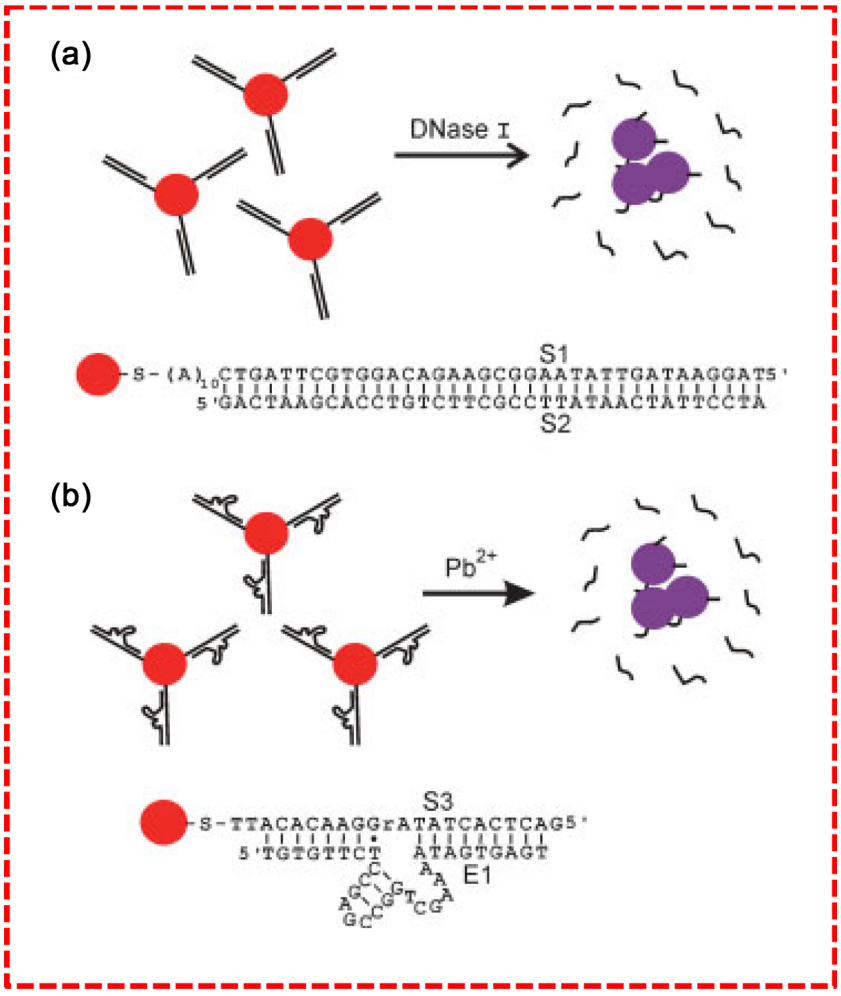

Figure 19. Schematic illustration of AuNP aggregation and color change triggered by the enzymatic cleavage of DNA on AuNPs. Before enzymatic cleavage, DNA-modified AuNPs are stable at a relatively high salt concentration, due to their electrostatic and steric stabilization. DNA removal from the AuNP surface by enzymatic cleavage destabilizes AuNPs and results in their rapid aggregation. a) Cleavage of a DNA duplex by DNase I. b) Pb^{2+}-mediated cleavage of an RNA-containing DNA substrate by the 8–17 DNA enzyme.[7i]

7-NH_2 3′ and non-complementary oligonucleotides with a 5′ TAC-GAG-TTG-AGA-GAG-TGC-CCA-CAT3′ sequence in which no hybridization product was reported.[50] The high stability of oligo-modified Ag@SiO_2 nano-probes at elevated temperatures (30–70 °C) was confirmed by the absence of peak shift and of broadening of well-dispersed nano-probes in their UV-Vis spectra after long heating. The fast hybridization kinetics of the resulting Ag@SiO_2 nano-probes with complementary target oligonucleotides render them very useful for fast colorimetric detection based on the sequence-specific hybridization properties of DNA.[50]

CSNs can also be used to introduce a second colorimetric change, distinct from the gold system, for monitoring two different oligonucleotide targets in one sample.[17b] For instance, when lactose-stabilized AuNPs are mixed with mannose (2-mercaptoethyl R-D-mannopyranoside)-stabilized AgNPs,[2] addition of concanavalin A (Con A) leads to the aggregation only of mannose-stabilized AgNPs, thereby demonstrating the system selectivity. Limited non-specific interaction occurs with lectin Con A, thereby enabling the subsequent specific interaction with the lectin from *Ricinus Communis* Agglutinin (RCA120). Although mannose-stabilized AgNPs show a longer LDR and faster reaction kinetics for the target lectin, mannose-stabilized AuNPs provide the most sensitive bioassay.[2]

Nevertheless, the synthesis of the CSNs can be a daunting task for quick assays.[4f]

7. Summary and Outlook

The detection of metals and molecules based on bare-eye observable colorimetric changes depends on various parameters that are even more complex for macromolecules. The functional groups on the NP surface are very influential in various areas of research, such as sensor arrays and biosensor detection. Overall in any given condition, both thiols, and nucleotides compete for adsorption sites, and the equilibrium shifts toward thiols adsorption as the salt concentration increases. Therefore,

nucleotide adsorption could be completely eliminated after being "crowded out" (steric hindrance) as more thiols are adsorbed onto the metal. In one-pot detection approach (where nanoparticles, analyte, DNA, or enzyme are mixed together) qualitative analyses is deemed imprecise because the color changes are not only due to the analyte, as they could be triggered also by DNA or enzyme adsorption to the NP surface.

Also, the multiplex aptasensors have some limitations. For instance, it is not possible to determine which target is detected when the sample gives a positive result (change of color). While enzyme-assisted assays have a huge potential for many applications in biomedicine and bio-imaging, the application of the described in vivo techniques faces formidable challenges. Indeed, the interactions of NPs with enzyme molecules are not yet fully understood.

Through the review, there are viable approaches that have been introduced, Firstly, aptamer truncation to overcome the limitations due to the DNA length, while maintaining the original binding affinity. Secondly, overcoming the limitation imposed by the stability of AgNPs by coating them with a thin layer of gold to produce a core–shell structure that retains the spectrophotometric signature of the silver core. Thirdly, use of chemometric approaches provides synergy in colorimetric discrimination or classification of small molecules and macromolecules.

Overall, the AuNP-based colorimetric aptasensors are currently used for many analytes, largely because of the ease of detection, high sensitivity, and potential for high-throughput analysis. Moreover, the synergy between chemometrics and biotechnology selectivity narrows the gap for the development of smart apta-based colorimetric sensing devices. In any case, careful interpretation of the findings is critical because the colorimetric changes are not general or universal, suggesting that they are highly dependent on the analytes and matrices.

Conflict of Interest

The authors declare no conflict of interest.

Keywords

colorimetric-based methods aggregation, gold and silver nanoparticles

Received: March 25, 2017
Revised: July 3, 2017
Published online: August 3, 2017

[1] a) V. Chegel, O. Rachkov, A. Lopatynskyi, S. Ishihara, I. Yanchuk, Y. Nemoto, J. P. Hill, K. Ariga, *J. Phys. Chem. C* **2012**, *116*, 2683; b) T. C. Prathna, N. Chandrasekaran, A. Mukherjee, *Colloids Surf. A Physicochem. Eng. Asp*. **2011**, *390*, 216; c) V. Amendola, O. Bakr, F. Stellacci, *Plasmonics* **2010**, *5*, 85; d) W. Wang, M. Yang, Z. Wang, J. Yan, C. Liu, *RSC Adv.* **2014**, *4*, 63079.

[2] C. L. Schofield, A. H. Haines, R. A. Field, D. A. Russell, *Langmuir* **2006**, *22*, 6707.

[3] a) J. Liu, Y. Lu, *J. Am. Chem. Soc*. **2003**, *125*, 6642; b) A. Ravindran, V. Mani, N. Chandrasekaran, A. Mukherjee, *Talanta* **2011**, *85*, 533; c) S. Hajizadeh, K. Farhadi, M. Forough, R. Molaei, *Anal. Methods* **2012**, *4*, 1747; d) J. M. Slocik, J. S. Zabinski, D. M. Phillips, R. R. Naik, *Small* **2008**, *4*, 548; e) L. Wang, X. Liu, X. Hu, S. Song, C. Fan, *Chem. Comm*. **2006**, *0*, 3780; f) F. Xia, X. Zuo, R. Yang, Y. Xiao, D. Kang, A. Vallée-Bélisle, X. Gong, J. D. Yuen, B. B. Y. Hsu, A. J. Heeger, K. W. Plaxco, *Proc. Natl. Acad. Sci*. **2010**, *107*, 10837; g) F. Wang, Y. Wu, S. Zhan, L. He, W. Zhi, X. Zhou, P. Zhou, *Aust. J. Chem*. **2013**, *66*, 113.

[4] a) Z.-S. Wu, S.-B. Zhang, M.-M. Guo, C.-R. Chen, G.-L. Shen, R.-Q. Yu, *Anal. Chim. Acta* **2007**, *584*, 122; b) R. Baron, M. Zayats, I. Willner, *Anal. Chem*. **2005**, *77*, 1566; c) J. Liu, Y. Lu, Angew. *Chem. Int. Ed*. **2006**, *45*, 90; d) J.-S. Lee, P. A. Ulmann, M. S. Han, C. A. Mirkin, *Nano Lett*. **2008**, *8*, 529; e) Z. Chen, S. Luo, C. Liu, Q. Cai, *Anal. Bioanal. Chem*. **2009**, *395*, 489; f) X. Xu, J. Wang, F. Yang, K. Jiao, X. Yang, *Small* **2009**, *5*, 2669; g) Y. S. Kim, J. H. Kim, I. A. Kim, S. J. Lee, J. Jurng, M. B. Gu, *Biosens. Bioelectron* **2010**, *26*, 1644; h) Y. Zhang, B. Li, X. Chen, *Microchim. Acta* **2010**, *168*, 107; i) Y. Zhang, B. Li, C. Xu, *Analyst* **2010**, *135*, 1579; j) K.-M. Song, M. Cho, H. Jo, K. Min, S. H. Jeon, T. Kim, M. S. Han, J. K. Ku, C. Ban, *Anal. BioChem*. **2011**, *415*, 175; k) C. Yang, Y. Wang, J.-L. Marty, X. Yang, *Biosens. Bioelectron*. **2011**, *26*, 2724; l) K.-M. Song, E. Jeong, W. Jeon, M. Cho, C. Ban, *Anal. Bioanal. Chem*. **2012**, *402*, 2153; m) J. Athilakshmi, M. Mohan, D. K. Chand, *Tetrahedron Lett*. **2013**, *54*, 427; n) A. Chen, X. Jiang, W. Zhang, G. Chen, Y. Zhao, T. M. Tunio, J. Liu, Z. Lv, C. Li, S. Yang, *Biosens. Bioelectron*. **2013**, *42*, 419; o) H. Gao, W. Shen, C. Lu, H. Liang, Q. Yuan, *Talanta* **2013**, *115*, 1; p) A. Liu, Y. Zhang, W. Chen, X. Wang, F. Chen, *Eur. Food Res. Technol*. **2013**, *237*, 323; q) Z. Mei, H. Chu, W. Chen, F. Xue, J. Liu, H. Xu, R. Zhang, L. Zheng, *Biosens. Bioelectron*. **2013**, *39*, 26; r) S. Chen, H. Gao, W. Shen, C. Lu, Q. Yuan, Sens. *Actuator B-Chem*. **2014**, *190*, 673; s) H.-H. Deng, C.-L. Wu, A.-L. Liu, G.-W. Li, W. Chen, X.-H. Lin, *Sens. Actuator B-Chem*. **2014**, *191*, 479; t) C. Han, K. Xu, Q. Liu, X. Liu, J. Li, Sens. *Actuator B-Chem*. **2014**, *202*, 574; u) S. Jongjinakool, K. Palasak, N. Bousod, S. Teepoo, *Energy Procedia* **2014**, *56*, 10; v) Y. S. Kwon, N. H. Ahmad Raston, M. B. Gu, *Chem. Comm*. **2014**, *50*, 40; w) W. Li, C. Pan, T. Hou, X. Wang, F. Li, *Anal. Methods* **2014**, *6*, 1645; x) J. Liu, W. Bai, S. Niu, C. Zhu, S. Yang, A. Chen, *Sci. Rep*. **2014**, *4*, 7571; y) L. Zhang, C. Xu, C. Liu, B. Li, *Anal. Chim. Acta* **2014**, *809*, 123; z) I. E. Paul, A. Rajeshwari, T. C. Prathna, A. M. Raichur, N. Chandrasekaran, A. Mukherjee, *Anal. Methods* **2015**, *7*, 1453; aa) A. Sarreshtehdar Emrani, N. M. Danesh, P. Lavaee, S. H. Jalalian, M. Ramezani, K. Abnous, S. M. Taghdisi, *Anal. Methods* **2015**, 3419; ab) K. V. Ragavan, L. S. Selvakumar, M. S. Thakur, *Chem. Comm*. **2013**, *49*, 5960; ac) Y. Zhang, J. Jiang, M. Li, P. Gao, Y. Zhou, G. Zhang, S. Shuang, C. Dong, *Talanta* **2016**, *161*, 520; ad) S. Wu, D. Li, J. Wang, Y. Zhao, S. Dong, X. Wang, *Sens. Actuator B-Chem*. **2017**, *238*, 427.

[5] a) V. Pavlov, Y. Xiao, B. Shlyahovsky, I. Willner, *J. Am. Chem. Soc*. **2004**, *126*, 11768; b) C.-S. Tsai, T.-B. Yu, C.-T. Chen, *Chem. Comm*. **2005**, *0*, 4273; c) C.-C. Huang, Y.-F. Huang, Z. Cao, W. Tan, H.-T. Chang, *Anal. Chem*. **2005**, *77*, 5735; d) J. Li, X. Chu, Y. Liu, J.-H. Jiang, Z. He, Z. Zhang, G. Shen, R.-Q. Yu, *Nucleic Acids Res*. **2005**, *33*, e168; e) J.-M. Nam, K.-J. Jang, J. T. Groves, *Natl. Protocols* **2007**, *2*, 1438; f) R.-Q. Liang, C.-Y. Tan, K.-C. Ruan, *J. Immunol. Methods* **2004**, *285*, 157; g) H. Wei, B. Li, J. Li, E. Wang, S. Dong, *Chem. Comm*. **2007**, *0*, 3735; h) S. Siddhartha, D. Debabrata, *Nano-Micro Lett*. **2010**, *2*, 164; i) M. Lepoitevin, M. Lemouel, M. Bechelany, J.-M. Janot, S. Balme, *Microchim. Acta* **2015**, *182*, 1223; j) J. Mao, Y. Lu, N. Chang, J. Yang, S. Zhang, Y. Liu, *Biosens. Bioelectron*. **2016**, *86*, 56.

[6] a) R. Kanjanawarut, X. Su, *Anal. Chem*. **2009**, *81*, 6122; b) R. Elghanian, J. J. Storhoff, R. C. Mucic, R. L. Letsinger, C. A. Mirkin, *Science* **1997**, *277*, 1078; c) J. J. Storhoff, R. Elghanian, R. C. Mucic, C. A. Mirkin, R. L. Letsinger, *J. Am. Chem. Soc*. **1998**, *120*, 1959; d) I. Alexandre, S. Hamels, S. Dufour,

J. Collet, N. Zammatteo, F. De Longueville, J. L. Gala, J. Remacle, *Anal. BioChem*. **2001**, *295*, 1; e) H. Li, L. Rothberg, *Proc. Natl. Acad. Sci. USA* **2004**, *101*, 14036; f) Y. C. Cao, R. Jin, C. S. Thaxton, C. A. Mirkin, *Talanta* **2005**, *67*, 449; g) Q. Shen, Z. Nie, M. Guo, C.-J. Zhong, B. Lin, W. Li, S. Yao, *Chem. Comm*. **2009**, *0*, 929.

[7] a) W. Zhao, W. Chiuman, J. C. F. Lam, M. A. Brook, Y. Li, *Chem. Comm*. **2007**, *0*, 3729; b) B. Liu, L. Wen, X. Zhao, *Mater. Chem. Phys*. **2007**, *106*, 350; c) J. Liu, Y. Lu, *J. Fluoresc*. **2004**, *14*, 343; d) Z. Wang, R. Lévy, D. G. Fernig, M. Brust, *J. Am. Chem. Soc*. **2006**, *128*, 2214; e) X. Xu, M. S. Han, C. A. Mirkin, *Angew. Chem* **2007**, *119*, 3538; f) Y.-M. Chen, C.-J. Yu, T.-L. Cheng, W.-L. Tseng, *Langmuir* **2008**, *24*, 3654; g) J. Oishi, Y. Asami, T. Mori, J.-H. Kang, T. Niidome, Y. Katayama, *Biomacromolecules* **2008**, *9*, 2301; h) H. Wei, C. Chen, B. Han, E. Wang, *Anal. Chem*. **2008**, *80*, 7051; i) W. Zhao, J. C. F. Lam, W. Chiuman, M. A. Brook, Y. Li, *Small* **2008**, *4*, 810; j) X. Lou, Y. Xiao, Y. Wang, H. Mao, J. Zhao, *Chem. BioChem* **2009**, *10*, 1973; k) G. Song, C. Chen, J. Ren, X. Qu, *ACS Nano* **2009**, *3*, 1183; l) C.-K. Chen, C.-C. Huang, H.-T. S *Biosens. Bioelectron*. **2010**, *25*, 1922; m) N. Tiwari, Rathore, A., Prabhune, A. S. Kulkarni, *Adv. Biosci. Biotechnol*. **2010**, *1*, , 322; n) R. Cao, B. Li, Y. Zhang, Z. Zhang, *Chem. Comm*. **2011**, *47*, 12301; o) X. Xie, W. Xu, T. Li, X. Liu, *Small* **2011**, *7*, 1393; p) W. Zhang, Y. Tang, J. Liu, L. Jiang, W. Huang, F.-W. Huo, D. Tian, *J. Agric. Food Chem*. **2015**, *63*, 39.

[8] L. Zhang, J. Zhao, J. Jiang, R. Yu, *Chem. Comm*. **2012**, *48*, 10996.

[9] N. L. Rosi, C. A. Mirkin, *Chem. Rev*. **2005**, *105*, 1547.

[10] C. Lee, M. A. Gaston, A. A. Weiss, P. Zhang, *Biosens. Bioelectron*. **2013**, *42*, 236.

[11] a) Y. Yu, Y. Hong, Y. Wang, X. Sun, B. Liu, *Sens. Actuator B-Chem*. **2017**, *239*, 865; b) F. Ghasemi, M. R. Hormozi-Nezhad, M. Mahmoudi, *Anal. Chim. Acta* **2015**, *882*, 58; c) L. Li, B. Li, *Analyst* **2009**, *134*, 1361; d) N. Fahimi-Kashani, M. R. Hormozi-Nezhad, *Anal. Chem*. **2016**, *88*, 8099.

[12] Z. Chen, C. Zhang, T. Zhou, H. Ma, *Microchim. Acta* **2015**, *182*, 1003.

[13] S. Basu, S. Jana, S. Pande, T. Pal, *J. Colloid Interface Sci*. **2008**, *321*, 288.

[14] B. C. Vidal Jr, T. C. Deivaraj, J. Yang, H.-P. Too, G.-M. Chow, L. M. Gan, J. Y. Lee, *New J. Chem*. **2005**, *29*, 812.

[15] M. Mancuso, L. Jiang, E. Cesarman, D. Erickson, *Nanoscale* **2013**, *5*, 1678.

[16] X. Zhang, M. R. Servos, J. Liu, *Chem. Comm*. **2012**, *48*, 10114.

[17] a) J.-S. Lee, A. K. R. Lytton-Jean, S. J. Hurst, C. A. Mirkin, *Nano Lett*. **2007**, *7*, 2112; b) Cao, R. Jin, C. A. Mirkin, *J. Am. Chem. Soc*. **2001**, *123*, 7961.

[18] C. A. Mirkin, R. L. Letsinger, R. C. Mucic, J. J. Storhoff, *Nature* **1996**, *382*, 607.

[19] G. Mie, *Ann. Phys*. **1908**, *330*, 377.

[20] S. Kundu, *Phys. Chem. Chem. Phys*. **2013**, *15*, 14107.

[21] a) V. Banerjee, K. P. Das, *Colloids Surf. B* **2013**, *111*, 71; b) X. Zhao, R. Liu, Y. Teng, X. Liu, *Sci Total Environ* **2011**, *409*, 892; c) C. Bhan, R. Mandlewala, A. Gebregeorgis, D. Raghavan, *Langmuir* **2012**, *28*, 17043; d) C. Bhan, T. L. Brower, D. Raghavan, *J. Colloid Interface Sci*. **2013**, *402*, 40.

[22] W. Zhao, M. A. Brook, Y. Li, *Chem. BioChem* **2008**, *9*, 2363.

[23] Q. Qian, J. Deng, D. Wang, L. Yang, P. Yu, L. Mao, *Anal. Chem*. **2012**, *84*, 9579.

[24] H. Chen, W. Hu, C. M. Li, *Sens. Actuator B-Chem*. **2015**, *215*, 421.

[25] S. Watanabe, K. Yoshida, K. Shinkawa, D. Kumagawa, H. Seguchi, *Colloids Surf. B* **2010**, *81*, 570.

[26] Y.-J. Chuang, X. Zhou, Z. Pan, C. Turchi, *Biochem. Biophys. Res. Commun*. **2009**, *389*, 22.

[27] Y. Zheng, Y. Wang, X. Yang, *Sens. Actuator B-Chem*. **2011**, *156*, 95.

[28] J.-J. Feng, H. Guo, Y.-F. Li, Y.-H. Wang, W.-Y. Chen, A.-J. Wang, *ACS Appl. Mater. Interfaces* **2013**, *5*, 1226.

[29] H. Su, B. Sun, L. Chen, Z. Xu, S. Ai, *Anal. Methods* **2012**, *4*, 3981.

[30] K. Rawat, S. Kailasa, *Microchim. Acta* **2014**, *181*, 1917.

[31] W. Zhao, W. Chiuman, M. A. Brook, Y. Li, *Chem. BioChem* **2007**, *8*, 727.

[32] a) S. Aryal, R. B.K .C, N. Dharmaraj, N. Bhattarai, C. H. Kim, H. Y. Kim, *Spectrochim. Acta Part A: Mol. Biomol. Spectrosc*. **2006**, *63*, 160; b) A. Kuhnle, T. R. Linderoth, B. Hammer, F. Besenbacher, *Nature* **2002**, *415*, 891.

[33] G. Song, C. Xu, B. Li, *Sens. Actuator B-Chem*. **2015**, *215*, 504.

[34] Y. Sun, H. Zhao, I. Boussouar, F. Zhang, D. Tian, H. Li, *Sens. Actuator B-Chem*. **2015**, *216*, 235.

[35] W. Xue, G. Zhang, D. Zhang, *Analyst* **2011**, *136*, 3136.

[36] C. Guarise, L. Pasquato, V. De Filippis, P. Scrimin, *Proc. Natl. Acad. Sci. USA* **2006**, *103*, 3978.

[37] S. Abdul Rahman, R. Saadun, N. E. Azmi, N. Ariffin, J. Abdullah, N. A. Yusof, H. Sidek, R. Hajian, *J. Nanomater*. **2014**, *2014*, 5.

[38] F. Ghasemi, M. R. Hormozi-Nezhad, M. Mahmoudi, *Analytica Chimica Acta* **2015**, *882*, 58.

[39] J. Mehta, B. Van Dorst, E. Rouah-Martin, W. Herrebout, M.-L. Scippo, R. Blust, J. Robbens, *J. Biotechnol*. **2011**, *155*, 361.

[40] Y. Choi, N.-H. Ho, C.-H. Tung, *Angew. Chem. Int. Ed*. **2007**, *46*, 707.

[41] R. Liu, R. Liew, J. Zhou, B. Xing, *Angew. Chem. Int. Ed*. **2007**, *46*, 8799.

[42] M. S. Han, A. K. R. Lytton-Jean, C. A. Mirkin, *J. Am. Chem. Soc*. **2006**, *128*, 4954.

[43] N. Uehara, M. Fujita, T. Shimizu, *Anal. Sci*. **2009**, *25*, 267.

[44] Z. Zeng, S. Mizukami, K. Kikuchi, *Anal. Chem*. **2012**, *84*, 9089.

[45] M. Wang, X. Gu, G. Zhang, D. Zhang, D. Zhu, *Langmuir* **2009**, *25*, 2504.

[46] J. Hu, P. Ni, H. Dai, Y. Sun, Y. Wang, S. Jiang, Z. Li, *Analyst* **2015**, *140*, 3581.

[47] T. A. Taton, C. A. Mirkin, R. L. Letsinger, *Science* **2000**, *289*, 1757.

[48] K. Sato, K. Hosokawa, M. Maeda, *J. Am. Chem. Soc*. **2003**, *125*, 8102.

[49] M. Famulok, G. Mayer, *Nature* **2006**, *439*, 666.

[50] S. Liu, Z. Zhang, M. Han, *Anal. Chem*. **2005**, *77*, 2595.

[51] I. Tokareva, E. Hutter, *J. Am. Chem. Soc*. **2004**, *126*, 15784.

[52] X. Xie, W. Xu, X. Liu, *Acc. Chem. Res*. **2012**, *45*, 1511.

Journal of Photochemistry & Photobiology, B: Biology 178 (2018) 560–567

Contents lists available at ScienceDirect

Journal of Photochemistry & Photobiology, B: Biology

journal homepage: www.elsevier.com/locate/jphotobiol

One-pot biosynthesis of silver nanoparticles using *Iboza* Riparia and *Ilex* Mitis for cytotoxicity on human embryonic kidney cells

Myalowenkosi I. Sabela[a,*], Talent Makhanya[a], Suvardhan Kanchi[a,*], Mohd. Shahbaaz[a], Danish Idress[b], Krishna Bisetty[a,*]

[a] Department of Chemistry, Durban University of Technology, P.O Box 1334, Durban 4000, South Africa
[b] Centre for Interdisciplinary Research in Basic Sciences, Jamia Millia Islamia, Jamia Nagar, New Delhi 110025, India

ARTICLE INFO

Keywords:
Silver nanoparticles
Diterpenes
Saponins
MTT assay
Antioxidant activity

ABSTRACT

Plant extracts continue gaining significant prominence in green synthesis of silver nanoparticles (AgNPs), due to their potential applications in nano-medicine and material engineering. This work reports on green synthesis of silver nanoparticles (AgNPs) from aqueous extracts of *Iboza* Riparia *leaf* and *Ilex* Mitis root bark with diterpenes (DTPs) and saponins (SPNs) as major components. After TEM, DLS, TGA/DSC, ATR, XRD and UV–Vis characterization, the relevant cytotoxicity studies were conducted with the MTT assay on human embryonic kidney cells (HEK293T) followed by antioxidant activity with ABTS. Overall, the AgNPs-*DTPs* (156 nm) were found to be less toxic with 49.7% cell viability, while AgNPs-*SPNs* (50 nm) and AgNPs-*PVA* (44 nm) had cell viability of 40.8 and 28.0% respectively at 400 μM. Based on the cytotoxicity and antioxidant activity, it is fair to report that these plant extracts have potential reducing and capping agents as they retain chemical properties on the surface of the nanoparticles.

1. Introduction

Medicinal plants have been used for centuries as traditional treatments for numerous human diseases throughout the globe. This has transpired to a vast interest from researchers to better phyto-medicines and biologically active compounds that are isolated from medicinal plants. Bioactive compositions of the corona influence nanoparticle–cell interactions and biological fates and functions of nanoparticles [1]. Currently, several physical and chemical processes are widely used to synthesize metal nanoparticles, which allow one to obtain particles with the desired characteristics [2]. However, these methods are usually expensive, labor-intensive, and are potentially hazardous to the environment and living organisms [3,4]. Thus, there is an obvious need for an alternative, cost-effective and at the same time safe and environmentally sound method of nanoparticle production [3,5–8]. Despite the fact that "green" synthesis of nanoparticles using plant material is of considerable interest, it is worth studying the equivalence of these nanoparticles with nanoparticles produced through physical and chemical methods, especially with regard to their potential applications and production scalability. Therefore, green synthesis of plant extract nanoparticles has emerged tremendously in the past decade due to the ability of the natural products to reduce the cytotoxicity of the nanoparticles. Furthermore, plant extracts in nanoparticles synthesis does not need any intricate processes like several steps in isolation and compound purification [9]. Hence, plants extract remained the most affordable and accessible source for green synthesis of bioactive nanoparticles. As several South African plants are playing a pivotal role as source of new drugs and treatment of many kinds of diseases. Therefore, these medicinal plants have a long historical usage by traditional healers and knowledgeable elders [10]. The *Ilex* Mitis shown in Fig. 1A consists of saponins which are secondary metabolites with high molecular weight that are naturally synthesized by many different plant species. They are glucosides with foaming characteristics and they normally consist of polycyclic aglycones that are attached to one or more sugar side chains [11–13]. They also consisted of either a sterols or more commonly triterpenoids and water soluble sugar residues. Due to their amphiphilic nature, they are highly surface active and their biological activities are related to their chemical structures [14–17]. Total saponins isolated from *Radix et Rhizoma Leonticis* have been reported to suppress tumor cells growth [18].

Iboza Riparia plant shown in Fig. 1B also known as *Tetradenia riparia* or Ginger Bush- that is traditionally used as a medicinal plant by mainly Zulu and Tswane people in South Africa (SA) to treat chest complaints, stomach ache, relieve headaches and malaria [19]. Most importantly, these plants have acceptable therapeutic index for the development of novel drugs. The compounds previously isolated from such species

* Corresponding authors.
E-mail addresses: myalos@dut.ac.za (M.I. Sabela), ksuvardhan@gmail.com (S. Kanchi), bisettyk@dut.ac.za (K. Bisetty).

https://doi.org/10.1016/j.jphotobiol.2017.12.010
Received 2 August 2017; Received in revised form 8 December 2017; Accepted 8 December 2017
Available online 13 December 2017
1011-1344/

Fig. 1. Pictures of (A) *Ilex* Mitis and (B) *Iboza* Riparia.

includes diterpenes and triterpenes, such as ibozol [20], umuravumbolide, deacetylumuravumbolide, deacetylboronolide [21], 8(14),15-sandaracopimaradiene-7α,18-diol [22]. Shakeel and coworkers have reported one-step methods for the green synthesis of AgNPs using *Withania somnifera*, *Crotalaria* retusa extracts and their antimicrobial and catalytic activities [23,24]. Vast literature is available on the green synthesis of AgNPs, however, this is the first report using *Iboza* Riparia leaf and *Ilex* Mitis root bark extracts for the biosynthesis of AgNPs. Some of the other green materials reported for the synthesis of AgNPs were shown in Table 1. However, there is very limited reports on biocompatibility studies such as MTT assay, instead there is vast analysis on nanoparticle bacterial activity.

This work is centred on the basis that there are immense potentials of green synthesized nanomaterials but their cytotoxicity and antioxidant activity remain a major concern. Therefore, after optimization of the synthesis protocol and characterization, the best nanoparticles were evaluated for antioxidant activity on ABTS and inhibitory effect on human embryonic kidney cells in a concentration dependent manner.

2. Materials and Methods

2.1. Materials

Phosphate buffered saline (PBS) 2, 2′-Azino-bis (3-ethylbenzothiazoline-6-sulfonic acid) diammonium salt (ABTS), and other common chemicals were purchased from Sigma (Durban, SA). The human embryonic kidney cells (HEK293T), fresh Dulbecco's modified Eagle's medium and 20 µL MTT (from 5 mg mL^{-1} stock) were purchased from HIMEDIA Laboratories, India. The root bark of *Ilex* Mitis and leaves of *Iboza* Riparia plants were obtained from Durban city central market (Durban, KwaZulu Natal, South Africa).

2.2. Extraction Procedure

2.2.1. Isolation of Saponin from Ilex Mitis

The root bark sample of *Ilex* Mitis, was grounded to fine powder and 20 g transferred into a conical flask before 100 mL of 20% aqueous ethanol was added. The mixture was heated over a water bath for 4 h with continuous stirring at 55 °C and then filtered after cooling to 25 °C. The extract was concentrated to 40 mL by rotary vapour and purified with 20 mL of diethyl ether during which the aqueous layer was recovered. Subsequently, the saponin was extracted from aqueous layer using n-butanol three times and washed twice with 10 mL of 5% aqueous sodium chloride. Finally, the organic layer was retained and concentrated by rotary vapour to dryness producing solid saponin [25].

2.2.2. Extraction of Diterpenes from Iboza Riparia

Approximately 5.0 g of *Iboza* Riparia fresh leaves were collected and shredded in a 250 mL beaker. Then, boiled with 200 mL deionized water at 60 °C for 20 min. After cooling to room temperature, the mixture was filtered with a Whatman filter paper no.1 and the extract was stored in a refrigerator at 4 °C.

2.3. Biosynthesis of Silver Nanoparticles

The bioconjugated AgNPs of silver colloidal solution was prepared as per method reported [26] with notable modifications. Briefly, a seed solution was prepared by mixing aqueous trisodium citrate (5 mL, 2.5 mM), aqueous poly(vinyl alcohol) (PVA; 0.25 mL, 500 mg L^{-1}; Sigma Aldrich, South Africa) and aqueous $NaBH_4$ (0.3 mL, 10 mM, freshly prepared). Thereafter, aqueous 5 mL of 0.5 mM $AgNO_3$ was added at a rate of 2 mL min^{-1} while stirring continuously. Subsequently, spherical like silver particles were produced by mixing (i) 5 mL distilled water, (ii) 75 mL of 10 mM aqueous ascorbic acid (freshly

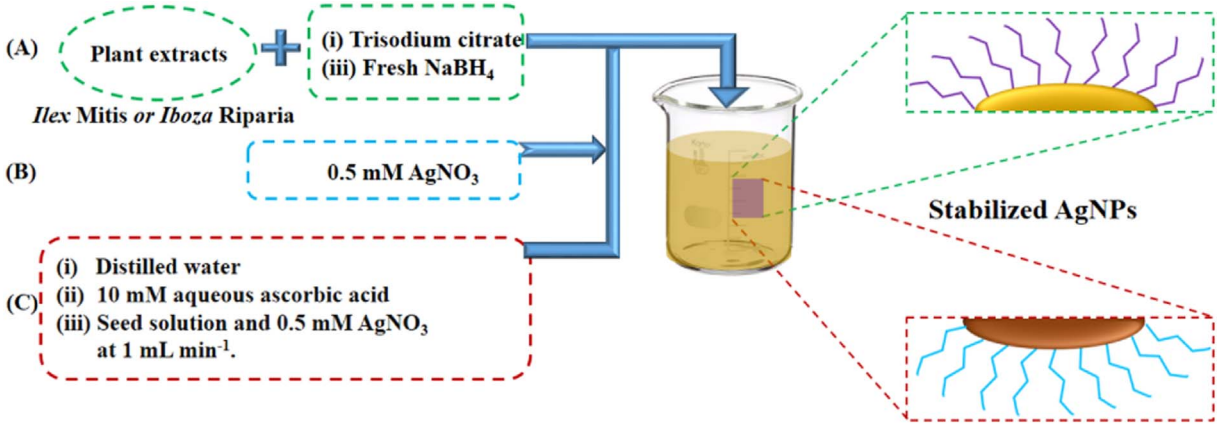

Fig. 2. Schematic representation of one pot-biosynthesis of AgNPs using *Ilex* Mitis and *Iboza* Riparia extracts.

Table 1
Literature review on the green synthesis of AgNPs.

Green Material	Size (nm)	Morphology	Applications	Citation
 *Solanum tuberosum*	16 ± 2	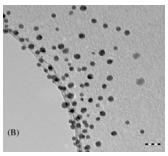	Drug delivery	[38]
 Radix Puerariae	35	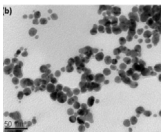	Catalysis	[39]
 *Syzygium jambos*	10	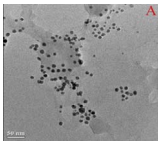	Antimalarial	[40]
 Salvadora persica	3	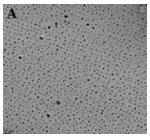	Antimicrobial	[41]
 *Viburnum opulus* L	25	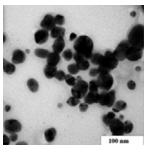	Anti-inflammatory	[42]
 *Brassica oleracea* var.	30	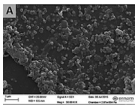	Antibacterial and antifungal activities	[43]
 Diospyros sylvatica	10	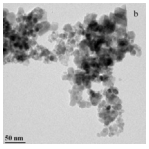	Antimicrobial activity	[44]
 *Beta vulgaris*	20	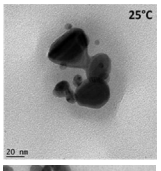	Anticancer	[45]
 *Sambucus nigra* L	26	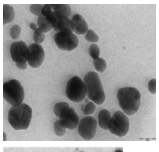	Antioxidant activity	[46]
 Vigna sp. L seeds	24	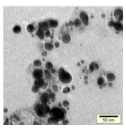	–	[47]
 *Cichorium intybus* L. var. sativus	64	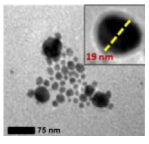	Antibacterial activity	[48]

(*continued on next page*)

Table 1 (*continued*)

Green Material	Size (nm)	Morphology	Applications	Citation
 Terminalia cuneata	25	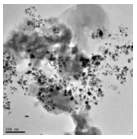	Catalytic activity	[49]
 *Artocarpus altilis*	38	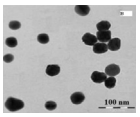	Biomedicine, water treatment or purification, and nanobiotechnology	[9]
 *Parkia speciosa* Hassk pods	50	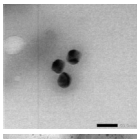	Antibacterial activity	[50]
 *Ginkgo biloba* leaf	16	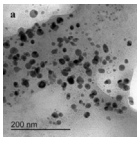	Antimicrobial activity	[51]
 *Calendula officinalis*	10	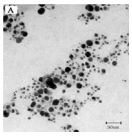	–	[52]
 *Butea monosperma* leaf	80	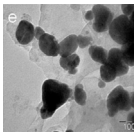	Anticancer	[53]
 *Azadirachta indica* leaf	5	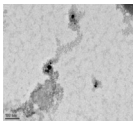	Antimicrobial activity	[54]

prepared), (iii) 100 µL of seed solution and lastly, aqueous 3 mL of 0.5 mM $AgNO_3$ at a rate of 1 mL min^{-1}. Immediately, post the synthesis, the particles were protected by stabilizing with 0.5 mL of 25 mM aqueous trisodium citrate. The formation of AgNPs is denoted by the color change of seed solution (yellow) as added to the clear violet. When using either *Ilex* Mitis or *Iboza* Riparia extracts instead of PVA, the final color of the nanoparticle solution was gray in color and the products were stable (Fig. 2).

2.4. Characterization of Silver Nanoparticles

The bio-reduction of Ag^+ ions in aqueous extract was monitored by UV–visible spectra (Shimadzu spectrophotometer (AV-1800)) while the corresponding morphology and size of the polymer and bio-stabilized AgNPs were measured using Transmittance Electron Microscopy (TEM) model JEM 2100 equipped with a LaB_6 emitter (MAXOXFORD instruments). The hydrodynamic particle size of nanoparticle was determined using Zetasizer Ver. 7.04 by Malvern Instruments Ltd. The conditions were set as follows: Temperature 25.0 °C, data collected at count rate of 261.5 kcps for a duration of 60 s in 7 attenuations, while the measurement position was kept at 4.65 mm. The attenuated total reflectance (ATR) spectra of nanoparticle powder was recorded on a Perkin-Elmer FTIR, (Midrand, South Africa) at 4000 cm^{-1} to 400 cm^{-1}. X-ray diffraction study was carried out using a Bruker AXS D8 diffractometer with CuKα radiation (λ = 1.5418 Å) at 40 kV over a 2θ range from 20° to 80° at a scanning rate of 0.05 min^{-1}. Further confirmation of the conjugation was performed with Thermogravimetric Analyzer (STARe system of TGA/DSC, 1 SF/1346) model supplied with a STARe Software version 9.20 by Mettler Toledo (Johannesburg, SA). The samples were placed in a 10 µL alumina sample holder for thermal analysis at a heating rate of 10 °C min^{-1}. The conductivity measurements were performed with Metrohm, 644 conductometer at 26.5 °C.

2.5. Cytotoxicity Studies with MTT Assay

Exponentially growing human embryonic kidney cells (HEK293T) were seeded in a 96-well micro-titer plate (cell count of 7000 cells per well). For checking cell proliferation, on the next day cells were treated with different concentrations (5–150 lM) of inhibitors. HEK293T without inhibitors was used as a positive control. At the end of 48 h incubation, the mixture was removed from the cells and after washing with PBS, 100 lL fresh Dulbecco's modified Eagle's medium and 20 µL MTT (from 5 mg mL^{-1} stock) was added to each well. The plates were incubated further for 4 to 5 h at 37 °C. After the incubation period elapsed, the bulk of the residual medium was carefully removed, using a multichannel pipette, without disturbing the formazan crystals formed behind. Thereafter, 100 µL of DMSO (dimethyl sulphoxide) was added to each well for dissolving the formazan crystals. The plates were then agitated for 15–20 min on an orbital plate shaker, after which they were read immediately on Titerplate reader (BioRad) at 570 nm. The relative percentage cell viabilities of the treated cells were calculated with reference to the control by comparing the viability.

2.6. Antioxidant Activity by ABTS

The radical scavenging activity of the biosynthesised AgNPs was measured against stable free radicals of ABTS. Approximately 2 mM solution of ABTS was prepared in 0.75 mM, potassium persulfate, and allowed to stand for approximately 16 h in a dark environment. Thereafter, a series of colloidal nanoparticle solutions were separately mixed with 30 µL of 1.8 µM ABTS* enzyme and then vortex mixed for 5 s followed by 30 min incubation at 25 °C to allow for the scavenging reaction to reach equilibrium before absorbance measurements were recorded at 734 nm.

3. Results and Discussion

3.1. Screening of Phytochemical in Iboza Riparia and Ilex Mitis

The plants used, *Iboza* Riparia leaf and *Ilex* Mitis predominantly consists of terpenoids and saponins. Therefore these compounds have been used in the synthesis of AgNPs. Essential oils from the extracts are composed of hydrocarbons, terpenes and their oxygenated derivatives, terpenoids. The formation of higher molecular weight terpenes namely; hemiterpene, monoterpene, sesquiterpene, diterpene, and triterpene is through the 'head' to 'tail' linkage of isoprene units. The terpenes may form oxygenated derivatives with different functional groups like alcohol, ester, aldehyde, ether, ketones etc. while terpenoids can be hemiterpnoid, monoterpnoid, sesqiterpenoid, diterpenoid, triterpenoids [27,28]. Plant surfactants are widely used in the synthesis of AgNPs as they contribute in amalgamation of metal ions to NPs [29]. Plant extracts contains surfactants which enables for nanoparticle formation without any special reducing agent/capping agent. The role of surfactants is to act as capping agent preventing the growth and aggregation of nanoparticles.

3.2. Morphology and Particle Size Analysis

During the synthesis, color changes from yellow to orange/red/gray, depending on the reducing and capping agents used. The AgNPs prepared from *Iboza* Riparia extract demonstrated more aggregation (with gray color) in contrast to polymer based nanoparticles which were violet in color.

The TEM and dynamic light scattering (DLS) results suggested that the average diameter of AgNPs-*PVA* was found to be 43.6 nm and conductivity of 0.11 mS while the intensity was 85.3% as shown in Fig. 3A. On the other hand, the *Ilex* Mitis and *Iboza* Riparia extracts (Fig. 1B–C) produced AgNPs-*SPNs* and AgNPs-*DTPs* with an average size of 50 nm and 156 nm, while their respective intensities were 96.4% and 93%. In Fig. 3B, we observed that NPs are generally small, however they are clustered due to the presence of the capping agent in the extract. Interestingly, there was a visible surface coating on the AgNPs-*SPNs* differing to the AgNPs-*DTPs* shown in Fig. 3C. The AgNPs-*DTPs* were the largest with 156 nm and conductivity of 0.494 mS, this signifies poor reduction and capping of nanoparticles by diterpenes in contrast to saponins. Saponins produce NPs that are much smaller with conductivity of 0.39 mS because structurally they have more hydrophilic glycoside moieties combined with a lipophilic triterpene derivative [30]. The significant difference in the conductivity results elucidates electrical potential difference between the inner and outer surface of the dispersed phase in a colloidal NPs. This enables NPs shown in Fig. 3B to be much smaller and relatively stable. The capping agents themselves are being known to form the basis for biologically important compounds and having antimicrobial and anti-inflammatory properties. However, adjusting the morphology of nanoparticles is of key importance for utilizing their properties in biomedical applications. For this purpose, we use a capping agent or appropriate surfactant that affect the morphology of nanoparticles at ambient conditions. The surfactants contribute a vital role because of their ability to modify the chemical behaviour of nanoparticles as discussed in Section 3.5.

3.3. UV–vis and ATR Spectroscopy

In all experiments, addition of plant extract of *Ilex* Mitis, *Iboza* Riparia and polymer into the beakers containing aqueous solution of silver nitrate led to the change in the color of the solution to yellow to orange/red/gray, depending on the reducing and capping agents used. The color change within reaction duration was due to excitation of surface plasmon vibrations in silver nanoparticles [31,32]. The reduction of silver ions during the reaction was confirmed by ultraviolet–visible spectroscopy and showed maxima's at 508.3 nm, 413.2 nm and 405.9 nm for AgNPs-*PVA*, AgNPs-*SPNs* and AgNPs-*DTPs* respectively (see Fig. 4A). These nanoparticles were allowed to stand for two months to assess their stability - interestingly they were found to be adequately stable as they retained their shape, size, color and distribution coefficient.

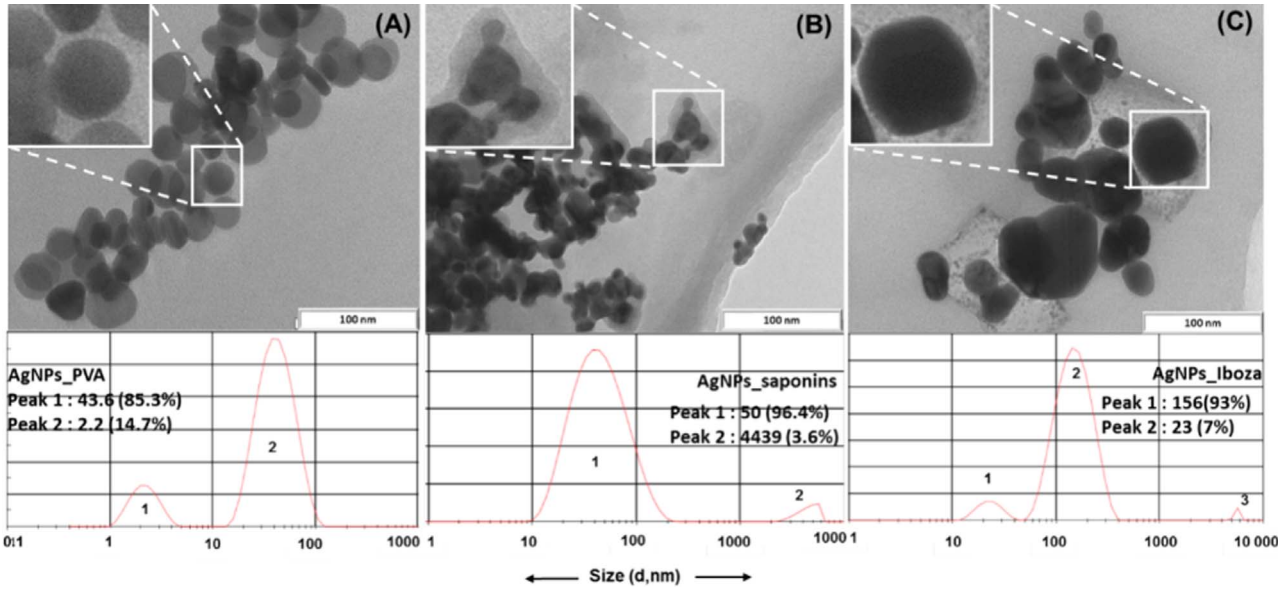

Fig. 3. Size distribution intensity of (A) AgNPs-*PVA* (B) AgNPs-*SPNs* (C) AgNPs-*DTPs*. Insert shows the TEM images of the corresponding particles prepared with *Image* J. Below is the hydrodynamic size distribution and intensity.

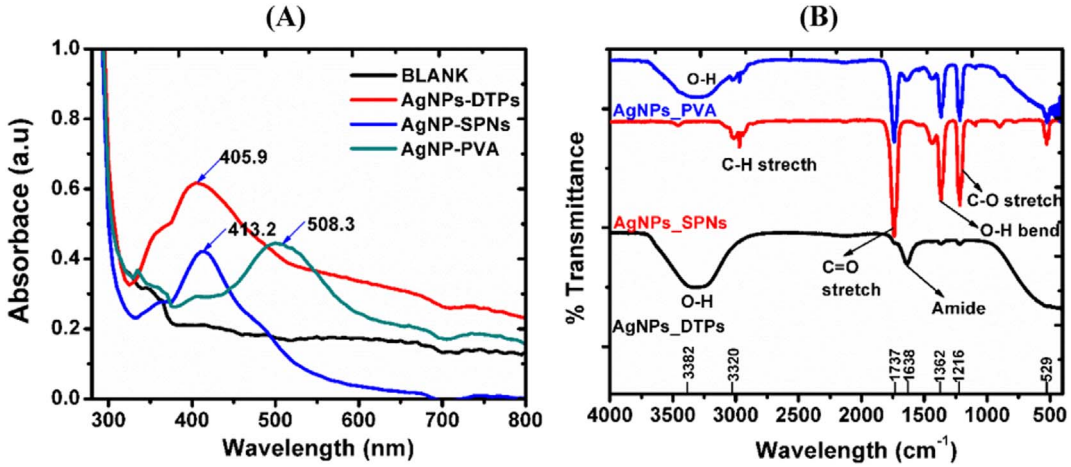

Fig. 4. (A) UV–Vis spectra from 300 nm to 800 nm (B) ATR spectra of AgNPs-*PVA*, AgNPs-*SPNs* and AgNPs-*DTPs*.

Further characterization was performed with ATR as illustrated in Fig. 4B, which showed C—O stretch at 1216 cm^{-1} and O—H bend at 1362 cm^{-1} for all the samples – but it was significantly small for AgNPs-*DTPs*. There was also a very intense C═O peak at 1737 cm^{-1} which probably arise from the citrate used for the preparation of seed solution. Again this peak is much smaller in the case of AgNPs-*DTPs* although there is a dominance of α-pyrone compounds from the extract [33]. While a distinctive C═O stretch, amide band at 1638 cm^{-1} was observed for AgNPs-*DTPs*. It is well established in the literature that amides can bind exceptionally strongly with AgNPs as confirmed by diminishing of the corresponding peak after the formation of NPs. On the other hand AgNPs-*SPNs* demonstrated the two intense C—O stretch at 1216 cm^{-1} and O—H bend at 1362 cm^{-1}. These intense bends attribute to their structures having more than one hydrophilic glycoside moieties combined with a lipophilic triterpene derivative. Ultimately the abundance of the C—O stretch arises from the connection of the glycoside moieties. Interestingly these peaks were similarly to those observed with AgNPs-*PVA*.

3.4. X-ray Diffraction and Thermal Analysis

X-ray diffraction analysis was utilized to calculate the crystallite size of AgNPs and the value was found to be 10 nm. The XRD analysis of NPs synthesized using with extracts exhibited typical diffraction peaks at 36.05° (100), 45.94° (200), 65.27° (220) and 76.14° (311) as shown in Fig. 5A. The four planes of the fcc crystal structure of metallic silver exhibited well-defined characteristic diffraction peaks. The AgNPs formed using PVA also exhibited the same peaks, however the peaks at 65.27° (220) and 76.14° (311) shown much less intensity compared to AgNPs from the extract. The results obtained are in agreement with previous reports where plant extracts have been used for synthesis of nanoparticles [32,34]. The sizes of the nanoparticle crystals calculated by the Debye-Scherrer equation were 44 nm (AgNPs-*PVA*), 156 nm (AgNPs-*SPNs*), 50 nm (AgNPs-*DTPs*), which are in good agreement with the sizes observed in TEM and DLS analysis. Peak broadening observed can be considered normal since the particles are < 100 nm and the full-width at half maximum is consistent for each peak. However, the varying peak intensity for all the synthesized samples is related to different sample sizes that were used for characterization.

From the DSC results, there was no clear indication whether any of the conjugated NPs will undergo any deformation as the energetics of the process were more favorable beyond 171 °C of heat flow measured at 10 °C s^{-1}. Overall the, ATR and DSC results of AgNPs-*PVA*, AgNPs-*SPNs* and AgNPs-*DTPs* in Fig. 4B and 5A; are very similar in many ways and they correlate with the morphology and size distribution (see Fig. 3).

3.5. Cytotoxicity Studies on Human Embryonic Kidney Cells (HEK293T)

The leaf and stem extracts of *Iboza* Riparia have been reported previously to be active against *S. aureus* and several mycobacteria [22,35], but not for cytotoxicity against metabolically active or dividing cells [36]. Cytotoxicity studies of the AgNPs synthesized with PVA, *Ilex* Mitis and *Iboza* Riparia extracts were studied for MTT assay

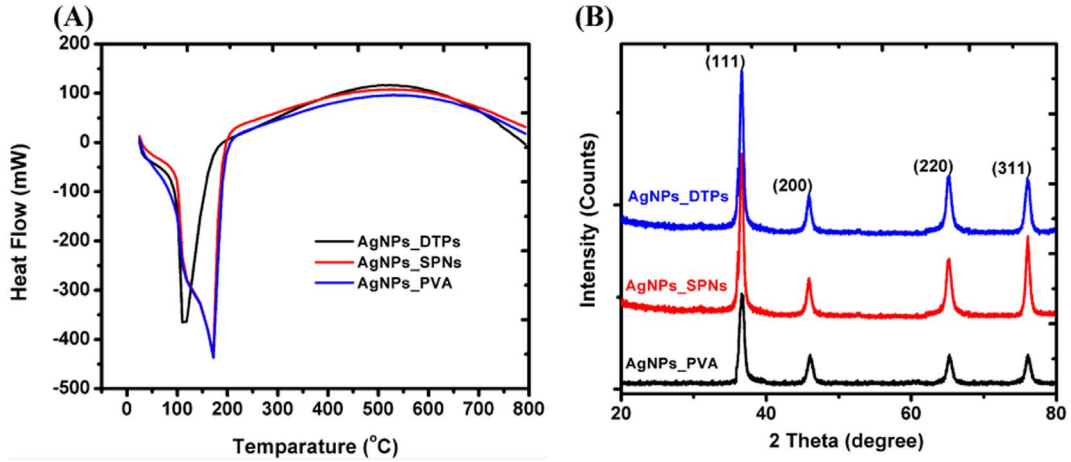

Fig. 5. (A) DSC thermogram and (B) X-Ray Diffraction pattern of AgNPs-*PVA*, AgNPs-*SPNs* and AgNPs-*DTPs*.

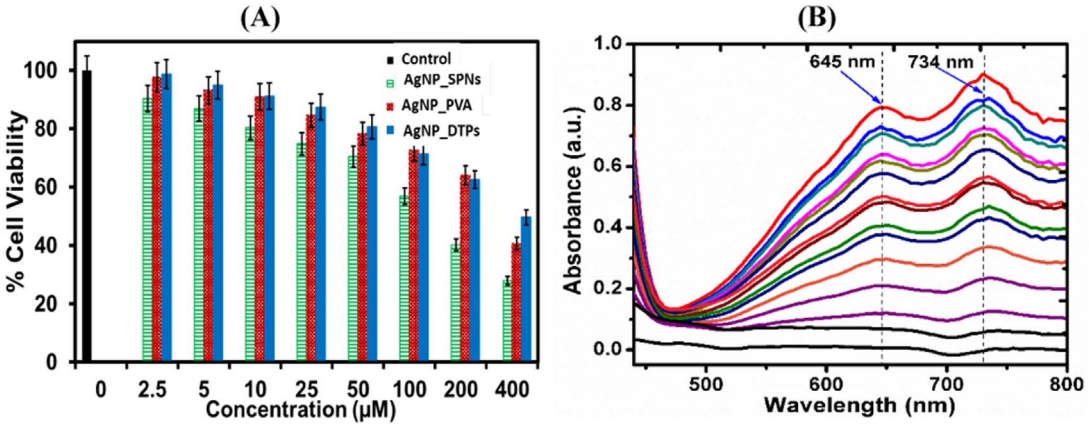

Fig. 6. (A) Cytotoxicity and cell-proliferation inhibition activity of the three designed inhibitors (AgNPs-*SPNs*, AgNPs-*PVC* and AgNPs-*DTPs*) on human embryonic kidney cells (HEK293T) against the control (B) UV–Vis spectra of ABTS* after 30 min incubation with bio-synthesized AgNPs.

which has gained high attention in cell proliferation studies. MTT is a tetrazolium salt, which can be easily reduced to a coloured formazan product with the help of reducing enzyme present only in metabolically active or dividing cells. The enzyme succinate dehydrogenase and cytochrome oxidase present in mitochondria of active cells that help in the reduction of MTT. Thus under a particular reduction conditions of MTT and subsequent formation of formazan is proportional to the number of viable or active cells present in the medium.

With the help of MTT-assay we have analysed the cytotoxicity and cell-proliferation inhibition activity of the three designed inhibitors (AgNPs-*SPNs*, AgNPs-*PVC* and AgNPs-*DTPs*) as shown in Fig. 6A. Using all the inhibitors at 100 μM, viability of the cells were maintained at ~50%. However at 200 μM, viability of cell in the presence of AgNPs-*PVA* inhibitor was found to be < 50% which is non-toxic to normal cells. Interestingly, AgNPs-*SPNs* and AGNPs-*DTPs* at 400 μM demonstrated the cell viability < 50%. Above this concentration, the reference and the tested inhibitors both became toxic to the normal cells. Overall, AgNPs-*DTPs* were found to be less toxic with 49.7% cell viability, while AgNPs-*PVA* and AgNPs-*SPNs* had cell viability of 28.0 and 40.8% respectively at 400 μM.

Recent report have demonstrated extensively that by changing the stabilizing ligand on the surface of the nanoparticles we can actually be able to vary the cytotoxicity of the particles making them user friendly for as variety of biological applications as the selected plants are used in traditional medicine against viral diseases.

3.6. ABTS Antioxidant Assay

Moreover, antioxidant activity information is also crucial, particularly for biosynthesized nanoparticles. For that reason antioxidant activity of the both AgNPs synthesized from *Iboza* Riparia leaf and *Ilex* Mitis extracts were studied on ABTS. ABTS is a suitable for antioxidant activity studies because it is relatively stable free radical but colourises in the presence of antioxidants [37]. The free radical model treated with varying concentrations from 0.1–1.5 mL and absorbance due to the extent of activity reaction at 734 nm were recorded for colloidal AgNPs, along with the absorbance of pure ABTS (see Fig. 6B). The antioxidant activity of AgNPs-*SPNs*, AgNPs-*DTS* and AgNPs-*PVA* on ABTS* with λ_{max} at 734 nm as shown in the spectra. The absorbance band reveals that AgNPs in the presence of phosphate buffer with the potential to dedicated hydrogen thus decreasing the intensity in the order AgNPs-*DTPs* > AgNPs-*PVA* > AgNPs-*SPNs*. The significant color change observed is one way to confirm that conjugated nanoparticles participate in the protonation possesses. Therefore, the scavenging efficiency of AgNPs-*SPNs*, AgNPs-*DTPs* were found to be 89.25% in 0.20 mL and 96.62% in 0.20 mL/0.05 mM.

4. Conclusions

Obviously, the synthesis of metal NPs in plant extracts (plant biomasses), despite obvious limitations, has a significant potential and a number of substantial advantages relative to traditional methods of NP synthesis. The use of *Iboza* Riparia and *Ilex* Mitis extracts acting as reducing and capping agents produced NPs that were stable with particles size of 156 nm and 50 nm for AgNPs-*DTPs* and AgNPs-*SPNs* respectively. The order of magnitude on human embryonic kidney cell viability was found to be AgNPs-*DTPs* (49.7%) > AgNPs-*SPNs* (40.8%) > AgNPs-*PVA* (28.0%) at 400 μM. Based on the cytotoxicity and antioxidant activity, it is fair to report that these plant extracts have potential reducing and capping agents as they retain chemical properties on the surface of the nanoparticles. The reported AgNPs also demonstrated good antioxidant activity with 89.25% in 0.20 mL and 96.62% in 0.20 mL/0.05 mM towards ABTS. This will explore the potential possibilities of nontoxic nanomaterials, which can be prepared in a simple and cost-effective manner. These nanoparticles are potential candidate for suitable formulation of new types of bactericidal materials with good antioxidant activity.

Conflict of Interest

The authors declare that they have no conflict of interest.

Acknowledgements

This study was funded by National Research Foundation (NRF) of South Africa and Durban University of Technology. One of the authors is gratefully acknowledged research scholarship grant from NRF (Reference: AEMD150725130836). Cytotoxicity studies were performed in the Centre for Interdisciplinary Research in Basic Sciences, Jamia Millia Islamia, New Delhi, India.

References

[1] C. Gunawan, M. Lim, C.P. Marquis, R. Amal, Nanoparticle–protein corona complexes govern the biological fates and functions of nanoparticles, J. Mater. Chem. B 2 (2014) 2060–2083.
[2] K. Okitsu, Y. Mizukoshi, T.A. Yamamoto, Y. Maeda, Y. Nagata, Sonochemical synthesis of gold nanoparticles on chitosan, Mater. Lett. 61 (2007) 3429–3431.
[3] H.S. Sharma, S.F. Ali, S.M. Hussain, J.J. Schlager, A. Sharma, Influence of engineered nanoparticles from metals on the blood-brain barrier permeability, cerebral blood flow, brain edema and neurotoxicity. An experimental study in the rat and mice using biochemical and morphological approaches, J. Nanosci. Nanotechnol. 9 (2009) 5055–5072.
[4] P.P. Gan, S.H. Ng, Y. Huang, S.F. Li, Green synthesis of gold nanoparticles using palm oil mill effluent (POME): a low-cost and eco-friendly viable approach, Bioresour. Technol. 113 (2012) 132–135.
[5] P. Raveendran, J. Fu, S.L. Wallen, Completely “green” synthesis and stabilization of

metal nanoparticles, J. Am. Chem. Soc. 125 (2003) 13940–13941.
[6] K.B. Narayanan, N. Sakthivel, Biological synthesis of metal nanoparticles by microbes, Adv. Colloid Interf. Sci. 156 (2010) 1–13.
[7] S. Shamaila, A.K.L. Sajjad, N.-u.-A. Ryma, S.A. Farooqi, N. Jabeen, S. Majeed, I. Farooq, Advancements in nanoparticle fabrication by hazard free eco-friendly green routes, Appl. Mater. Today. 5 (2016) 150–199.
[8] S. Shamaila, A. Khan Leghari Sajjad, A. Quart ul, S. Shaheen, A. Iqbal, S. Noor, G. Sughra, U. Ali, A cost effective and eco-friendly green route for fabrication of efficient graphene nanosheets photocatalyst, J. Environ. Chem. Eng. 5 (2017) 5770–5776.
[9] V. Ravichandran, S. Vasanthi, S. Shalini, S.A. Ali Shah, R. Harish, Green synthesis of silver nanoparticles using *Artocarpus altilis* leaf extract and the study of their antimicrobial and antioxidant activity, Mater. Lett. 180 (2016) 264–267.
[10] Y. Ndamane, L. Kambizi, S.P. Songca, O.S. Oluwafemi, Antibacterial effectiveness of *Tetradenia riparia* extract, a plant traditionally used in the Eastern Cape Province to treat diseases of the respiratory system, J. Med. Plant Res. 7 (2013) 2755–2760.
[11] K. Mikołajczyk-Bator, A. Błaszczyk, M. Czyżniejewski, P. Kachlicki, Characterisation and identification of triterpene saponins in the roots of red beets (*Beta vulgaris* L.) using two HPLC–MS systems, Food Chem. 192 (2016) 979–990.
[12] L. Guo, S.-L. Zeng, Y. Zhang, P. Li, E.H. Liu, Comparative analysis of steroidal saponins in four *Dioscoreae* herbs by high performance liquid chromatography coupled with mass spectrometry, J. Pharm. Biomed. Anal. 117 (2016) 91–98.
[13] I. Horo, M. Masullo, A. Falco, S.G. Şenol, S. Piacente, Ö. Alankuş-Çalışkan, New triterpene saponins from *Phryna ortegioides*, Phytochem. Lett. 14 (2015) 39–44.
[14] Y. Huang, T. Zhang, H. Zhou, Y. Feng, C. Fan, W. Chen, J. Crommen, Z. Jiang, Fast separation of triterpenoid saponins using supercritical fluid chromatography coupled with single quadrupole mass spectrometry, J. Photochem. Photobiol. B 121 (2016) 22–29.
[15] Z. Kerem, H. German-Shashoua, O. Yarden, Microwave-assisted extraction of bioactive saponins from chickpea (*Cicer arietinum* L), J. Sci. Food Agric. 85 (2005) 406–412.
[16] C.L. Lencina, M.C.d. Cardoso, I. Zancanaro, G. Gosmann, V.S. Pires, P. Sonnet, D. Guillaume, E.P. Schenkel, Triterpenes and new saponins from *Ilex chamaedryfolia*: chemotaxonomic tool to ilex species differentiation, Quim. Nova 34 (2011) 222–225.
[17] J.-m. Lu, Y.-f. Wang, H.-l. Yan, P. Lin, W. Gu, J. Yu, Antidiabetic effect of total saponins from *Polygonatum kingianum* in streptozotocin-induced daibetic rats, J. Ethnopharmacol. 179 (2016) 291–300.
[18] Y. Zhan, R. Liu, W. Wang, J. Li, X. Ou Yang, Y. Zhang, Total saponins isolated from Radix et Rhizoma Leonticis suppresses tumor cells growth by regulation of PI3K/Akt/mTOR and p38 MAPK pathways, Environ. Toxicol. Pharmacol. 41 (2016) 39–44.
[19] S. Gairola, Y. Naidoo, A. Bhatt, A. Nicholas, An investigation of the foliar trichomes of Tetradenia riparia (Hochst.) Codd [Lamiaceae]: an important medicinal plant of Southern Africa, Flora 204 (2009) 325–330.
[20] R. Zelnik, E. Rabenhorst, A.K. Matida, H.E. Gottlieb, D. Lavie, S. Panizza, Ibozol, a new diterpenoid from Iboza riparia, Phytochemistry 17 (1978) 1795–1797.
[21] L. Van Puyvelde, S. Dube, E. Uwimana, C. Uwera, R.A. Dommisse, E.L. Esmans, O. Van Schoor, A.J. Vlietinck, New α-pyrones from Iboza riparia, Phytochemistry 18 (1979) 1215–1218.
[22] L. Van Puyvelde, S. Nyirankuliza, R. Panebianco, Y. Boily, I. Geizer, B. Sebikali, N. De Kimpe, N. Schamp, Active principles of Tetradenia riparia. I. Antimicrobial activity of 8(14),15-sandaracopimaradiene-7α,18-diol, J. Ethnopharmacol. 17 (1986) 269–275.
[23] S. Ahmed, Annu, K. Manzoor, S. Ikram, et al., J. Bionanosci. 10 (2016) 282–287.
[24] S. Ahmed, Annu, I. Zafeer, S. Ikram, One-step method for formation of silver nanoparticles using *Withania somnifera* extract for antimicrobial activities, J. Bionanosci. 10 (2016) 47–53.
[25] H.O. Edeoga, D.E. Okwu, B.O. Mbaebie, Phytochemical constituents of some Nigerian medicinal plants, Afr. J. Biotechnol. 4 (2005) 685–688.
[26] D. Aherne, D.M. Ledwith, M. Gara, J.M. Kelly, Optical properties and growth aspects of silver nanoprisms produced by a highly reproducible and rapid synthesis at room temperature, Adv. Funct. Mater. 18 (2008) 2005–2016.
[27] W.C. Evans, D. Evans, G.E. Trease, Trease and Evans' Pharmacognosy, WB Saunders, Edinburgh, New York, 2002.
[28] P. Patil Shriniwas, T. Kumbhar Subhash, Antioxidant, antibacterial and cytotoxic potential of silver nanoparticles synthesized using terpenes rich extract of *Lantana camara* L. leaves, Biochem. Biophys. Rep. 10 (2017) 76–81.
[29] R. Geethalakshmi, D.V.L. Sarada, Characterization and antimicrobial activity of gold and silver nanoparticles synthesized using saponin isolated from *Trianthema decandra* L, Ind. Crop. Prod. 51 (2013) 107–115.
[30] K. Hostettmann, A. Marston, Saponins, Cambridge University Press, Cambridge, 1995.
[31] R. Veerasamy, T.Z. Xin, S. Gunasagaran, T.F.W. Xiang, E.F.C. Yang, N. Jeyakumar, S.A. Dhanaraj, Biosynthesis of silver nanoparticles using mangosteen leaf extract and evaluation of their antimicrobial activities, J. Saudi Chem. Soc. 15 (2011) 113–120.
[32] J.-H. Lee, J.-M. Lim, P. Velmurugan, Y.-J. Park, Y.-J. Park, K.-S. Bang, B.-T. Oh, Photobiologic-mediated fabrication of silver nanoparticles with antibacterial activity, J. Photochem. Photobiol. B 162 (2016) 93–99.
[33] L.V. Puyvelde, N.D. Kimpe, S. Dubé, M. Chagnon-Dubé, Y. Boily, F. Borremans, N. Schamp, M.J.O. Anteunis, 1′,2′-Dideacetylboronolide, an α-pyrone from Iboza riparia, Phytochemistry 20 (1981) 2753–2755.
[34] J. Judith Vijaya, N. Jayaprakash, K. Kombaiah, K. Kaviyarasu, L. John Kennedy, R. Jothi Ramalingam, H.A. Al Lohedan, M.A.V. Mohammed, M. Maaza, Bioreduction potentials of dried root of *Zingiber officinale* for a simple green synthesis of silver nanoparticles: antibacterial studies, J. Photochem. Photobiol. B 177 (2017) 62–68.
[35] L. Van Puyvelde, J.D. Ntawukiliyayo, F. Portaels, E. Hakizamungu, In vitro inhibition of mycobacteria by Rwandese medicinal plants, Phytother. Res. 8 (1994) 65–69.
[36] A.J. Vlietinck, L. Van Hoof, J. Totté, A. Lasure, D.V. Berghe, P.C. Rwangabo, J. Mvukiyumwami, Screening of hundred Rwandese medicinal plants for antimicrobial and antiviral properties, J. Ethnopharmacol. 46 (1995) 31–47.
[37] O. Erel, A novel automated direct measurement method for total antioxidant capacity using a new generation, more stable ABTS radical cation, Clin. Biochem. 37 (2004) 277–285.
[38] M.S. Ali, M. Altaf, H.A. Al-Lohedan, Green synthesis of biogenic silver nanoparticles using solanum tuberosum extract and their interaction with human serum albumin: evidence of "corona" formation through a multi-spectroscopic and molecular docking analysis, J. Photochem. Photobiol. B 173 (2017) 108–119.
[39] S.G. Balwe, V.V. Shinde, A.A. Rokade, S.S. Park, Y.T. Jeong, Green synthesis and characterization of silver nanoparticles (Ag NPs) from extract of plant Radix Puerariae: an efficient and recyclable catalyst for the construction of pyrimido[1,2-b]indazole derivatives under solvent-free conditions, Catal. Commun. 99 (2017) 121–126.
[40] P.P. Dutta, M. Bordoloi, K. Gogoi, S. Roy, B. Narzary, D.R. Bhattacharyya, P.K. Mohapatra, B. Mazumder, Antimalarial silver and gold nanoparticles: green synthesis, characterization and in vitro study, Biomed Pharmacother 91 (2017) 567–580.
[41] R. Mamatha, S. Khan, P. Salunkhe, S. Satpute, S. Kendurkar, A. Prabhune, A. Deval, B.P. Chaudhari, Rapid synthesis of highly monodispersed silver nanoparticles from the leaves of *Salvadora persica*, Mater. Lett. 205 (2017) 226–229.
[42] B. Moldovan, L. David, A. Vulcu, L. Olenic, M. Perde-Schrepler, E. Fischer-Fodor, I. Baldea, S. Clichici, G.A. Filip, *In vitro* and *in vivo* anti-inflammatory properties of green synthesized silver nanoparticles using *Viburnum opulus* L. fruits extract, Mater. Sci. Eng. C 79 (2017) 720–727.
[43] I. Ocsoy, A. Demirbas, E.S. McLamore, B. Altinsoy, N. Ildiz, A. Baldemir, Green synthesis with incorporated hydrothermal approaches for silver nanoparticles formation and enhanced antimicrobial activity against bacterial and fungal pathogens, J. Mol. Liq. 238 (2017) 263–269.
[44] L. Pethakamsetty, K. Kothapenta, H.R. Nammi, Lakshmi Kalyani Ruddaraju, P. Kollu, S.G. Yoon, S.V.N. Pammi, Green synthesis, characterization and antimicrobial activity of silver nanoparticles using methanolic root extracts of *Diospyros sylvatica*, J. Environ. Sci. 55 (2017) 157–163.
[45] K. Venugopal, H. Ahmad, E. Manikandan, T.K. Arul, K. Kavitha, M.K. Moodley, K. Rajagopal, R. Balabhaskar, M. Bhaskar, The impact of anticancer activity upon Beta vulgaris extract mediated biosynthesized silver nanoparticles (ag-NPs) against human breast (MCF-7), lung (A549) and pharynx (Hep-2) cancer cell lines, J. Photochem. Photobiol. B 173 (2017) 99–107.
[46] B. Moldovan, L. David, M. Achim, S. Clichici, G.A. Filip, A green approach to phytomediated synthesis of silver nanoparticles using *Sambucus nigra* L. fruits extract and their antioxidant activity, J. Mol. Liq. 221 (2016) 271–278.
[47] S. Mohammadi, S. Pourseyedi, A. Amini, Green synthesis of silver nanoparticles with a long lasting stability using colloidal solution of cowpea seeds (Vigna sp. L), J. Environ. Chem. Eng. 4 (2016) 2023–2032.
[48] M.N. Gallucci, J.C. Fraire, A.P.V.F. Maillard, P.L. Páez, I.M.A. Martínez, E.V.P. Miner, E.A. Coronado, P.R. Dalmasso, Silver nanoparticles from leafy green extract of Belgian endive (*Cichorium intybus* L. var. sativus): biosynthesis, characterization, and antibacterial activity, Mater. Lett. 197 (2017) 98–101.
[49] T.N.J.I. Edison, Y.R. Lee, M.G. Sethuraman, Green synthesis of silver nanoparticles using *Terminalia cuneata* and its catalytic action in reduction of direct yellow-12 dye, Spectrochim. Acta A Mol. Biomol. Spectrosc. 161 (2016) 122–129.
[50] I. Fatimah, Green synthesis of silver nanoparticles using extract of Parkia speciosa Hassk pods assisted by microwave irradiation, J. Adv. Res. 7 (2016) 961–969.
[51] Y.-y. Ren, H. Yang, T. Wang, C. Wang, Green synthesis and antimicrobial activity of monodisperse silver nanoparticles synthesized using Ginkgo biloba leaf extract, Phys. Lett. A 380 (2016) 3773–3777.
[52] A. Baghizadeh, S. Ranjbar, V.K. Gupta, M. Asif, S. Pourseyedi, M.J. Karimi, R. Mohammadinejad, Green synthesis of silver nanoparticles using seed extract of *Calendula officinalis* in liquid phase, J. Mol. Liq. 207 (2015) 159–163.
[53] S. Patra, S. Mukherjee, A.K. Barui, A. Ganguly, B. Sreedhar, C.R. Patra, Green synthesis, characterization of gold and silver nanoparticles and their potential application for cancer therapeutics, Mater. Sci. Eng. C 53 (2015) 298–309.
[54] S. Ahmed, Saifullah, M. Ahmad, B.L. Swami, S. Ikram, Green synthesis of silver nanoparticles using *Azadirachta indica* aqueous leaf extract, J. Radiat. Res. Appl. Sci. 9 (2016) 1–7.

Journal of Photochemistry & Photobiology, B: Biology 162 (2016) 199–207

Contents lists available at ScienceDirect

Journal of Photochemistry & Photobiology, B: Biology

journal homepage: www.elsevier.com/locate/jphotobiol

Biosynthesis of ZnO nanoparticles using *Jacaranda mimosifolia* flowers extract: Synergistic antibacterial activity and molecular simulated facet specific adsorption studies

Deepali Sharma [a,*], Myalowenkosi I. Sabela [a], Suvardhan Kanchi [a,*], Phumlane S. Mdluli [a], Gulshan Singh [b], Thor A. Stenström [b], Krishna Bisetty [a,*]

[a] Department of Chemistry, Durban University of Technology, P.O. Box 1334, Durban 4000, South Africa
[b] SARChi Chair, Institute for Water and Wastewater Technology, Durban University of Technology, P.O. Box 1334, Durban 4000, South Africa

ARTICLE INFO

Article history:
Received 18 May 2016
Received in revised form 22 June 2016
Accepted 23 June 2016
Available online 25 June 2016

Keywords:
Biosynthesis
Jacaranda mimosifolia flowers extract
Zinc oxide nanoparticles
Antibacterial activity

ABSTRACT

The naturally occurring biomolecules present in the plant extracts have been identified to play an active role in the single step formation of nanoparticles with varied morphologies and sizes which is greener and environmentally benign. In the present work, spherical zinc oxide nanoparticles (ZnO NPs) of 2–4 nm size were synthesized using aqueous extract of fallen *Jacaranda mimosifolia* flowers (JMFs), treated as waste. The microwave assisted synthesis was completed successfully within 5 min. Thereafter, phase identification, morphology and optical band gap of the synthesized ZnO NPs were done using X-ray diffraction (XRD), high resolution transmission electron microscopy (HRTEM) and UV–Visible spectroscopy techniques. The composition of JMFs extract was analyzed by gas chromatography–mass spectrometry (GC–MS) and the ZnO NPs confirmation was further explored with fourier transform infrared spectroscopy (FTIR). The GC–MS results confirmed the presence of oleic acid which has high propensity of acting as a reducing and capping agent. The UV–Visible data suggested an optical band gap of 4.03 eV for ZnO NPs indicating their small size due to quantum confinement. Further, facet specific adsorption of oleic acid on the surface of ZnO NPs was studied computationally to find out the impact of biomolecules in defining the shape and size of NPs. The viability of gram negative *Escherichia coli* and gram positive *Enterococcus faecium* bacteria was found to be 48% and 43%, respectively at high concentration of NPs.

1. Introduction

Nature acts as a "bio-laboratory" which provides ways and insight into the synthesis of advanced nanomaterials using a biomimetic approach. Synthesis of nanoparticles (NPs) with controlled size and morphology is a challenging part which is highly dependent on the design of the protocols. Different viable methodologies have been designed for the fabrication of NPs with unique size dependent properties. The concept of green chemistry and engineering has provided a guidance for the environmentally synthesis which are not harmful to environment and human health [1]. In the past few years, biotemplates from natural sources like microorganisms and plant extracts have been a source of inspiration for designing complex nanomaterials with high surface area and potent applications in commercial products, biosensors, catalysis, as well as environmental technologies [2]. The biological approach is alternative to the chemical methods being greener, energy saving and cost effective. Regarding the stability, the NPs are innoxious due to coating of biological molecules and hence, they are more biocompatible than the NPs prepared by chemical methods [3]. The biomolecules present in the extract of plants act as stabilizing agents in the formation of NPs [4,5].

Among different semiconductors and metal oxides, ZnO is one of the most promising materials because of its unique characteristics which are responsible for novel biological functionalities. In the nanostructure form it has become the focus of attention for research community due to its unique antifungal [6], antibacterial [7], antiviral [8], wound healing [9], UV filtering properties, high catalytic and photochemical activity, excellent stability, biocompatibility, environmental friendliness and low cost [10,11]. Therefore, it is crucial to devise tunable synthesis of ZnO NPs with desired morphology and size to further explore their unveiled potentials thereby enabling researchers to manipulate the present material for the fabrication of devices. The literature provides an insight into different approaches for the fabrication of ZnO nanostructures like gas phase methods which include chemical vapour deposition

* Corresponding authors.
E-mail addresses: dpschem@gmail.com (D. Sharma), ksuvardhan@gmail.com (S. Kanchi), bisettk@dut.ac.za (K. Bisetty).

http://dx.doi.org/10.1016/j.jphotobiol.2016.06.043
1011-1344/

(CVD), physical vapour transport (PVT) and pulsed layer deposition (PLD) [12]. Chemical methods have been found to be cost effective and alternative to gas phase methods. Mechanochemical [13,14], solvothermal [15,16], sol-gel [17,18], precipitation [19], hydrothermal [20,21] and microwave methods [22,23] have been classified under chemical methods. Among these, hydrothermal method is widely used due to green, low cost and low temperature synthesis. This method is modified with the use of capping or templating agents which aid in modifying the shape of NPs by adsorbing on the specific facet of a metal oxide crystal [24].

In the recent years, different types of plant extracts have been reported to be used as reducing or capping agents in the synthesis of NPs. Some of the examples include the eco-friendly synthesis of ZnO NPs using leaves extract of *Pongamia pinnata* [25], *Nerium oleander* [26], aloe leaf broth [27], *Solanum nigrum* [28], apple pectin [29] and aqueous extract of *Vitex negundo L.* [30]. The biomolecules present in the plant extracts act as efficient capping agents thereby playing a pivotal and versatile role in the NPs synthesis. The capping agents appear to stabilize NPs by different mechanisms that include electrostatic stabilization, steric stabilization, stabilization by hydration forces, depletion stabilization and stabilization using van der Waals forces. The stabilization of NPs is important for their functions and different applications [31].

Flowers are of great aesthetic value and maintain ecological balance in the environment. They are mainly utilized for their beauty as they radiate different colours to the surroundings. They serve the purpose when they bloom but when once wilt they fall off as trash. *Jacaranda mimosifolia* belongs to Bignoniaceae family and is widely grown in warm parts of the world. It has showy blue or violet flowers and has been found to have antiseptic and antibiotic qualities. Traditionally, the flowers, leaves and barks are used to ease neuralgia and varicose veins and also being scientifically proven to treat leukemia [32]. In the present work, the fallen flowers of *Jacaranda mimosifolia* plant normally regarded as waste were used for the biosynthesis of ZnO NPs for the first time to the best of our knowledge. ZnO nanostructures have been reported to be effective against the growth of bacteria [33]. Thus, the synthesized ZnO NPs were evaluated for the antibacterial activity against gram positive (*Enterococcus faecium*) and gram negative (*Escherichia coli*) bacteria. Generation of reactive oxygen species (ROS) mainly hydroxyl and superoxide radicals resulting in the oxidative stress is found to be the underlying mechanism for the bacterial cell death or static growth. The release of metal ions on interaction with the cellular components contributes to the bioactivity of the NPs [34]. To elucidate the contribution of oleic acid in the formation of ZnO NPs, its adsorption on different facets of ZnO was carried out computationally as the NP shape and size is dependent on the exposure of different facets of a crystal.

2. Experimental

2.1. Chemicals and Reagents

Zinc gluconate hydrate ($C_{12}H_{22}O_{14}Zn.xH_2O$, purity 97%), sodium hydroxide (NaOH, purity ≥98%) and methanol (CH_3OH, HPLC grade, ≥99.9%) were purchased from Alfa Aesar, Fluka and Sigma Aldrich, respectively. Phosphate buffered saline (PBS) tablets (pH 7.4) were acquired from Sigma Aldrich. Ultra-pure deionized water from PURITE (18 MΩ) system was used in all the experiments.

2.2. Synthesis of ZnO NPs Using the Extract of Jacaranda mimosifolia Flowers

The extract used in the synthesis of ZnO NPs was prepared by dissolving 1.0 g of dried and powdered *Jacaranda mimosifolia* flowers (collected in Durban, South Africa) in 100 mL deionized water and heating at a constant temperature of 90 °C for 1 h on a magnetic stirrer with a hot plate. The extract was filtered and used further in the synthesis. In a typical experiment, to 100 mL of zinc gluconate hydrate (0.1 M), 100 mL of *Jacaranda mimosifolia* flowers (JMFs) extract and 100 mL of NaOH (0.4 M) was added while stirring the mixture for 15 min. The mixture was then exposed to microwave irradiation for 5 min in a microwave oven (SAMSUNG ME9114W operating at 100% power of 1000 W and frequency of 2.45 GHz). The use of microwave irradiations offers homogenous heating, rapid and facile synthesis. The formation of ZnO NPs was indicated by the milky white precipitate powder which was filtered and subsequently washed with ethanol and deionized water. The final product was dried in an oven at a constant temperature of 60 °C for about 3 h. To know the effect of capping agent present in the extract, ZnO NPs were synthesized using 0.1 M zinc gluconate hydrate and 0.4 M NaOH without the use of extract keeping the reaction conditions same.

2.3. Materials Characterization

X-ray diffraction study was carried out using a Bruker AXS D8 diffractometer with CuKα radiation (λ = 1.5418 Å) at 40 kV over a 2θ range from 10° to 70° at a scanning rate of 0.05 min^{-1}. The size and morphology of the ZnO NPs was investigated by high resolution transmission electron microscope (HRTEM) model JEM 2100 (MAX OXFORD Instruments) equipped with a LaB_6 emitter. The samples were dispersed in distilled water and ultrasonicated for 30 min before analysis following the standard protocol. The absorption studies were carried out on a UV 2450 Spectrophotometer (Shimadzu, Japan) within the wavelength ranging from 200 to 800 nm. The colloidal solution of the sample was prepared by dissolving approximately 1.0 mg of ZnO nanopowder in 50 mL ultra-pure deionized water. FTIR spectra of ZnO NPs samples and extract of JMFs were recorded in the range of 4000–500 cm^{-1} on Varian 800 FTIR Scimitar Series supplied by SMM Instruments (Durban, SA).

To predict the composition of JMFs extract and predominent capping agent, GC–MS analysis of the methanolic extract was carried out. Accurately weighed 1.0 mg of the dried and powdered sample of JMFs was dissolved in methanol and stirred for 30 min followed by filtering through 0.45 μm nylon filter. Finnigan MAT GCQ system with splitless injector mode was employed for the sample analysis. The injector temperature was set at 250 °C and 200 °C for a ZB-5MS fused silica capillary column with dimensions 30 m × 0.25 mm × 1 μm. The carrier gas was helium with flow rate of 1 mL min^{-1} and the amount of sample injected was 1 μL. The MS conditions were as follows: full scan in EI mode (50 to 650 amu), transfer line temperature: 270 °C and ion source temperature: 200 °C. The compounds identified in JMFs extract sample were verified by comparing them to those within the NIST library.

2.4. Adsorption Studies Using Molecular Modeling

To understand the role of capping agents present in the JMFs extract, adsorption studies were carried out using adsorption locator and forcite modules in MATERIALS STUDIO 8.0 [35,36]. The capping agent i.e. oleic acid was sketched in Accelrys Materials Studio software package and geometrically optimized with COMPASS forcefield using forcite module to get the energy minimized structure. Three dimensional (3D) ZnO surfaces (101, 100 and 002) were built by importing the crystal structure of ZnO from the structure library of MATERIALS STUDIO 8.0. The oleic acid molecules were allowed to adsorb on each of the designed ZnO surface by setting up the task to *simulated annealing* with *fine* quality where *adsorbate* was oleic acid with different *loading* values. The COMPASS forcefield was assigned to charges of atoms with *Ewald & group based* summation method. The concentration profile of oleic acid molecules on the ZnO surface was obtained by running forcite calculation on the whole system (oleic acid molecules adsorbed on the surface of ZnO).

2.5. Bacteriological Toxicity Assessment by Standard Plate Count Method/ Colony Forming Units (CFU) Measurements

The viability of ZnO NPs treated and untreated *E. coli* cultures were determined by standard plate count method. The *Escherichia coli* ATCC 25922 and *Enterococcus faecium* ATCC 35667 cells were grown to O.D of 0.6 at 600 nm (35 ± 1 °C, 10^6 CFU mL^{-1}), pelletized by centrifugation (4000 ×*g* for 3 min at 4 °C), washed thrice by phosphate buffer saline (PBS, pH = 7.4) and finally suspended into PBS containing varying concentrations (10, 25, 50, 75, 100 μg mL^{-1}) of NPs synthesized using JMFs extract and without JMFs extract. Bacterial culture in Luria Bertani (LB) broth without NPs served as negative control. The cells were grown for 120 min at 35 ± 1 °C and were serially diluted in PBS at pH 7. The dilutions were plated on LB agar plates. After overnight incubation at 37 °C, the number of CFU was counted manually. All the experiments were conducted in triplicate.

3. Results and Discussion

ZnO NPs were formed via the simple method of alkali precipitation of zinc gluconate where the compounds present in the JMFs extract reduced the formed $Zn(OH)_2$ precursors. The schematic synthesis of ZnO NPs is shown in Fig. 1. The mechanism is explained on the basis that the biomolecules such as fatty acids, phenolic compounds, saponins, alkanoids, flavanoids present in the extract form complexing agents with the precursors which initially starts the process of nucleation forming reverse micelle and then further causing reduction and shaping of NPs [37–39]. The GC–MS results reveals that 1,6 dimethyldecahydro napthalene, oleic acid and citronellyl propionate are predominantly present in the JMFs extract. Based on the GC–MS, purity and fit values, oleic acid was selected as a reducing and capping agent for the synthesis of ZnO NPs. When zinc gluconate was dissolved in water, colourless solution was formed due to the presence of $[Zn(H_2O)_6]^{2+}$ ions. The addition of NaOH produces a white precipitate of ZnO NPs in the core of a micelle. The capping agent acts as a stabilizing agent by adhering onto the surface of NPs forming a protective layer and controlling the particle size [40].

The microwave irradiations act as an efficient, environment friendly and economical heating method for the synthesis of NPs while maximizing the yield. The household microwave ovens also lead to formation of metal and metal oxide NPs with good crystallinity and optical properties [41,42].

In the case of synthesis of NPs, the reaction rate and nucleation are dependent on the heating rate. The microwave heating is an alternative source for rapid volumetric heating with shorter reaction time, high reaction rate, selectivity and yield as compared to conventional heating methods. The enhancement in the reaction rate is caused predominantly by the rapid superheating of the solvent by microwaves. The solvent is also found to play an important role in the microwave-assisted synthesis. The more polar the solvent is higher is its ability to couple with microwave energy, leading to the rapid increase in temperature and fast reaction rate. The dielectric heating effect of microwaves is generated due to dipole moment interaction of the molecules and high frequency electromagnetic radiations. Since, water has a high dipole moment; it is a best solvent for the synthesis of NPs using microwaves [43]. As soon as aqueous solution containing zinc gluconate, extract and NaOH were exposed to microwave heating, the reaction completed within 5 min; there was enhancement in the reaction rate and nucleation which was indicated by the milky white precipitate powder leading to the formation of ZnO seeds.

The formation of NPs take place in two steps, nucleation and growth. When the supersaturation stage is achieved, the system enters the growth phase in which there is no formation of additional nuclei but existing clusters grow larger in size. Subsequently, nucleation and

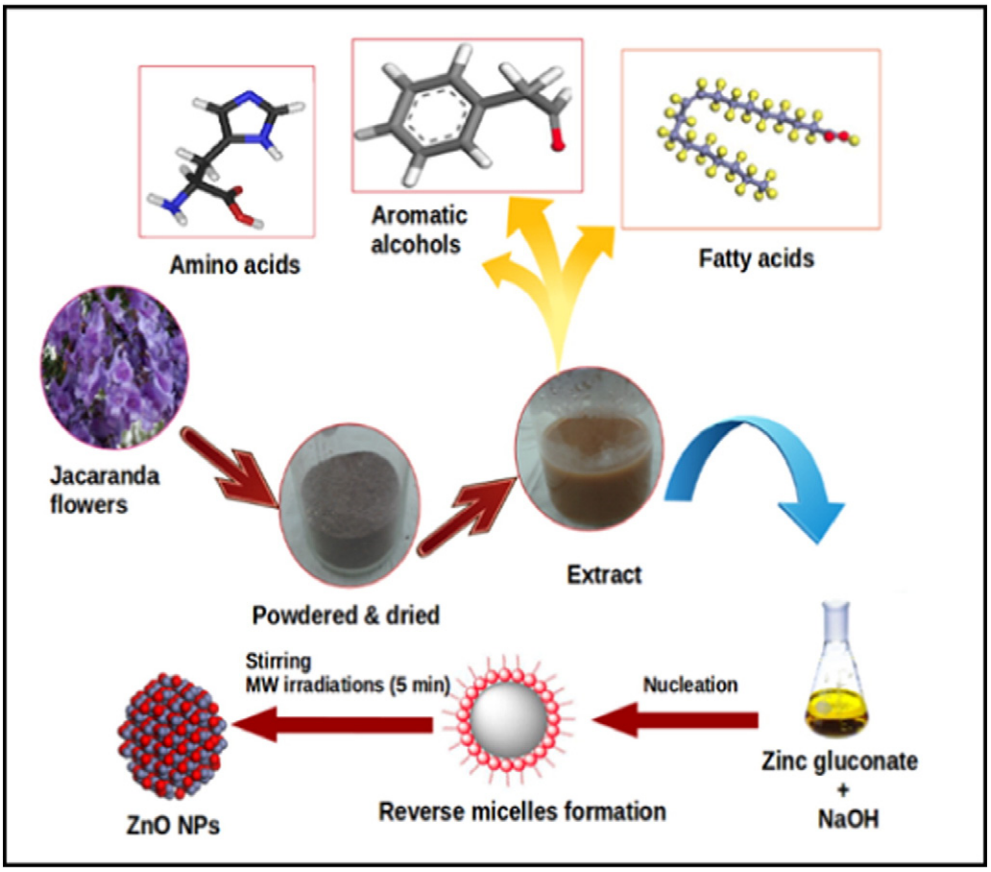

Fig. 1. Schematic representation of synthesis of ZnO NPs using JMFs extract.

growth are influenced by the heating rate, the microwave radiations leads to the formation of large amount of nuclei. Once the nucleation starts, the reaction system enters the growth process and nuclei with small sizes grow rapidly thereby shortening the overall process of formation of NPs. The extract used acts as a capping agent and use of microwave irradiations leads to formation of NPs with smaller size. These seeds assemble together as clusters due to their high surface energy which grow rapidly to form NP aggregates [44].

The XRD analysis of ZnO NPs synthesized using the JMFs extract exhibited typical diffraction peaks at 32.25° (100), 34.90° (002), 36.74° (101), 47.99° (102), 57.06° (110) and 63.31° (103) indexed to the crystalline ZnO wurtzite structure with P63mc space group whereas NPs formed without the use of JMFs extract exhibited peaks at 32.38° (100), 35.08° (002), 36.80° (101), 48.12° (102), 57.14° (110) and 63.42° (103), respectively [45] (Fig. 2). The lattice parameters for the hexagonal unit cell such as d-spacing (d), lattice constants (a, c) and unit cell volume (V) were calculated using the Lattice Geometry Equations [46] and also summarized in Table 1:

$$\frac{1}{d^2} = \frac{4}{3}\left(\frac{h^2 + hk + k^2}{a^2}\right) + \frac{l^2}{c^2} \quad (1)$$

$$V = \frac{\sqrt{3a^2c}}{2} \quad (2)$$

where, *h, k* and *l* are miller indices.

The calculated values of c/a ratio for ZnO NPs (Table 1) are close to ideal value of 1.633 for ZnO hexagonal cell. The deviation from the ideal wurtzite crystal is probably due to lattice stability and ionicity [47].

The morphology and size of the ZnO NPs was demonstrated by HRTEM images. Fig. 3A represents the ZnO NPs in the size range of 2–4 nm synthesized with JMFs extract whereas Fig. 3B shows the ZnO NPs with average diameter of 8–11 nm and spherical morphology prepared without the use of JMFs extract. The dark spots in the micrographs are the NPs clustered together due to their small size. The clear lattice fringe widths with the values of 0.24 nm and 0.26 nm in the HRTEM images (Fig. 3A and B) corresponds to 101 and 002 crystal planes and are indicative of the crystalline nature of ZnO NPs.

The semiconductor band structure of ZnO NPs has been characterized via UV–Visible absorption spectroscopy. Fig. 4 inset shows the UV–Visible spectra of ZnO NPs synthesized with and without JMFs extract showing absorption peaks at 265.91 nm and 278.9 nm, respectively. Therefore to better understand the role of capping agent in the JMFs extract, the optical band gap for the ZnO NPs was calculated using the

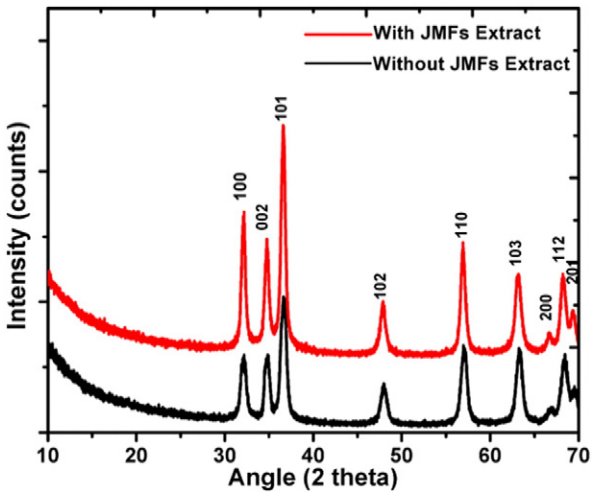

Fig. 2. XRD diffraction pattern of ZnO NPs with and without the use of JMFs extract.

Table 1
Lattice parameters of ZnO NPs synthesized using with and without JMFs extract.

Sample	2θ	hkl	d-spacing (Å)	LP (Å)	UCV (Å^3)
ZnO NPs (with extract)	32.25°	100	2.773	a = 3.205	45.73
	34.90°	002	2.568	c = 5.141	
	36.74°	101	2.443	c/a = 1.604	
ZnO NPs (without extract)	32.28°	100	2.770	a = 3.202	45.42
	35.08°	002	2.555	c = 5.116	
	36.80°	101	2.440	c/a = 1.598	

LP: Lattice parameters; UCV: Unit cell volume.

expression proposed by Tauc, Davis and Mott [48],

$$(h\nu\alpha) = A(h\nu - Eg)^n \quad (3)$$

where, h is Planck's constant, ν is frequency of vibration, α is absorption coefficient, Eg is band gap, A is proportionality constant and n denotes the nature of sample transition. The respective direct band gaps were found to be 4.07 eV and 3.74 eV for ZnO NPs synthesized with and without JMFs extract, probably due to quantum confinement (Fig. 4). With the decrease of the particle size, there is an increase in the energy gap of electronic transitions [49] i.e., as the system becomes more confined, the energy separation between adjacent levels increases and also discrete energy levels arises at the band edges [50].

The FTIR was employed to further probe the role of biomolecules present in the JMFs extract for the formation of ZnO NPs. As shown in Fig. 5, the FTIR spectrum of JMFs extract exhibits broad peak at 3373.12 cm^{-1} corresponding to O—H stretching vibration whereas the peaks at 2942.29 cm^{-1}, 2830.04 cm^{-1}, 1647.43 cm^{-1} and 1031.62 cm^{-1} correspond to C—H stretching, carbonyl group (C═O) and C—H bending, respectively. The peaks related to the following functional groups in the extract indicate the existence of different biomolecules; the major being oleic acid which was further confirmed through GC–MS analysis. The spectra of ZnO NPs synthesized with and without JMFs extract shows characteristic peaks of Zn—O stretching at 745.54 cm^{-1} and 779.45 cm^{-1}, respectively confirming the formation of ZnO NPs [51]. There was also a significant disappearance of peaks corresponding to that of extract in the spectra of ZnO NPs. The weak peak around 1445.85 cm^{-1} was broadened as seen in the spectra of NPs which could be attributed to C—H bending in methanol since the samples were prepared in methanol.

From the literature reports on the synthesis of metal oxide NPs with plant extract [52–54], it is evident that biomolecules play a pivotal role in the reduction of metal oxide salts and stabilization of NPs, but very few identify the biomolecules involved in the process of formation of NPs. In this regard, GC–MS analysis of methanolic extract of JMFs was carried out to identify the biomolecules present in the extract and to understand their impact on the morphology and size of NPs. Fig. 6 illustrates the GC–MS chromatogram of the methanolic extract of the JMFs where different components were identified. In the retention time ranging from 15:03 to 20:03 min where the high intensity peaks were present, the elution order was 1, 6 dimethyldecahydronapthalene, oleic acid and citronellyl propionate. On the basis of purity fit, oleic acid was found to be the most significant capping agent molecule. Therefore, facet-specific binding adsorption studies were carried out to comprehend its role as a capping agent which has been explained in the subsequent section.

3.1. Adsorption of Oleic Acid on the Surface of ZnO NPs

Apart from many studies which focus on the quantum confinement effect of quantum dots such as ZnO NPs, the surface chemistry is very significant in order to understand the physical and chemical properties of NPs. Consequently, the selective interaction of ZnO NPs with capping agents such as oleic acid is critically vital to enhance biocompatibility and viability, making these nanomaterials a suitable candidate in applications involving biological studies. In this paper, we therefore,

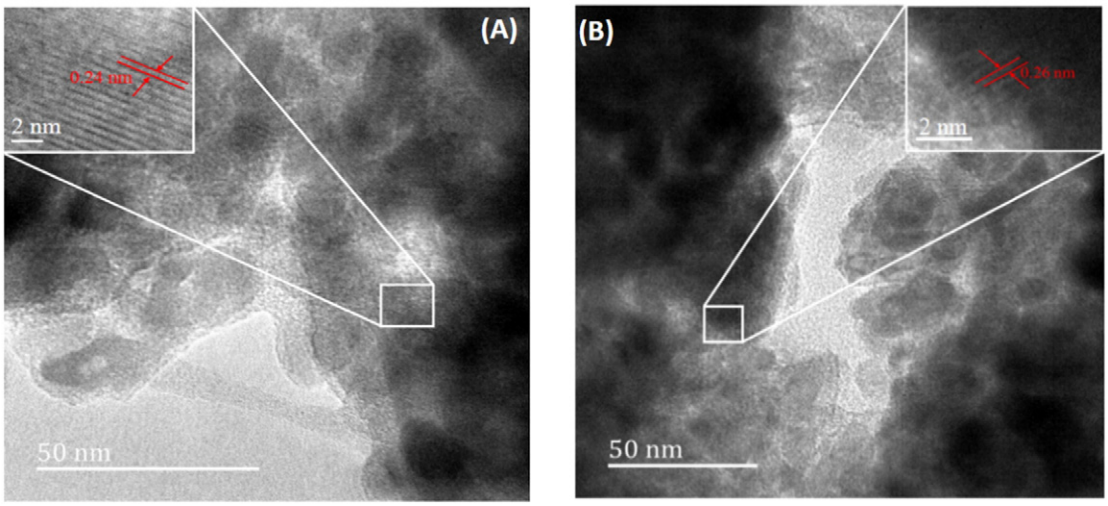

Fig. 3. HRTEM micrographs of ZnO NPs (**A**) with JMFs extract; (B) without JMFs extract.

employed molecular dynamics to demonstrate that physical and chemical properties of ZnO nanocrystal is induced by surface chemistry which preferably lead to isotropic and anisotropic nanomaterials. The role of capping agent in defining the size and shape was studied by simulating three crystal lattice parameters as shown in Fig. 7. It was demonstrated that ZnO NPs have varied shape evolution and potentially different facets which lead to facet-driven growth of ZnO to different shapes, thereby fine-tuning their optical properties. For many studies, facets such as (111) and (101) are highly studied because of their potential to drive preferential growth of nanomaterial which is the main contributor of their varied optical properties [55]. In order to simulate the variation of the reaction parameters, three facets, (002), (100) and (101), were studied. It was demonstrated that as the concentration of oleic acid was increased, the strength of adsorption favoured the (101) facet. The preferential passivation of (101) facet was evident from concentration profile shown in Fig. 8C. In these Fig. 8(A, B and C), it can be seen that the average distance of oleic acid on the surface of ZnO cluster were located within the distance of an average of 1.4 Å as compared to other facets on which the oleic molecules were located on the varying distance of 4 and 9 Å for (100) and (002) facets, respectively. These results confirmed previous study which indicated that the presence of oleic acid could drive the preferential growth of zinc oxide nanomaterials to nanorods array and other structures [56].

The most favoured model from Fig. 7 was obtained by further calculating the interaction energy of each model. The interaction ($E_{interaction}$) was calculated as follows:

$$E_{interaction} = E_{complex} - (E_{ligand} + E_{surface}) \quad (4)$$

$E_{complex}$ is the energy of the surface and oleic acid, E_{ligand} is the energy of the oleic acid and $E_{surface}$ is the energy of the surface (ZnO-100, ZnO-002 and ZnO-101) without ligands. The negative $E_{interaction}$ values indicate an attractive or strong oleic acid to ZnO interactions. The interaction energies of models depicted in Fig. 7 were calculated using Eq. (4) as presented in Table 2.

The interaction energies in Table 2 reveals the trend, ZnO-101 > ZnO-002 > ZnO-100. The high interaction for ZnO-101 symbolizes that oleic acid binds stronger on ZnO-101 surface than the other surfaces. Although, the interaction gives the general picture of the interaction of oleic acid with ZnO surface, this trend does not eliminate the fact that all surfaces can potentially interact with oleic acid but to the lesser extent than the 101-surface. This is merely an indication that more oleic

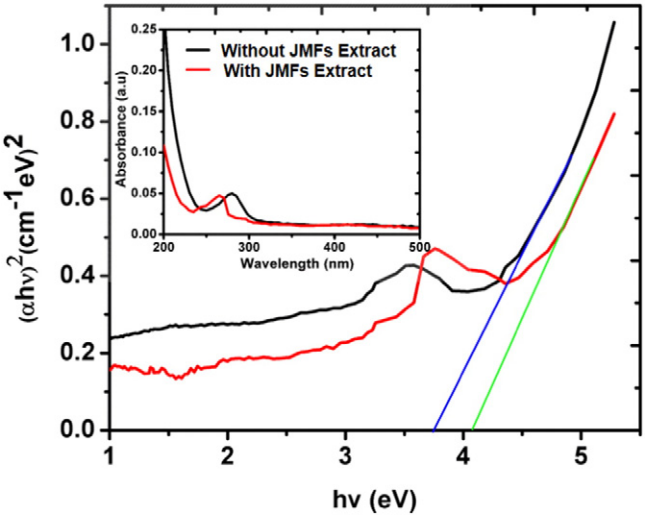

Fig. 4. Tauc Plot of ZnO NPs with and without use of JMFs extract showing inset of UV–Vis spectra.

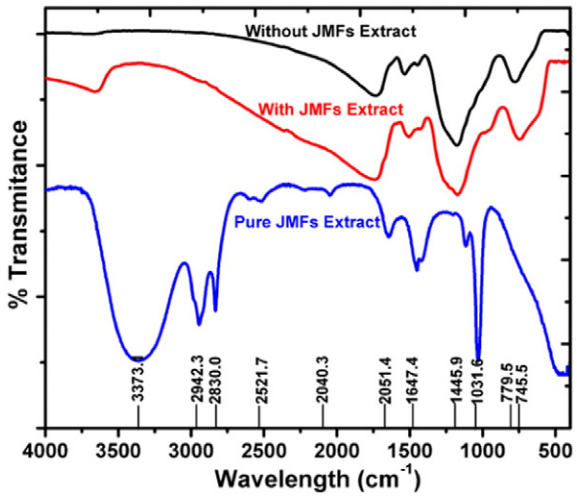

Fig. 5. FTIR spectra of methanolic pure JMFs extract , ZnO NPs synthesized with and without the use of extract.

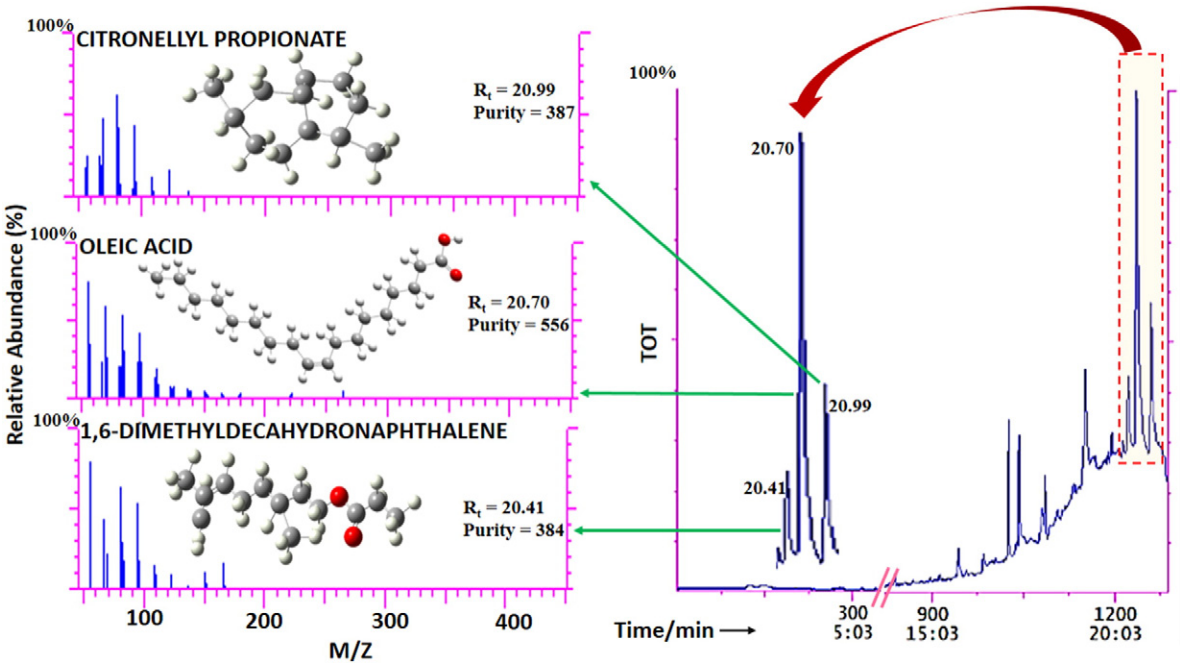

Fig. 6. GC–MS chromatogram of methanolic extract of JMFs.

acid molecules shall interact with 101 surfaces leaving the other surfaces (ZnO-002 and ZnO-100) with less number of oleic acid molecules. The concentration profiles of different facets of ZnO shown in Fig. 8A, B and C are good indicators to probe the vicinity of functional groups on the surface of metal oxide. The concentration profile proved that the affinity of the oleic acid is more pronounced on 101 facet, which are situated closer to the surface by about 1.4 Å. This selective adsorption was reported elsewhere to drive the rapid growth of ZnO NPs to pencil-like nanorods [57].

3.2. Antibacterial Activity of Synthesized ZnO NPs

Antibacterial property of ZnO NPs was analyzed by treating bacterial culture (gram negative and gram positive) with varying concentration

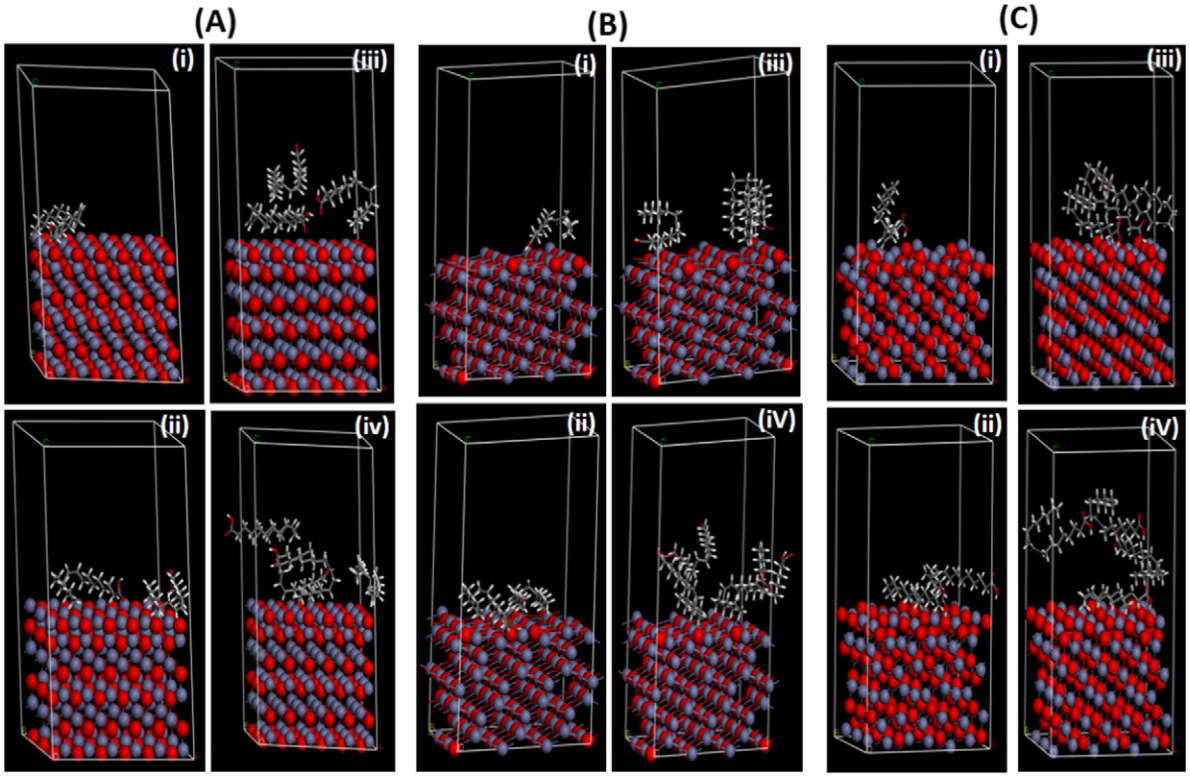

Fig. 7. Adsorption of oleic acid molecules onto different surfaces (A) 002 (B) 100 and (C) 101 of ZnO clusters.

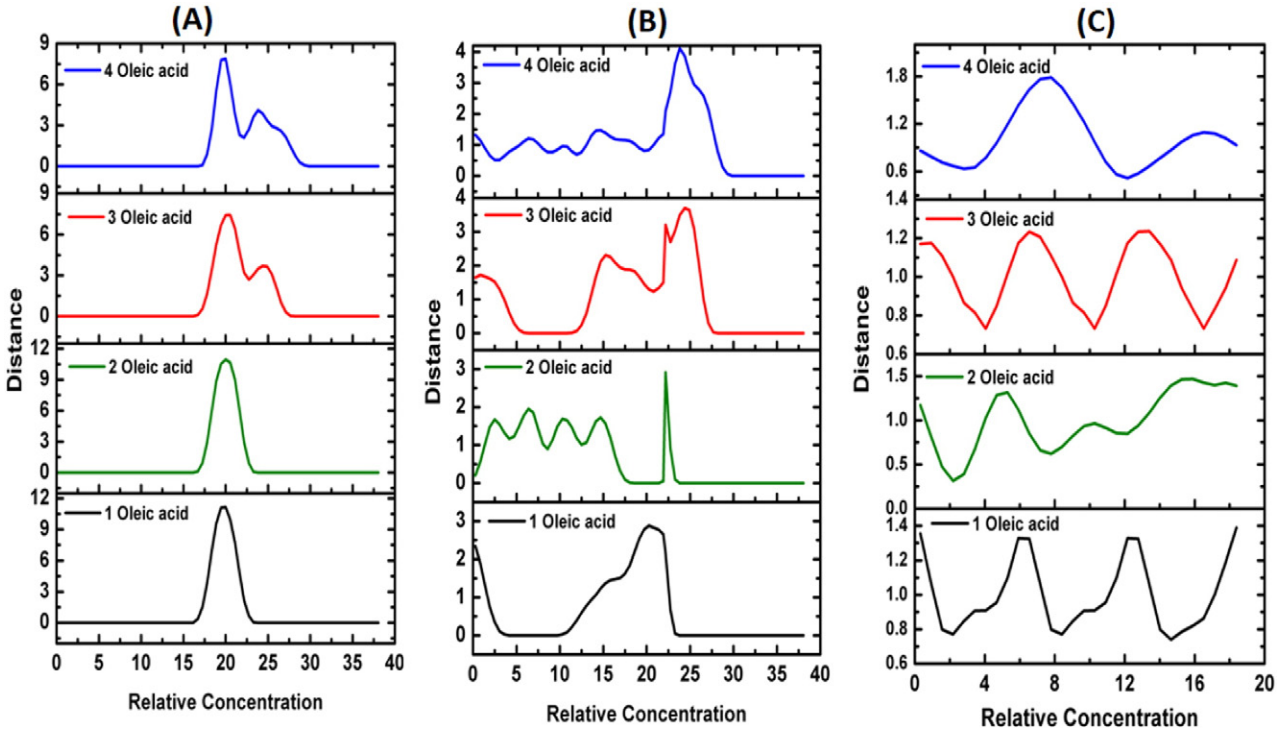

Fig. 8. Concentration profile of oleic acid molecules adsorbed on (A) 002 (B) 100 (C) 101 facets of ZnO.

of NPs (10–100 μg mL^{-1}) and viability was assessed by standard plate count method. It was observed that as the concentration of ZnO NPs increased, colony forming units (CFU) count of gram negative (*Escherichia coli*) and gram positive (*Enterococcus faecium*) bacterial cultures decreased in the standard plate count method. ZnO NPs prepared using JMFs extract and without JMFs extract exhibited antibacterial property as evident from the present results (Fig. 9A–B). The viability of *E.coli* and *E. faecium* was assessed in the presence of different concentrations of NPs (10–100 μg mL^{-1}). The percent viability of the ZnO NPs exhibited stronger antibacterial activity against gram positive *E. faecium* than against gram negative *E. coli.* The results reported were in concurrence with previously published reports showing the antibacterial activity of ZnO NPs [58]. The important reason could be the difference in the cell wall structure of gram positive and gram negative bacteria. The cell wall of gram positive bacteria is normally composed of peptidoglycan which forms 80% of the cell wall. The remaining 10–20% of the cell wall is composed of teichoic acids, other proteins and lipopolysaccharides which is outer membrane. In the case of gram negative bacteria, peptidoglycan forms 10% of the cell wall but the outer membrane is composed of 50% lipopolysaccharides, 35% phospholipids and 15% lipoproteins. Thus, outer membrane in gram negative bacteria is tightly packed, hence, providing protection and sensitivity to antibacterial agents [59]. Moreover, the antibacterial activity depends on the size of NPs and also infectivity and sensitivity of different strains vary [60]. Therefore, ZnO NPs synthesized using the extract of JMFs were in the range of 2–4 nm size as compared to NPs fabricated in the absence of JMFs extract (8–11 nm) and the *E. faecium* ATCC 35667 strain has been reported to be more pathogenic than *E. coli* ATCC 25922.

Table 2
Adsorption energy of oleic acid molecules on the facets of ZnO nanocluster.

Facet	Adsorption energy (kcal/mol) of number of oleic acid molecules			
	1	2	3	4
100	−31.242	−65.724	−97.977	−121.28
002	−45.668	−92.127	−135.95	−167.62
101	−64.297	−128.69	−178.6	−221.92

E.coli and *E. faecium* when treated with 100 μg mL^{-1} concentration of ZnO NPs synthesized without extract were found to be 59% and 51% viable (Fig. 9B) whereas the percent viability was 48% and 43%, respectively for the NPs synthesized using JMFs extract (Fig. 9A). The results indicated that the antimicrobial property of JMFs extract mediated synthesized ZnO NPs was higher than that of the NPs synthesized without JMFs extract at higher concentrations (Fig. 9A–B).

Furthermore, there was statistically significant difference in cell viability at 100 μg mL^{-1} in *E.coli* and *E. faecium* when treated with ZnO NPs using extract ($p = 0.0448$). Similar trend was observed for concentrations 75, 50, and 25 μg mL^{-1} of NPs.

4. Conclusions

The results presented in the present work demonstrate the biosynthesis of ZnO NPs with a narrow size range of 2–4 nm using the extract of JMFs. The major finding was the presence of oleic acid as a capping agent in the synthesis of ZnO NPs, identified by GC–MS and FTIR. The peaks corresponding to the oleic acid and ZnO NPs were well depicted in the FTIR spectra as well. The capping agent, oelic acid was found to stabilize the resulting NPs. Furthermore, the other identified molecules like 1,6 dimethyldecahydronapthalene and citronellyl propionate could also function as capping agents. The second major finding is the facet specific binding of the oleic acid molecule on to the different surfaces of the ZnO. It was established on the basis of interaction energy and concentration profile that oleic acid preferred to adsorb on to (101) facet of ZnO as compared to the other (002) and (100) facets. This would lead to the understanding of the selective adsorption of molecules on to the surface of different NPs thereby driving into the formation with varied shapes and sizes.

The oleic acid stabilized ZnO NPs showed fairly good antibacterial activity against both gram negative *E. coli* and gram positive *E. faecium* bacteria. The antibacterial activity was pronounced in the case of gram positive bacteria (*E. faecium*) as the NPs could penetrate easily through the outer membrane due to the less compact nature as compared to that of gram negative bacteria. The synthesis reported here is reproducible in

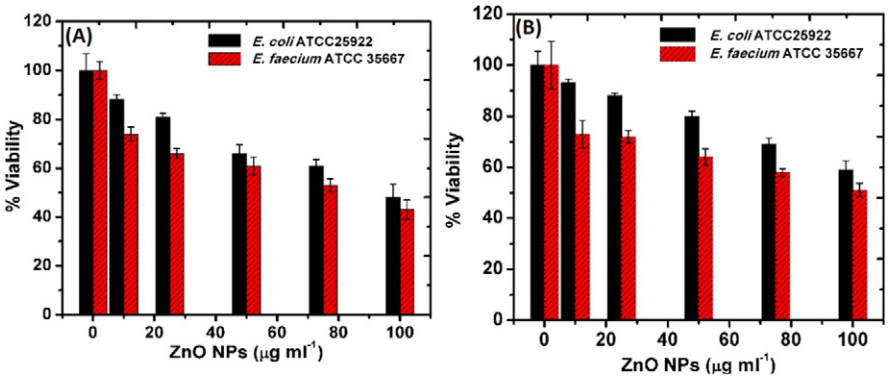

Fig. 9. Viability of bacteria in the presence of ZnO NPs synthesized using (**A**) JMFs extract, (B) without JMFs extract.

short time, cost effective and environmentally safe as it makes use of extract from the fallen waste JMFs for the first time.

Acknowledgements

Our grateful acknowledgement goes to Mr. S. R. Chetty for the GC–MS analysis; Durban University of Technology and National Research Foundation of South Africa for the financial support. We also thank the Centre for High Performance (CHPC), Cape Town, South Africa for the access to the Accelrys MATERIALS STUDIO 8.0 license and national cluster system.

References

[1] J.M. Patete, X. Peng, C. Koenigsmann, Y. Xu, B. Karn, S.S. Wong, Viable methodologies for the synthesis of high-quality nanostructures, Green Chem. 13 (2011) 482–519.
[2] M. Francavilla, A. Pineda, A.A. Romero, J.C. Colmenares, C. Vargas, M. Monteleone, R. Luque, Efficient and simple reactive milling preparation of photocatalytically active porous ZnO nanostructures using biomass derived polysaccharides, Green Chem. 16 (2014) 2876–2885.
[3] R. Selvakumar, N. Seethalakshmi, P. Thavamani, R. Naidu, M. Megharaj, Recent advances in the synthesis of inorganic nano/microstructures using microbial biotemplates and their applications, RSC Adv. 4 (2014) 52156–52169.
[4] R.M. Tripathi, A.S. Bhadwal, R.K. Gupta, P. Singh, A. Shrivastav, B.R. Shrivastav, ZnO nanoflowers: novel biogenic synthesis and enhanced photocatalytic activity, J. Photochem. Photobiol. B 141 (2014) 288–295.
[5] S. Ahmed, S. Annu, S. Ikram, S. Yudha, Biosynthesis of gold nanoparticles: a green approach, J. Photochem. Photobiol. B 161 (2016) 141–153.
[6] D. Sharma, J. Rajput, B.S. Kaith, M. Kaur, S. Sharma, Synthesis of ZnO nanoparticles and study of their antibacterial and antifungal properties, Thin Solid Films 519 (2010) 1224–1229.
[7] V. Lakshmi Prasanna, R. Vijayaraghavan, Insight into the mechanism of antibacterial activity of ZnO: surface defects mediated reactive oxygen species even in the dark, Langmuir 31 (2015) 9155–9162.
[8] T. Antoine, Y.K. Mishra, J. Trigilio, V. Tiwari, R. Adelung, D. Shukla, Prophylactic, therapeutic and neutralizing effects of zinc oxide tetrapod structures against herpes simplex virus type-2 infection, Antivir. Res. 96 (2012) 363–375.
[9] A.K. Barui, V. Veeriah, S. Mukherjee, J. Manna, A.K. Patel, S. Patra, K. Pal, S. Murali, R.K. Rana, S. Chatterjee, C.R. Patra, Zinc oxide nanoflowers make new blood vessels, Nanoscale 4 (2012) 7861–7869.
[10] C. Tamuly, I. Saikia, M. Hazarika, M. Bordoloi, N. Hussain, M.R. Das, K. Deka, Bio-derived ZnO nanoflower: a highly efficient catalyst for the synthesis of chalcone derivatives, RSC Adv. 5 (2015) 8604–8608.
[11] X. Sun, Q. Li, J. Jiang, Y. Mao, Morphology-tunable synthesis of ZnO nanoforest and its photoelectrochemical performance, Nanoscale 6 (2014) 8769–8780.
[12] B. Andrey, B. Arne, W. Alexander, W. Andreas, Fabrication of ZnO Nanostructures, Zinc Oxide Nanostructures, Pan Stanford Publishing, 2014 1–42.
[13] S. Liming, B. Ningzhong, Y. Kazumichi, D. Kazunari, G. Arunava, A.G. Craig, Direct synthesis of ZnO nanoparticles by a solution-free mechanochemical reaction, Nanotechnology 17 (2006) 5117.
[14] J. Lu, K.M. Ng, S. Yang, Efficient, one-step mechanochemical process for the synthesis of ZnO nanoparticles, Ind. Eng. Chem. Res. 47 (2008) 1095–1101.
[15] X. Bai, L. Li, H. Liu, L. Tan, T. Liu, X. Meng, Solvothermal synthesis of ZnO nanoparticles and anti-infection application in vivo, ACS Appl. Mater. Interfaces 7 (2015) 1308–1317.
[16] T. Ghoshal, S. Biswas, M. Paul, S.K. De, Synthesis of ZnO nanoparticles by solvothermal method and their ammonia sensing properties, J. Nanosci. Nanotechnol. 9 (2009) 5973–5980.
[17] M. Lima, D. Fernandes, M. Silva, M. Baesso, A. Neto, G. de Morais, C. Nakamura, A. de Oliveira Caleare, A. Hechenleitner, E. Pineda, Co-doped ZnO nanoparticles synthesized by an adapted sol–gel method: effects on the structural, optical, photocatalytic and antibacterial properties, J. Sol-Gel Sci. Technol. 72 (2014) 301–309.
[18] Y.L. Zhang, Y. Yang, J.H. Zhao, R.Q. Tan, P. Cui, W.J. Song, Preparation of ZnO nanoparticles by a surfactant-assisted complex sol–gel method using zinc nitrate, J. Sol-Gel Sci. Technol. 51 (2009) 198–203.
[19] Y. Wang, C. Zhang, S. Bi, G. Luo, Preparation of ZnO nanoparticles using the direct precipitation method in a membrane dispersion micro-structured reactor, Powder Technol. 202 (2010) 130–136.
[20] D. Ramimoghadam, M.Z. Bin Hussein, Y.H. Taufiq-Yap, Hydrothermal synthesis of zinc oxide nanoparticles using rice as soft biotemplate, Chem. Cent. J. 7 (2013) 136.
[21] M. Søndergaard, E.D. Bøjesen, M. Christensen, B.B. Iversen, Size and morphology dependence of ZnO nanoparticles synthesized by a fast continuous flow hydrothermal method, Cryst. Growth Des. 11 (2011) 4027–4033.
[22] D. Sharma, S. Sharma, B.S. Kaith, J. Rajput, M. Kaur, Synthesis of ZnO nanoparticles using surfactant free in-air and microwave method, Appl. Surf. Sci. 257 (2011) 9661–9672.
[23] I. Bilecka, P. Elser, M. Niederberger, Kinetic and thermodynamic aspects in the microwave-assisted synthesis of ZnO nanoparticles in benzyl alcohol, ACS Nano 3 (2009) 467–477.
[24] S.K. Ramakrishnan, M. Martin, T. Cloitre, L. Firlej, C. Gergely, Design rules for metal binding biomolecules: understanding of amino acid adsorption on platinum crystallographic facets from density functional calculations, Phys. Chem. Chem. Phys. 17 (2015) 4193–4198.
[25] M. Sundrarajan, S. Ambika, K. Bharathi, Plant-extract mediated synthesis of ZnO nanoparticles using *Pongamia pinnata* and their activity against pathogenic bacteria, Adv. Powder Technol. 26 (2015) 1294–1299.
[26] T.R. Lakshmeesha, M.K. Sateesh, B.D. Prasad, S.C. Sharma, D. Kavyashree, M. Chandrasekhar, H. Nagabhushana, Reactivity of crystalline ZnO superstructures against fungi and bacterial pathogens: synthesized using *Nerium oleander* leaf extract, Cryst. Growth Des. 14 (2014) 4068–4079.
[27] S. Gunalan, R. Sivaraj, V. Rajendran, Green synthesized ZnO nanoparticles against bacterial and fungal pathogens, Prog. Nat. Sci.: Mater. Int. 22 (2012) 693–700.
[28] M. Ramesh, M. Anbuvannan, G. Viruthagiri, Green synthesis of ZnO nanoparticles using *Solanum nigrum* leaf extract and their antibacterial activity, Spectrochim. Acta A Mol. Biomol. Spectrosc. 136 (Pt B) (2015) 864–870.
[29] A.-J. Wang, Q.-C. Liao, J.-J. Feng, P.-P. Zhang, A.-Q. Li, J.-J. Wang, Apple pectin-mediated green synthesis of hollow double-caged peanut-like ZnO hierarchical superstructures and photocatalytic applications, Cryst. Eng. Comm. 14 (2012) 256–263.
[30] S. Ambika, M. Sundrarajan, Green biosynthesis of ZnO nanoparticles using *Vitex negundo* L. extract: Spectroscopic investigation of interaction between ZnO nanoparticles and human serum albumin, J. Photochem. Photobiol. B 149 (2015) 143–148.
[31] B. Ajitha, Y.A. Kumar Reddy, P.S. Reddy, H.-J. Jeon, C.W. Ahn, Role of capping agents in controlling silver nanoparticles size, antibacterial activity and potential application as optical hydrogen peroxide sensor, RSC Adv. 6 (2016) 36171–36179.
[32] J. Joselin, T.S.S. Brintha, A.R. Florence, S. Jeeva, Phytochemical evaluation of Bignoniaceae flowers, J. Chem. Pharm. Res. 5 (2013) 106–111.
[33] K. Akhil, J. Jayakumar, G. Gayathri, S.S. Khan, Effect of various capping agents on photocatalytic, antibacterial and antibiofilm activities of ZnO nanoparticles, J. Photochem. Photobiol. B 160 (2016) 32–42.
[34] W. He, H.-K. Kim, W.G. Wamer, D. Melka, J.H. Callahan, J.-J. Yin, Photogenerated charge carriers and reactive oxygen species in ZnO/Au hybrid nanostructures with enhanced photocatalytic and antibacterial activity, J. Am. Chem. Soc. 136 (2014) 750–757.
[35] S. Kirkpatrick, C.D. Gelatt, M.P. Vecchi, Optimization by simulated annealing, Science 220 (1983) 671–680.
[36] S.W. Bunte, H. Sun, Molecular modeling of energetic materials: the parameterization and validation of nitrate esters in the COMPASS force field, J. Phys. Chem. B 104 (2000) 2477–2489.
[37] D. Sharma, S. Kanchi, K. Bisetty, Biogenic Synthesis of Nanoparticles: A Review, Arabian J, Chem, 2015.

[38] W.J. Crookes-Goodson, J.M. Slocik, R.R. Naik, Bio-directed synthesis and assembly of nanomaterials, Chem. Soc. Rev. 37 (2008) 2403–2412.
[39] A.K. Gade, P. Bonde, A.P. Ingle, P.D. Marcato, N. Durán, M.K. Rai, Exploitation of aspergillus Niger for synthesis of silver nanoparticles, J. Biobased Mater. Bioenergy 2 (2008) 243–247.
[40] H. Kumar, R. Rani, Structural and optical characterization of ZnO nanoparticles synthesized by microemulsion route, Int. Lett. Chem. Phys. Astron. 14 (2013) 26.
[41] A. Bhattacharjee, M. Ahmaruzzaman, T. Sinha, Surfactant effects on the synthesis of durable tin-oxide nanoparticles and its exploitation as a recyclable catalyst for the elimination of toxic dye: a green and efficient approach for wastewater treatment, RSC Adv. 4 (2014) 51418–51429.
[42] M.A. Bhosale, D.R. Chenna, J.P. Ahire, B.M. Bhanage, Morphological study of microwave-assisted facile synthesis of gold nanoflowers/nanoparticles in aqueous medium and their catalytic application for reduction of *p*-nitrophenol to *p*-aminophenol, RSC Adv. 5 (2015) 52817–52823.
[43] B. Baruwati, V. Polshettiwar, R.S. Varma, Chapter 7 Microwave-assisted synthesis of nanomaterials in aqueous media, aqueous microwave assisted chemistry, The Royal Society of Chemistry, 2010 176–216.
[44] X. Wang, J. Tian, C. Fei, L. Lv, Y. Wang, G. Cao, Rapid construction of TiO_2 aggregates using microwave assisted synthesis and its application for dye-sensitized solar cells, RSC Adv. 5 (2015) 8622–8629.
[45] K. Yoshio, A. Onodera, H. Satoh, N. Sakagami, H. Yamashita, Crystal structure of ZnO: Li at 293 K and 19 K by X-ray diffraction, Ferroelectrics 264 (2001) 133–138.
[46] C. Suryanarayana, M.G. Norton, Crystal structure determination. II: hexagonal structures, in: C. Suryanarayana, M.G. Norton (Eds.), X-Ray Diffraction: A Practical Approach, Springer US, Boston, MA 1998, pp. 125–152.
[47] H. Morkoç, Ü. Özgür, General Properties of ZnO, Wiley-VCH Verlag GmbH & Co. KGaA, Zinc Oxide, 2009 (pp. 1-76).
[48] J. Tauc, A. Menth, States in the gap, J. Non-Cryst. Solids 8–10 (1972) 569–585.
[49] L. Spanhel, Colloidal ZnO nanostructures and functional coatings: a survey, J. Sol-Gel Sci. Technol. 39 (2006) 7–24.
[50] R. Koole, E. Groeneveld, D. Vanmaekelbergh, A. Meijerink, C. Mello Donegá, Size effects on semiconductor nanoparticles, in: C. de Mello Donegá (Ed.), Nanoparticles: Workhorses of Nanoscience, Springer, Berlin Heidelberg, Berlin, Heidelberg 2014, pp. 13–51.
[51] V. Musat, A. Tabacaru, B.S. Vasile, V.-A. Surdu, Size-dependent photoluminescence of zinc oxide quantum dots through organosilane functionalization, RSC Adv. 4 (2014) 63128–63136.
[52] P. Rajiv, S. Rajeshwari, R. Venckatesh, Bio-fabrication of zinc oxide nanoparticles using leaf extract of *Parthenium hysterophorus* L. and its size-dependent antifungal activity against plant fungal pathogens, Spectrochim. Acta A Mol. Biomol. Spectrosc. 112 (2013) 384–387.
[53] M. Nasrollahzadeh, M. Maham, A. Rostami-Vartooni, M. Bagherzadeh, S.M. Sajadi, Barberry fruit extract assisted in situ green synthesis of Cu nanoparticles supported on a reduced graphene oxide-Fe_3O_4 nanocomposite as a magnetically separable and reusable catalyst for the *o*-arylation of phenols with aryl halides under ligand-free conditions, RSC Adv. 5 (2015) 64769–64780.
[54] M. Atarod, M. Nasrollahzadeh, S.M. Sajadi, Green synthesis of a Cu/reduced graphene oxide/Fe_3O_4 nanocomposite using Euphorbia wallichii leaf extract and its application as a recyclable and heterogeneous catalyst for the reduction of 4-nitrophenol and rhodamine B, RSC Adv. 5 (2015) 91532–91543.
[55] J. Chang, E.R. Waclawik, Colloidal semiconductor nanocrystals: controlled synthesis and surface chemistry in organic media, RSC Adv. 4 (2014) 23505–23527.
[56] A. McLaren, T. Valdes-Solis, G. Li, S.C. Tsang, Shape and size effects of ZnO nanocrystals on photocatalytic activity, J. Am. Chem. Soc. 131 (2009) 12540–12541.
[57] H. Wang, Y. Lian, A mechanistic study of oleic acid-mediated solvothermal shape controllable preparation of zinc oxide nanostructures, J. Alloys Compd. 594 (2014) 141–147.
[58] B. Pang, J. Yan, L. Yao, H. Liu, J. Guan, H. Wang, H. Liu, Preparation and characterization of antibacterial paper coated with sodium lignosulfonate stabilized ZnO nanoparticles, RSC Adv. 6 (2016) 9753–9759.
[59] X. Li, Y. Xing, Y. Jiang, Y. Ding, W. Li, Antimicrobial activities of ZnO powder-coated PVC film to inactivate food pathogens, Int. J. Food Sci. Technol. 44 (2009) 2161–2168.
[60] K.R. Raghupathi, R.T. Koodali, A.C. Manna, Size-dependent bacterial growth inhibition and mechanism of antibacterial activity of zinc oxide nanoparticles, Langmuir 27 (2011) 4020–4028.